Marco Michele Sisto

Optical Distribution Links for OFDM-based Wireless Networks

Thèse de doctorat présentée
à la Faculté des études supérieures de l'Université Laval
dans le cadre du programme de doctorat en Génie Électrique
pour l'obtention du grade de Philosophiæ Doctor (Ph. D.)

Département de Génie Électrique et de Génie Informatique
Faculté Des Sciences Et De Génie
Université Laval
Québec

2009

A Laora, che illumina le mie giornate

A Iris, che mi ha dato paziente supporto

Alle mie nonne, a cui devo la persona che sono

E un pensiero vola in cielo per te, madre.

Abstract

We present a study of radio over fibre (ROF) distribution links for indoor and campus wireless networks employing standard IEEE 802.11a orthogonal frequency division multiplexing (OFDM) modulated RF signals. ROF distribution links are an enabling technology for the implementation of centralized network management, which allows the application of several advanced network management techniques aimed at increasing the wireless communication rate and the number of simultaneous users supported by the wireless network. Also, ROF links should enable an extensive use of antenna arrays in multi-input multi-output (MIMO) or beam-former configurations. In this context, we study optical links with external modulators and optical amplifiers, exploring their performance in terms of noise, RF gain and linearity in order to identify under which conditions the link has minimum impact on the OFDM signal quality. We give particular attention to the optimization of the modulator bias, which we prove has the potential to significantly improve the link gain, noise and linearity. In particular, the link gain is increased when the modulator bias is shifted in order to reduce the optical amplifier saturation level. Also, bias optimization allows the reduction of the amount of average power transmitted over the fibre, thereby decreasing the impact of stimulated Brillouin scattering (SBS) on the link noise. Finally, the modulator bias can be optimized to increase the link linearity through a form of mutual compensation of the distortion from the link fibre and the distortion introduced by the modulator itself.

In the last part of this work, we explore the potential benefits of all-optical manipulation and filtering of RF signals, in order to integrate high level functions, such as signal phase and amplitude control for beam-forming, in the optical link itself. We propose a novel all-optical beam-former, which allows for independent adjustment of both amplitude and phase of the signals fed to each antenna in an array. This beam-former features high RF carrier frequency operation, compatibility with double side-band (DSB) modulation systems, good performance/complexity compromise and easy integration with antenna remoting links based on wavelength division multiplexing (WDM) for antenna addressing.

Résumé

Nous présentons une étude sur les réseaux « radio sur fibre » (ROF) pour la distribution de signaux utilisés pour les communications sans fil, et nous analysons plus particulièrement la transmission de signaux utilisant le multiplexage par répartition orthogonale de la fréquence (OFDM), adhérant au protocole standard IEEE 802.11a. Les réseaux de distribution fibrés sont une technologie habilitante pour l'implémentation de réseaux de communication à gestion centralisée. La gestion centralisée des réseaux permet l'application de plusieurs techniques avancées d'optimisation des ressources des réseaux sans fil qui visent à augmenter sensiblement le taux de transmission de données et le nombre d'usagers supportés simultanément. Dans ce contexte, nous étudions les liens optiques à modulation externe utilisant des amplificateurs optiques et nous explorons les performances de ces liens en fonction du bruit, du gain RF et de la linéarité. Nous cherchons à identifier quelles conditions minimisent l'impact du lien optique sur la qualité des signaux OFDM. Nous étudions en particulier les effets de la variation de la tension de polarisation du modulateur, et nous montrons que l'optimisation de ce paramètre peut améliorer le gain, la linéarité et le bruit du lien optique. En particulier, le gain RF du lien est augmenté si le niveau de saturation de l'amplificateur optique varie en fonction du point de polarisation du modulateur. Aussi, l'optimisation du point de polarisation permet de réduire la puissance optique transmise sur le lien : ce qui permet de limiter les effets non linéaires de la fibre telle que la diffusion Brillouin stimulée. Enfin, la polarisation du modulateur peut être optimisée pour améliorer la linéarité du lien, grâce à une forme de compensation mutuelle entre la distorsion causée par la fibre et celle causée par le modulateur lui-même.

Dans la dernière partie de cet ouvrage, nous explorons les possibles avantages des manipulations et filtrages tout-optiques des signaux RF. Cela permet d'intégrer dans les réseaux ROF des fonctions avancées telles que la manipulation de l'amplitude et de la phase des signaux RF pour le contrôle du diagramme de rayonnement d'un réseau d'antennes. Nous proposons un nouveau type de ligne à délai tout-optique qui permet l'ajustement indépendant de l'amplitude et de la phase des signaux injectés en chaque antenne du réseau, qui supporte des fréquences de porteuse RF élevées, et qui permet une intégration facile dans les liens ROF.

Acknowledgements

A thesis is never solely the creation of the author: this work would not have been possible without the support and encouragement of many friends, colleagues and professors that worked and had fun with me in the last few years. First of all, I would like to express my deep and sincere gratitude to my supervisor, Professor Sophie LaRochelle, for her serious and experienced guidance on this research topic. In 2001 she first welcomed me in COPL, and she gave me a chance to work with her research group. Indeed, a group that deserves to play in the "major league" of research in optics, formed by great researchers and friends. Sophie, I thank you also for ensuring my continuous funding along the years of my studies.

I would like to sincerely thank my co-supervisor, Professor Leslie A. Rusch. Indeed, this work would not have been possible without her support, encouragement and guidance. I must thank her twice for the amazing chance she gave me to work for few months in Intel: an unforgettable and highly formative experience, so important for a young researcher like me.

Another coworker and friend I really want to thank is Dr. Philippe Giaccari, with whom I've had the chance to talk a lot about my work. Along these chats, Philippe's critical thinking and scientific judgment several times turned into "disturbing" questions that challenged my conclusions. Answering to those questions helped me a lot to clarify and polish my thoughts. Philippe is a great fiend, with a fantastic taste for good food and good music.

Many thanks to Professors Pierre Tremblay and Jerome Genest: very good teachers and friends. I have been using all the time the notions of optoelectronics and laboratory practice that they taught me. Also, during our chats in lunchtime, many times they enlightened me with their strictly scientific approach to the most varied topics: from very serious discussions on the future of oil-based car fuel to the much hilarious calculation of the optimum walk speed under a rain shower that would allow to stay dry as much as possible, and it is not necessarily the speed of light. Those chats were enlivened by many other friends as Erik Kretschmer, Simon A. Roy, Philippe Saucier, Philippe Giaccari, and others whose name I forgot but not the good moments spent

together.

Many friends at COPL helped me a lot not only with my scientific formation, but also by welcoming and integrating me as an immigrant with little knowledge of french language. A great merci to Serge Doucet for his invaluable help in the lab: he is our Bragg grating master. Many thanks also to José Bernardo Rosas-Fernández, now a research associate in the Photonic System Group at Cambridge, Francesco Vacondio, Amir Ghazisaeidi, Julien Penon, Mohammad Abtahi, Pegah Seddighian, Simon Ayotte, Walid Mathlouthi, Ziad El Sahn, Julien Magne, Nezih Belhadj, Guillaume Brochu, Alexandre Delisle-Simard, Sylvain Boudreau, Youngjae Kim and all the others researchers and students of Sophie's and Leslie's groups.

A special thanks to Mohammad Ebrahim Mousa Pasandi, who helped me a lot with the experimental measurements in the last part of my work.

Many thanks also to the technicians and professionals working every day in COPL to support and make our research possible: mostly, I had the pleasure to work with Philippe Chrétien, Patrick Larochelle and Marco Béland.

And last but not least, a very special **grazie!** to my wife Iris, who had so much patience in supporting and encouraging me when the work was not giving the results I wished.

Contents

Acronyms and symbols

Acronyms

AC	access controller
ACI	adjacent channels interference
ACPR	adjacent channel power ratio
AGC	automatic gain control
AP	access point
ASE	amplified spontaneous emission
ARMA	autoregressive moving average
AWG	arrayed waveguide grating
AWGN	additive white gaussian noise
BER	bit error rate
BF	beam-former
CATV	cable TV
CDMA	code division multiple access
CNR	carrier-to-noise ratio
COPL	*Centre d'optique, photonique et laser*
CP	cyclic prefix
CS	central station
CSMA	carrier sense multiple access
CW	continuous wave
CWDM	coarse WDM
DWDM	dense WDM
DANL	displayed average noise level
DFB	distributed feedback
DFB-SC	distributed feedback semiconductor
DFT	discrete Fourier transform
DSB	double side-band
EAM	electroabsorption modulator
EDFA	erbium-doped fibre amplifier
EVM	error vector magnitude
FBG	fibre Bragg grating
FCC	federal communications commission

FEC	forward error correction
FFT	fast Fourier transform
FSR	free spectral range
FWM	four-wave mixing
Gbps	gigabits per second
GPIB	general purpose interface bus
GSM	*Groupe Spécial Mobile*
GT	Gires-Tournois
GT-CC	Gires-Tournois with coupled cavities
GTE	General Telephone and Electronics
HD3	third order harmonic distortion
ICI	inter-carrier interference
IMD3	third order intermodulation distortion
IDFT	inverse discrete Fourier transform
IEEE	Institute of Electrical and Electronics Engineers
IETF	Internet Engineering Task Force
IFFT	inverse fast Fourier transform
ISM	industrial, scientific & medical
ISI	inter-symbol interference
LAN	local area network
LOS	line of sight
MAC	media access control
Mbps	megabits per second
MIMO	multi-input multi-output
M-QAM	quadrature amplitude modulation of order M
MMF	multimode fibre
MZ	Mach-Zehnder
NF	noise figure
NRZ	non-return to zero
OFDM	orthogonal frequency division multiplexing
OMD	optical modulation depth
ONA	optical network analyzer
OOK	on-off keying
OSA	optical spectrum analyzer
PA	power amplifier
PAPR	peak-to-average-power ratio
PSD	power spectral density
QAM	quadrature amplitude modulation
QoS	quality of service
QPSK	quadrature phase-shift keying

RBW resolution bandwidth

RIN relative intensity noise

RMS root mean square

RN remote node

ROF radio over fibre

SBS stimulated Brillouin scattering

SDMA spatial division multiple access

SIFS short inter frame space

SIPD surface-illuminated photodetector

SIR signal-to-interference ratio

SFDR spurious-free dynamic range

SNR signal-to-noise ratio

SMF single mode fibre

SOA semiconductor optical amplifier

SOI silicon-on-insulator

SPM self-phase modulation

SSB single side-band

TACS total access communications system

TDMA time division multiple access

TS-BF two-stages beam-former

TTD-BF true time delay beam-formers

U-NII unlicensed national information infrastructure

VoIP voice over internet protocol

VSA vector signal analyzer

VSG vector signal generator

W-CDMA wideband code division multiple access (CDMA)

WLAN wireless local area network

WDM wavelength division multiplexing

WTP wireless termination point

XPM cross-phase modulation

Symbols

Symbol	Name	Definition
i	Complex unit	$\sqrt{-1}$
$x^\star$	Conjugate of x	
$\mathsf{Re}\,\{\}$	Real part of a complex number	
$\mathsf{Im}\,\{\}$	Imaginary part of a complex number	
sinc	Cardinal sinus function (unnormalized)	$\mathrm{sinc}\,(x) = \frac{\sin(x)}{x}$
$\sqcap$	Rectangular function	$\sqcap(x-nT)=\begin{cases} 1, & nT<x\leqslant(n+1)T \\ 0, & \text{elsewhere} \end{cases}$
$\mathcal{R}$	Detector Responsivity	
$\triangleq$	Definition symbol	
J_n	Bessel function of the first kind and order n	
$\mathfrak{k}$	Boltzmann's constant	$1.380\,650\,4(24)\times10^{-23}$ J/K
$\boldsymbol{e}$	Elementary charge	$1.602\,176\,487(40)\times10^{-19}$ C

Chapter 1

Introduction

1.1 The evolution of wireless access networks

FIBRE OPTIC TECHNOLOGY proved very well its potential to support the high throughput backbone connections needed by the modern communication networks. Since 1977, when first AT&T and GTE installed fiber optic telephone systems in Chicago and Boston respectively, the scientific and industrial communities have been working to improve the capacity and performance of backbone links, leading to an incredible revolution in the way people communicate. The effects of this revolution have surely not been limited to military applications and high end commercial users, but they have changed common people's everyday life. Just remember that two generations ago there was no way to have a voice communication overseas whereas now millions of simultaneous communications can be supported by a single transoceanic fibre cable.

The communication revolution has been doubled by a great development in access networks, which has led to the development of new services like high speed internet, on demand cable TV and high speed wireless networks. Wireless access networks, which are now ubiquitous, are evolving amazingly rapidly: for example, a new version or amendment of the IEEE local area network (LAN) standard 802.11, commonly known as *WiFi*, has been released about every four years since 1997 [2].

A common trend strongly drives the evolution of both backbone and access networks: users want faster data throughput and an ever better quality of service. The need for faster and more reliable networks is driven by the increasing number of network simultaneous users and diffusion of new applications and functionalities such as, for example, the merging of data, multimedia and voice services. In the first generation of wireless networks, there was a clear separation between wide area networks for voice specialized cellular telephony (like TACS, Total Access Communications System) and

wireless networks for data communications among computers. The performance needs were different: voice networks had to provide low latency, low bandwidth, wide coverage area and to support a high number of subscribers; computer wireless networks needed high bandwidth, but could support a lower coverage area and a lower number of subscribers. Today, in some cases these distinctions are falling due to the increasing diffusion of new multimedia services like videoconferencing and voice over internet protocol (VoIP), which demands both low latency and high transfer bandwidth. Also, computer wireless networks are more and more pervasive and may often merge with and be superimposed on cellphone networks: for example, computer wireless networks may cover a whole city like New York or San Francisco [3, 4]. Finally, the last generation of cellphones offers computer-like functionalities such as access to internet, email and multimedia communications using embedded digital cameras. Furthermore, the wireless networks are now pervasive and today there is a clear tendency to offer ubiquitous connection to the network, indoors as well as outdoors: people want to be connected anywhere and anytime. Also, in the near future some analysts foresee the diffusion of an increasing number of everyday life objects enhanced by the ability to connect to the network and communicate among themselves or with human users. Such a diffusion of the wireless networks in the everyday life demands a significant increase in the amount of traffic the networks must sustain.

The above overview of the evolution of modern wireless networks is far from being complete but it provides a glance at the level of performance needed for upcoming wireless networks:

- High throughput per user. For this parameter, the numbers seems to continually grow: some analysts forecast about 100 megabits per second (Mbps) [5], which could be enough to support multimedia communications. Other analysts push this value as far as 1 gigabit per second (Gbps) [6], which is reached using multi-input multi-output (MIMO) systems.
- Improved link reliability. The link performance should be constant over time and within the space covered by the network.
- Low latency. Modern data networks typically feature poor latency performance. For example, VoIP needs less than 150 ms of communication delay but a mobile user can experience up to 400 ms of delay when moving in a 802.11x network [7].
- High capacity to support a large number of users connected simultaneously.
- Flexibility and scalability: the networks must be able to grow with the number of users and must allow for interoperability with other networks.
- Low deployment cost.

Some of the points raised above must be faced by developing new network protocols, which are outside the scope of this work. However, the architecture of the physical layer

can greatly help in enabling higher network performance. In the next sections, we will show how fibre links can be the base for the next generation of wireless LAN, in the same way that they supported the evolution of the backbone links in the past 30 years.

1.2 Centralized and distributed wireless LANs

While many concepts expressed in this work are general and applicable to several types of wireless networks, from now on we focus our discussion on the most extensively deployed type of data-oriented wireless LANs (or WLANs), which is defined by the IEEE 802.11 protocol family. All IEEE 802.11 WLANs are constituted by some basic functional entities. The Internet Engineering Task Force (IETF), in its effort to classify these functional entities and provide a standard nomenclature [8], defines:

Access Point (AP): An entity that provides access to distribution services via the wireless medium for associated stations. This is a logical entity which encapsulates high level functions like RF signal coding and decoding, media access control (MAC) translation, and network management protocols.

Wireless Termination Point (WTP): The physical entity that contains an RF antenna and the physical layer used to transmit and receive station traffic for the Institute of Electrical and Electronics Engineers (IEEE) 802.11 WLAN access networks. The wireless termination point (WTP) can incorporate the hardware needed to implement the access point (AP) logic functionalities.

Access Controller (AC) or Central Station (CS): In a centralized network architecture, this is the network entity that provides to the WTPs an access to the wired backbone infrastructure, which is typically an Ethernet network.

In the mostly accepted convention, the difference between AP and WTP fades out because in most installed network architectures there is no physical separation between these two entities. In such architectures, called *autonomous architectures* by the IETF, the AP functions are implemented within the WTP hardware, which is, consequently, complex and expensive. Fig. 1.1a shows an example of this architecture. Also, the IETF describes the concept of *centralized architecture*: in one possible embodiment, the WTP is designed as lightweight as possible, incorporating only the radio interfaces while all the logic AP functions are transferred to a central station (CS).

Today, the majority of the installed 802.11 WLANs follow the autonomous architecture with the APs connected to a backbone ethernet network, which is shared with wired equipment. This solution is widely used because the APs can be installed anywhere a wired ethernet cable is available. Hence, the deployment of the wireless network as an extension of pre-existing wired networks is simple and potentially low cost. The

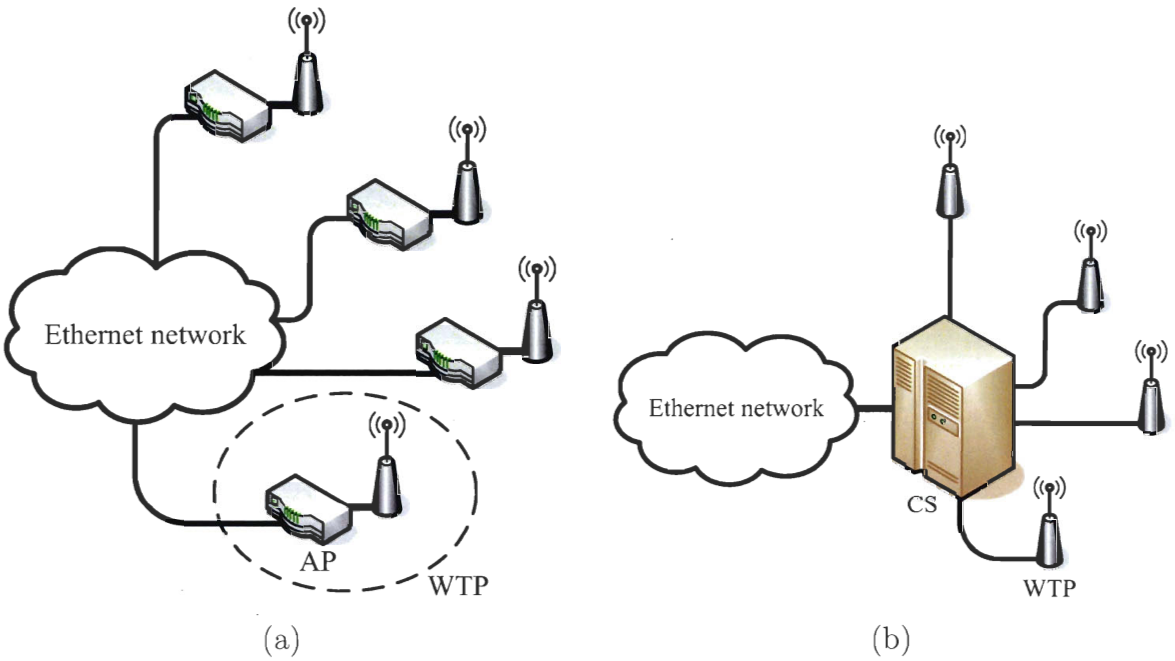

Figure 1.1: Autonomous and centralized architectures. (a) Autonomous architecture: the access points (APs) logic functions are localized at the wireless termination points (WTPs), and separate APs do not intercommunicate. (b) Centralized architecture: the WTPs are simplified down to an RF interfaces and all the APs functions are gathered in a centralized computing unit.

APs are "intelligent" or "autonomous" in the sense that they are standalone devices: each AP implements all the features, settings, and algorithms of a complete network transport device such as a router or a switch. The rest of the network infrastructure does not require wireless-specific awareness [9] and there is no communication or interaction of any sort among the APs [10]. However, the autonomous architecture has some drawbacks, especially for outdoor installations:

- Expensive APs equipment: AP intelligence makes it complex and relatively expensive.
- Expensive maintenance: sensitive processing equipment is part of the APs, which must support uncontrolled environmental conditions and requires on site maintenance.
- Difficult to adapt to new interfaces: network upgrades and enhancements require a visit to the antenna sites and a modification of each AP hardware and software.

Furthermore, the autonomous architecture presents significant challenges for the improvement of network capacity and per-user throughput as required by future wireless networks.

The network capacity may be defined as the aggregate throughput (per-user bitrate multiplied by the number of simultaneous users) that the network can sustain while

respecting a given quality of service (error rate, latency or other parameters). A number of network parameters may affect the link capacity, as:

- Protocol overhead: some of the data transmitted over the network is used only for handoff and management.
- Cell dimension.
- Signal power transmitted by the APs.
- Inter-cell interference.
- Relative position of the cells.
- Available spectrum and number of available non-overlapping channels.

The 802.11 cellular networks available bandwidth is fixed by the federal communications commission (FCC) regulations, and the 802.11x WLAN protocols split the allotted spectrum band in a limited number of channels (e.g., 12 channels for 802.11a [1]). Each channel can serve a limited number of users via multiple access techniques like time division multiple access (TDMA) or carrier sense multiple access (CSMA), used in all 802.11x protocols. Sectoring and cell splitting are commonly used methods for increasing the network capacity by subdividing the network in smaller sections. Hence, in the hypothesis that the users are uniformly distributed over the space covered by the network, the need for channel sharing and multiple access is reduced. This improves the user throughput, not only by ensuring that more users have unshared access to their allotted channel, but also by reducing the MAC overhead needed to manage the channel sharing. However, reducing the cell dimension inevitably increases co-channel interference and adjacent-channel interference from near cells. In fact, it is generally accepted that wireless systems are interference limited and the implementation of techniques to reduce the interference often leads to an increased network capacity [11] and reliability. For example, some installations of 802.11 WLANs try to reduce the inter-cell interference by accurately planning the position of the APs. Network planning is expensive and often suboptimal due to the physical constraint of the space where the network is installed, which may not allow for best positioning of all the APs. Unplanned inexpensive WLANs installations provide much less than optimum capacity and reliability. Controlling the power transmitted by the APs can help in reducing the interference, but decreases the signal-to-noise ratio (SNR) perceived by the users, who receive a power-reduced signal from the APs. Also, in an autonomous multi-cell architecture with several users it may be difficult to identify the optimum values of power to provide the best quality of service. This problem assumes the characteristics of a noncooperative power control game (in the sense of game theory) [12], in which every user wants to receive and transmit at maximum power to improve his communication speed. However, speed is limited by interference from other users who also want to communicate at maximum power and speed.

Network centralization permits the use of near optimal algorithms for resource allocation and management, as for example:

Centralized power control. Centralized power control is used to optimize the power level on a given wireless link and minimize the interference to non-targeted users, while maintaining sufficient transmission quality to the targeted receiver. This is a typical problem that can take advantage of network centralization because power management requires information gathered from all over the network. Hence, global network knowledge of power levels for all the users allows for optimum solution of the power control problem [13], whereas power control based only on "local" knowledge is intrinsically less effective [14].

Multi-cell scheduling and coordination. Intra-cell interference, caused by simultaneous transmission of several users in the same cell, and inter-cell interference, originating from signals in other cells, can all be reduced by scheduling and coordinating the user access to the APs [15]. A centralized scheduler benefits from the global information on the whole network and the high processing power available at the central station [16].

Load balancing and dynamic channel allocation. User load is often unevenly distributed among APs, which results in unfair bandwidth allocation among users. This can be alleviated by intelligently associating users to APs rather than having users greedily associate to APs with best received signal strength [17]. An example of dynamic load balancing based on centralized control capabilities is presented in [18] and offers more efficient systems resources reutilization than conventional methods. Channel allocation schemes are also used to avoid co-channel interference among nearby cells. Centralized dynamic channel allocation has been proven to be more efficient than conventional fixed channel allocation schemes [19].

Antenna diversity algorithms. Macro-diversity is a technique that can be used to combat multi-path fading by allowing a user to connect to more than one AP at the same time [20]. In a centralized embodiment of this technique, the APs are interconnected and exchange data through the central station, which performs the signal equalization and recombination: this provides a so called diversity gain and improves the link quality. Alternatively, the central station can simply select the best link based on received power or SNR. Macro-diversity can also be used to reduce handover of users moving on the edge of different cells of the network [21].

These techniques can reduce interference and improve the network capacity, reliability and general quality of service (QoS), even with limited or no network planning.

The centralized architecture has some other advantages: it reduces the redundant equipment with respect to an autonomous architecture because the network hardware is shared among the APs. Hence, all available computational power is always used

to manage the network even if some APs are inactive. Also, centralization simplifies the maintenance of the hardware, which can be installed in a controlled environment to reduce the probability of a system fault. Thus, most of the network electronics no longer needs to be ruggedized and protected against harsh environment as is the case of autonomous architectures. Finally, centralization allows for easy protocol upgrades and enhancements, which can be performed without physical access to deployed WTPs hardware.

Centralized management also has some drawbacks. First, a centralized architecture requires dedicated network cabling for the WTP-to-CS connections, whose deployment may be challenging and expensive. The dedicated cabling makes the centralized architecture more difficult to scale up with the network coverage growth. By having all the network processing and managing equipment gathered in the same location the maintenance is simplified but the networks becomes much less resilient to a system failure. The strongest limit of the centralized architecture is probably the high computational power needed to properly and timely execute the network management algorithms described before. For example, the power control algorithm exposed in [13] requires the calculations of the eigenvalues of a $n \times n$ matrix, where n is the number of network users. Calculating the matrix eigenvalues to a given normalized precision b is a problem of complexity $O\left(n^3 + n \log^2 n \log b\right)$ [22]. Surely, the Moore's law always reminds us that the computational power available for network management grows with every new generation of processors. Nevertheless, centralized architectures must trade-off the frequency / precision of control updates and the size of the network which can be managed. This can be alleviated using some new approaches, as the agent-based management systems proposed in [23, 24], which reduce the amount of data to be accessed and computed for operating the network management functions. This method still takes advantage of the centralization of all the information on the network but is more efficient in managing large number of users than algorithms based on brute force calculation of an optimum management solution.

From the description above, it is clear that the centralized architecture promises to increase significantly the capacity and reliability of future indoor and campus wireless networks.

1.3 Radio over fiber for centralized architectures

As explained is the previous sections, the centralized architectures gather all the logic and high-level network functions in a CS. In most situations, the dedicated network used to connect the antennas and the CS cannot be built using standard RF coaxial cables because such cables feature significant losses at the relatively high RF frequencies used in wireless communication systems (2.5 GHz and more, see Fig. 1.2). The cable losses are inversely proportional to the cable cross section area, the quality of

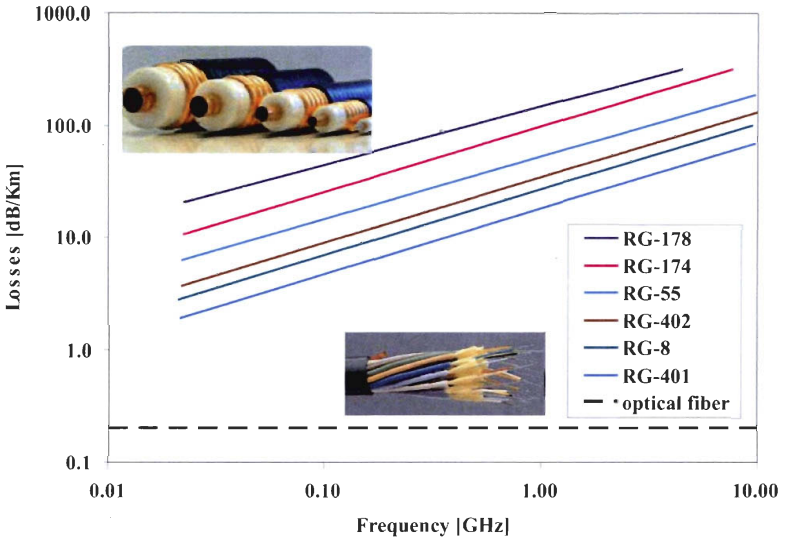

Figure 1.2: Losses of common coaxial cables compared to fiber. From [25, page 708].

the cable dielectric and the cable cost. Hence, low loss cables at high frequency are extremely rigid, heavy, bulky and expensive. Furthermore, such cables have a very limited bending radius, which makes difficult and expensive the cabling of a building for the installation of indoor wireless networks: the cables must be routed into small spaces, inside walls and below room ceilings. The optical fibre has been proposed as a viable alternative because it has THz-large available bandwidth and losses are of the order of 0.2 dB/km, regardless of the signal RF frequency. Furthermore, fiber is thin and light, and the bending radius is in the order of centimeters, which makes indoor cabling much easier and less expensive. Finally, signals in optical fibres are insensitive to electromagnetic interference, unlike those in coaxial cables. Indeed, when using a fibre link, the cost of electrical-to-optical and optical-to-electrical converters at the extremities of the link must be taken into account, but still the optical solutions appears to be advantageous for links longer than few hundreds of meters. This is confirmed by the work of Hunziker, reported in [26, page 134], where the cost of a distribution network with coax cables/repeaters and fiber/optical transceivers are compared (Fig. 1.3). While the fiber-based solution has a higher cost for short links, the coax cable becomes rapidly more expensive as the length of the link is increased, even at relatively low GSM frequencies (900 MHz and 1800 MHz) considered in Hunziker's work. Higher frequencies should exacerbate the cost divergence. As an extreme example, carrier frequencies around the water absorptions peaks (the strongest is at 60 GHz) have attracted some interest in the literature for indoor networks with very small cells [27, 28, 29]. The high propagation loss at 60 GHz allows for good carrier reusability between adjacent cells. For such systems, the distribution network can only be fibre-based because copper-based solutions cannot accommodate for such high carrier frequencies.

Another important advantage of fibre-based antenna feeding links is that the terahertz-wide fibre bandwidth allows the number of installed cables to be minimized

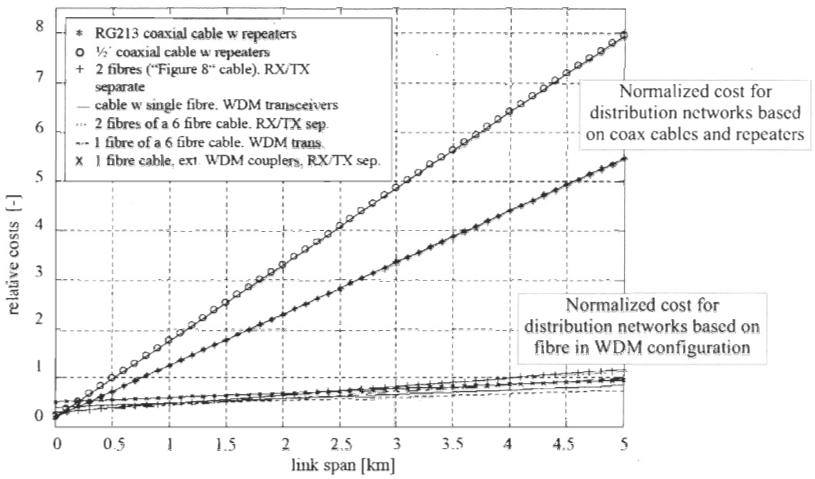

Figure 1.3: Comparison of the normalized cost of copper-based and fibre-based distribution networks, taking into account the hardware cost (transmitters, receivers, repeaters, cables) in the frequency range of 900-1800 MHz (GSM). Installation costs are not considered. From [26, page 134].

by exploiting optical wavelength division multiplexing (WDM). The signals to and from different antennas can be assigned to separate wavelengths and transmitted simultaneously over the same fibre. This well known technique for digital optical links potentially permits fitting a hundred wireless channels on the fibre, because of the relatively small bandwidth needed for *WiFi* formats. For example, in a 20 nm-wide coarse WDM (CWDM) channel it is possible to fit a (theoretical) maximum of 100 double side-band (DSB) or 200 single side-band (SSB) 5 GHz *WiFi* analog channels.

The centralized architecture requires the propagation of the wireless signal from the CS to the antennas (and vice-versa) in its analog RF form, because the signal is modulated and demodulated at the CS. The propagation of analog signals over optical fibre-based links is commonly referred to as radio over fibre (ROF). This definition is quite large and indeed the research domain of ROF is vast and diversified, covering system level research on optical analog network architectures as well as the study of the specific behavior of optical devices with analog signals. The work presented in this thesis belongs to the ROF field, but we focus our research by making some specific choices to best support a specific *WiFi* modulation format and multi-antenna arrays, as discussed in sections 1.4 and 1.5. The choices we make on the design of the ROF link are listed in section 1.6.

1.4 Orthogonal Frequency Division Multiplexing

Centralization and advanced network management are only some of the possible ways to improve the network capacity and per-user throughput: another way is to somehow fight against the properties of the indoor wireless channels which most affect the channel capacity. Indeed, the "air" channel is a hostile propagation medium for fast

mobile data communication: in the general case it is affected by frequency-, space- and time-dependent fading due to dynamic multipath propagation delay spread. Hence, a mobile user experiences a frequency selective channel varying in time and space, which causes inter-symbol interference (ISI) and poor SNR. On the good side, multipath delay spread is a linear effect, so that an adaptive equalizer can, in theory, regenerate a signal affected by ISI, even in a changing environment. However, adaptive equalization is (computing) power hungry and alternative solutions may be preferred for mobile devices, like handheld phones, with limited computing capabilities and/or limited power available from batteries.

The orthogonal frequency division multiplexing (OFDM) is a modulation format designed to be robust to multipath propagation. To form an OFDM symbol, multiple data M-QAM[1] symbols are transmitted simultaneously over orthogonal spectral subcarriers. The orthogonality of the subcarriers is ensured by choosing a frequency spacing that is reciprocal to the OFDM symbol period. Compared to other modulation methods, OFDM symbols have a relatively long time duration, whereas each subcarrier has a narrow bandwidth. The bandwidth of each subcarrier is small enough to assume a flat (nonselective) fading channel in a moderately frequency-selective environments. This allows for greatly simplified signal equalization in time-invariant multipath channels: equalization is reduced to a matrix multiplication of the received spectrum with the inverse of a channel matrix, representing the channel amplitude and phase response for each subcarrier. Then, within a data stream, successive OFDM symbols are kept orthogonal by using a cyclic extension of each OFDM symbol in the time domain. A practical implementation exploits an inverse fast Fourier transform (IFFT) at the transmitter and a fast Fourier transform (FFT) at the receiver.

Although OFDM enables simple equalization, it introduces the following well-known problems. First, the narrowband nature of subcarriers makes the signal robust against frequency selectivity caused by a multipath delay spread, but also makes it relatively sensitive to channel time selectivity, which is due to rapid time variations of a mobile channel. Time variations corrupt the orthogonality of the OFDM subcarrier waveforms and inter-carrier interference (ICI) and ISI may occur. Furthermore, OFDM is sensitive to transmit-receive oscillator mismatch and Doppler effects, both of which cause subcarrier frequency offsets. Finally, the peak-to-average-power ratio (PAPR) of the transmitted signal power is large, which makes the signal sensitive to nonlinear distortion caused by any nonlinear device part of the transmission channel.

Even with these drawbacks, the simple equalization and the spectral efficiency inherent with parallel orthogonal multicarrier transmission have made this modulation format very attractive for high speed wireless links. For example, OFDM is used in the highest performance *WiFi* protocols already approved by the IEEE: the IEEE 802.11a [1]. Also, OFDM will be part of the new protocol IEEE 802.11n, still to be approved in its definitive form. For these reasons, it appears important to see how the OFDM sig-

[1]M-QAM: quadrature amplitude modulation of order M.

nal behaves when used in conjunction with ROF links for centralized wireless networks: these networks will have to support properly this modulation protocol. Compared to a wireless channel, the optical link is strongly nonlinear, and OFDM is particularly sensitive to nonlinear distortions and features a large PAPR. Hence, proper attention should be paid to the comprehension of the impact of the ROF distribution link nonlinearities on the wireless network performance. This topic will be explored in chapter 5. Also, in chapter 2, we review all the most important characteristics of OFDM signals and of the IEEE 802.11a protocol.

The literature work on OFDM over ROF or optical links is quite limited and much more oriented to the description of how the OFDM modulation format can be modified to work better with optical links, instead of trying to optimize the behavior of the link in order to adapt it to support the OFDM modulation without degradation. For example, Djordjevic, Vasic [30, 31], and Lowery [32] presented a SSB OFDM system as an alternative to classical on-off keying (OOK) systems for long-haul and high speed data transmission. In these systems, the simple equalization mechanism offered by OFDM is used to correct for fibre dispersion. The authors show that in linear links OFDM can have about 1.6 dB of power advantage for the same bit error rate (BER) over non-return to zero (NRZ) signaling format. Some preliminary work on the performance and feasibility of OFDM-ROF links have been presented by Berceli [33], who identifies in the link distortion the main source of OFDM BER degradation. Later, Mitchell [34] presented an experimental analysis of the transport of 802.11a signals on a 23 km ROF link with external modulation and optical amplification. He first observed the distortion caused by the optical amplifier dynamic response, but he attributed the measured BER degradation to the amplifier noise. We will analyze the effects of erbium-doped fibre amplifier (EDFA) dynamic response in chapter 5. In [35], Niiho studies the performance of 802.11a and 802.11b signals in a link with direct laser modulation, evaluating the third-order distortion, dynamic range and BER. Niiho also demonstrate the simultaneous transmission of four 802.11a channels in configuration. In [36], Tang investigates the transmission characteristics of a ROF link with electroabsorption modulators, with signals in cellular bands (900 MHz, 1.8 GHz, 1.9 GHz) as well as *WiFi* bands (2.4 GHz, 5.8 GHz). He measured the error vector magnitude (EVM) and BER as a function of the modulator bias to find an optimum value.

1.5 Multi-antenna systems: MIMO and beamforming

Recently, multi-antenna systems attracted much attention because they can increase the wireless link capacity by improving the SNR, or by mitigating (or even taking advantage of) the multipath fading, which is traditionally a pitfall of wireless transmission. Depending on how the antennas are used, we distinguish between three main applications: spatial diversity, beam forming and multi-input multi-output (MIMO).

1.5.1 Spatial diversity

In the presence of multipath fading, the probability of losing the signal decreases with the number of decorrelated radiation sources being used: the signals transmitted by multiple largely spaced antennas (spacing $\gg \lambda$, where λ is the RF carrier wavelength) propagate in a different environment and are affected by fading in different ways. Hence, there is a high probability that at least one antenna receives an unfaded signal for all positions in space. Then, a simple and widespread way to improve performance is to exploit diversity in a multi-antenna receiver by the simple selection of the antenna which receives the most powerful signal. The concept of diversity can be extended to time, frequency and polarization domains.

1.5.2 Beamforming

Several antennas are typically organized in a regularly spaced array. The same signal is sent to each antenna, properly weighted and delayed in order to focus the antenna energy into a desired direction or, in a more general case, to shape the antenna radiation pattern. In this way the antenna gain in the direction of the targeted receiver can be maximized and interference signals can be minimized to improve the signals SNR and signal-to-interference ratio (SIR).

Adaptive beamforming is most commonly applied in outdoor wireless networks. However, it has been also proposed in indoor networks to reduce interference and mitigate multipath fading, hence improving capacity. For example, Wang [37] uses beamforming in indoor networks to fight multipath fading using a diversity combining technique. Morelos-Zaragoza [38] and Katz [39] combine beam forming and block coding to improve the link diversity of indoor channels. Good performance of antenna arrays in suppressing multipath fading in typical indoor environments have been presented in [40] by Jeng. In [41], Hayashi proposes a beamforming-based spatio-temporal equalization technique to compensate for intersymbol interference due to multipath fading. Recently, Chen proposed the use of adaptive arrays in OFDM-based systems [42], in such a way as to exploit the characteristics of the OFDM signal to find the radiation pattern shape that minimizes interference. Interference minimization can be optimized if full control of the antenna radiation pattern is available through simultaneous amplitude and phase control of the antenna elements, in contrast with phase only control [43].

Beamforming techniques can be used to implement spatial division multiple access (SDMA). A rather large body of literature can be found about SDMA solutions; here we only cite [44], where the authors propose beamforming-based SDMA for multi-user indoor wireless networks employing OFDM. Also, in [45], Alastalo reports on the

performance of SDMA in IEEE 802.11a networks.

We present a solution for beamforming in WDM-based ROF links in chapter 6.

1.5.3 MIMO

multi-input multi-output (MIMO) wireless links are believed to be one of the technologies that will resolve the bottleneck of capacity in future traffic intensive wireless networks. A very good review of MIMO can be found in [46]. A MIMO system is equipped with multiple antenna elements both at the receiving and transmitting ends. The signals transmitted and received by each antenna are combined in some way in order to improve the signal quality and data rate. MIMO systems retain the benefits of conventional multi-antenna systems since they can provide a joint transmit-receive diversity gain, as well as a beam-forming gain (if the propagation channel is known). Hence, MIMO systems can potentially offer improved spectral efficiency and link reliability.

However, the advantages of MIMO are more fundamental. The signals to be transmitted by each antenna in the array are derived from the data symbol sequence using space-time coding algorithms, with benefits that go beyond just diversity or beam-forming gain. Diversity and beam-forming improve the capacity indirectly by fighting the fading or improving the SNR; space-time coding provides a direct capacity gain through spatial multiplexing. In a system with N transmitting and M receiving antennas, the information symbols are mixed in time (offering time diversity) and among the antennas (offering spatial diversity). Hence, the data is simultaneously transmitted over $N \times M$ "virtual" channels. The channels can transmit symbol streams that range from independent to fully redundant, depending on a trade off between transmission rate and link reliability. These channels naturally mix together in the air, as they occupy the same frequency band. At the receiver, a channel mixing matrix can be identified using training symbols and used to separate and recover the received data streams. In channels with rich scattering, the space-time coding makes the channels orthogonal, so that the receiver can separate the different streams, yielding a maximum growth in capacity which goes linearly with $\min(M, N)$ [47, 48].

In its simplest form, MIMO can offer the cited capacity gain in flat channels [47]. OFDM can be combined with MIMO to deal with frequency selective propagation environments. Because of its simple channel equalization, OFDM can significantly reduce the complexity of MIMO receivers in wireless broadband systems, with respect to single carrier solutions.

The maximum MIMO capacity is obtained in environments with rich scattering. Indeed, if line of sight (LOS) propagation is dominant, the MIMO "virtual" channels are

highly correlated, channel orthogonality is lost and the link experiences a strong capacity penalty. One proposed solution to this problem is the integration of beamforming technology with the MIMO system [49]: the beamforming is used to improve the environment scattering richness by suppressing the LOS propagation. The beam-former presented in chapter 6 can be used for this function.

1.6 Objectives of this work, assumptions, choices and methodology

All along the preceding sections, we explained the interest of centralized networks, OFDM modulation and multi-antenna systems for the next generation of indoor wireless networks. We also showed that ROF is an enabling technology for network centralization, and we explained that it is important to assess the performance of OFDM modulation in the presence of a ROF distribution link. The main objective of this thesis is to understand the sources of OFDM signal quality degradation in a ROF link with a specific structure, determined by the requirement to support centralization and multi-antenna systems. Also, we seek to find conditions under which the link performance (gain, EVM) can be improved.

We focus on the transmission of OFDM-modulated signals from a CS to a remote WTP over a ROF link designed for signal distribution for indoor wireless networks enhanced by MIMO and beam forming technologies. The choice of this specific application allows the definition of some important characteristics of the ROF distribution network, as the WDM architecture and the maximum fiber length. In this section we list and justify all the assumptions and choices we made, and we clarify the methodology of our work.

As an additional objective, we focus on the study of ROF links with optical amplification and high power RF output, so to evaluate the possibility of deriving an antenna at the link end without the need for RF amplification after a detector. Later on in this section, we explain in detail the reasons for this choice.

Finally, we want to explore the potentialities of all-optical manipulation and filtering of RF signals, in order to integrate high level functions such as signal phase and amplitude control for beam-forming in the optical link itself.

1.6.1 Choice on the signal format

One of the objectives of this work is the study of the impact of an optical ROF channel on the OFDM transmission. Indeed, the OFDM format has been created to be used in the air channel and its performance in a ROF system, where the air channel is chained to a fibre channel, must be studied to identify the most important sources of signal degradation in the optical domain and how to avoid them. The OFDM signal is a particularly good choice to test the impact of the optical link nonlinearities, because it features a high PAPR and it is sensitive to nonlinear distortion. In order to be able to apply our work to wireless networks, we chose the IEEE 802.11a as reference *WiFi* protocol. This fixes a number of properties of the OFDM format that will be discussed in chapter 2. As a consequence, all along this work we studied if and under which conditions this specific type of signal can be transmitted over a ROF link without significant degradation. Therefore, we characterized a number of possible sources of signal degradation to identify the optimum working point for the various optical components that ensures less signal degradation and maximum link efficiency. It is important to point out that we worked on a system level, trying to characterize the interaction of the various optical components in the ROF link with the OFDM signal.

An important property of the signal format chosen for this study is that it features a narrow RF bandwidth (20 MHz), and the RF carrier frequency is much greater than the RF signal bandwidth: this is a so called sub-octave signal. This has heavy consequences on the ROF link design, and permits some design choices that would not be appropriate for wideband signals.

The IEEE 802.11a being a very narrowband signal compared to the optical bandwidth typically available, many properties of the optical link can be studied using simpler test signals like simple unmodulated RF carriers. The use of simple test signals allows for simpler experimental setups and simulation algorithms, while still providing good insight in the behavior of link gain and noise performance. However, the use of OFDM modulated signals is of primary importance when investigating the nonlinear properties of the ROF link.

We assume that the target RF performance at the WTP must be better than the minimum performance required by IEEE 802.11a protocol. For example, the maximum allowed EVM for 54 MBps 802.11a signal is -25 dB: the optical link must provide a significantly better EVM. Note that, after propagation over the optical link, the signal is degraded by the propagation over the wireless channel. Hence, the optical link must appear as transparent as possible to the signal. We do not include the wireless channel in this study. However, we collaborated with Kostko and Pasandi to report a first feasibility test of ROF link followed by the wireless channel [50].

1.6.2 Choices on the link architecture

We restricted our work to indoor and small campus networks, for which the centralized architecture is most effective. This allows us to fix a reasonable maximum link length from the CS to the WTP: 10 km of fibre, which we think is enough to cable a large building or a campus.

We adopted standard single mode fibre (SMF) as the optical propagation medium, and not multimode fibre (MMF). The multimode dispersion effect in MMFs limits the band-length product of the fibre: the maximum typical bandwidth of MMF is about 1.5 GHz/km at 850 nm[2]. Hence, MMF have been used successfully to propagate 5 GHz *Wifi* signals over 300 m without degradation [51]. However, reaching a 10 km propagation length is much more challenging, even if propagation beyond the band-length product limit is possible by exploiting periodic passband regions in the MMF frequency response [52, 53] and subcarrier multiplexing [54]. Thus, MMF did not appear to be a viable medium choice for this work. Furthermore, we considered that in our laboratory a much larger variety of devices is available for SMF systems with respect to MMF systems: for example, fibre amplifiers, splitters, filters, fibre Bragg gratings, etc. MMF may be included in future extensions of this work.

We only considered external modulated links. This is a rather arbitrary choice for ROF links, where the use of expensive components like external modulators should be limited. However, this choice can be partially justified by the following considerations:

- The noise/gain performance of externally modulated links is typically higher than direct modulated links [55, 56]. Also, balanced x-cut $LiNbO_3$ Mach-Zehnder (MZ) modulators have no modulation chirp, which may affect the link linearity [57]. Finally, the MZ modulator is a very well known device, easier to model with respect to laser direct modulation. This work on ROF being the first on this topic in our laboratory, we decided to gain an insight on the operation of ROF links in the favorable condition offered by external modulation. Other students are now starting the investigation of direct modulated links, and the comparison with external modulation is a valuable starting base.
- In chapter 6, we propose a novel all-optical beam-former architecture where one single modulator is used to modulate simultaneously all the wavelength from a multi-wavelength source. Each wavelength is assigned to a specific antenna in the beam-former array, so that the cost of the modulator is split over the number of antennas in the array.
- In the future, the cost of external modulation devices may drop with the introduction of silicon-on-insulator (SOI) devices. Intel, for example, is working on SOI modulators [58, 59].

[2]Standard ISO/IEC 11801:2002 2nd Edition, fibre type OM3.

- In dense WDM ROF links, the temperature stability of the laser is important to avoid excessive wavelength drift. Temperature stabilization is easier in externally modulated links, where the output power of the laser is kept always constant.

We focus on the double side-band (DSB) modulation format, which is easier to generate compared to the SSB format. The latter is often proposed in literature for dispersive ROF links, because it is not affected by the dispersion-induced power fading that is observed in DSB systems. However, we prove in chapter 3 that the total accumulated dispersion over a 10 km-long SMF link causes negligible fading on a 5 GHz DSB signal, so there is no need to embrace a more complex modulation format as the SSB. Furthermore, the SSB format has a 3 dB RF gain penalty versus the DSB format [60].

We assume that the ROF link supports antenna arrays. Hence, we assume a link architecture as shown in Fig. 1.4. The CS is connected to the WTP through a remote node (RN). Each remote node is addressed by a 20 nm CWDM channel, which is subdivided into 200 GHz WDM channels, each addressing one WTP. At the WTP, each antenna in the array is addressed by a separated wavelength in a 25 GHz dense WDM (DWDM) configuration. In this way, each WTP can support a maximum of 8 antennas fed by DSB 5 GHz *WiFi* analog signals, and each RN can support a maximum of 10 WTPs[3].

The WDM architecture may appear expensive for a ROF application, but it has the advantage of permitting full exploitation of the available optical bandwidth. Hence, WDM is commonly proposed in ROF systems (some examples: [61, 28, 62, 63]), and adapts particularly well to links supporting antenna arrays. In fact, filtering and manipulation of the signals fed to each antenna can be done in the optical domain by manipulating the corresponding wavelengths. An example of optical beam-former that exploits this concept is presented in chapter 6. Note that in this thesis, except for the work on the beam-former, we focus only on the transmission of one single wavelength and we do not study the interaction of multiple wavelengths simultaneously propagating over the link.

Note that the IEEE 802.11a protocol is half duplex: transmission in every instant is either from the CS to the wireless (downlink) users or vice-versa from the users to the CS (uplink). The minimum time interval between the two modes is referred to as short inter frame space (SIFS) and is fixed at 16 µs by the protocol [1, table 93]. This potentially simplifies the WTP and permits wavelength reuse for downlink and uplink. However, the installation cost of two fibres per antenna is practically the same as for one fibre only, so we assume separated fibres for uplink and downlink. In collaboration with Vacondio and Mathlouthi, in [64] we proposed a novel ROF WTP based on semiconductor optical amplifiers (SOAs), which uses separated upload and download links. However, the work presented in this thesis is focused on the optimization of the downlink only.

[3]Reserving about 500 GHz of bandwidth for guard bands and CWDM filters roll-off.

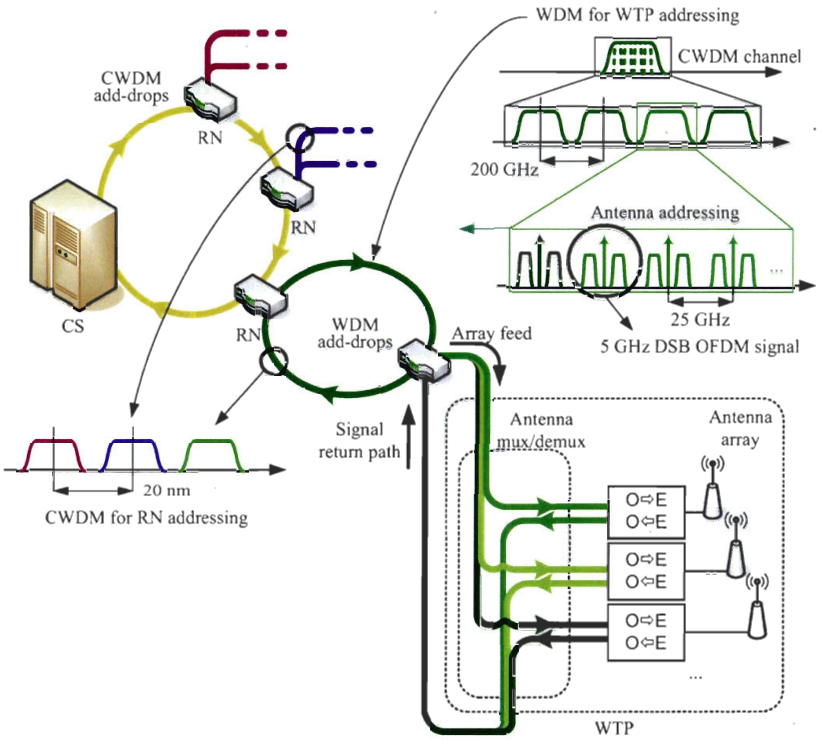

Figure 1.4: Proposed wavelength multiplexing strategy and link architecture showing 20 nm CWDM for RN addressing and 25 GHz DWDM for antenna feeding. Optical carriers are modulated by DSB 5 GHz *WiFi* analog signals.

Based on the link architecture, we can sketch a reasonable optical loss budget for the downlink: it includes a coarse WDM filter (we assume 3 dB of insertion losses), a dense WDM mux/demux (an arrayed waveguide grating (AWG) would have at least 7 dB losses), 10 km of standard fibre (2 dB losses). Hence, we assume a total propagation loss of about 15 dB. This amount of losses imposes the use of an optical amplifier; hence, we focus our work on optically amplified links.

1.6.3 The RF power challenge

The 802.11a standard [1] defines a limit for the maximum total emitted power from an antenna (or antenna array): 40 mW for indoor communications. If we assume that the network under study employs arrays composed of 8 antennas, the maximum power from each antenna must not exceed 5 mW. To reach such an emitted power, each antenna in the array requires its own RF amplification chain. This is one of the main drawbacks of multi-antenna arrays, because these chains are source of interference, and the power amplifiers (PAs) are a significant source of signal distortion. Furthermore, as described in chapter 2, the OFDM signals are characterized by a relatively high PAPR and are particularly sensitive to amplifier distortion. Hence, the PAs used in the RF chains must be oversized to avoid signal distortion, increasing costs, physical dimensions, thermal

dissipation problems and electrical power needs at the WTP. For these reasons, we explored an alternative solution and in chapter 3 we assume that no electrical amplifier is used at the WTP: instead, we optimize the link parameters to improve the optical link gain. If EDFAs are used for amplification, this approach has a great advantage, which will be highlighted in chapter 5: the EDFAs feature a very linear response to the modulation and they do not introduce distortion. Also, as shown in chapter 4, optical amplified links can have a lower noise factor than electrically amplified links. However, our tests showed also the limits of an optical amplified link: it is relatively hard to achieve a 5 mW (7 dBm) output power with good signal quality, even for a single wavelength link [50]. This is due to the compression and distortion caused by the detector. A comprehensive discussion of the source of distortion in a photodetector would require a whole essay, and it is not needed here. We want only to point out that it is possible to design optical photodetector with high input saturation power, which would maintain a linear response even with relatively high output photocurrent levels [65, 66, 67]. There are currently a few research groups working on this problem, because the needs for high power photodetectors for ROF link applications have been recognized [68]. One among the most active, headed by Williams, reported a link with a high power detector, which yields a maximum linear output power of 6 dBm over more than 6 GHz [69]. Hence, a properly designed detector would be capable of handling high photocurrents and provide high RF output power without distortion. However, high power linear detectors are not yet commercially available, and none was available to us for testing. Hence, in this work we assume the detector as linear by properly attenuating the optical power right before detection.

Another limit of optical amplification is the high cost of optical amplifiers, especially EDFAs, compared to electrical amplifiers. This is alleviated by placing the amplifier at the CS, and sharing it among several wavelengths, i.e., several antennas. This allows to share the cost of the optical amplifiers among the WTP.

1.7 Organization of the thesis

This thesis is organized in the following way. In the next chapter we introduce the most important features of the OFDM modulation format for the convenience of the reader that may not be familiar with this type of signal. We define mathematically the structure of an OFDM symbol and we show how it can be constructed by using an FFT. Then, we briefly describe why this modulation format is resilient to multipath fading, and why it features a high PAPR. We also introduce the IEEE 802.11a frame format and the specifications of the 802.11a physical layer that are most pertinent to our work. In the last part of the chapter, we describe the set of programs, coded in MatLab, that we wrote to simulate the behavior of ROF links with OFDM signals. In particular, we give details on how the code generates the OFDM frames. Because we payed close attention to fully respect the IEEE 802.11a protocol, the OFDM frames from the generator can be

used without modifications for both simulations and measurements, so that numerical and experimental results can be compared properly.

Chapter 3 is dedicated to the gain of ROF links. First, we discuss a model for links with unsaturated optical amplifiers, taking into account impedance matching, particularly at the detector. We show that the RF gain of ROF links is greatly improved by the use of narrowband lossless matching. We show that this impedance matching technique can be used with 20 MHz-wide OFDM signals. In fact, the matching bandwidth is typically much larger than the OFDM bandwidth because of the parasitic resistive losses in the detector and the matching circuit itself. In the second part of the chapter, we extend the model to links with saturated optical amplifier, and we present original results on the optimization of the modulator bias to increase the link gain. The modulator bias optimization is also useful to improve the link gain when the amplifier is shared among several optical sources. Finally, we discuss the impact of link dispersion on the gain, showing that dispersion causes excess losses in DSB systems. However, the dispersion-related losses are lower than 0.1 dB for 5 GHz signals propagating over 10 km-long links.

Chapter 4 is dedicated to the description of the most important sources of noise in optically amplified ROF links. We compare the noise figure of optically amplified links and links with an electrical amplifier after the detector, and we discuss under which conditions the former has better noise figure. Then, we introduce a general stochastic model of the detected noise in ROF links with high optical modulation depth. The model takes into account for the filtering effect due to the limited bandwidth of the detector. It is used to demonstrate the stochastic stationarity of noise arising from the beating of optical amplifier spontaneous emission with itself and with a deterministic signal. The same model is also applied to noise generated by stimulated Brillouin scattering (SBS), which is shown to be non-stationary. Also, the model explains some peculiar characteristics of the SBS-induced noise detected at low frequencies and around the RF carrier. Noise around the carrier from SBS is shown to be a significant limitation of link carrier-to-noise ratio (CNR), and we show that the modulator bias can be optimized to reduce the SBS and, consequently, improve the CNR. The noise stemming from laser relative intensity noise (RIN) is also interpreted on the basis of the stochastic noise model. We compare two types of laser: fibre lasers based on Bragg gratings engraved in photosensitive erbium-ytterbium fibre, and distributed feedback (DFB) semiconductor lasers. The former has higher RIN, and we show that this can limit the link CNR.

Chapter 5 is dedicated to the study of link nonlinear distortion and its impact on OFDM signal transmission. We first discuss the distortion stemming from the nonlinear transfer function of MZ modulators, and we describe the evolution of third order harmonic distortion, third order intermodulation distortion, bit error rate and error vector magnitude as functions of the RF modulation power. We also briefly discuss the nonlinearity of other types of modulators, like those based on the electroabsorption effect and the SOAs used as modulators. Then, we discuss the linearity of EDFAs, and

we show that they cause negligible signal distortion unless the OFDM signal is divided into frames or bursts. Then, if the modulator bias is off quadrature, the presence or absence of a frame causes fluctuations of average optical power at the EDFA input and, consequently, signal distortion because of the dynamic response of the EDFA gain to slow optical power fluctuations. Finally, we discuss in detail the distortion stemming from fibre dispersion and $\chi^{(3)}$ nonlinearities. We show that in some cases the fibre distortion can actually compensate for distortion generated by the MZ modulator: we discuss this observation thoroughly, showing that in some cases the modulator bias can be optimized to minimize the link distortion and maximize the link gain simultaneously.

The last chapter is dedicated to a novel optical beam-former well adapted to be integrated into WDM ROF links. The beam-former allows independent and simultaneous control of the amplitude and the phase of the signal fed to each antenna in an array. We describe its advantages over other devices presented in the literature, and we detail its principle of operation. We present two possible realizations of the filter that performs amplitude and phase manipulation for a single antenna. Both solutions are based on fibre Bragg gratings. Against our expectations, we find that the first is not well adapted to a compact implementation of a multi-antenna device. The second solution is an improved design that allows easier implementation of the full beam-former. For both solutions, we compare simulations and experimental measurements of the signal amplitude and phase control capability, and we find good matching.

Chapter 2

Orthogonal Frequency Division Multiplexing

The topic of this thesis embraces a variety of notions, ranging from optical communications to theory of microwave transmission lines (exploited for calculations of link gain in chapter 3) to wireless modulation formats and communication protocols like OFDM and the IEEE 802.11a. For the convenience of those readers unfamiliar with OFDM modulation format, in this chapter we describe its most important properties and we define the concept of error vector magnitude (EVM), often used as an estimator of the OFDM signal quality. We also describe the standard frame format of an IEEE 802.11a compliant OFDM signal.

In the second part of the chapter, we introduce the structure and the most important algorithms of the simulator we used all along this work. In particular, we give details on the OFDM frame generator that we coded paying great attention to fully respect the IEEE 802.11a protocol. This is important because our simulator can create a numerical representation of an OFDM burst, which can be used for simulation but also directly fed to a vector signal generator (VSG) hardware. This is a programmable arbitrary signal generator available in our laboratory, which allows to transmit an image of the very same OFDM burst used in simulation onto a real optical link. After the receiver, a vector signal analyzer (VSA) is used to detect the OFDM signal, identify the data bits and constellations and calculate EVM and BER. In this way, simulated and measured results can be compared properly. However, the VSA can not operate properly if the signal is not strictly compliant to the 802.11a protocol: hence, the importance of a proper generation of the OFDM frames.

2.1 Analytical definition of the OFDM signal, and its main properties

OFDM is a spectrally efficient multicarrier transmission protocol where multiple user symbols are transmitted simultaneously over N_{subc} independent densely spaced orthogonal subcarriers. Each subcarrier is modulated by a quadrature amplitude modulation of order M (M-QAM) symbol, with symbol rate T_{OFDM} equal to:

$$T_{OFDM} = 1/\Delta f_{OFDM}, \tag{2.1}$$

where Δf_{OFDM} is the subcarrier separation. This particular choice for the symbol rate ensures that the subcarriers are orthogonal and the transmission can be exempt from ICI. Furthermore, Δf_{OFDM} is usually chosen small enough to assume a flat (nonselective) channel response over the subcarrier bandwidth.

Probably, the first discussion about OFDM can be traced back to a paper by Saltzberg [70], who describes a parallel quadrature amplitude modulation (QAM) data transmission system. He also gives a first general mathematical expression for an OFDM signal, which can be written as:

$$\begin{aligned} x(t) = \mathrm{Re}\left\{ \frac{1}{\sqrt{N_{subc}}} \sum_{n\to-\infty}^{+\infty} \sum_{k=0}^{N_{subc}-1} a_k^n \cdot w\left(t - nT_{OFDM}\right) \times \right. \\ \left. \times \exp\left[i\, 2\pi\, \left(f_c + k\Delta f_{OFDM}\right)\left(t - nT_{OFDM}\right)\right] \right\}, \end{aligned} \tag{2.2}$$

where N_{subc} is the number of subcarriers, a_k^n are the complex M-QAM symbols, $w(t)$ is a real pulse shaping or windowing function, f_c is the carrier frequency and $\sqrt{N_{subc}}$ normalization factor used to ensure that the signal power is not dependent on the number of subcarriers. The baseband equivalent is:

$$\breve{x}(t) = \frac{1}{\sqrt{N_{subc}}} \sum_{n\to-\infty}^{+\infty} \sum_{k=0}^{N_{subc}-1} a_k^n \cdot w\left(t - nT_{OFDM}\right) \cdot \exp\left[i\, 2\pi\, k\Delta f_{OFDM}\left(t - nT_{OFDM}\right)\right]. \tag{2.3}$$

As shown in appendix A, the baseband spectrum of this signal can be written as:

$$S_{\breve{x}}(f) = \frac{\sigma_a^2}{T_{OFDM}} \sum_{k=0}^{N_{subc}-1} \frac{\left|W\left(2\pi f - 2\pi k\Delta f_{OFDM}\right)\right|^2}{N_{subc}}, \tag{2.4}$$

where σ_a^2 is the variance of the a_k^n symbols, and $W(f)$ is the Fourier transform of $w(t)$.

From equations (2.3) and (2.4) it is clear that the pulse shaping function $w(t)$ must be properly defined to preserve subcarrier orthogonality at the transmitter and avoid

ICI between different subcarriers, and ISI between OFDM symbols. The orthogonality is satisfied if and only if:

$$\forall m \neq 0, \forall n \neq 0 : \int_{-\infty}^{+\infty} w(t) \cdot w(t - nT_{OFDM})\, e^{-i\,2\pi\, m\, \Delta f_{OFDM} t} dt = 0. \tag{2.5}$$

If $n = 0$, recalling that $w(t)$ is real and using the generalized Plancherel identity [71, page 39, eq. 17], equation (2.5) can be written as:

$$\int_{-\infty}^{+\infty} W(f) \cdot W(f + m\Delta f_{OFDM})\, df = 0. \tag{2.6}$$

This is similar to the classical orthogonality integral for transmission without ISI, but applied to the frequency domain instead of the time domain. Hence, ICI is avoided by using pulses with a spectral shape that respects the Nyquist criterion, written in frequency domain:

$$W(m\Delta f_{OFDM}) = \begin{cases} 1 & m = 0 \\ 0 & m \neq 0 \end{cases} \quad \Rightarrow \quad \sum_{n \to -\infty}^{+\infty} w(t + nT_{OFDM}) = \text{constant} \tag{2.7}$$

One well known family of functions which respects this criterion include the raised cosine function. Hence, ICI is avoided with $W(f)$ described by:

$$W(f) = \operatorname{sinc}\left(\pi \frac{f}{\Delta f_{OFDM}}\right) \frac{\cos\left(\frac{\pi \beta f}{\Delta f_{OFDM}}\right)}{1 - 4\left(\frac{\beta f}{\Delta f_{OFDM}}\right)^2} e^{-\frac{i\,\pi f}{\Delta f_{OFDM}}}, \tag{2.8}$$

where $\beta \in (0, 1]$ is called the roll-off factor. This corresponds to the $w(t)$ given in Fig. 2.1, that is:

$$w(t) = \begin{cases} 1, & \varphi \leqslant \frac{(1-\beta)T_{OFDM}}{2} \\ \frac{1}{2}\left[1 + \cos\left(\frac{\pi}{\beta T_{OFDM}}\left[\varphi - \frac{(1-\beta)T_{OFDM}}{2}\right]\right)\right], & \frac{(1-\beta)T_{OFDM}}{2} < \varphi \leqslant \frac{(1+\beta)T_{OFDM}}{2} \\ 0, & \text{otherwise} \end{cases}$$
$$\varphi = |t - \frac{T_{OFDM}}{2}|. \tag{2.9}$$

The orthogonal integral in (2.5) must be respected also for $m = 0$ to avoid ISI. The pulse repetition rate of exactly T_{OFDM} in (2.3) limits the choices of spectrum shapes described by (2.8): only the case with $\beta = 0$ avoids ISI (at the transmitter). Hence, the windowing function $w(t)$ becomes a rectangular T_{OFDM}-wide pulse, defined as:

$$\sqcap(t) = \begin{cases} 1 & 0 < t \leqslant T_{OFDM} \\ 0 & \text{elsewhere} \end{cases}, \tag{2.10}$$

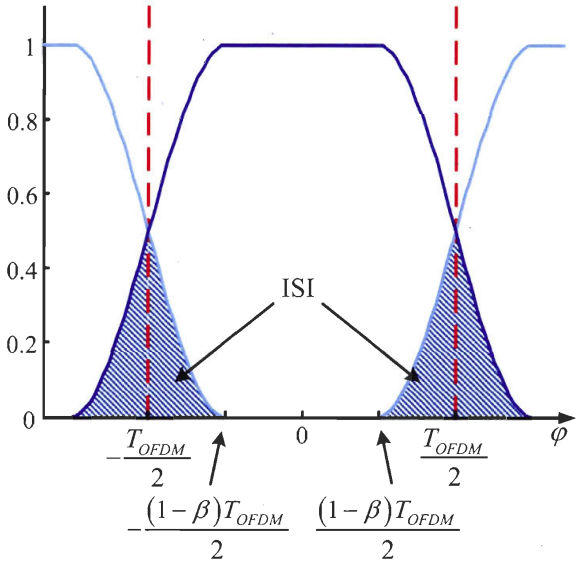

Figure 2.1: Raised cosine temporal pulse shape, with ISI regions highlighted.

and the spectrum has a $\mathrm{sinc}\,(f)$ magnitude. The rectangular pulse allows for ICI- and ISI-free generation of the signal described by the (2.3). Note that the transmission channel properties may break the ICI- and ISI-free conditions.

The OFDM symbols could be generated using a bank of filters. However, this is impractical and usually an alternative generation technique is used. Sampling the signal in (2.3) at rate $T_s = \frac{T_{OFDM}}{N_{subc}}$, gives:

$$\breve{x}\,(hT_s) = \frac{1}{\sqrt{N_{subc}}} \sum_{n\to-\infty}^{+\infty} \sum_{k=0}^{N_{subc}-1} a_k^n \cdot \sqcap\,(hT_s - nNT_s) \cdot \exp\left[i\,2\pi\,k\frac{hT_s}{NT_s}\right]. \tag{2.11}$$

Using the definition of inverse discrete Fourier transform (IDFT) [72, page 543], we rewrite the (2.11) as:

$$\breve{x}\,(h) = \sqrt{N_{subc}} \sum_{n\to-\infty}^{+\infty} \sqcap\,(h - nN_s) \cdot \mathrm{IDFT}\left\{A\,(h, a_k^n)\right\}. \tag{2.12}$$

Hence, each OFDM symbol can be generated by calculating the IDFT of the sequence of M-QAM symbols $\left\{a_0^n, a_1^n \ldots, a_{N_{subc}-1}^n\right\}$.

This IDFT-based method of generating an OFDM signal is among the most important advantages of this modulation format: the discrete Fourier transform (DFT) can be calculated using very efficient FFT algorithms. This is probably one of the reasons that made this modulation format widely adopted in the newest wireless protocols. Indeed, efficient, low power consumption and relatively cheap hardware implementations of the FFT algorithms are commonly available. Furthermore, OFDM exploits a very simple FFT-based equalization technique (described later), which contributes to simplify the

receiver and makes OFDM particularly well adapted to low power portable wireless devices. The first discussion about generation of OFDM by an IDFT was presented by Weinstein *et al.* in [73].

2.1.1 OFDM in multipath fading and frequency selective environments

One of the main advantages of OFDM is its potential effectiveness against the multipath delay spread encountered in wireless channels. Compared to other modulation methods, OFDM symbols have relatively long time duration, T_{OFDM}, making it intrinsically more robust to ISI generated by multipath fading compared to short-pulse, single carrier formats. Still, for the OFDM signals described previously, multipath fading will always generate some ISI and ICI. In the presence of a delay spread of τ, the orthogonality integral can be written as:

$$\Upsilon = c_0 \int_{-\frac{T_{OFDM}}{2}}^{-\frac{T_{OFDM}}{2}+\tau} e^{i\,2\pi\,h\,\Delta f_{OFDM} t} e^{-i\,2\pi\,k\,\Delta f_{OFDM}(t-nT_{OFDM}-\tau)} dt + \\ + c_1 \int_{-\frac{T_{OFDM}}{2}+\tau}^{\frac{T_{OFDM}}{2}} e^{i\,2\pi\,h\,\Delta f_{OFDM} t} e^{-i\,2\pi\,k\,\Delta f_{OFDM}(t-nT_{OFDM}-\tau)} dt, \quad (2.13)$$

where $\{c_0, c_1\} \in \mathbb{R}$. The amplitude of Υ then is:

$$|\Upsilon| = (c_0 - c_1) \frac{\sin\left(\frac{(h-k)\pi\tau}{T_{OFDM}}\right)}{\frac{(h-k)\pi}{T_{OFDM}}}, \quad (2.14)$$

and does not depend on n. Hence, the (2.14) represents the loss of orthogonality among subcarriers of the same symbol (ICI, with $n = 0$ and $h \neq k$), as well as the ISI among different symbols (with $n \neq 0$ and $h = k$). A simple way to avoid loss of symbol orthogonality due to multipath propagation is the addition of a cyclic prefix (CP) to the OFDM signal. The CP is a cyclical extension of each OFDM symbol for a time span (guard time) that must be chosen to be larger than the expected delay spread. The CP extends the duration of each OFDM symbol, so that it causes some penalty on the transmission rate: the guard time in an OFDM can be seen as a power penalty since it carries no information. In fact, at the receiver, only a T_{OFDM}-long portion of the symbol is retained, chosen where the symbol is unaffected by the delay spread. Hence, in (2.13), $c_0 = c_1$ over the T_{OFDM} time frame and orthogonality is respected. The use of a CP has been first proposed by Peled and Ruiz in [74].

The CP has another important consequence: by increasing the symbol duration, it relaxes the constraints on the pulse shaping function. The pulse must always be

a Nyquist function like the raised cosine described by (2.9), but the guard time may include the pulse roll off and allows for $\beta > 0$ without loss of orthogonality because the guard time is discarded at the receiver. The advantage of choosing a pulse shaping function with $\beta > 0$ is that the corresponding spectrum has much steeper out-of-band spectrum roll off. Hence, adjacent channels interference (ACI) is reduced as well as ICI caused by Doppler spread in mobile wireless environments.

A channel affected by multipath propagation can be frequency selective if the response of the channel is not flat over the signal bandwidth. In the frequency domain, the long OFDM symbol time duration translates into a narrow subcarrier bandwidth. As suggested by the (2.4), the total OFDM signal bandwidth is subdivided into N_{subc} subcarriers. If properly designed, each subcarrier has a bandwidth narrow enough to assume its portion of the propagation channel as flat (nonselective). This allows to greatly simplify the signal equalization in time-invariant multipath channels: equalization may be reduced to a matrix multiplication of the received spectrum with the inverse of a channel matrix. The channel matrix, representing the channel amplitude and phase response for each subcarrier, may be estimated using a training sequence appended to the data stream or using pilot tones, which are subcarriers in the OFDM spectrum reserved for sampling of the phase and amplitude channel response. Other more complex techniques exist for identifying the channel matrix, but their description is beyond the scope of this thesis. Note that the training sequence and pilot tones do not carry any payload information and cause a penalty on the information transmission rate.

Although OFDM enables simple equalization, it introduces some well-known problems: synchronization, sensitivity to channel variations in time, and sensitivity to nonlinear channels. A word about synchronization of OFDM transmitters and receivers: the baseband OFDM signals are affected by synchronization errors due to receiver oscillator impairments (phase noise) and sample clock differences between the transmitter and the receiver. Also, the received signal demodulation involves oscillators, whose frequencies may not be perfectly aligned with the transmitter frequencies, resulting in carrier frequency offsets. These synchronization issues may exacerbate the signal degradation due to the channel noise or multipath fading, but are not directly caused by the link. All along this work we assumed perfectly synchronized transmitter and receiver, and this (optimistic) assumption seemed to never fail significantly.

2.1.2 OFDM in time varying channels

The narrowband nature of subcarriers makes the signal robust against frequency selectivity caused by a multipath delay spread, but also makes it relatively sensitive to rapid time variations of a mobile channel. Time variations corrupt the orthogonality of the OFDM subcarrier waveforms, and ICI and ISI may occur. Furthermore, the time-invari-

ant channel assumption is important for the equalization algorithms based on training sequences, because the training sequence is typically transmitted as a preamble to a longer stream of OFDM symbols. As we said before, the training symbol causes some penalty on the transmission bit rate. Hence, the number of training symbols generated for transmission and the resulting resilience to the channel variations are traded off with the bit rate penalty. We will see in chapter 5 an example of an optical time variant channel causing distortion and errors in OFDM transmission.

2.1.3 The peak-to-average-power ratio (PAPR)

The OFDM spectrum given by equation (2.4) is flat over a bandwidth as wide as $N_{subc} \cdot \Delta f_{OFDM}$, that is about 16 MHz for a IEEE 802.11a compliant signal. Hence, the baseband complex envelope of the signal behaves like a filtered white noise, and shows a large envelope PAPR. The maximum value of PAPR is equal to $10 \cdot \log_{10}(N_{subc})$, or about 17 dB for 802.11a. Such a peak is indeed a rare event and average PAPR is much less than this extreme value [75]. However, statistically there is a 20% probability that the instantaneous power of a 64-QAM OFDM signal is 8 dB higher than the average power [75]. Therefore, nonlinearities in the communication link may get overloaded by high signal peaks, causing peak clipping, intermodulation among subcarriers and undesired out-of-band radiation.

Furthermore, the OFDM BER is severely degraded by distortions. A typical source of distortion are the RF PAs used to boost the signal before the transmission antennas. A 64-QAM OFDM signal passing trough a smooth limiter, which is a good model for most RF PAs, undergoes a power penalty of 2.5 dB for as low as 0.01% clipping at BER= 10^{-5} [76]. Distortion also creates out-of-band radiation and adjacent channel cross-talk that may further decrease the signal quality.

The combination of high PAPR and sensitivity to nonlinear distortion imposes the RF PAs to be operated with large power back-offs (i.e., the amplifier is fed with attenuated signals), so that the amplifier response stays linear even in presence of signal peaks. This leads to very inefficient amplification and expensive transmitters, because the amplifiers are used at their full power only for a small fraction of the time (when the signal PAPR reaches the highest values). Also, excessive power back-off decreases the signal SNR and degrades the BER: there is an optimum value of power back-off that ensures low distortion and high SNR, and it depends on the type of nonlinearity. For a smooth limiter, the optimum back-off is as high as 10 dB [76].

Several methods have been proposed in the literature to reduce the OFDM PAPR at the expense of transmission rate or transmitter/receiver complexity. An exhaustive review is given by Han in [77]. In this work we do not apply any PAPR reduction technique because these are not included in the IEEE 802.11a standard.

2.2 Assessing the quality of OFDM signals

The quality of OFDM transmission is most often evaluated using a few quantities and measurements: adjacent channel power ratio (ACPR), spectrum mask, EVM and BER. The BER is the ultimate quality factor, but it usually gives little information on the impairment causing the transmission errors. Also, accurate evaluations of BER requires long measurements and simulations. Alternatively, in this work we very often simulate and measure the EVM. The constellation of an OFDM signal is identical to the constellation associated to the M-QAM modulation adopted for the OFDM subcarriers. Hence, we can define the EVM as:

$$EVM_{dB} = 20\log_{10}\left(\sqrt{\frac{\sum_n |r-z|^2}{\sum_n |r|^2}}\right), \tag{2.15}$$

where r represents the transmitted M-QAM symbols and z the received ones. A graphical definition of EVM is shown in Fig. 2.2.

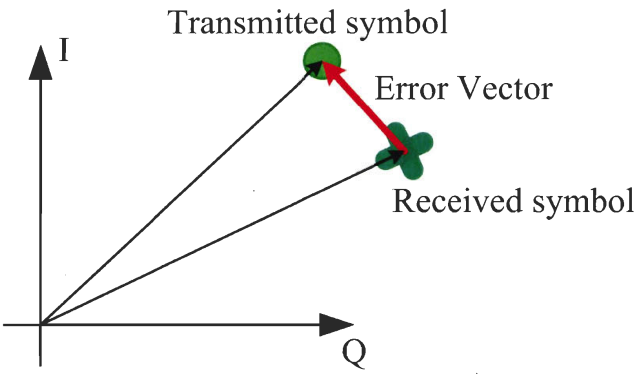

Figure 2.2: Graphical definition of the error vector.

In systems affected by additive white gaussian noise (AWGN), the EVM is related to the baseband SNR (defined as the symbol energy over the noise power spectral density (PSD)) by [78, 79]:

$$EVM_{linear} = \sqrt{\frac{1}{SNR}} \tag{2.16}$$

$$EVM_{dB} = -SNR. \tag{2.17}$$

Through the SNR, EVM can be related to BER: the BER for each QAM modulated OFDM subcarrier can be calculated from the SNR using the well known Q function [80]. Then, the total BER for the OFDM signal is calculated averaging the BER from each subcarrier. The relation between EVM and BER is more complex if other sources of colored noise or systematic errors are added on the received signal. However, low EVM is always associated to low BER and measuring or simulating the EVM remains a good way to assess the quality of the transmission link. The advantage in using EVM

instead of BER is that the former typically requires much shorter measurements and simulations.

When measuring or simulating EVM and BER, it is important to pay attention to the presence of distortion effects in the link: a small distortion can be considered a source of noise, which degrades the link SNR. If the statistics of the signal and the link nonlinearity respect some conditions (see chapter 5 for details), the distortion noise can be assumed gaussian, white and uncorrelated with the signal itself, so that it can be treated as a form of AWGN. This assumption is statistically valid only if many different realizations of the OFDM signal are transmitted over the link and used to calculate the EVM and BER, in order to assure that the distortion noise statistics are not biased by the repetitive transmission of a specific signal waveform. In this sense, we can do a parallel with measuring the BER in digital systems, where it is preferable to use very long period pseudo-random data.

2.3 The IEEE 802.11a frame format [1] and physical layer specifications

In this section we summarize the most important characteristics of a standard IEEE 802.11a compliant frame. The IEEE 802.11a is the wireless protocol, which offers the highest communication speed (54 Mbps) among those presently approved in the standard. For this reason, we took this standard as reference all along this thesis. A new protocol named 802.11n, still under certification, will offer even faster speed by incorporating MIMO interfaces and other improvements. The IEEE 802.11n is still based on OFDM in a very similar way to 802.11a. Hence, all the knowledge gained in this thesis on 802.11a will be transferrable to 802.11n systems.

The IEEE 802.11a utilizes 300 MHz of bandwidth for 12 independent transmission channels in the 5 GHz unlicensed national information infrastructure (U-NII) band (see Fig. 2.3). It is the only *WiFi* protocol, except maybe the 802.11n, to use the 5 GHz band. This band is free from interference from other legacy protocols like IEEE 802.11b/g and from sources like microwave ovens, all within or near the 2.4 GHz industrial, scientific & medical (ISM) band. Each 802.11a transmitter must respect a precise spectral mask, as shown in Fig. 2.4. The transmission power levels are summarized in table 2.1.

Table 2.1: Maximum admitted power levels in the 802.11a bands.

Frequency bands	Maximum output power with up to 6 dBi antenna gain
5.15-5.25 GHz - indoor	40 mW
5.25-5.35 GHz - indoor / outdoor	200 mW
5.72-5.82 GHz - outdoor	800 W

In the highest bit rate mode, which we use all along this work as a worst case signal to test the optical link, the 802.11a OFDM symbols exploit 48 data subcarriers with 64-QAM modulation, interleaved with 4 pilot tones. The subcarrier frequency spacing is 312.5 kHz, giving a symbol period of 3.2 µs, to which is added a 0.8 µs CP, for a total OFDM symbol duration of 4 µs. The OFDM symbols are multiplied by a 4 µs-long windowing function, with roll-off interval of 100 ns. The signal bandwidth is precisely 16.6 MHz.

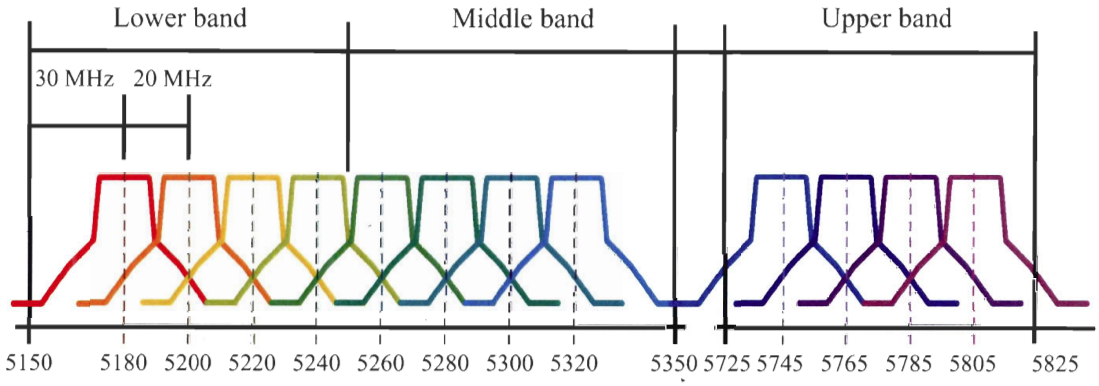

Figure 2.3: 802.11a spectrum channels.

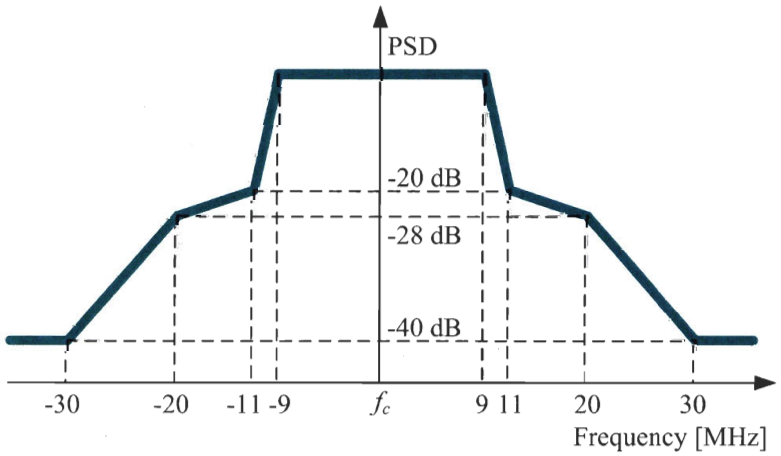

Figure 2.4: 802.11a transmit spectrum mask.

The frame format schematic is shown in Fig. 2.5. The frame starts with a preamble composed of a synchronization symbol and a training symbol. These are two 8 µs-long OFDM symbols used for signal detection, automatic gain control (AGC), coarse and fine synchronization and frequency offset estimation. The training symbol is especially important because it may be used at the receiver to estimate the channel response. After, some service bits are used to define the code rate and the length of the payload, formed by a variable number of OFDM symbols.

The channel is considered static over a time span larger than the frame length: the pilot tones included in the OFDM symbols of the DATA sequence are usually not

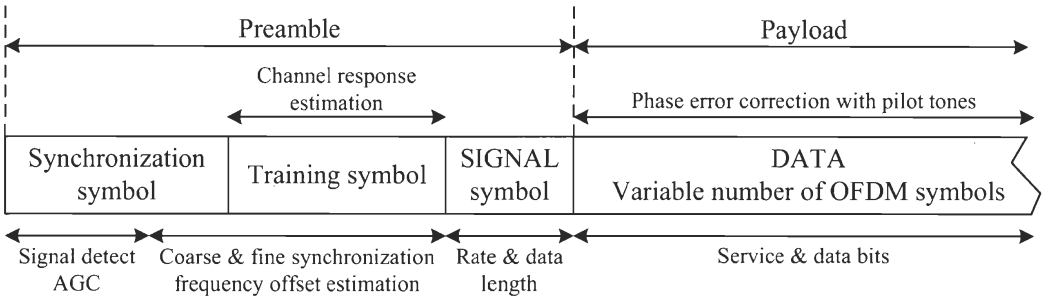

Figure 2.5: IEEE 802.11a frame format. The frame starts with a preamble composed of a synchronization symbol, used for signal detection and automatic gain control (AGC) and coarse synchronization, a training symbol, used for fine synchronization and channel response estimation, and a SIGNAL symbol, which declares the data rate and length of the payload. The payload and the preamble are all composed of OFDM symbols.

used to compensate for channel variations but for frequency and phase drifts along the frame, due to loss of synchronization between the signal and the receiver local oscillator. However, the protocol does not impose any algorithm for signal synchronization, equalization and decoding, and front-end receiver manufacturers can define their own way to exploit the synchronization symbol, training symbol and pilot tones to achieve these functions.

Finally, the physical layer section of the 802.11a protocol defines the scrambling, descrambling and interleaving algorithms, as well as the convolutional encoder used as error correction code. Viterbi decoder is suggested but not imposed by the protocol.

Many other features of the 802.11a signal format defined by the protocol are not discussed here because they are not relevant to this work. We refer the reader to the original IEEE protocol publications, available on the internet.

2.4 A simulator of ROF links supporting OFDM signals

All along this work, we will present a number of simulations of ROF links in different configurations. To execute these simulations we wrote from scratch about 4500 lines of Matlab code divided in a number of simulation modules. Each module simulates a particular device useful for ROF links. We coded simple models for:

Laser: the model includes the RIN noise, which is simulated by filtered white noise. The filter parameters are chosen in such a way to reproduce the RIN PSD found in experimental measurements. Phase noise is not simulated being of scarce relevance in our work.

Modulator: we implemented a linear ideal modulator and a MZ modulator.

Fibre: linear, dispersive or nonlinear. The latter model is based on a split step algorithm[1].

Detector: very simple linear noiseless model.

EDFA: the model takes into account the gain saturation. The amplified spontaneous emission (ASE) is not simulated. In one version, we included code from Bononi[2] *et al.* to simulate the amplifier dynamic response.

RF signal generation: the generator module can produce single carrier modulation, two tones modulation for simulation of third order intermodulation distortion, and a complete 802.11a compliant OFDM signal frame.

Signal analysis modules: a number of modules can be used for analyzing the signal in electrical or optical domain. For example: analysis of spectrum in optical and RF domain, harmonic distortion and intermodulation distortion. We paid close attention to the proper calculation of OFDM related quantities like EVM, PAPR, constellation, and BER with and without convolutional coding.

The models' complexity is a careful compromise between accuracy, complexity and relevance to this work.

A typical modulation file structure is sketched in Fig. 2.6: the simulator modules, coded as Matlab functions, are chained in a way that reproduces the signal flow of an optical link. Typically, some parameters in the simulation, like the bias point in the modulator module, are defined as an array of values, which is scanned value-by-value by the simulation. For each value, some analysis is performed on the simulated data, and the results are collected and reported in graphic format.

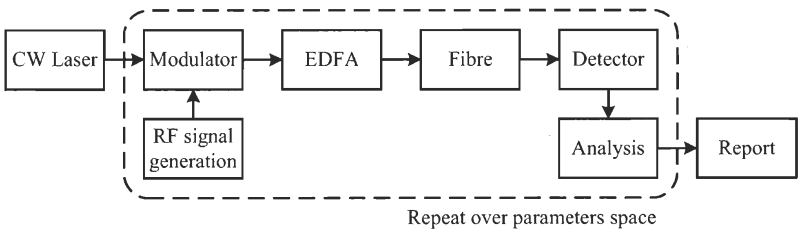

Figure 2.6: Structure of a typical simulation file.

The optical part of the simulator is based on the baseband description of the electric field propagating over the ROF link. Note that the electric field is modulated by the RF signal in its bandpass and not baseband description: for example, if the electric field is modulated by a 5 GHz carrier, the simulated electric field spectrum must extend

[1]We thank Dr. Pascal Kockaert, now professor at the "Université Libre de Bruxelles", for his help in developing this module.

[2]Prof. Alberto Bononi is with "Università di Parma", Parma, Italy.

from DC to over 5 GHz. When simulating the link nonlinear response, the bandwidth of the electric field must be enlarged enough to properly capture the behavior of at least third order harmonics at 15 GHz. This peculiarity of our simulator has important consequences for the generation of the 802.11a signal: we have to generate the full 5 GHz description of the 802.11a RF signal and not only the baseband version, as it is most often the case in other OFDM simulators.

The 802.11a signal generation and analysis modules are an important part of our simulator. The signal generation can be sketched as shown in Fig. 2.7: random data bits are generated and used to build the complex baseband description of an 802.11a frame. Then, this is properly oversampled and used to modulate a RF carrier in phase and quadrature. Then, the power of the modulated signal is leveled to a value fixed in the simulation. The most interesting part is the baseband frame generator, described in Fig. 2.8: the information bits to be transmitted are parallelized and Gray-coded into M-QAM symbols. These symbols are concatenated to form a description of the complex spectrum of the OFDM symbols, whose time domain waveform is calculated using an IFFT algorithm. A CP is added and time windowing is applied before concatenating the OFDM symbols into a frame.

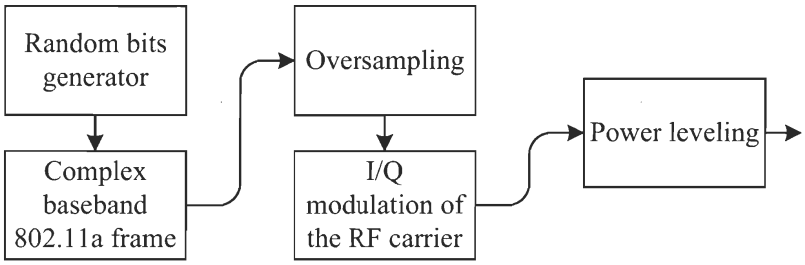

Figure 2.7: 802.11a signal generation algorithm.

We put a significant effort in coding a fully 802.11a compliant generator: the baseband signal built by the signal generation module includes the training symbol, synchronization symbol, convolutional coding, interleaving and scrambling. This choice, even if may create some overhead in the simulation, has an important advantage: the baseband signal from the simulator can be fed unchanged to the `Agilent E4438C` VSG available in COPL. The VSG uses the complex baseband signal description to modulate an RF carrier in phase and in quadrature. In the laboratory, the signal analysis at the link end is performed using an `Agilent E4440A` VSA with embedded 802.11a analysis software. The VSA software can not analyze the signal if it is not compliant to the IEEE 802.11a protocol. Hence, the importance of generating a fully compliant OFDM frame in the simulator: exactly the same signal can be propagated over a real experimental link and over a simulated link, ensuring that the measured and simulated results can be properly compared. In the simulator, the analysis module is programmed as shown in Fig. 2.9: note that in the simulator there is no propagation delay and the beginning of the frame is perfectly known, so that no synchronization step is needed.

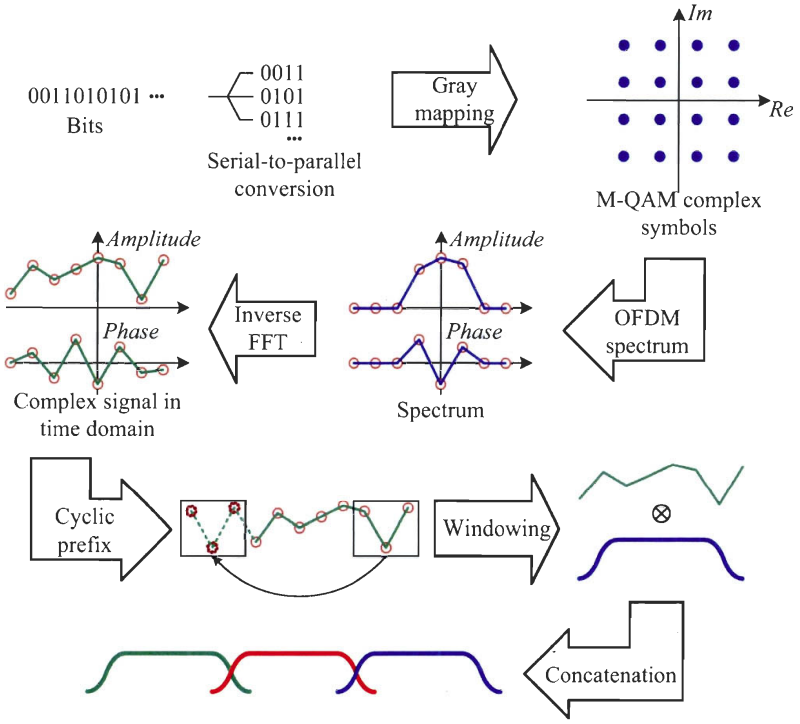

Figure 2.8: OFDM symbol generation algorithm.

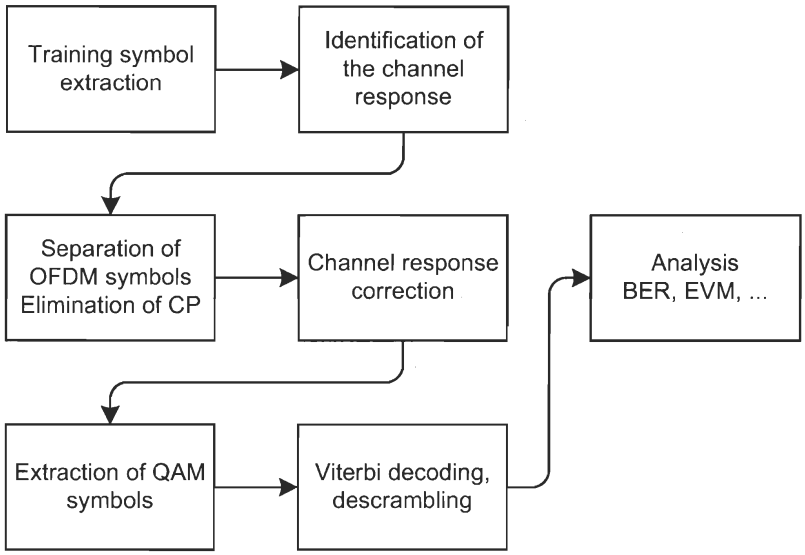

Figure 2.9: Algorithm for signal decoding and analysis.

One important step at the decoder is the channel response correction. We implemented a zero-forcing algorithm, as used by the VSA: the channel response vector for all data subcarriers in the OFDM frame is estimated in the frequency domain exploiting the difference between the expected training symbol sequence, which is known, and the actual received sequence. Then, the inverse of the channel response vector is multiplied to the received signal to calculate a corrected received data constellation, which we use to calculate the EVM and BER.

2.4.1 Validation of the simulator

The simulator has been validated in many different ways to test each module. For example, we simulated a simple sinusoidal signal propagating over a dispersive fibre and compared the results with the output of the commercial simulator OptSim, finding perfect agreement, as shown in Fig. 2.10a. Details on the attenuation related to dispersion are given in chapter 3.

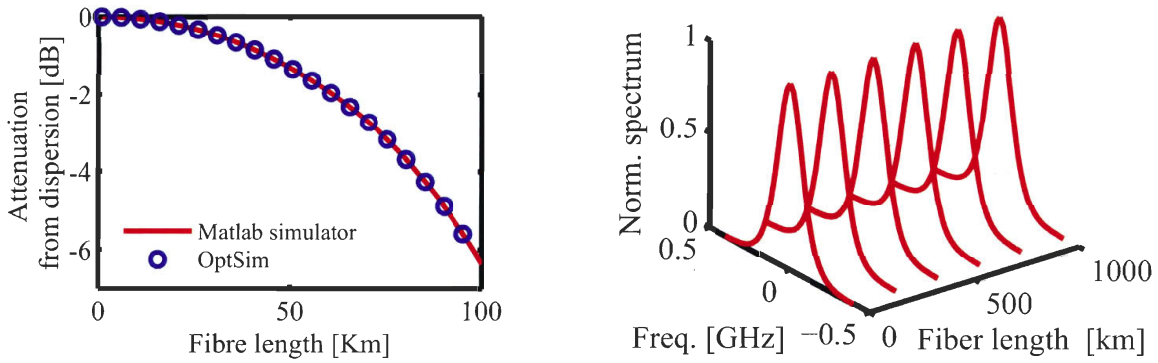

(a) (b)

Figure 2.10: (a) Simulation of 5 GHz signal propagation over dispersive fibre, without propagation losses: comparison between our simulator and OptSim. (b) Soliton propagation. Simulation parameters as in [81, fig. 4.8].

The nonlinear fibre model has been validated by simulating soliton transmission (see Fig. 2.10b). We also propagated gaussian pulses and compared their spectra after propagation with those given by Agrawal in [81, fig. 4.11].

The OFDM signal generator has been validated in two ways: first, Agilent provides its own software for programming the VSG with 802.11a compliant signal, and we compared its output with the output of our simulator, finding an exact match. Also, we compared simulation results against measured 802.11a transmission performance in short back-to-back electrical links with added white gaussian noise. The result is shown in Fig. 2.11, where we note that the simulated and measured EVM are in good agreement.

Note that in Fig. 2.11: EVM $\simeq -$CNR, where CNR is the carrier-to-noise ratio. This is a result of the choice of measuring the CNR over the whole bandwidth of the OFDM signal, i.e., 20 MHz.

In Fig. 2.11, the VSG and VSA have a minimum EVM of about -43 dB. Later, a better calibration of the VSG lowered the minimum EVM down to about -46 dB - -49 dB for a 0 dBm signal.

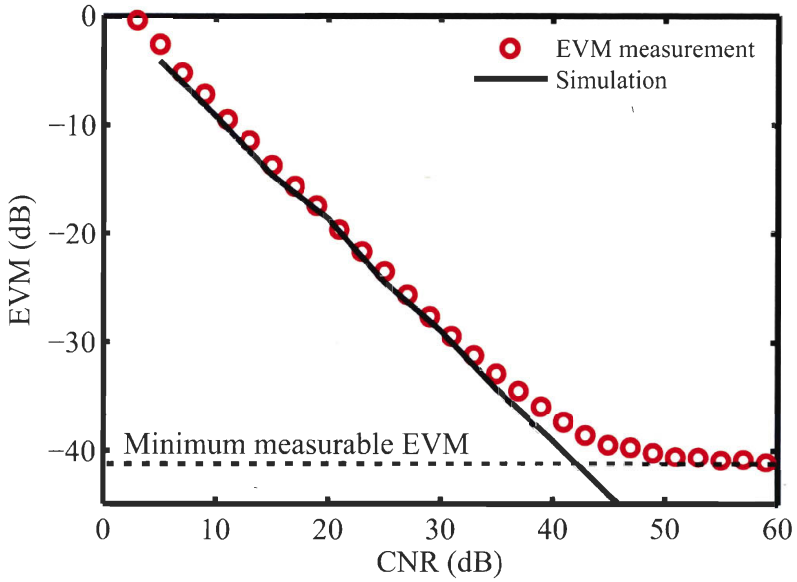

Figure 2.11: Measured and simulated EVM versus carrier-to-noise ratio (CNR) for 64-QAM OFDM Noise is integrated over a 20 MHz bandwidth.

2.5 Conclusions

In this chapter we briefly introduced the OFDM signal format, which we adopt as a reference signal for this work, and the IEEE 802.11a physical layer. We aimed to describe the most important features of OFDM, including its construction from a set of data, its spectrum, and the PAPR. We also defined the EVM, that we will use often in this work as a measure of the OFDM signal quality.

We described the simulator used for all the simulations along this work, highlighting its modular structure. Also, we detailed the algorithms used for the generation and analysis of OFDM signals. This is important because the BER and EVM of the OFDM signal may depend on the specific algorithms used in the simulator. For example, we used a simple zero-forcing algorithm for channel response compensation, but more complex algorithms, which are out of the topic of this thesis, may provide better performance in presence of noise or distortion. To ensure that the simulated results can be properly compared with measurements, we implemented the same algorithms used in our analysis hardware (an `Agilent E4440A` VSA). Also, we coded the simulator in such a way that the same OFDM frames can be used for simulations and measurements, by properly programming a VSG (`Agilent E4438C`).

We used this simulation tool to support all the original contributions of this work, which are reported in the following chapters.

Chapter 3

RF gain in ROF links

A ROF link can be studied as a form of active RF transmission line or two-port network (Fig. 3.1). Active two-port networks are fully described by four main properties: gain, bandwidth, added noise and nonlinear distortion. These properties are often interlaced and can be characterized using a number of figures of merit. For example, microwave engineers use three definitions of gain depending on the impedance matching at the input and output of the two-port network. We like to work with the transducer gain, defined as the ratio between the available power from a generator onto the power effectively delivered to the load[1]. In our case, the power generator is feeding its signal to the ROF link modulator, and the load is an antenna at the link end.

To understand the gain performance of a link, we do not need to specify the protocol of the transmitted signal (OFDM or other), but we just have to specify if the link is to be used with wideband or narrowband signals. As we specified in the introduction, we focus on narrowband links, or sub-octave links, because this is the nature of the OFDM signals we propagate on the fibre. Sub-octave RF signals are characterized by a RF carrier f_{RF} much greater than the signal bandwidth, and this allows some

[1]The transducer gain is defined as:

$$G_T = \frac{P_L}{P_{av,S}}, \tag{3.1}$$

where P_L is the active power dissipated onto a load of impedance Z_L. As a function of the voltage amplitude V_L on Z_L, this is given by:

$$P_L = \frac{|V_L|^2}{2\,\mathrm{Re}\{Z_L\}}. \tag{3.2}$$

$P_{av,S}$ is the active power dissipated on a load Z_S when the source impedance and load are conjugately matched. Then, $P_{av,S}$, function of the source amplitude voltage, is expressed as:

$$P_{av,S} = \frac{|V_S|^2}{8\,\mathrm{Re}\{Z_S\}}. \tag{3.3}$$

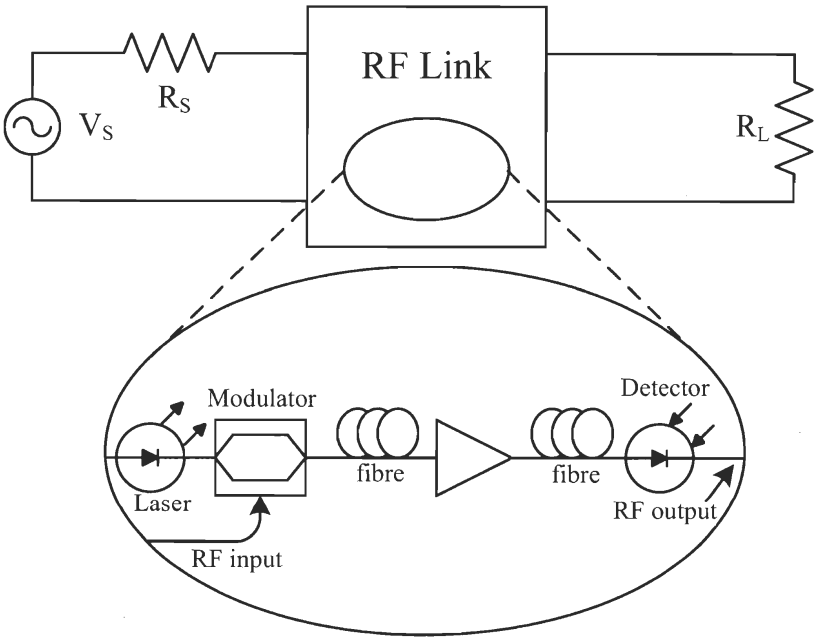

Figure 3.1: Cartoon of a ROF link seen as an RF transmission line.

design choices that would not be appropriate for wideband signals. Also, we assume that the link transfer function can be considered constant over the narrow bandwidth of sub-octave signals. Hence, for the study of link gain performance, these can be modeled by a simple RF tone, and the results and measurements obtained with such a simple signal will be valid for the much more complex OFDM stream. Other link properties like noise, usually described using noise figure (NF) and CNR, nonlinear harmonic distortion and intermodulation distortion will be described in chapters 4 and 5.

Optical EDFAs are commonly used to increase the link RF gain, dynamic range [82], and even noise figure [83] in links with high optical losses. The link described in this chapter includes optical amplification to ensure sufficient link gain and output power: as explained in the introduction, we aim to optimize the link output RF power to reduce the number of RF amplifiers in the WTP, or even eliminate them. This helps to simplify the RF chains of optically fed antenna arrays in the WTPs, reducing RF crosstalk problems and cost. Furthermore, we cannot trade off the output optical RF power with the output signal quality: the optical link must be as transparent as possible to the OFDM signal, and link added noise and distortion must be as low as possible. RF amplifiers are a well known source of signal distortion, which may severely affect the link BER. Hence, by eliminating the RF amplifiers, we also aim to improve the link linearity. This is the main motivation for the indepth study of the link gain presented in this chapter, and for the study of link distortion presented in chapter 5.

This is the core of the ROF link design problem: is it possible to have a high power link with good linearity? Some considerations:

- The external optical modulator is well known to be a severe source of distortion, as described later in chapter 5. Surely, one solution to this problem is to develop linear modulators, but these devices are often complex (see [84, page 242] for a review on linearized modulators) and expensive: in a WDM system with many modulators, a simpler solution is needed. Another option is the use of electronic predistortion, but again this increases the complexity of the modulation stage and we choose not to explore this solution.
- The fibre is another significant source of distortion.
- One important experimental observation is that EDFAs **do not** introduce RF signal distortion (see chapter 5 for a complete discussion on this topic).
- As discussed in chapter 1, we assume the detector to be a linear device.

The modulator distortion can be kept under control by limiting the power of the RF modulation signal. The fibre distortion can be reduced by limiting the peak propagated optical power. At the same time, the link gain must be increased to compensate for the input power back-off. When the link uses a MZ electro-optic modulator, we found that these three conditions can be met by optimizing the modulator bias point. This allows to simultaneously maximize the link gain and the optical modulation depth (OMD), by reducing the propagated peak and average optical power. The OMD is defined as:

$$\text{OMD } [\%] = 100 \cdot \frac{(P_{max} - P_{min})}{(P_{max} + P_{min})}, \tag{3.4}$$

where P_{max} and P_{min} are the maximum and minimum optical power transmitted over the fibre. The OMD can be taken as a figure of merit of the efficiency of the link, because a low OMD means that most of the optical power does not convey meaningful information over the fiber, but is lost as unmodulated carrier. This unused power is harmful for several reasons: it saturates the optical amplifiers thereby reducing the available gain, it can saturate the detector (invalidating the assumption of a linear detector) and trigger fibre Kerr effects and SBS.

In this chapter, we discuss the optimization of the link gain and OMD. We start with a description of the loss performance of externally modulated linear optical links. Considering the presence of linear non-saturable optical amplifiers, we draw on a known model of the optical link seen as a form of RF transmission line to show rigorously which link parameters affect the link gain, and how. After, we extend the model considering the case of saturable optical amplifiers, and we report original results on the advantages of controlling the modulator bias in such links. The analysis is based on an analytical description of the achievable RF gain and OMD as a function of modulator bias and amplifier parameters. We report experimental results for validation of the model, finding excellent agreement with simulation. Then, we demonstrate that controlling the modulator bias allows the amplifier to be shared among several transmitters without loss in link RF gain with respect to links without bias optimization. This result opens

the way to optical amplifier sharing and related cost reduction for distribution links serving antenna arrays.

Finally, we briefly discuss the impact of fibre dispersion and detector impedance matching on link losses. In particular, we show the importance of using narrowband impedance matching to increase the link gain.

3.1 Optical links with unsaturated amplifiers

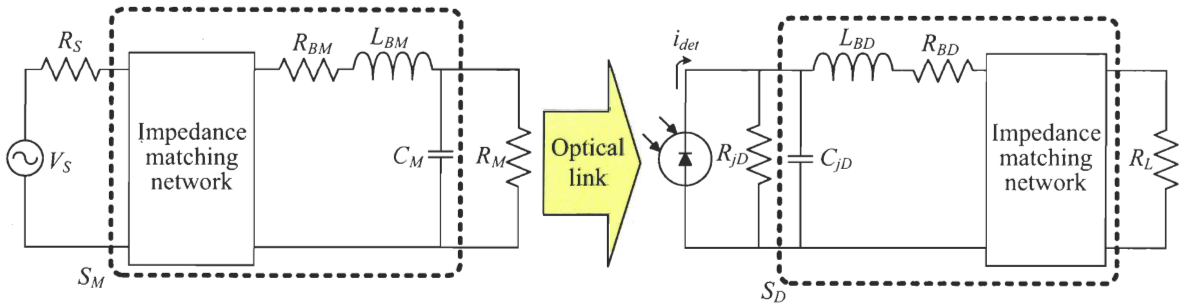

Figure 3.2: Circuit model for a MZ modulator and a detector.

In the literature, among others, Daryoush [85], Betts [86], Cox [55] and Stephens [87] described the gain[2] of linear optical links with external modulation. We adopt here the model of Daryoush because it takes into account the amount of impedance matching of a MZ modulator and a surface-illuminated photodetector (SIPD) with the link source and load, respectively. The model is pictured in Fig. 3.2: a signal generator with output voltage V_S and impedance R_S feeds the MZ through an impedance matching network. The modulator and detector internal models include networks of capacitances, inductances and resistances, which represent their internal losses and frequency behavior. These electric networks are described, along with impedance matching circuitry, with the two-port microwave scattering matrices S_M and S_D, for the modulator and detector respectively.

It is well known that the optical power $P_{out,MZ}$ at the output of a MZ can be written as:

$$P_{out,MZ}(t) = \frac{P_{laser}}{2}\left\{1 - \cos\left[\Gamma + \frac{\pi}{V_\pi}V_{R_M}(t)\right]\right\}, \tag{3.5}$$

where P_{laser} is the average optical power from the laser source, V_π is the modulator halfwave switching voltage, Γ is determined by the modulator bias point and $V_{R_M}(t)$ is the voltage over C_M and R_M. We consider a simple tone modulating signal:

$$V_{R_M}(t) = V_{RF}\cos(2\pi f_{RF}t). \tag{3.6}$$

[2]We use "gain" here in the most general sense: insertion loss is simply a gain comprised within 0 and 1 in linear units.

In a linear optical link with propagation loss L and optical gain G, the received photocurrent i_{det} is:

$$\begin{aligned} i_{det}(t) &= [\mathcal{R}P_{out,MZ}(t) * h_{link}(t)] * h_{det}(t) \\ h_{link}(t) &\overset{Fourier}{\longleftrightarrow} H_{link}(f) = \frac{G}{L}, \end{aligned} \tag{3.7}$$

where $H_{link}(f)$ is the intensity transfer function of the optical link that is considered a constant, $\mathcal{R}$ is the detector responsivity, also assumed constant with frequency, and $h_{det}(t) \overset{Fourier}{\longleftrightarrow} H_{det}(f)$ takes into account all detector frequency dependent behavior that is not included in the impedance matching analysis. Assuming that the detector bandwidth is higher than the frequency of interest f_{RF}, we can consider $H_{det}(f) = 1$. At the receiver, we are interested in the detected photocurrent at f_{RF}, which can be written as:

$$i_{det}(t) = \mathcal{R}\frac{G}{L}P_{laser}\sin(\Gamma)\, J_1\left(\frac{\pi}{V_\pi}V_{RF}\right)\cos(2\pi f_{RF}t), \tag{3.8}$$

where J_1 is a Bessel function of the first type and order. Equation (3.8) is developed in appendix B.

The signal amplitude V_{RF} in general depends on the efficiency in transferring power from the source signal generator to the MZ modulator arms. The signal generator available power (i.e., the power delivered to a conjugate matched load) is:

$$P_{av,V_s} = \frac{|V_S|^2}{8R_S}. \tag{3.9}$$

Then, V_{RF} can be written as:

$$V_{RF} = \sqrt{2R_M P_{av,Vs} G_{TM}}, \tag{3.10}$$

where G_{TM} is the transducer gain of the modulator two-port network model S_M. In the most general case, G_{TM} is function of frequency, but we assume it to be constant. Equation (3.10) is demonstrated in section 3.4. If $\frac{\pi}{V_\pi}V_{RF} \to 0$:

$$J_1\left(\frac{\pi V_{RF}}{V_\pi}\right) \approx \frac{\pi V_{RF}}{2V_\pi}, \tag{3.11}$$

and (3.8) can be written as:

$$i_{det}(t) \approx \mathcal{R}\frac{G}{L}P_{laser}\sin(\Gamma)\left(\frac{\pi\sqrt{2R_M P_{av,Vs} G_{TM}}}{2V_\pi}\right)\cos(2\pi f_{RF}t). \tag{3.12}$$

Now, the power delivered at the end of the link to R_L can be written as:

$$P_L = G_{TD}\frac{R_{jD}\,|i_{det}|^2}{8}, \tag{3.13}$$

where G_{TD} is the transducer gain associated to the detector two-port network model S_D, and R_{jD} is the detector junction resistance. Hence, the whole link transducer gain is:

$$G_{link} = \frac{P_L}{P_{av,Vs}} = \sin^2(\Gamma)\left(\frac{\pi}{4V_\pi}\mathcal{R}\frac{G}{L}P_{laser}\right)^2 G_{TD}R_{jD}G_{TM}R_M. \tag{3.14}$$

This small-signal model of the link gain clearly shows that the ideal gain is dependent on the square of the average optical power at the link end, i.e., $\frac{G}{L}P_{laser}$. This means that optical amplification is exceptionally effective in increasing the RF signal power: 30 dB of optical amplification correspond to 60 dB of electrical amplification! The gain is also dependent on the square of $\sin(\Gamma)$. This clearly shows that in links featuring an optical gain G constant with bias, the best choice for the modulator bias is the "quadrature point", i.e., $\Gamma = \frac{\pi}{2}$. This is the case for links with unsaturated optical amplifiers, as we see in the next section.

Note that if the modulating signal is large, so that $\frac{\pi}{V_\pi}V_{RF} \gg 0$, the link gain G_{link} saturates due to the nonlinear behavior of the Bessel function in equation (3.8). This goes with distortion from the modulator. Hence, to conserve link linearity we must limit the modulation signal within the small signal regime defined by $\frac{\pi}{V_\pi}V_{RF} \to 0$. In these conditions, the link OMD is poor and most of the optical power transmitted over the fibre is lost as unmodulated carrier.

The link gain model described above is known in the literature. In the next section, we present our contribution to this topic, first published in [88]: we introduce a more realistic model for the link gain, which includes saturation of the amplifier. Then, we show that the best choice for the modulator bias may no longer be the quadrature point: moving the bias off quadrature can improve link gain and OMD without introducing unwanted distortion. The theory and measurements presented here assume a linear non-dispersive response from the fibre. The impact of dispersion and fibre nonlinear effects will be treated in chapter 5.

3.2 Optical links with saturable amplifiers

In many wideband optical links, the MZ modulator bias is set at the quadrature point in order to increase modulation efficiency and reduce second order distortion, as shown by equation (3.8) and in [89]. This bias setting gives maximum spurious-free dynamic range (SFDR) and minimum distortion in wideband links [90]. We define narrowband systems, or sub-octave systems, those with signal bandwidth much smaller than the frequency of the RF carrier. In contrast to wideband systems, sub-octave systems show no superposition between the bands occupied by the fundamental transmitted frequency and the harmonics generated by nonlinear effects. Thus, sub-octave systems are mostly affected by third order intermodulation distortion (IMD3), because second order harmonic distortion terms are out of band and can be filtered in the RF domain

(more on this topic will be developed in chapter 5). Furthermore, we know from the theory of MZ modulators, and we demonstrate in appendix B, that the IMD3 is not affected by the bias but it is fixed by the amplitudes of the modulation voltage and the modulator halfwave switching voltage ([89] and equation (B.20b) in appendix B). Hence, in the hypothesis of negligible fibre distortions, nonlinearity-induced transmission errors in sub-octave links are only affected by the modulation amplitude and not by the bias, which becomes a free parameter for optimization. In this section we explicitly consider the case of linear non-dispersive fibre, i.e., a simple attenuator.

In the following, we define the modulator bias as:

$$\Gamma = \frac{\pi V_{bias}}{V_\pi} \tag{3.15}$$

where V_π is the modulator halfwave switching voltage. Without loss of generality, we assume that $V_{bias} = 0$ at the modulator minimum transmission point (see Fig. 3.3).

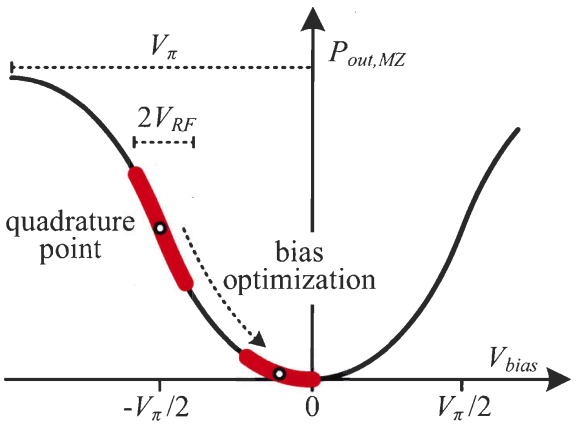

Figure 3.3: Transfer function of the MZ modulator with $V_{bias} = 0$ at the minimum transmission point.

Early published works on bias optimization of narrowband ROF signals include [91], where the authors show that bias out of quadrature can improve the signal-to-noise ratio and SFDR of shot noise limited links. In [92], Bulmer and Burns investigated the intermodulation distortion and SFDR for an external modulation link, but did not predict superior performance resulting from a modulator bias voltage out of quadrature. In [90], Ackerman and coworkers study gain, noise figure and SFDR as a function of many link parameters, including the modulator bias. Their conclusion is that, unless high optical power is available, optimum bias is at quadrature where the link offers high gain. Recently, Ackerman [93] and Roussell [94] demonstrated very low noise figures in low-biased links without optical amplification. In [95, 96], low-biasing the modulator has been proposed in MZ based radio frequency downconverters in order to lower the conversion losses. In [97, 98], Farwell and Nichols showed that in narrowband high optical power links, the modulator bias can be moved towards the minimum transmission point in order to increase the SFDR. Farwell's work is interesting because he states that SFDR is increased only if enough excess optical power is available in the link. This

is important because availability of excess power (or, in other words, optical gain) is needed in low-biased links to compensate for excess losses due to modulator low-biasing (described by the term $\sin^2(\Gamma)$ in the (3.14)).

The link excess power may come from a high power laser source or from an EDFA. The EDFA option is interesting because the amplifier can potentially be shared between many channels, thus reducing the link cost in a WDM environment. However, Farwell's analysis does not assume any limit on the availability of excess power coming, for example, from EDFA gain saturation, which prevents full compensation of low-biasing losses. Furthermore, available gain of an EDFA depends on its input power and thus varies with the modulator bias. To our knowledge, the published literature previous to our work did not explore the interaction between the EDFA operating point and the modulator bias in narrowband ROF links. Thus, we analyzed theoretically and experimentally the link RF gain achievable when a low biased modulator and an EDFA amplifier are used together. Contemporary to our work, Urick *et al.* reported an optically amplified link with more than 40 dB gain and 6 dBm output power at 1 dB compression, based on a low-biased MZ modulator [69] and a specially designed high power detector. Urick did not present any analytical justification to the observed gain improvement at low bias. However, his work is important to us because it proves that high output power levels and good linearity can be achieved in the kind of link studied here, provided that the detector is properly designed to respect the assumption of linear response of the optical-to-electrical conversion.

In ROF links, potential sources of distortion are the fibre and the detector. In order to avoid both without sacrificing the detected signal power, the OMD should be as high as possible. We show here that the OMD can be optimized when moving the modulator bias to the minimum transmission point, and we identify under which conditions it is possible to have maximum link gain and OMD simultaneously.

Later, the analysis is extended to the case of many low biased signals amplified by the same EDFA.

3.2.1 RF gain with saturable amplifiers

Let us take the link shown in Fig. 3.4 as reference: the link is built using a DFB laser that is intensity modulated by a MZ modulator after polarization control. The modulator output is amplified by an EDFA and propagated over 10 km of standard fibre. The fibre is assumed to be linear, so in the experimental setup it is replaced by a 2 dB attenuator. An attenuator is also added at the link end in order to control the detector saturation, and observe gain curves unaffected by the detector nonlinear behavior. Total link attenuation after the amplifier, including fibre losses, is set to 20 dB. The detected RF power is observed on a RF spectrum analyzer. The modulating signal

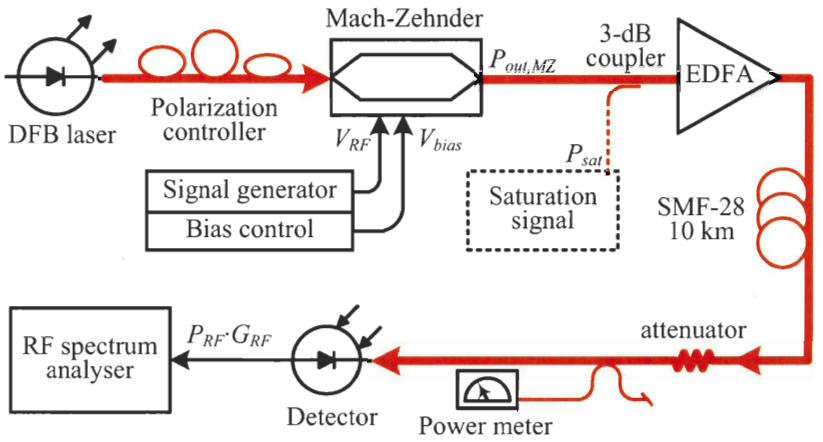

Figure 3.4: Experimental setup for measuring the RF gain of a ROF link with a saturable optical amplifier.

is a simple tone at $f_{RF} = 5\,\text{GHz}$, which is the carrier frequency of interest for 802.11a/g based ROF links. A saturating unmodulated optical signal can be coupled to the EDFA input through a 3 dB coupler. The function of the saturating signal is described later. Other details on the experimental link are given in table 3.1.

Table 3.1: Details on the hardware used in Fig. 3.4 and in the simulation code.

Device	Model	Settings and Comments
Fibre	SMF-28	Length: 10 km Losses: 0.2 dB/km
Laser	DFB HP LSC2500	Pump current: 100 mA Output power: 7 dBm Max. power at EDFA input: -2 dBm
Modulator	MZ JDS OC-1	Bandwidth: 10 GHz Extinction ratio: > 35 dB Insertion loss: 5 dB V_π: 3.35 ± 0.07 V
EDFA	JDS OAB1552+1FA0	G_0: 37 dB $P_{out,max}$: 17 dBm
Detector	Agilent 11982A	Bandwidth: 15 GHz Responsivity: 300 V/W Gain: 20 dB

As seen in the preceding section, the RF gain (G_{RF}) of the link is proportional to:

$$G_{RF} \propto \left[G_{EDFA} \sin\left(\pi V_{bias}/V_\pi\right)\right]^2, \tag{3.16}$$

where G_{EDFA} is the amplifier available optical gain. The proportionality sign is due to the dependence of gain on system parameters, such as optical losses and detector responsivity, which are kept constant in the experiments and theoretical developments presented below.

Without loss of generality, we assume that $V_{bias} = 0$ at the modulator minimum transmission point, and we assume $V_{RF} < \frac{V\pi}{2}$.

The EDFA saturated gain can be modeled by [99]:

$$G_{EDFA} = \frac{G_0}{1 + \left(\frac{G_0 \langle P_{out,MZ} \rangle}{P_{out,max}}\right)^{\alpha}}, \tag{3.17}$$

where G_0 is the small signal gain of the amplifier, $P_{out,MZ}$ is the modulator output optical power, $P_{out,max}$ is the saturated maximum output optical power from the amplifier, and α is an empirical parameter with values close to 1. The EDFA saturation level is fixed by the input mean optical power $\langle P_{out,MZ} \rangle$, which depends on V_{bias} as described in [89]:

$$\langle P_{out,MZ} \rangle = \frac{P_{laser}}{2}\left[1 - J_0\left(\frac{\pi V_{RF}}{V_\pi}\right)\cos\left(\frac{\pi V_{bias}}{V_\pi}\right)\right], \tag{3.18}$$

where P_{laser} is the unmodulated optical power from the DFB and J_0 is the zero-order Bessel function of the first kind. Equation (3.18) is also derived in appendix B.

Inspection of (3.16) and (3.17) suggests that if the mean optical power from the modulator at the quadrature point is high enough to saturate the EDFA, the RF gain can be maximized by moving the bias away from the quadrature point toward the minimum transmission point. This may appear surprising because the (3.16) implies that such a bias shift reduces the MZ modulation efficiency. However, the lower EDFA input power at low bias reduces its saturation level and increases the EDFA available gain. This effect may dominate over the reduction in MZ modulation efficiency and the bias which gives maximum overall gain may not be at the quadrature point. Gain optimization has been confirmed through numerical simulation, as well as verified using the experimental setup in Fig. 3.4. Note that moving the bias towards the minimum transmission point is not equivalent to simply adding losses before the amplifier: an attenuation reduces the average optical power and the amplitude of the detected RF signal (i.e., the MZ modulation efficiency) by the same amount, whereas moving the bias towards the zero transmission point decreases the average optical power as $1 - \cos\left(\frac{\pi}{V_\pi}V_{bias}\right)$, and the amplitude of the detected signal as $\cos\left(\frac{\pi}{V_\pi}V_{bias}\right)$. This is demonstrated in appendix B by developing mathematically the instantaneous optical power at the modulator output. The variations of average optical power and amplitude of RF signal detected at the output of the MZ as a function of bias are shown in Fig. 3.5: the average optical power decreases more quickly than the RF signal amplitude.

Some notes on the experimental values for the parameters used in the calculations are given in the following. The values for α, $P_{out,max}$ and G_0 are given in table 3.1 and derived from experimental characterization of the EDFA used in the experiments, as reported in Fig. 3.6.

The DFB provided a power P_{laser} =7 dBm. However, the value to be used in (3.18)

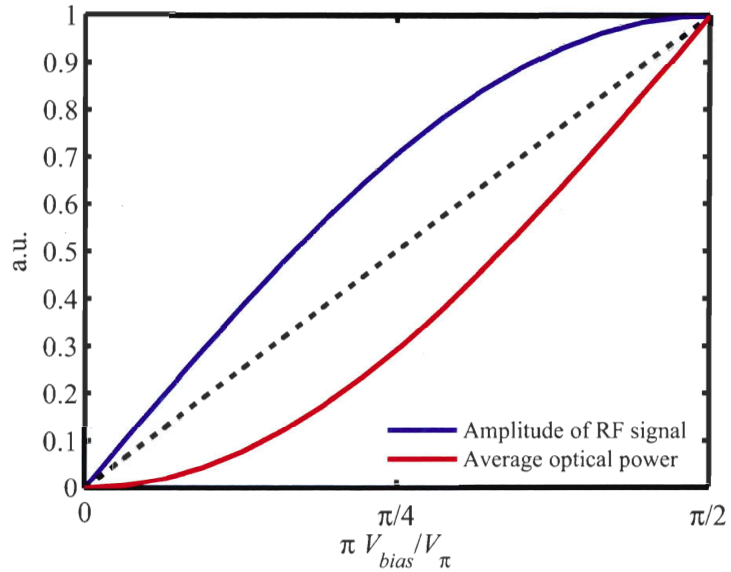

Figure 3.5: Normalized variations of average optical power and detected RF signal amplitude (i.e., MZ modulation efficiency) at the output of the MZ as a function of bias. Small signal modulation.

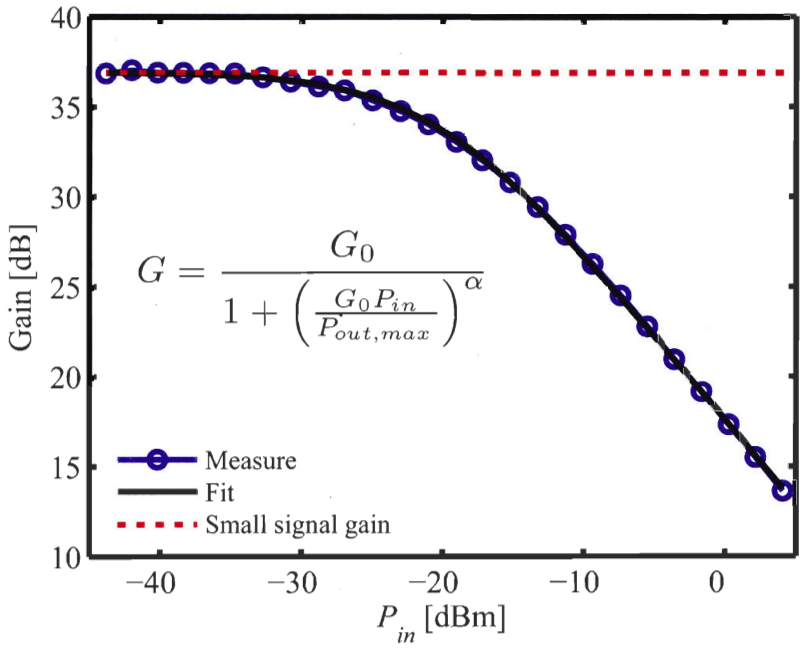

Figure 3.6: Saturated EDFA gain as a function of input optical power

must include the total insertion losses of all the devices inserted between the laser and the EDFA, including the losses of the MZ (at maximum transmission point), given in table 3.1. Hence, the modulator V_π was estimated at (3.35 ± 0.07) V. Details on the estimation of V_π are reported in section 3.3.

Simulations and measurements are compared in Fig. 3.7, where we show the link RF

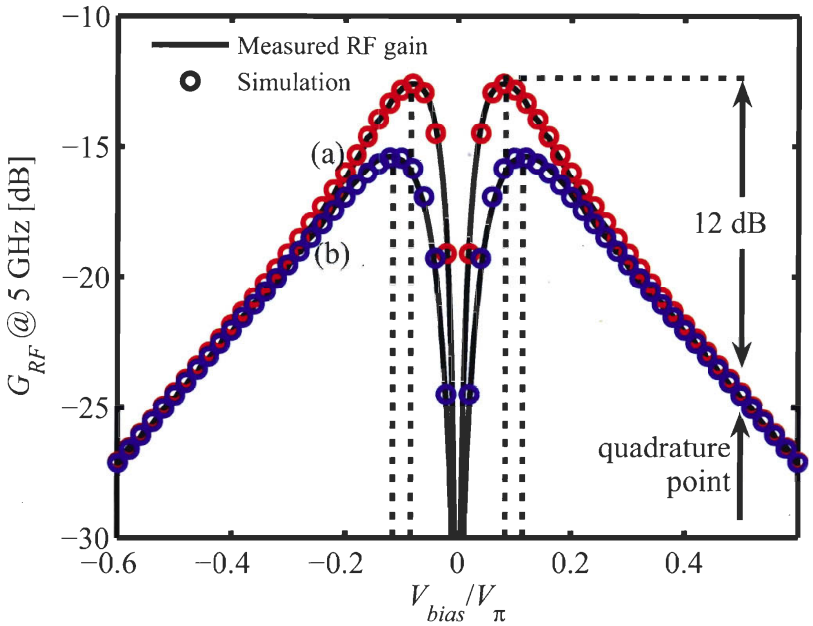

Figure 3.7: Comparison between measured and simulated RF gain for the reference link as a function of V_{bias}. In a): $P_{RF} = 0\,\text{dBm}$ (estimated $V_{RF}/V_\pi = 0.038 \pm 0.001$) and $|V_{bias,Gmax}/V_\pi| = 0.083 \pm 0.001$. In b): $P_{RF} = 10\,\text{dBm}$ (estimated $V_{RF}/V_\pi = 0.119 \pm 0.002$) and $|V_{bias,Gmax}/V_\pi| = 0.114 \pm 0.001$. $G_0 = 37\,\text{dB}$, $P_{out,max} = 17\,\text{dBm}$ and $P_{laser} = -2\,\text{dBm}$. For numerical simulation: $\alpha = 0.973$ and extinction ratio: 42 dB. For analytically calculated values of $V_{bias,Gmax}$: $\alpha = 1$ and extinction ratio is infinite.

gain for RF modulation powers P_{RF} of 0 dBm (curve a, estimated $V_{RF}/V_\pi = 0.038 \pm 0.001$) and 10 dBm (curve b, estimated $V_{RF}/V_\pi = 0.119 \pm 0.002$). Note that V_{RF} is related to P_{RF} as described by equation (3.10), which we rewrite here as:

$$V_{RF} = \sqrt{2 \cdot R \cdot P_{RF} \cdot G_{TM}} \tag{3.19}$$

where R is a 50 Ω resistance, and G_{TM} is the modulator transducer gain experimentally estimated in this link at -8 dB for 5 GHz, and is function of frequency and of the impedance matching level. P_{RF} is the power read on the screen of the signal generator used as source, and represent the available power P_{av,V_s} defined by the (3.9).

In this link, the RF gain is negative because of losses induced by the optical attenuator, but we observe in Fig. 3.7 an improvement in gain by moving the bias from $|V_{bias}/V_\pi| = 0.5$ to an optimum bias $V_{bias,Gmax}$ at $|V_{bias,Gmax}/V_\pi| = 0.083 \pm 0.001$ for curve (a) and at $|V_{bias,Gmax}/V_\pi| = 0.114 \pm 0.001$ for curve (b). The gain improvement reaches about 12 dB for curve (a), with $P_{RF} = 0\,\text{dBm}$, and 9 dB for (b), with $P_{RF} = 10\,\text{dBm}$: it decreases with higher modulation power due to the increase of the mean optical power with V_{RF} for a given $V_{bias} < V_\pi/2$, as described by the zero-order Bessel function in equation (3.18).

In order to identify the conditions at which maximum gain is attained for a given link, we differentiate with respect to V_{bias} an analytical expression for G_{RF} based on

(3.16)-(3.18), with $\alpha = 1$. The V_{bias} that maximizes the gain is defined by:

$$\cos\left(\pi V_{bias,Gmax}/V_\pi\right) = \frac{G_0 P_{laser} J_0\left(\pi V_{RF}/V_\pi\right)}{A}, \tag{3.20}$$

where $A = G_0 P_{laser} + 2P_{out,max}$. Equation (3.20) gives the bias values identified by dotted vertical lines in Fig. 3.7. Note that the $\alpha = 1$ approximation has a negligible effect over the $V_{bias,Gmax}$ calculation. With $V_{bias} = V_{bias,Gmax}$, the maximum gain is:

$$G_{RF,max} \propto 2\left[\frac{J_1\left(\pi V_{RF}/V_\pi\right)}{V_{RF}}\right]^2 \frac{\left[G_0 P_{laser} P_{out,max}\right]^2}{[A]^2 - \left[G_0 P_{laser} J_0\left(\pi V_{RF}/V_\pi\right)\right]^2}. \tag{3.21}$$

where J_1 is the first-order Bessel function of the first kind.

Equation (3.20) shows that $V_{bias,Gmax}$ approaches the quadrature point if V_{RF} increases because, for very high values of V_{RF}, the bias does not affect much the average power at the modulator output. Variation of $V_{bias,Gmax}$ with P_{RF} is shown later in Fig. 3.11. Also, if $P_{out,max} \gg \frac{G_0 P_{laser}}{2}$, i.e., if the EDFA is never saturated for any value of bias, then $V_{bias,Gmax}$ is near to the quadrature point: the $V_{bias,Gmax}$ is far from the quadrature only if the EDFA saturation conditions vary with the bias setting.

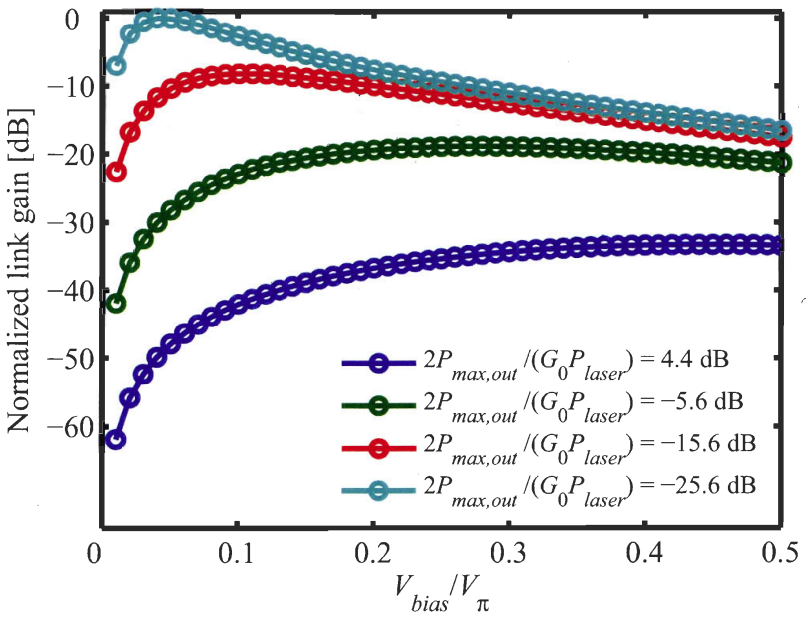

Figure 3.8: Simulation of the normalized link gain versus bias, for different values of $2P_{out,max}/\left(G_0 P_{laser}\right)$.

The link gain as a function of bias and $G_0 P_{laser}$ is shown in Fig. 3.8. The $P_{out,max}$ is constant at 17 dBm. Hence, when increasing $G_0 P_{laser}$ the optimum bias moves nearer to 0, with greater advantage with respect to quadrature bias setting. Also, a higher value of $G_0 P_{laser}$ permits a higher RF link gain. In practice, there is always a gain advantage in using a high power laser as signal source, even if the EDFA is used to boost the signal after the modulator: for a given EDFA, the higher the laser power, the lower the

optimum bias and the higher the RF link gain (see Fig. 3.9). For $G_0 P_{laser} \gg P_{out,max}$, the optimum bias is fixed by V_{RF}:

$$V_{bias,Gmax}|_{G_0 P_{laser} \gg 2P_{out,max}} = \pm \frac{V_\pi}{\pi} \text{acos}\left[J_0 \left(V_{RF} \frac{\pi}{V_\pi} \right) \right]. \tag{3.22}$$

The position of the optimum bias as a function of $G_0 P_{laser}$, with $P_{out,max}$ as in table 3.1, is shown in Fig. 3.10

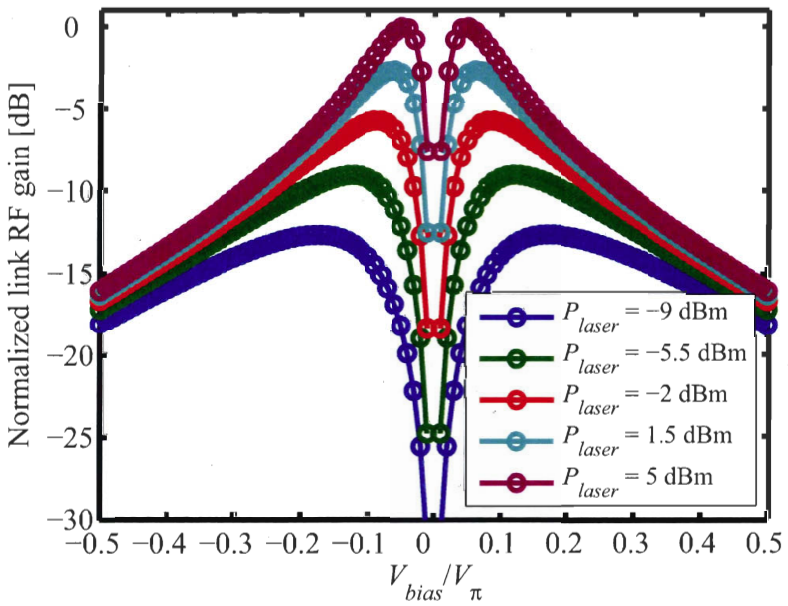

Figure 3.9: Simulation of the link gain versus bias for increasing values of P_{laser}. Assumptions: $P_{RF} = 0\,\text{dBm}$, $\alpha = 0.973$.

Ultimately, for large values of $G_0 P_{laser}$, the RF gain is limited by $P_{out,max}$. Hence, the higher the $P_{out,max}$, the larger the achievable gain is. This confirms that the maximum advantage in moving the bias is obtained when large excess power is available from a powerful laser and a high saturation EDFA.

In order to evaluate the impact of the gain saturation effect observed in Fig. 3.7, we calculated the variation of gain improvement at $V_{bias,Gmax}$ with respect to the quadrature point as a function of P_{RF} for the values of G_0, P_{laser} and $P_{out,max}$ of table 3.1. In Fig. 3.11 we show the result (curve a), along with the corresponding curve of $V_{bias,Gmax}$ (curve b). This calculation shows that, even at a modulation power corresponding to $V_{RF} = \frac{V\pi}{2}$, a small improvement in RF gain of about 2 dB is accessible for an optimum $V_{bias,Gmax} = 0.27 V_\pi$. However, in such a case, simulation has shown that the bias control is much less critical to link gain performance, as very low variations of RF gain are observed for a relatively wide span of bias values.

The calculations and theory developed here, and in particular equation (3.18), are

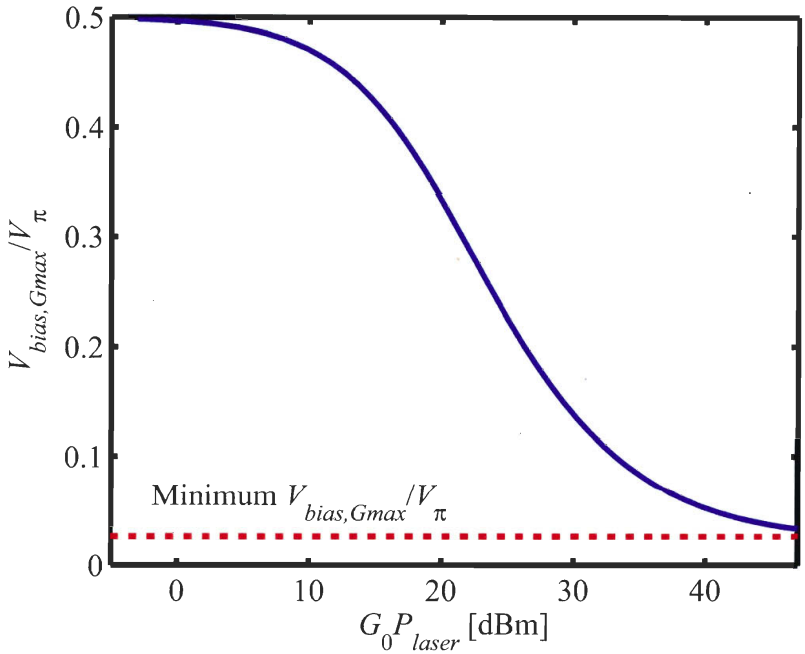

Figure 3.10: Simulation of $V_{bias,Gmax}$ as a function of G_0P_{laser} Assumptions: $P_{RF} = 0\,\text{dBm}$, $\alpha = 0.973$.

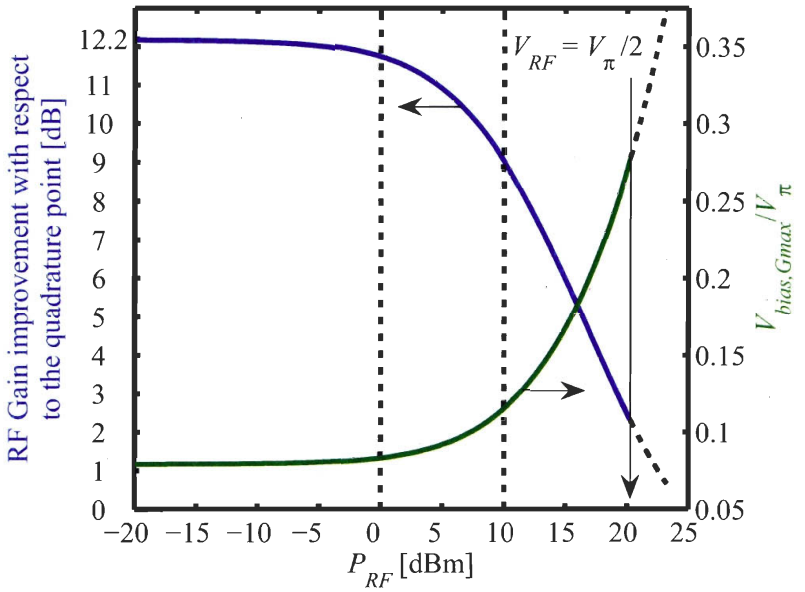

Figure 3.11: Simulation of $G_{RF,max}$ and $V_{bias,Gmax}$ as a function of the modulation power. Curve (a): calculation of the gain improvement at $V_{bias,Gmax}$ with respect to the quadrature point. Curve (b): corresponding values of $V_{bias,Gmax}$. $\alpha = 1$.

valid for high extinction ratio modulators. The extinction ratio is defined as:

$$\text{Extinction ratio} = 10 \cdot \log_{10}\left(\frac{P_{opt,max}}{P_{opt,min}}\right) \tag{3.23}$$

where $P_{opt,max}$ and $P_{opt,min}$ are the modulator output power at maximum and minimum

transmission points. With proper polarization control, the modulator used in our setup showed an extinction ratio higher than 35 dB.

3.2.2 Conditions for simultaneous improvement of gain and OMD

The OMD is fixed uniquely by the modulator and is not influenced by the EDFA. For a MZ, considering $V_{RF} \ll V_\pi/2$, the definition of OMD given by (3.4) can be approximated by:

$$\mathrm{OMD} = \begin{cases} \left| \frac{\sin(\pi V_{bias}/V_\pi)\sin(\pi V_{RF}/V_\pi)}{1-\cos(\pi V_{bias}/V_\pi)\cos(\pi V_{RF}/V_\pi)} \right| \cdot 100 & |V_{bias}| > V_{RF} \\ 100 & |V_{bias}| \leqslant V_{RF} \end{cases} . \tag{3.24}$$

The condition for maximum gain given by (3.20) does not necessarily correspond to a high OMD. From (3.24), OMD = 100% if $|V_{bias}| \leqslant V_{RF}$, or equivalently:

$$\cos(\pi V_{bias}/V_\pi) \geqslant \cos(\pi V_{RF}/V_\pi) . \tag{3.25}$$

Therefore, to attain OMD = 100% and maximum G_{RF}, the link parameters must satisfy the following inequality, obtained by developing (3.25) for $V_{bias,Gmax}$ from (3.20):

$$\frac{\cos(\pi V_{RF}/V_\pi)}{J_0(\pi V_{RF}/V_\pi)} \leqslant \frac{G_0 P_{laser}}{A} . \tag{3.26}$$

This relation can be used to guide the design of a link with optimized RF gain and OMD = 100%. Solving equation (3.26) with respect to $G_0 P_{laser}$ and $P_{out,max}$ gives the space of solutions shown as gray areas in Fig. 3.12. This calculation shows that for a given $G_0 P_{laser}$ value, the higher the EDFA saturation power, the higher the V_{RF} must be to respect the (3.26). This is because the optimum bias point moves near the quadrature point if $P_{out,max} \gg \frac{G_0 P_{laser}}{2}$.

The combination of G_0, P_{laser} and $P_{out,max}$ of our experiments are shown by the bold dot in Fig. 3.12: for P_{RF} =10 dBm equation (3.26) is respected, but not for P_{RF} =0 dBm (OMD = 75%).

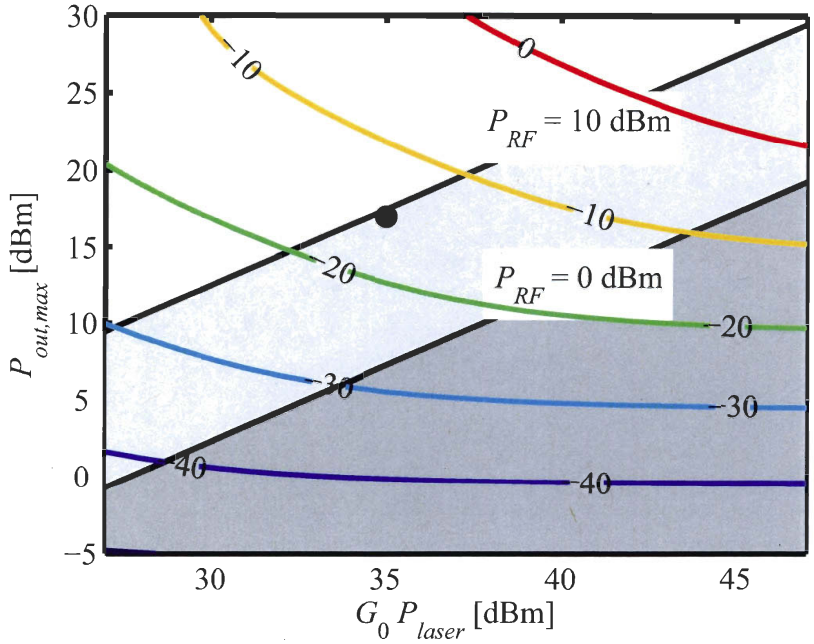

Figure 3.12: Space of $G_0 P_{laser}$ and $P_{out,max}$ values that allow simultaneous optimization of the link gain and the OMD. In light grayed region, condition (3.26) is respected only for P_{RF} = 10 dBm, whereas in dark grayed region the (3.26) is respected for both P_{RF} = 10 dBm and P_{RF} = 0 dBm. Color lines are the simulated received power at link end, for P_RF =0 dBm and $\alpha = 1$.

3.2.3 Gain behavior with multiplexed signals

We extended our model to include the case of an EDFA used to amplify many wavelength multiplexed signals, all with bias control, as could be the case of a real multiplexed link. In order to check the validity of our model, we measured and simulated the behavior of G_{RF} for different EDFA saturation levels. We coupled at the EDFA input an unmodulated laser acting as a controlled saturation signal with power P_{sat}, as shown in Fig. 3.4. Thus, the (3.17) is transformed into:

$$G_{EDFA} = \frac{G_0}{1 + [G_0 (< P_{out,MZ} > + P_{sat})/P_{out,max}]^{\alpha}}. \tag{3.27}$$

By following the same mathematical derivation that leads to equations (3.20) and (3.21), we can calculate new expressions for $V_{bias,Gmax}$ and $G_{RF,max}$. They have the same form as equations (3.20) and (3.21), but the parameter A is now expressed as:

$$A = G_0 P_{laser} + 2\,(P_{out,max} + G_0 P_{sat})\,. \tag{3.28}$$

In this case, the small signal EDFA gain may not be accessed anymore by adjusting the bias. Thus, a solution for the (3.26) exists only for:

$$2P_{sat} < P_{laser}\,[\sec(\pi V_{RF}/V_\pi)\,J_0(\pi V_{RF}/V_\pi) - 1]\,, \tag{3.29}$$

However, equations (3.20) and (3.21), with (3.28), are still valid and can fully predict $V_{bias,Gmax}$ and the corresponding value of G_{RF}. Measurements, simulation and prediction by the (3.20) and (3.21) are compared in Fig. 3.13 for P_{RF} = 0 dBm.

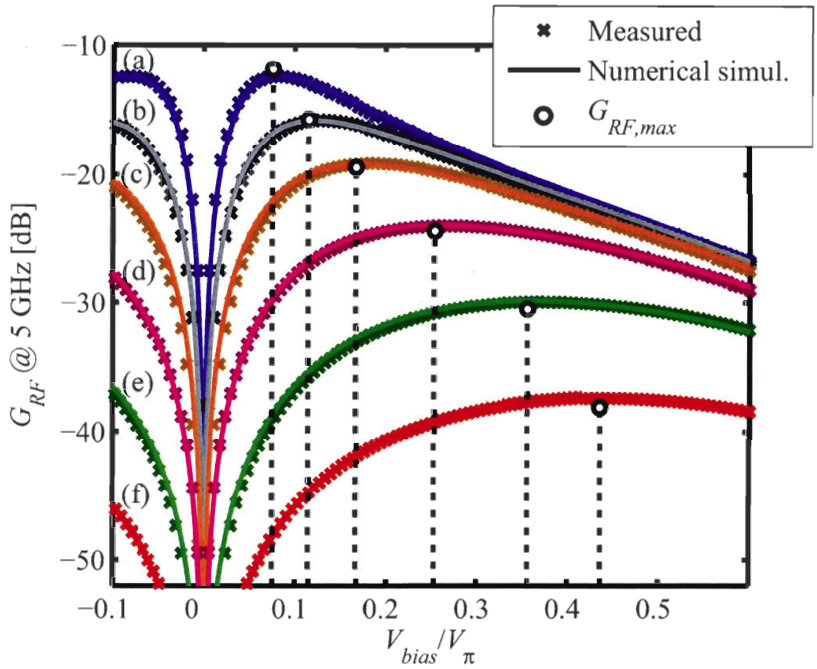

Figure 3.13: Link RF gain with external saturation signal. Comparison between measured gain curves as a function of bias, numerical simulation and predictions by (3.20) and (3.21), with (3.28). $P_{RF} = 0\,\text{dBm}$. From (b) to (f), power of saturation signal before coupler in dBm is P_{sat} =-15, -10, -5, 0, 5. For (a), the saturation signal is off. Other parameters for numerical simulation are as in table 3.1. For analytical solution: $\alpha = 1$ and modulator extinction ratio is infinite.

We observe a reduction of $G_{RF,max}$ and a displacement of $V_{bias,Gmax}$ towards the quadrature point with an increasing saturation signal power. A good fit is obtained for $G_{RF,max}$ and $V_{bias,Gmax}$ between the analytical solutions and the measured values, thus confirming the validity of equations (3.20) and (3.21). Note that, when the saturation signal is added, the mean optical power at the input of the EDFA cannot reach very low values and the bias optimization is much less effective. In Fig. 3.13, the small differences between the numerical simulation and the analytical solution are due to $\alpha = 1$ and the infinite extinction ratio approximations used in the analytical development.

Having verified the validity of our model, we simulated the behavior of G_{RF} for N modulated signals coupled at the EDFA input, all with optimized bias. In this case, the power at the EDFA input is equal to $N\langle P_{out,MZ}\rangle$ and equation (3.18) is transformed into:

$$G_{EDFA} = \frac{G_0}{1 + (NG_0 < P_{out,MZ} > /P_{out,max})^{\alpha}}. \tag{3.30}$$

A becomes:

$$A = G_0 P_{laser} + \frac{2P_{out,\max}}{N}, \tag{3.31}$$

and $G_{RF,max}$ at $V_{bias,Gmax}$:

$$G_{RF,max} \propto 2\left[\frac{J_1(\pi V_{RF}/V_\pi)}{V_{RF}}\right]^2 \frac{\left[G_0 P_{laser}\frac{P_{out,max}}{N}\right]^2}{A^2 - \left[G_0 P_{laser} J_0(\pi V_{RF}/V_\pi)\right]^2}. \tag{3.32}$$

Note the dependence on the N factor, which comes from the fact that N signals must share the same available $P_{out,max}$ at the EDFA output. Note also that the same $G_{RF,max}$ accessible to one signal with an EDFA with given $P_{out,max}$ is also accessible to N signals using an EDFA with maximum output power equal to $N \cdot P_{out,max}$. The RF gain as a function of bias and N is calculated and presented in Fig. 3.14. This calculation is valid if each signal has the same $P_{laser} = -2\,\text{dBm}$, taking into account the insertion losses of all the components placed before the EDFA.

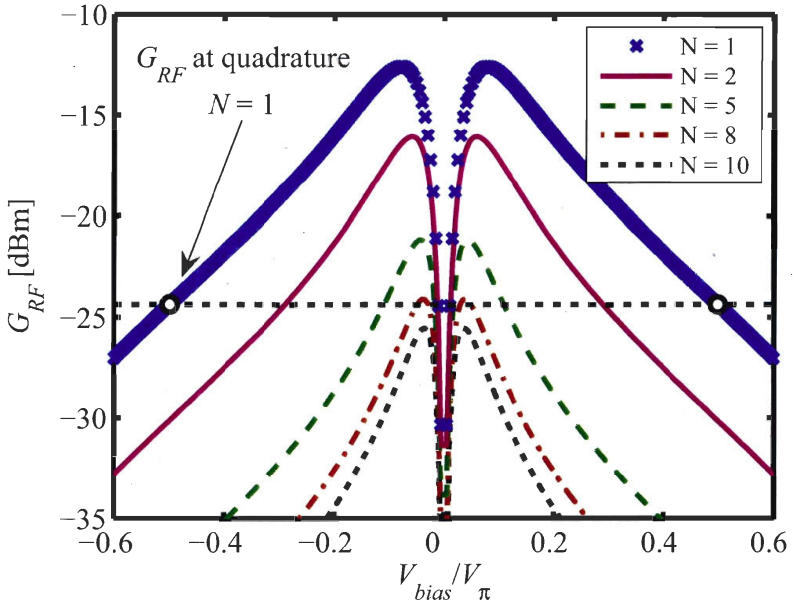

Figure 3.14: Simulation of G_{RF} versus bias and number of intensity modulated lasers coupled to the EDFA. The bias control allows the amplification of up to 8 signals with the same EDFA with, for each signal, a higher G_{RF} than the value observed at quadrature for only one signal. In this simulation the modulator has infinite extinction ratio.

When the number of signals is greater than one, the maximum G_{RF} for each signal decreases because the EDFA is more saturated. However, it is possible to amplify up to 8 signals and still obtain an RF gain for each signal higher than the gain that only one signal would show at quadrature. This observation is important because, in these conditions, the bias optimization allows the reduction of the number of amplifiers to be used in a wavelength multiplexed ROF link without loss of RF signal gain. In other words, bias optimization allows EDFA sharing among the wavelengths fed to and antenna array, so that the cost of the amplifier is shared among all the antennas in the array.

We now seek a general expression for the maximum number of signals that can be amplified with the same EDFA, while maintaining the RF output power to the same level that one single signal would experience with the modulator bias set at quadrature. This is found using $G_{RF} = G_{RF}\,(V_{bias}, N)$, considering G_0 and $P_{out,max}$ constant for all

the N signals, and solving:

$$G_{RF}\left(\frac{V_\pi}{2}, 1\right) = G_{RF}\left(V_{bias,Gmax}, N\right), \tag{3.33}$$

where on the left side is the RF gain for 1 laser at quadrature and on the right side is the gain for N lasers with optimized bias. If we use again the $\alpha = 1$ approximation, we can find an upper bound for the maximum N, equal to:

$$N_{max} = \sqrt{k^2 + 2k + \frac{1}{1 - \left[J_0\left(\pi V_{RF}/V_\pi\right)\right]^2}} - k \tag{3.34}$$

$$k = \frac{2P_{out,max}}{G_0 P_{laser}\left(1 - \left[J_0\left(\pi V_{RF}/V_\pi\right)\right]^2\right)} \tag{3.35}$$

This expression can be used to identify under which conditions the bias optimization is most effective as a function of the system parameters. In Fig. 3.15 we show the

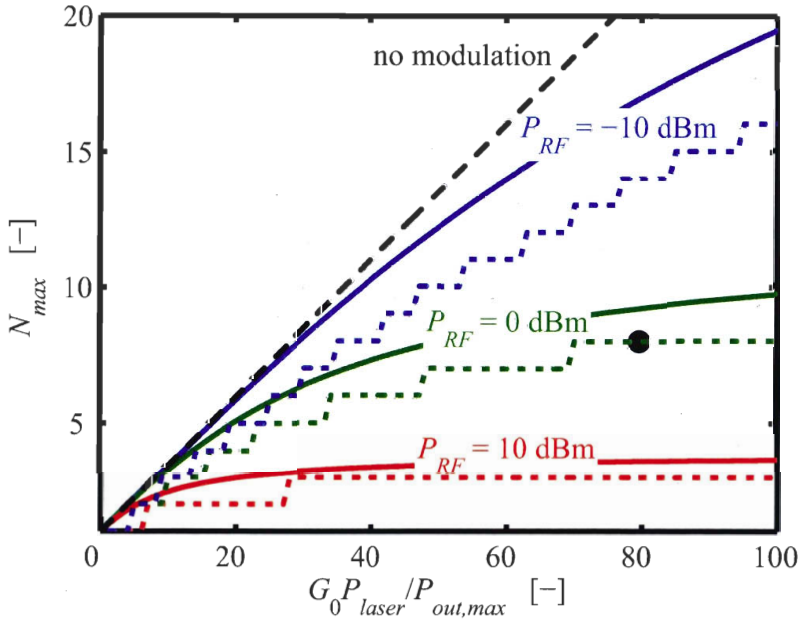

Figure 3.15: Number of signal that one EDFA can amplify without decreasing the RF gain. Each signal RF gain at $V_{bias,Gmax}$ is equal to the RF gain experienced by only one signal at EDFA input with bias at quadrature. Dotted lines represent numerical calculations with $\alpha = 0.973$, filled lines are upper bound given by (3.34), with $\alpha = 1$. Bold dot represent the case simulated in Fig. 3.14. In this simulation the modulator has infinite extinction ratio.

variation of N_{max}, calculated numerically as a function of $G_0 P_{laser}/P_{out,max}$ and P_{RF} with $\alpha = 0.973$, along with the upper bound given by (3.34). Not surprisingly, the bias optimization is most effective for low RF powers and when the EDFA is strongly saturated at quadrature. Note that the $\alpha = 1$ approximation may cause some over-estimation of N_{max}. The maximum number of signals that can be amplified with the same EDFA is also affected by the modulator extinction ratio, which actually limits the minimum mean power at the modulator output.

The dependence of N_{max} on the modulator extinction ratio is shown in Fig. 3.16. Note that, for $P_{RF} = 0\,\text{dBm}$ and considering an extinction ratio between 40 dB and 45 dB, the value of N_{max} is 5 instead of 8, as calculated with infinite extinction ratio in figures 3.14 and 3.15 (bold dot).

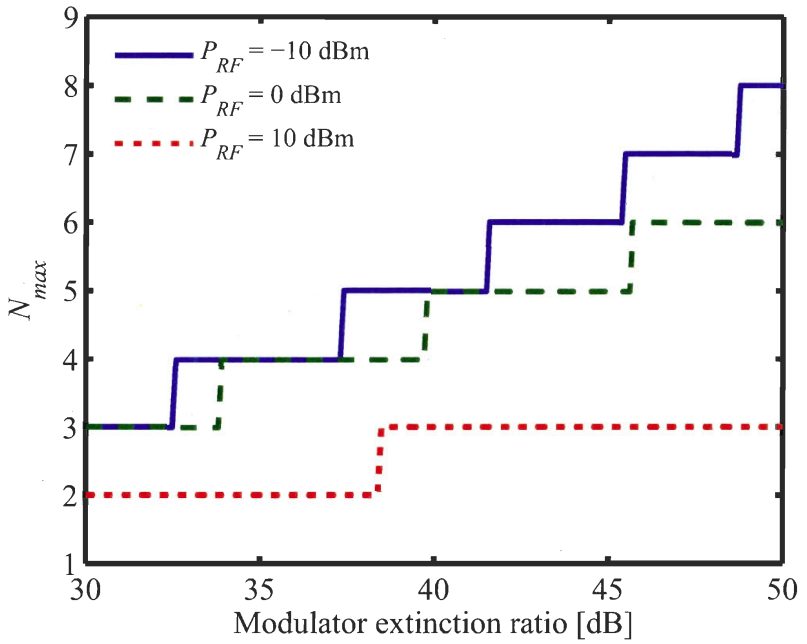

Figure 3.16: Number of signal that one EDFA can amplify without decreasing the RF gain, as a function of the modulator extinction ratio. As in Fig. 3.15, each signal RF gain at $V_{bias,Gmax}$ is equal to the RF gain experienced by only one signal at EDFA input, with bias at quadrature. This simulation takes into account the effect of finite extinction ratio. $\alpha = 0.973$.

3.3 Estimation of the Mach-Zehnder parameters

It is well known that Lithium Niobate ($LiNbO_3$) MZ modulators are affected by drift of the bias point over time scales ranging from tens of seconds to thousands of hours [100, 101, 102, 103, 104]. This drift is caused by different mechanisms: temperature can affect the bias point and the modulator V_π through the pyroelectric effect and trough a change in the $LiNbO_3$ temperature-dependent electrical conductivity [105, 103]. Also, the modulator bias setting changes the amount of input optical power that is dissipated inside the modulator, changing its temperature. Yamada [104] reports two kinds of DC bias drift: one is a short time DC drift with several seconds relaxation time and the other is a long drift, whose relaxation time is several hours. Yamada showed that the former originates from current leakages from the bias pads. For the latter, he proposes that the main origin is a photorefractive effect. Beaumont [106] found that the environment humidity can strongly affect the bias stability. Our modulator was hermetically sealed in its package, so humidity was not a concern.

For the measurements like those presented in figures 3.7 and 3.13, it was important to be able to precisely measure $\frac{V_{bias}}{V_\pi}$, $\frac{V_{RF}}{V_\pi}$ and the V_π itself. A very good way to measure the values of V_π and $\frac{V_{bias}}{V_\pi}$ is based on the dependence of the second order harmonic distortion (HD2) with bias:

$$\mathrm{HD2} = \frac{\cos\left(\pi\frac{V_{bias}}{V_\pi}\right) J_2\left(\pi\frac{V_{RF}}{V_\pi}\right)}{\sin\left(\pi\frac{V_{bias}}{V_\pi}\right) J_1\left(\pi\frac{V_{RF}}{V_\pi}\right)}. \tag{3.36}$$

Hence, the HD2 nulls are in $\frac{V_{bias}}{V_\pi} = \pm 0.5$ and HD2 maximum is in $\frac{V_{bias}}{V_\pi} = 0$. V_π is immediately defined by the voltage difference between the two HD2 nulls. This definition has the advantage that the HD2 extrema are easy to measure with high accuracy. A good way to measure the $\frac{V_{RF}}{V_\pi}$ is based on the third order harmonic distortion (HD3), because it is not bias dependent:

$$\mathrm{HD3} = \frac{J_3\left(\pi\frac{V_{RF}}{V_\pi}\right)}{J_1\left(\pi\frac{V_{RF}}{V_\pi}\right)}. \tag{3.37}$$

Another possible way is based on the measurement of the minimum mean optical power at the modulator output. From equation (3.18) at $V_{bias} = 0$:

$$\langle P_{out,MZ}\rangle = \frac{P_{laser}}{2}\left[1 - J_0\left(\frac{\pi V_{RF}}{V_\pi}\right)\right]. \tag{3.38}$$

This method is not preferred whenever a good HD3 signal is measurable, because its accuracy depend on the accuracy of P_{laser}, which depends also on the polarization matching between the laser source and the MZ. However, it allows the measurement of $\frac{V_{RF}}{V_\pi}$ if the HD3 reading is affected by the detector bandwidth, other link nonlinearities, or is below detection noise. Equations (3.36)-(3.38) are demonstrated in appendix B.

We first characterized V_π. We noted that, when measuring the HD2 as a function of bias, the bias point drift after each bias change was affecting our characterizations of the modulator V_π. The measurements were taken at regular intervals using a computer-controlled setup, so that the net effect of the bias drifting was a stretching of the measured curves on the bias axis. This affects the measurements where V_{bias} is scanned from negative to positive values by making the collected data not symmetrical with respect to the minimum transmission point ($V_{bias} = 0$), unless the measurement is completed in less than a couple of minutes. In order to avoid temperature related component of the drift, we mounted the MZ modulator onto a Peltier cell and fixed the temperature to 16°C. This increased the modulator V_π from about 2.7 V (at uncontrolled room temperature) to about (3.35 ± 0.07) V, and stabilized its value. The increase of V_π at lower temperature agrees with the measurements shown in [103]. In Fig. 3.17 we show the measured second order harmonic distortion (HD2) before and after the installation of the temperature control setup. Note that the measured HD2 with controlled temperature is much more symmetrical with respect to $V_{bias} = 0$. We characterized

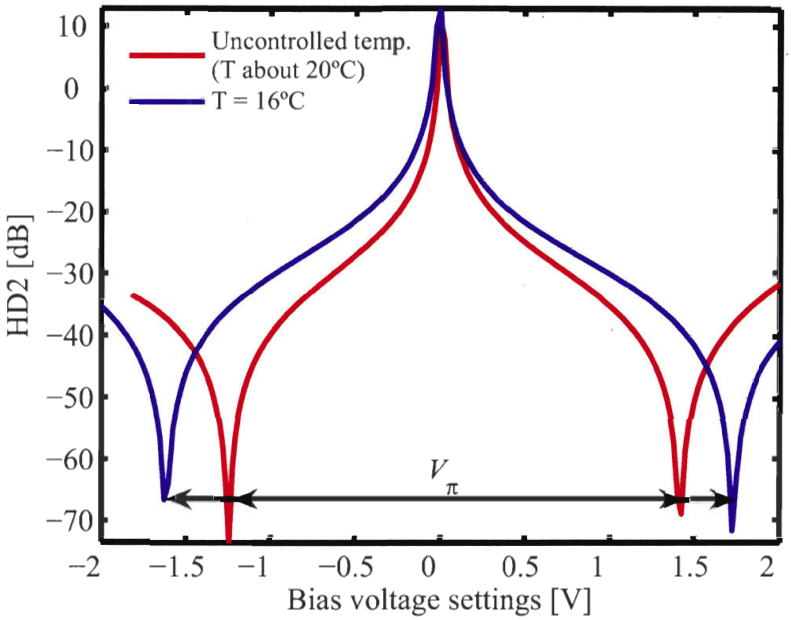

Figure 3.17: Measured HD2 as a function of bias for temperature controlled and uncontrolled MZ.

the modulator V_π twice during our research, using the same controlled experimental conditions (laser input power, polarization control, modulator temperature). We found that the value of V_π drifted slightly with modulator aging, but the drift was within the measurement error: the first characterization gave $V_\pi = (3.35 \pm 0.07)$ V. About one year later we found $V_\pi = (3.37 \pm 0.07)$ V. Data from this second measurement is shown in Fig. 3.18. The measurements (about 300 samples) have been taken over three days, using a a computer controlled voltage source and by measuring the voltage values that null the HD2. Even with temperature control, some residual drift was present and contribute to the spreading of the data points.

In measurements like those shown in figures 3.7 and 3.13, the $\frac{V_{bias}}{V_\pi}$ values on the abscissa axis had to be properly calibrated to minimize the effects of the bias drift. For this reason, for each single measurement function of V_{bias} presented in this thesis, we collected data on the harmonic distortion or the optical power at the modulator output. Hence, after thermal stabilization, any residual (first order) bias drift have been corrected by using the HD2 minima and maxima to identify the quadrature and minimum bias settings. When HD2 is not available, the power at modulator output can be used to identify the minimum and maximum transmission points. If the measurement is fast (less than a couple of minutes), the bias drift along the measurement is negligible and the identification of the minimum transmission point using the link transmitted power is sufficient to properly plot the collected data. Higher order bias drifts have not been corrected, but this does not appear to affect much the fitting between theory and measurement in figures 3.7 and 3.13, and others.

The packaging of the modulator used in our experiments has some filtering effect.

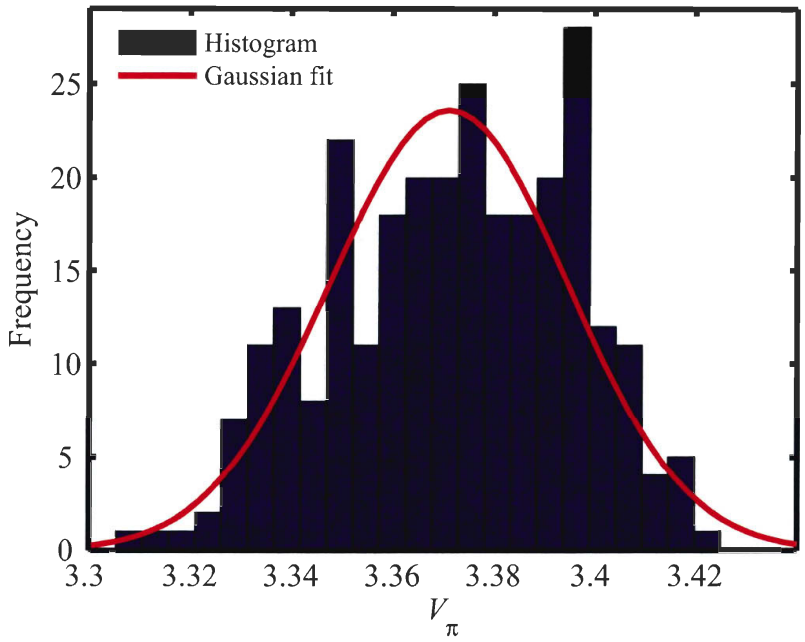

Figure 3.18: Histogram of measured values of V_π. Measurement over 3 days, based on distance between HD2 nulls (about 300 samples). MZ temperature: $T = 16$°C; $P_{RF} = 0$ dBm $f_{RF} = 5$ GHz.

The modulator itself is characterized by a frequency dependent efficiency factor (i.e., the transducer gain G_{TM}), and its internal impedance matching is not perfect at all frequencies. Hence, the RF power fed to the modulator is not all available as effective modulation voltage at the MZ arms, and we have defined:

$$P_{RF,effective} = G_{TM}(f) \cdot P_{RF}, \tag{3.39}$$

where $P_{RF,effective} = \frac{V_{RF}^2}{2 \cdot R}$, $R = 50\,\Omega$, and P_{RF} is the RF power read on the screen of the signal generator that feeds the MZ. Calibration of the efficiency factor, i.e., calibration of effective $\frac{V_{RF}}{V_\pi}$, has been done using both the distortion and mean optical power methods, at 1 GHz, 2.5 GHz and 5 GHz.

We found $G_{TM} = -8$ dB at 1 GHz, $G_{TM} = -7.25$ dB at 2.5 GHz, and $G_{TM} = -8$ dB at 5 GHz with MZ at room temperature, using a `HP 83731B` signal generator (see Fig. 3.19). Later, we found $G_{TM} = -5.4$ dB at 5 GHz and $G_{TM} = -5.2$ dB at 1 GHz at 16°C using an `Agilent E4438C` VSG. The variations of G_{TM} are not completely explained, but indeed the different temperatures of the modulator may explain them partially. The calibration of G_{TM} has been performed every time we started a new series of measurements, in order to have well calibrated data. This procedure appears to have given good results, always well fitting with simulations based on the numerical values of V_π and G_{TM} given here.

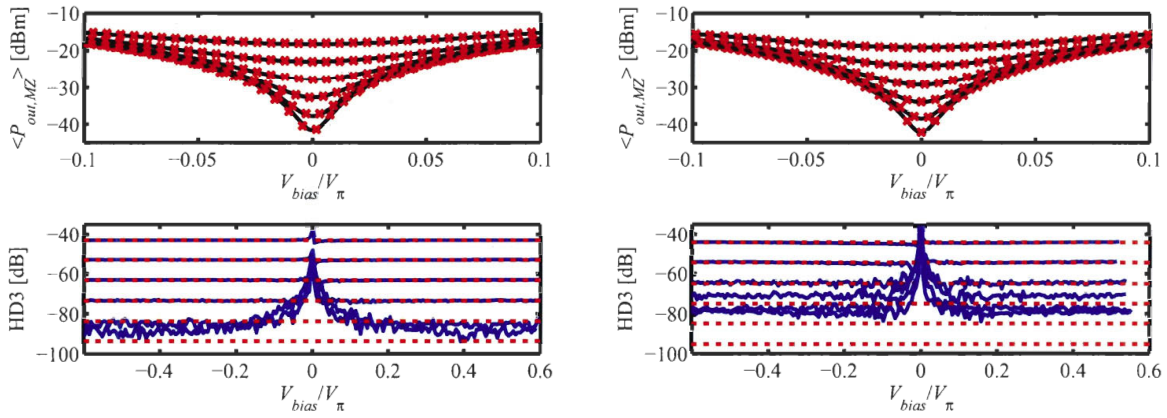

Figure 3.19: Calibration of $\frac{V_{RF}}{V_\pi}$. (a) 2.5 GHz. Signal source: `HP 83731B`, detector: `Agilent 11982A`. (b) 5 GHz. Same signal source and detector as in (a). The detector frequency response at 15 GHz has been taken into account by a correction factor measured using a HP optical component analyzer (model `HP 8703A`).

3.4 Impact of impedance matching on link gain

In the literature, some papers present the RF gain of an optical link considering perfect impedance matching at the modulator and the receiver (see for example [107] and [56]). In this section we discuss a more general approach to take into account imperfect matching at the modulator and the detector. The concepts discussed are well known to microwave engineers and have already been applied to optical link gain and noise figure calculations by, among others, Cox and Daryoush [108, 85]. We report here the calculations of link gain to justify our formulation, which is somewhat simpler than Daryoush's work. This analysis will also help us to explain why perfect match of the modulator and detector is impossible in real systems. In practice this is not a problem for the modulator, but it is a significant source of loss at the detector. However, imperfect matching at the detector is useful to assure that the link gain is almost flat over the bandwidth of the OFDM signal.

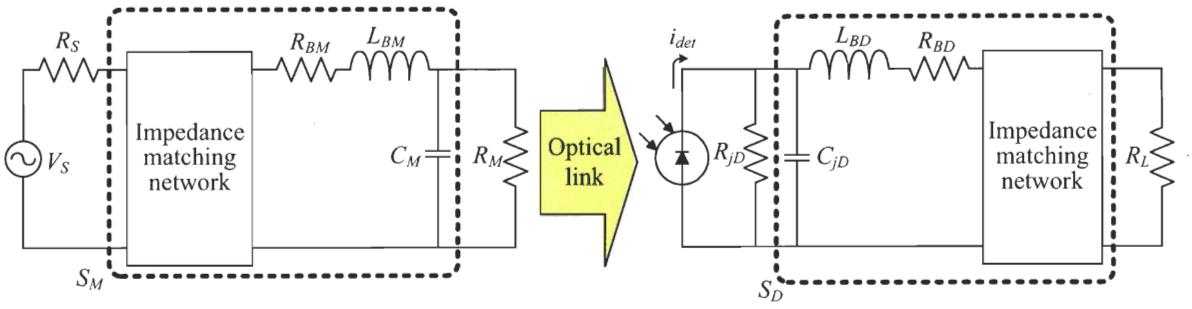

Figure 3.20: Circuit model for a MZ modulator and a detector

For reference, we repeat here Fig. 3.2. We will also refer to Fig. 3.21, which shows the general model for a two-port network inserted between a generator (Norton

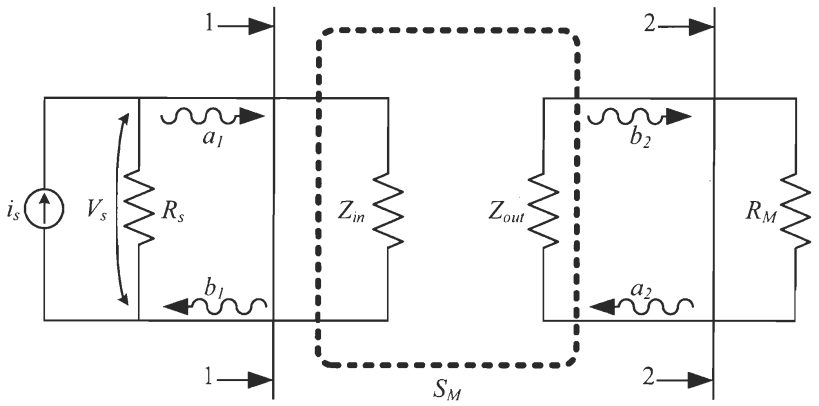

Figure 3.21: power flux model for a two-port network.

equivalent) and a real load.

In the case of the modulator without impedance matching, the power transferred to R_M is given by the transducer gain G_{TM} [109, 110]:

$$G_{TM} = \frac{P_M}{P_{av,Vs}} = \frac{\left(1 - |\Gamma_S|^2\right)|S_{21}|^2\left(1 - |\Gamma_M|^2\right)}{\left|\left(1 - S_{11}\Gamma_S\right)\left(1 - S_{22}\Gamma_M\right) - S_{12}S_{21}\Gamma_S\Gamma_M\right|^2}, \tag{3.40}$$

where Γ_S and Γ_M are the generator and load reflection coefficients with respect to the reference impedance Z_0:

$$\Gamma_S = \frac{R_S - Z_0}{R_S + Z_0} \tag{3.41}$$

$$\Gamma_M = \frac{R_M - Z_0}{R_M + Z_0}, \tag{3.42}$$

and the scattering matrix S_M is written as:

$$S_M = \begin{pmatrix} S_{11} & S_{12} \\ S_{21} & S_{22} \end{pmatrix}. \tag{3.43}$$

Maximum power transfer to the two-port network is obtained if the generator impedance and the input impedance Z_{in} of the network are conjugate matched. Assuming a transmission line with impedance Z_0, length l and propagation phase factor $e^{-i\beta l}$ between the generator and the network, the conjugate matching condition becomes:

$$\begin{aligned} \Gamma_{in,S_M} &= \Gamma_S^{\star} e^{i\,2\beta l} \\ \Gamma_{in,S_M} &= \frac{Z_{in,S_M} - Z_0}{Z_{in,S_M} - Z_0} \end{aligned} \tag{3.44}$$

where Γ_{in,S_M} is the reflection coefficient at the input of S_M. Typically, the generator is impedance matched to the transmission line, with $Z_0 = 50\,\Omega$. Then, $\Gamma_S = 0$. Hence, the maximum power transfer condition imposes $\Gamma_{in,S_M} = 0$, or $Z_{in,S_M} = Z_0$. A matching

network is included in the modulator two port network to match Z_{in,S_M} to Z_0. If $\Gamma_S = 0$, the transducer gain reduces to:

$$G_{TM} = \frac{|S_{21}|^2 \left(1 - |\Gamma_M|^2\right)}{|(1 - S_{22}\Gamma_M)|^2} \tag{3.45}$$

that is only dependent on the impedance matching at the load.

In the case of the modulator, in order to calculate the optical modulation amplitude for a given input RF power, we need the voltage levels on the arm of the modulator. In the modulator microwave model these are given by the amplitude of the voltage on R_M, which can be written as [109, page 414]:

$$|V_{R_M}| \triangleq V_{RF} = \sqrt{Z_0 \, |a_2 + b_2|^2}, \tag{3.46}$$

where a_2 and b_2 are the incident and reflected normalized waves on R_M. Equation (3.45) allows us to calculate the total power dissipated on R_M [109, page 417]:

$$P_M = \frac{1}{2}\left(|b_2|^2 - |a_2|^2\right) = \tag{3.47}$$

$$= P_{av,Vs} \cdot \frac{|S_{21}|^2 \left(1 - |\Gamma_M|^2\right)}{|(1 - S_{22}\Gamma_M)|^2}. \tag{3.48}$$

By recalling that, by definition, $a_2 = \Gamma_M b_2$ [109, page 419], from (3.47) we obtain:

$$|b_2|^2 = \frac{2P_M}{1 - |\Gamma_M|^2} \tag{3.49}$$

$$|a_2 + b_2|^2 = |b_2|^2 \, |1 + \Gamma_M|^2 . \tag{3.50}$$

and so:

$$V_{RF} = \sqrt{2Z_0 P_{av,Vs} \frac{|S_{21}|^2 \, |1 + \Gamma_M|^2}{|1 - S_{22}\Gamma_M|^2}}. \tag{3.51}$$

This is the expression given by Daryoush in [85, eq. 41]. However, recalling that R_M is real, from the definition of Γ_M we can easily show that Γ_M is real and:

$$Z_0 \left(1 + \Gamma_M\right) = R_M \left(1 - \Gamma_M\right) \tag{3.52}$$

$$Z_0 \, |1 + \Gamma_M|^2 = R_M \left(1 - |\Gamma_M|^2\right). \tag{3.53}$$

Hence, equation (3.51) can also be simplified:

$$V_{RF} = \sqrt{2R_M P_{av,Vs} \frac{|S_{21}|^2 \left(1 - |\Gamma_M|^2\right)}{|1 - S_{22}\Gamma_M|^2}}, \tag{3.54}$$

that is:

$$V_{RF} = \sqrt{2R_M P_{av,Vs} G_{TM}}. \tag{3.55}$$

We retain this last expression because of its simplicity and its validity for any condition of matching, as long as R_M is real. This formulation is simpler in form than Daryoush's, from which it differs for two reasons:

- If the general expression for G_{TM} is used, it does not imply that the generator is perfectly matched to the modulator, as it is in (3.51).
- We state the hypothesis that the load (R_M) is purely resistive, which is well the case if we include all reactive elements of the modulator model in S_M.

Daryoush uses a somewhat different electrical model for the modulator, without R_M, so that the load to S_M is C_M. This is the case in some modulators where R_M is very high. However, in most commercial models, as well as in those we worked with, $R_M = 50\,\Omega$ to match the MZ input as much as possible to $50\,\Omega$ over the modulator bandwidth.

Note that if S_M is lossless, the conservation of energy imposes that perfect impedance matching of Z_{in,S_M} to Z_0 implies also perfect conjugate matching of the load. In fact, all power entering S_M must be eventually transferred to the load and nothing is reflected back to the source. The load being a real valued resistance, conjugate matching means $\Gamma_M = 0$. Also, the S_M assumes a very simple form with $S_{11} = S_{22} = 0$ and $G_{TM} = |S_{21}|^2 = 1$. However, the modulator and the detector are not lossless, and (3.45) must be used to calculate the power dissipated into the load.

In the presence of loss, $|S_{21}|^2 < 1$ and it is impossible to perfectly match both sides of the scattering matrix S_M to both the source and the load using only one matching network on the signal source side[3]. This statement, demonstrated in appendix C, justifies the form we chose for the G_{TM} in equation (3.45), with perfect impedance matching only at the source.

Note that any imperfection in impedance matching and any internal loss in the modulator will affect the link gain by decreasing the effective V_{R_M} on the modulator arms. However, a real link is also impaired by nonlinear distortion from the modulator, which also imposes a limit on V_{R_M}. We assume that the maximum V_{R_M} fixed by the modulator distortion can always be met by the signal source, even taking into account the losses and impedance mismatch. In fact, the modulator is at the central station, where high power modulator drivers can be used.

3.4.1 Impedance matching at the detector

The detector can be described using the model shown in Fig. 3.22: the photocurrent amplitude i_D is generated by a current source with output impedance R_{jD}, which represents the junction resistance. C_{jD} is the junction capacitance. R_{BD} and L_{BD} represent series resistance and inductance parasitics, including the effect of packaging. This kind of model is adopted by various authors in the literature [85, 90, 111]. In

[3]We have physical access only to the source side of S_M, because R_M is embedded in the modulator as part of its electrical model.

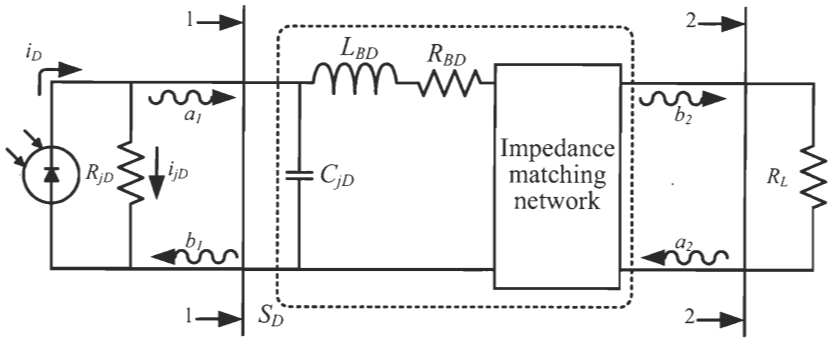

Figure 3.22: Circuit model of p-i-n photodetector.

the case of the detector, we can not assume that any impedance mismatch or internal losses are compensated by an external amplifier because we want to avoid using RF amplification stages after the detector. Hence, we have to ensure the maximum power transfer from the generator (the active region of the diode) to the load R_L, which models the antenna. In this case, following a reasoning similar to the one developed in the previous section for the modulator, the power P_L delivered to R_L can be written as:

$$P_L = R_{jD}\frac{i_{jD}^2}{2}G_{TD}, \tag{3.56}$$

where G_{TD} is the diode transducer gain. Note that R_{jD} is typically on the order of 1 MΩ or more [85]: this makes it very important to achieve good impedance matching with R_L, which is typically 50 Ω, or link losses may increase dramatically. For example, if no impedance matching is used at all, then $G_{TD} = 1 - \left|\frac{R_{jD}-R_L}{R_{jD}+R_L}\right|^2 \simeq -37\,\text{dB}$ in the region of frequencies where the reactive part of S_D can be neglected.

Most detectors, optimized to be used in wideband links, employ wideband lossy impedance matching: the matching circuit is a resistor network that ensures matching on a 50 Ω load over the bandwidth of the detector, where the reactive elements of the diode circuit model in Fig. 3.22 can typically be neglected. As shown in appendix C, the resistive matching network can be a significant source of link losses. This is a well known fact that reactive matching using stubs (see Fig. 3.23) or matching transmission lines provide much lower RF losses than wideband resistive matching. The problem is that there exists a general limit on the bandwidth over which an arbitrarily good impedance reactive match can be obtained: this is the so called Bode-Fano limit [112]. Also, the larger the match bandwidth, the more complex the matching circuit has to be. For a simple circuit, a perfect reactive match is valid only at one frequency. Theoretically, this is the situation encountered in the laboratory, where the easiest way to reactively match a photodiode to its load is to use matching stubs. However, we tested and verified experimentally that the bandwidth of the stub-matched detector available in our laboratory is much larger than 20 MHz: the bandwidth of an OFDM signal. In Fig. 3.24 we show a typical example of loss spectrum for an experimental link employing a reactively matched photodetector. This is explained by the presence of losses in within the diode circuit model, which are modeled by the R_{BD} is Fig. 3.22,

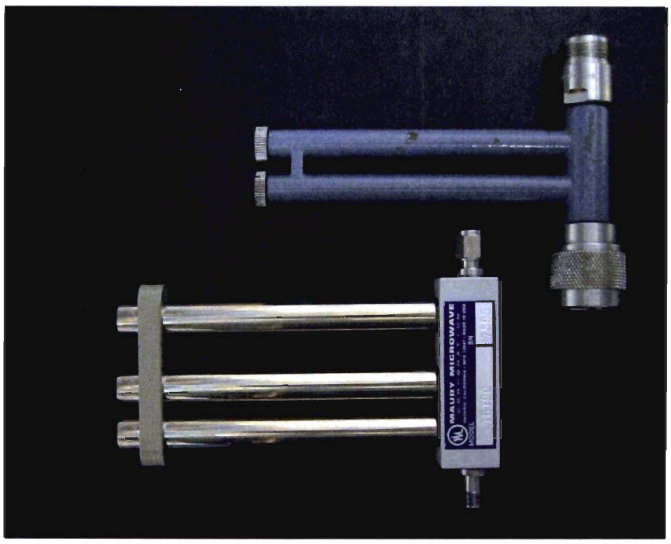

Figure 3.23: Matching triple and double stubs: devices rarely seen in a photonic laboratory. Theory of operation of these devices is well explained in [109].

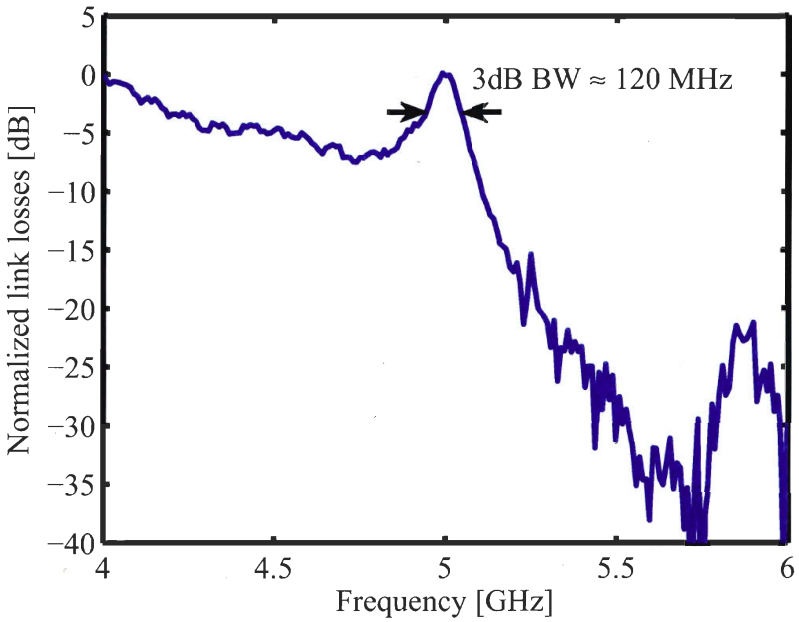

Figure 3.24: Typical loss spectrum of a link using a `Discovery Semiconductors DSC-50` photodetector and reactive matching at 5 GHz.

and in the stubs. We simulated the optical link losses and bandwidth for different values of R_{BD}, taking into account the detector circuit model and matching. We did not measure the circuit model elements of the detectors in our laboratory: instead, we used the values $R_{jD} = 1\,\mathrm{M\Omega}$, $C_{jD} = 0.19\,\mathrm{pF}$ and $L_{BD} = 0.29\,\mathrm{nH}$ given in [85] for a high speed InGaAs p-i-n photodiode. The simulated link losses and link bandwidth as a function of R_{BD} are shown in figures 3.25 and 3.26.

In Fig. 3.25, we simulated both resistive and reactive impedance matching to com-

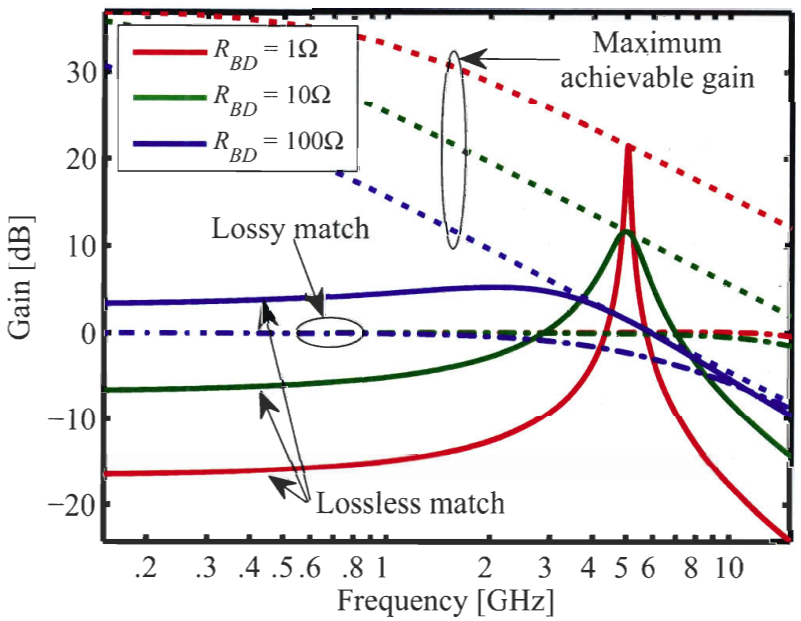

Figure 3.25: Link losses with resistive and reactive match as a function of frequency and for different values of R_{BD}. Dash-dot lines are link losses with wideband resistive matching. The solid lines are reactive matching revealing the narrowband nature of this matching technique. Dotted lines represent maximum achievable link gain with lossless match.

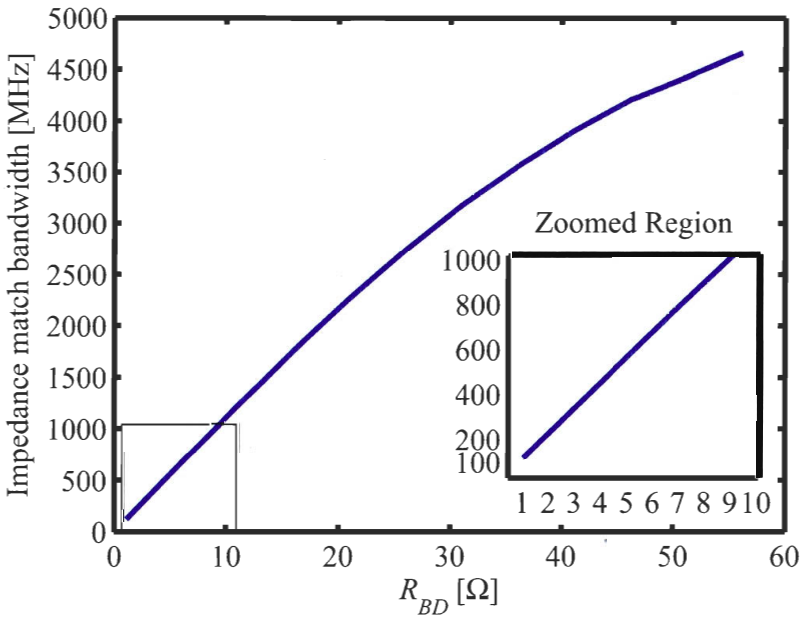

Figure 3.26: Bandwidth of lossless matched link as a function of R_{BD}.

pare the loss performance: with a low diode internal loss $R_{BD} = 1\,\Omega$, reactive matching can provide more than 20 dB link gain improvement over resistive matching. However, the improvement decreases quickly with higher diode resistive parasitics. Typical values of R_{BD} encountered in the literature are around $10\,\Omega$. Note that the R_{BD} also decreases

the maximum achievable gain for each frequency, which is calculated by finding the peak values of lossless matched gain for each frequency. This can be explained by the considerations discussed in appendix C. In Fig. 3.26 we show that even with R_{BD} as low as $1\,\Omega$, the link bandwidth is larger than 100 MHz (precisely: 115 MHz). In this case, on a 20 MHz bandwidth around the carrier, the variations of link gain due to matching is lower than 0.15 dB. Hence, the losses in the photodetector ensures that the reactively matched link bandwidth is wide enough to accommodate for the OFDM signal.

3.5 Signal fading due to dispersion

The chromatic dispersion arising from propagation over standard fibre or through chirped fibre Bragg grating (FBG) is a well known source of RF signal fading in ROF links. A general analytic treatment of the dispersive propagation over ROF links is given in [113] and in [114]. For small OMD, the detected RF power P_{RF} after dispersive propagation is proportional to:

$$P_{RF} \propto \left[\cos\left(\frac{\pi L D \lambda_{laser}^2 f_{RF}^2}{c}\right)\right]^2, \tag{3.57}$$

where D is the dispersion coefficient, L is the fibre length, λ_{laser} is the optical carrier frequency, f_{RF} is the RF modulation frequency, and c is the speed of light. A similar equation can be written for dispersion from chirped FBGs replacing the LD term by the total grating dispersion at λ_{laser}. In low OMD links, (3.57) can be easily proved by writing the baseband equivalent of the electric field E as the sum of three components:

$$E(t) = Ce^{j\varphi_C} + S_L e^{j(-\omega_{RF}t+\varphi_{SL})} + S_U e^{j(\omega_{RF}t+\varphi_{SU})}, \tag{3.58}$$

where C and φ_C are the amplitude and the phase of the carrier, S_L, S_U, φ_{LU}, φ_{SU} are the amplitudes and the phases of the modulation sidebands. At the input of the dispersive element, in the absence of sideband filtering, we can assume: $S_L = S_U$ and $\varphi_{LU} = \varphi_{SU} = \varphi_C$. If the dispersive element is a fibre, after propagation the three components accumulate different phase retardations:

$$\varphi_C = \beta(0)\, L \tag{3.59a}$$

$$\varphi_{SL} = \beta(-\omega_{RF})\, L \tag{3.59b}$$

$$\varphi_{SU} = \beta(\omega_{RF})\, L, \tag{3.59c}$$

where $\beta(\omega)$ is the fibre mode propagation constant, which is expanded in a Maclaurin series as:

$$\beta(\omega) = \beta_0 + \beta_1\omega + \frac{1}{2}\beta_2\omega^2 + \ldots \tag{3.60}$$

After detection at the fibre end, the detected photocurrent $i_{det}(t)$ is proportional to $|E(t)|^2$. The, photocurrent detected at f_{RF} is proportional to:

$$i_{det,f_{RF}}(t) \propto \cos\left(\varphi_C - \frac{\varphi_{SL}+\varphi_{SU}}{2}\right)\cos\left(\omega_{RF}t - \frac{\varphi_{SL}-\varphi_{SU}}{2}\right). \tag{3.61}$$

Inserting (3.59) gives:

$$i_{det,f_{RF}}(t) \propto k_D \cos\left[\omega_{RF}\left(t + L\beta_1\right)\right] \tag{3.62}$$

$$k_D = \cos\left(\frac{L\omega_{RF}^2\beta_2}{2}\right), \tag{3.63}$$

where we recognize a propagation delay term and a fading term k_D, which can also be written as:

$$k_D = \cos\left(\frac{\pi D L f_{RF}^2 \lambda_{laser}^2}{c}\right). \tag{3.64}$$

From the equations above, the action of dispersion can be interpreted as follows: it causes the upper and lower electric field modulation sidebands to accumulate a phase difference. At the fibre input the optical carrier is amplitude modulated, so that the modulation sidebands are perfectly in phase. Along the fibre, the modulation sideband phase variations caused by the dispersion gradually transforms the amplitude modulation into a phase modulation, which is characterized by a phase difference of π between the sidebands [71, page 236]. Hence, the detected photocurrent fades out. Note that, for a fixed dispersion, the fading is periodic with fibre length and f_{RF}^2. Assuming $D = 17\,\text{ps/nm/km}$, the value of k_D varies for different fibre length and f_{RF} as shown in Fig. 3.27: the periodic behavior of k_D is clearly revealed and we note that the nulls repeat more often for long fibre lengths and high frequency.

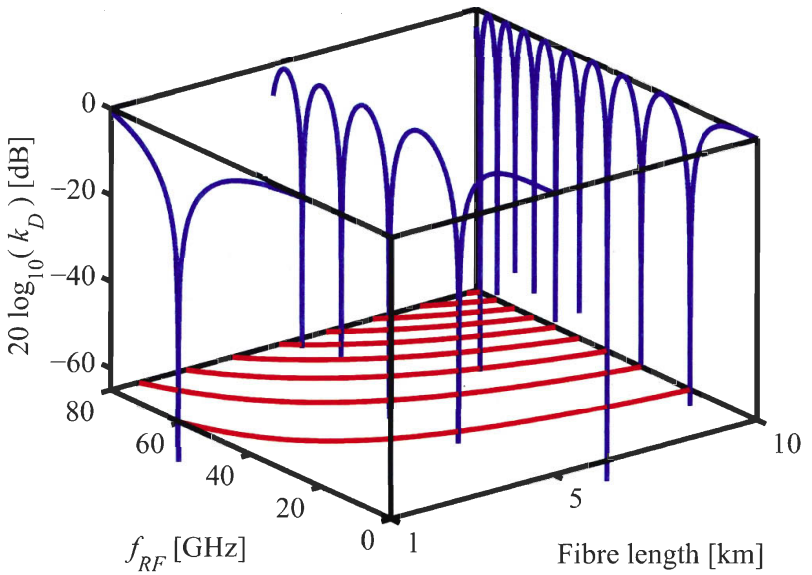

Figure 3.27: Signal power fading due to dispersion as a function of signal frequency and fibre length. Assumptions: $D = 17\,\text{ps/nm/km}$. Red lines are the loci of k_D nulls.

We also present in Fig. 3.28 the interesting case of the propagation of a 5 GHz signal on a fibre with length up to 100 km: this is a relatively low frequency and no nulls in k_D are present in this fibre length range. Also, for fibre length lower of 10 km, the fading due to dispersion is lower than 0.05 dB: negligible in most situations.

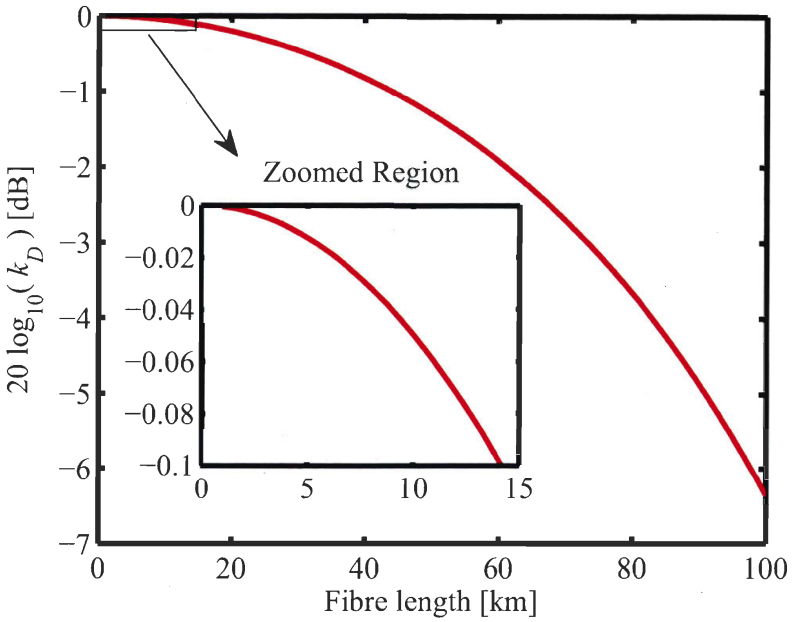

Figure 3.28: Power fading of a 5 GHz signal. Assumptions: $D = 17$ ps/nm/km.

In links where the dispersion induced losses are larger, typical countermeasures include:

- Dispersion compensation by using FBGs and/or dispersion compensating fibre modules.
- Optical phase conjugation [115].
- Generation of SSB modulation format instead of DSB.

The latter method is probably the most widely used when dispersion in a ROF link is an issue. SSB format can be generated by filtering a sideband with a narrowband FBG [116], or by properly biasing a dual-electrode MZ [117]. However, compared to the DSB modulation format adopted in this work, it requires a relatively complex and expensive modulation stage. Also, DSB modulation has a 3 dB advantage in both gain and NF over SSB modulation [60].

3.6 Conclusions

In this chapter we discussed the gain of ROF links with external modulation, with and without a saturable optical amplifier. We found that the use of an amplifier can greatly enhance the link gain, especially if the modulator bias is optimized near the

minimum transmission point. The gain enhancement is a consequence of the fact that in saturated EDFAs, a lower input power reduces the saturation level and increases the available gain, up to a maximum that is the unsaturated or small signal gain. Moving the bias off quadrature towards the minimum transmission point reduces the average optical power at the EDFA input by suppressing the optical carrier and enhancing the signal OMD. However, moving the bias off quadrature also reduces the MZ modulation efficiency, decreasing the link gain. The two effects compete and there is an optimum bias values $V_{bias,Gmax}$ that provides maximum link RF gain. Decreasing the bias reduces the average optical power at the EDFA input quicker that the MZ modulation efficiency, so $V_{bias,Gmax}$ is always below the quadrature point.

$V_{bias,Gmax}$ depends on several parameters:

- the laser power: higher laser power and lower losses before the EDFA increase the maximum link gain and shift the $V_{bias,Gmax}$ towards the minimum transmission point. This is because the laser power increases the EDFA saturation level and the maximum amplifier gain is accessed only for an attenuation of the average power, which is reached for a smaller modulator bias.
- the modulation power: a higher modulation increases the average optical power for modulator bias values near to the minimum transmission point. Hence, a lower amplifier gain is typically accessible for high modulation power, and the $V_{bias,Gmax}$ moves towards the quadrature.
- the EDFA saturation level: if the amplifier is not saturated with the modulator at the quadrature point, this is the optimum bias. The higher the saturation level of the amplifier, the lower is $V_{bias,Gmax}$, down to a limit that is given by the modulation amplitude.

The bias optimization allows either to increase the link gain or to increase the number of signals amplified by the same EDFA, while keeping the same gain that would be observed at quadrature for one signal only. This opens the way to amplifier sharing in links supporting antenna arrays. We also noted that bias optimization can increase the link OMD, which is useful to reduce the optical power propagated over the link.

In the second part of the chapter, we examined briefly the impact of impedance matching onto the link gain, and we described the advantages of reactive match versus resistive match in narrowband link. We showed that proper narrowband impedance matching at the detector is mandatory to improve the link output power. Finally, we discuss the impact of fibre dispersion on link gain, finding that, for the RF frequency and fibre length considered in this work, the dispersion induced power fading is negligible.

The link gain is an important design challenge, and we will show in chapter 5 that the distortion from the modulator fixes a severe limit on the received OFDM signal quality.

Consequently, the modulation power cannot be increased indefinitely in the hope to improve the output signal power while maintaining a good signal quality. Maximizing the link gain allows to reduce the modulation power while maintaining the same link output RF power, so that the signal quality is improved. A significant limitation to the maximum link output RF power is the photodetector linearity. With the detectors available commercially, it was not possible to reach a RF output power higher than -3 dBm (without RF amplification) while maintaining a good OFDM signal quality. We reached as much as 9 dBm of output power from a JDS EPM 745 diode at 1.51 GHz, before (smelly) failure of the device, but the signal was heavily distorted by the detector. This is a significant limit for the realization of optically amplified links that do not use an electrical amplifier after the detector. In the introduction we discussed that the link should be able to provide about 7 dBm per antenna in an array with 7 antennas to fulfill the maximum power limits for the 802.11a protocol: such output power levels require specially designed high power RF detectors as the one proposed by Urick in [69].

In the next chapter we examine the noise performance of ROF links.

Chapter 4

Noise in ROF links

In this chapter, we discuss the impact of optical noise sources on the CNR and NF of a ROF link. We start with a description of the noise in unamplified and amplified links, and we discuss the impact of thermal noise, shot noise and ASE on NF and CNR. Then, we describe how these noise terms vary in links where the modulator bias is moved out of quadrature. We also detail the dependence of noise related to stimulated Brillouin scattering (SBS) on the modulator bias.

Later, we present a general noise model in optical modulated links, which leads to a rigorous expression of the detected noise variance in links with high optical modulation depth, and we apply this model to the description of noise due to ASE, shot noise, RIN and SBS-induced noise. We show that in links with high modulation depth the statistics of RIN noise and SBS-induced noise are not stationary, even if bandpass filtering follows the detector, and they depend on the modulation depth. This discussion leads to a novel description of the SBS-induced noise, which is supported by experimental work on SBS in links with optimized modulator bias. Finally, we present experimental results comparing the impact of RIN from a type of fibre laser and from distributed feedback semiconductor (DFB-SC) lasers on CNR and EVM of IEEE 802.11a signals.

As described in chapter 3, we are mostly interested in links with high gain and high RF output power. Hence, more often the signal quality is distortion limited than noise limited. However, this is not always the case: for example, noise sources other than distortion may dominate for very low values of bias or in the presence of strong stimulated Brillouin scattering (SBS).

4.1 Noise in amplified ROF links

Among others, Cox [56, 108, 84] and Ackerman [118] described the noise characteristics of externally amplified analog optical links. Ackerman [90], Betts [119], and Daryoush [85] showed that shifting the modulator bias towards the zero transmission point can reduce the link NF in unamplified links, because shot noise and RIN contributions are minimized. Recently, Ackerman [93] and Roussell [94] demonstrated noise figures lower than 7 dB (with a record of 3.4 dB) in low-biased links without optical amplification. In [83], Betts briefly describes the impact of optical amplifiers on the link NF. In general, in the assumption[1] that the amplifier does not add distortion to the RF signal, any improvement of the NF is reflected in an improvement of the link SFDR. In [82], Sabido explores the impact of EDFAs on SFDR as a function of the link losses.

For the sake of completeness, we study here the link NF and CNR, taking into account the effect of variations of the modulator bias on the link received mean optical power and ASE power. This is a immediate extension of some of the literature cited above. The NF can be written as:

$$\mathrm{NF} = 10 \cdot \log_{10}\left(1 + \frac{N_{link}}{N_{in} G_{RF}}\right), \tag{4.1}$$

where N_{link} is the excess link noise PSD dissipated onto the link load, $N_{in} = \mathfrak{k}T$ is the input available noise PSD, $\mathfrak{k}$ is Boltzmann's constant, T is the room temperature in kelvin, and G_{RF} is the available RF gain. The NF expressed in linear units is referred to as "noise factor". In the case of passive lossless reactive impedance matching at transmitter and receiver, Ackerman [118] gives N_{link} (on unitary bandwidth) as:

$$N_{link} = kT\left(1 + G_{RF}\right) + \underbrace{\left(\sigma^2_{i_{RIN}} + \sigma^2_{i_{shot}}\right)\frac{|Z_L|^2}{4R_L}}_{\circledast}. \tag{4.2}$$

The part marked $\circledast$ is the noise PSD contribution associated to RIN- and shot-noise-generated photocurrent, transferred to the load Z_L, with $R_L = \mathrm{Re}\{Z_L\}$. Note that we consider a unitary electrical bandwidth, and we assume all the noise sources are white.

We add to (4.2) the noise components introduced by the optical amplifier:

$$N_{link} = \mathfrak{k}T\left(1 + G_{RF}\right) + \left(\sigma^2_{i_{RIN}} + \sigma^2_{i_{shot}} + \sigma^2_{i_{sig\text{-}ASE}} + \sigma^2_{i_{shot,ASE}} + \sigma^2_{i_{ASE\text{-}ASE}}\right)\frac{|Z_L|^2}{4R_L}. \tag{4.3}$$

[1] This assumption is valid, as we will show in chapter 5.

The photocurrent noise variances or one-sided PSD terms on unitary bandwidth are:

$$\sigma^2_{i_{shot}} = 2e\mathcal{R}\langle P_{det,sig}\rangle \tag{4.4a}$$

$$\sigma^2_{i_{RIN}} = \left(\mathcal{R}\langle P_{det,sig}\rangle\right)^2 r \tag{4.4b}$$

$$\sigma^2_{i_{sig\text{-}ASE}} = 4\mathcal{R}^2\langle P_{det,sig}\rangle\, S_{det,ASE} \tag{4.4c}$$

$$\sigma^2_{i_{shot,ASE}} = 4e\mathcal{R}S_{det,ASE}B_o \tag{4.4d}$$

$$\sigma^2_{i_{ASE\text{-}ASE}} = 4\mathcal{R}^2 S^2_{det,ASE}B_o \tag{4.4e}$$

where e is the elementary charge, B_o is the ASE bandwidth, $\mathcal{R}$ is the detector responsivity, $\langle P_{det,sig}\rangle$ is the average signal optical power on the detector, $r = 10^{\frac{\text{RIN}}{10}}$ is the two-sided optical relative intensity noise, the RIN is expressed in decibels relative to 1/Hz (dB/Hz), and $S_{det,ASE}$ is the ASE PSD on the detector for one polarization. We neglect the dark current noise contribution at the detector. Equations (4.4) are demonstrated in section 4.2.

Recalling (3.18) and (3.17), the signal average optical power on the detector can be written as:

$$\langle P_{det,sig}\rangle = \frac{G_0 P_{laser}}{2L}\frac{\left[1 - J_0(\Lambda)\cos(\Gamma)\right]}{1+K} \tag{4.5}$$

$$K = \left(\frac{G_0 P_{laser}}{2P_{out,max}}\left[1 - J_0(\Lambda)\cos(\Gamma)\right]\right)^{\alpha}, \tag{4.6}$$

where L are the link propagation losses, $\Lambda = \frac{\pi V_{RF}}{V_\pi}$, $\Gamma = \frac{\pi V_{bias}}{V_\pi}$, and the other parameters are the same as defined in chapter 3. For all practical cases, moving the bias towards the minimum transmission point decreases the average signal power at the amplifier output. Hence, lowering the bias reduces the signal shot and RIN noise contributions to N_{link}. In the case of a saturated amplifier, the ASE power also varies with bias: ASE is high when the amplifier saturation level is low. Hence, ASE increases at low bias, and so does ASE-related detected noise. The ASE power of the EDFA used in chapter 3 and average amplified signal power as a function of bias are shown in Fig. 4.1.

In order to identify how the noise terms in (4.4) vary with the modulator bias setting, we measured N_{link} for the link presented in chapter 3, Fig. 3.4. Note that we set the total optical losses L to 20 dB, in order to avoid fibre nonlinearities, to ensure a linear response from the detector and to keep the received mean optical power and RF power identical to the measurements reported in chapter 3, Fig. 3.7. The N_{link}, shown in Fig. 4.2, is measured using an RF spectrum analyzer (model `HP 8565E`). The measurement is taken 1 MHz aside a 5 GHz RF carrier ($P_{RF} = 0$ dBm) to avoid the analyzer oscillator phase noise, which is dominant near the carrier. In this measurement, we used no optical filtering after the EDFA: the ASE spectrum was measured for each modulator bias setting. $S_{det,ASE}$ was calculated from the ASE noise level near the optical carrier, and B_o was calculated as the noise equivalent bandwidth of a rectangular spectrum with amplitude $S_{det,ASE}$ and the same total area as the measured ASE spectrum. As may be expected, near the minimum transmission point the ASE-induced noise levels

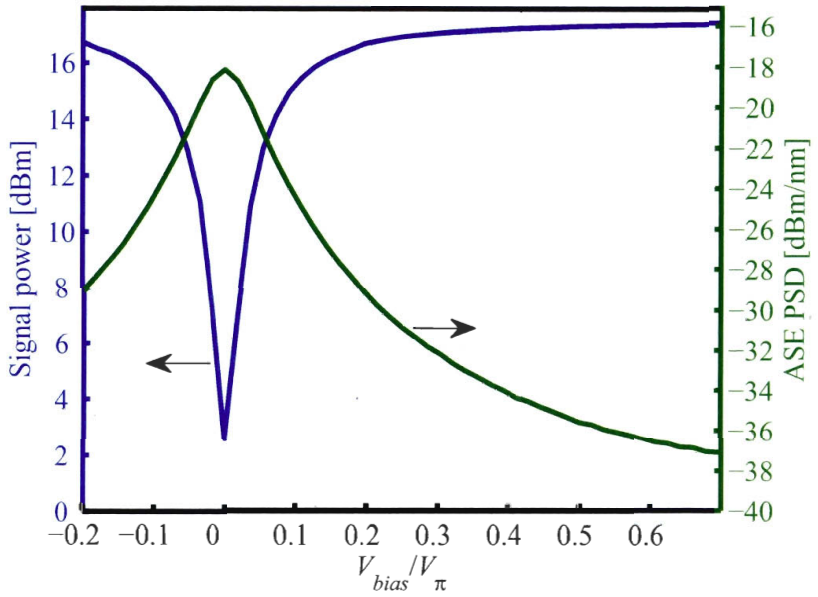

Figure 4.1: Measured signal power and ASE PSD at amplifier output. Measurement using an optical spectrum analyzer (OSA) `ANDO AQ6317B` with resolution bandwidth (RBW)= 0.2 nm.

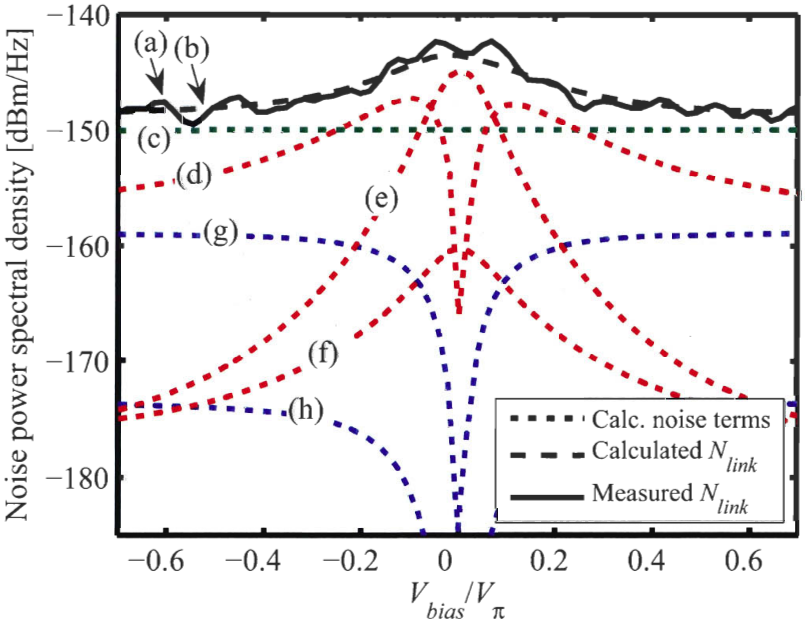

Figure 4.2: N_{link} as a function of the bias. (a) is the measured noise, (b) is the sum of all the calculated noise contributions, in red are all ASE-related noise contributions: (c) is displayed average noise level (DANL) of the spectrum analyzer (RBW = 10 Hz), (d) is ASE signal beat noise, (e) is ASE-ASE beat noise, (f) is ASE shot noise. In blue: (g) is signal shot noise, (h) is noise from laser RIN. The received mean optical power at quadrature is about 1 dBm. No optical filtering was used.

increase. The ASE-signal beat noise is a somewhat special case because, moving the bias from $\pi/2$ to 0, its PSD first increases with ASE to a maximum and then sharply decreases following the average signal power. Far from the minimum transmission point,

the thermal noise dominates in this link with high losses. Fig. 4.2 can be generalized to links with any loss L by recognizing in (4.4) that the ASE-ASE beat noise, ASE-signal beat noise and the RIN are proportional to L^2, while the signal and ASE shot noises are proportional to L. However, if the link losses were lower, ASE-ASE and ASE-signal beat noises would be higher than other noise contributions, because they both scale quadratically with $1/L$. In such conditions, ASE-signal beat noise would be dominant for a large range of bias values. Also, an optical filter with band B_o may be used to filter out some ASE power, thus decreasing the ASE-ASE beat noise but not the ASE-signal beat noise. Hence, ASE-signal beat noise can be made dominant for all practical values of bias. In the literature, ASE-signal beat noise is typically considered the dominant noise contribution of amplified ROF links (see, for example, [120, 121]), and bias optimized links are no exception.

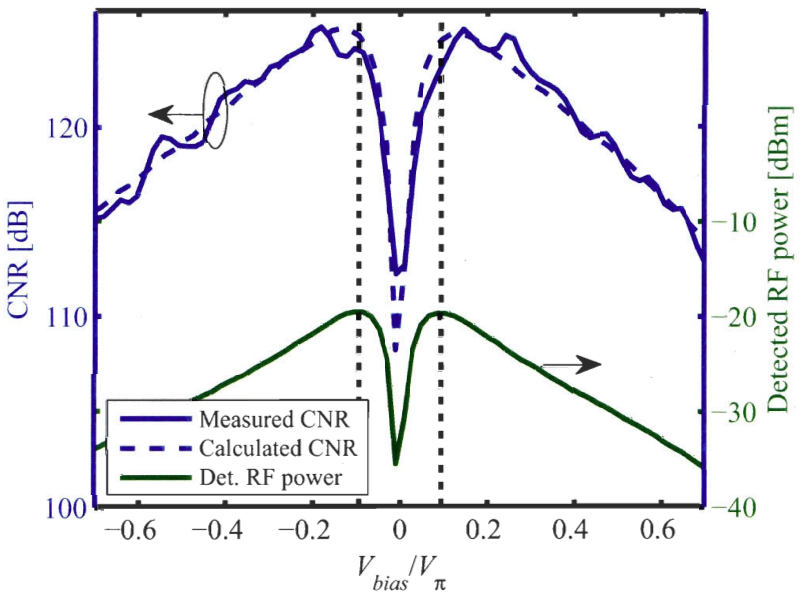

Figure 4.3: Link CNR and gain versus bias. The measured CNR is compared to CNR calculated from N_{link} and received signal power. The CNR is measured using a HP 8565E spectrum analyzer and reading the signal power and the noise power (in noise measurement mode) in 1 Hz bandwidth, 1 MHz aside the carrier to avoid the analyzer (and generator) phase noise.

In Fig. 4.3 we show the CNR and gain of the link under test, with input signal P_{RF}=0 dBm. The CNR is defined as the ratio between the power of the received RF signal and noise level over 1 Hz bandwidth. At the bias which gives maximum gain ($V_{bias,Gmax}$), the link CNR is about 125 dB/Hz with an improvement of about 7 dB with respect to the quadrature point, where CNR is about 118 dB/Hz. Hence, even if the noise level worsens near the minimum transmission point, the link CNR improves because of the better link gain.

The link NF has the same behavior: assuming a thermal noise limited input CNR of 150 dB/Hz, the link NF at $V_{bias,Gmax}$ can be evaluated at 26 dB, against 33 dB at quadrature. If the link loss is reduced and optical filtering is added to decrease the detected ASE power, the NF can be improved to a maximum value of about 24 dB,

limited by ASE-signal beat noise.

If we consider an ASE-signal beat noise or thermal noise limited link and a real Z_L, the noise factor $F = 10^{\frac{NF}{10}}$ can be written as:

$$F = 2 + \frac{1}{G_{RF}} \left(1 + \frac{\mathcal{R}^2}{kT} \langle P_{det,sig} \rangle S_{det,ASE} R_L \right). \tag{4.7}$$

The 2 factor represent the well known passive match F limit [108, 118]. This expression shows that the NF can be improved by the bias optimization technique we presented in chapter 3, because it allows to a simultaneous increase in the link gain and reduction in the $\langle P_{det,sig} \rangle$. Fig. 4.3 demonstrates that these two effects more than counterbalance the increase in ASE power (and EDFA noise figure) due to the EDFA reduced saturation level.

4.1.1 Comparing optically and electrically amplified links

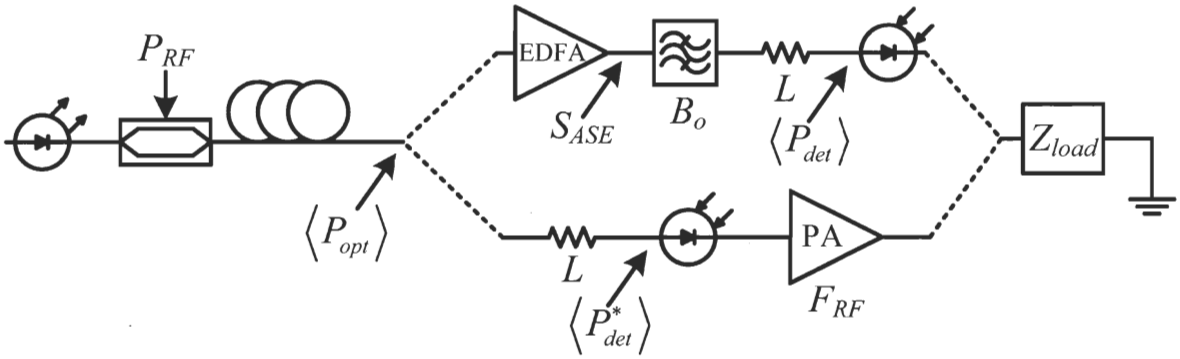

Figure 4.4: Link with optical or electrical amplification.

In the introduction to this thesis we suggested the possibility of using optical amplification instead of electrical amplification in ROF links, in order to simplify the electrical chain near the antenna at the link end. In chapter 3, we showed that the optical amplification can be very effective in increasing the link gain, and that in some situations one optical amplifier can be shared among several WDM links. Here, we want to compare the noise performance of an optically amplified link with that of a link with electrical post-amplification. The two links are shown in Fig. 4.4.

For the noise factor comparison, we assume that ASE-ASE beating noise and ASE shot noise are negligible because the optical bandwidth B_o of the bandpass filter after the EDFA is small. Also, we assume standard operating conditions for the EDFA: $G_{EDFA} \langle P_{opt} \rangle \gg S_{ASE} B_o$, and $G_{EDFA} \gg 1$, where G_{EDFA} is the amplifier optical gain. The noise factor of a link without optical or electrical amplification is given by:

$$F_{unamplified} = 2 + \frac{1}{G^*_{RF}} \left[1 + a \langle P^*_{det} \rangle + b \langle P^*_{det} \rangle^2 \right], \tag{4.8}$$

where P^*_{det} is the average detected optical power in the unamplified link, G^*_{RF} is the unamplified link RF gain and:

$$\begin{aligned} a &= \frac{e\mathcal{R}R_L}{2\mathbb{k}T}, \quad [W^{-1}] \\ b &= \frac{\mathcal{R}^2 R_L}{4\mathbb{k}T} r. \quad [W^{-2}] \end{aligned} \tag{4.9}$$

Note that the $\frac{1}{G^*_{RF}}$ term is related to the thermal noise contribution, $\frac{a\langle P^*_{det}\rangle}{G^*_{RF}}$ is the shot noise contribution, and $\frac{b\langle P^*_{det}\rangle^2}{G^*_{RF}}$ is the RIN contribution. If the unamplified link is followed by an RF amplifier of noise factor F_{RF}, we can calculate the total noise factor F^* by using the Friis' formula [71, page 612]:

$$F^* = F_{unamplified} + \frac{F_{RF} - 1}{G^*_{RF}}. \tag{4.10}$$

Hence,

$$F^* = 2 + \frac{1}{G^*_{RF}} \left[F_{RF} + a \langle P^*_{det} \rangle + b \langle P^*_{det} \rangle^2 \right]. \tag{4.11}$$

If the EDFA is used in the link instead of the RF amplifier, the resulting noise factor F is derived from (4.3) and (4.1), neglecting ASE-ASE beating noise and ASE shot noise:

$$F = 2 + \frac{1}{G_{RF}} \left[1 + a \langle P_{det} \rangle + b \langle P_{det} \rangle^2 + c \langle P_{det} \rangle \frac{S_{ASE}}{L} \right], \tag{4.12}$$

where S_{ASE} is the ASE PSD at the amplifier output for one polarization, L are the link optical losses after the amplifier and:

$$c = \frac{\mathcal{R}^2 R_L}{\mathbb{k}T}, \tag{4.13}$$

$$G_{RF} = G^*_{RF} G_{EDFA}, \tag{4.14}$$

$$\langle P_{det} \rangle = \langle P^*_{det} \rangle G_{EDFA}. \tag{4.15}$$

The most common definition of the EDFA noise factor is [122, page 222, equation 7.76]:

$$F_{EDFA} = \frac{1}{G_{EDFA}} \left(1 + \frac{2\mathcal{R} S_{ASE}}{\eta e} \right), \tag{4.16}$$

where η is the detector quantum efficiency and $\mathcal{R} = \eta \frac{e}{h\nu}$. For $G_{EDFA} \gg 1$, we can simplify (4.16) and express S_{ASE} in terms of F_{EDFA}. Then, (4.12) becomes:

$$F = 2 + \frac{1}{G_{RF}} \left[1 + a \langle P_{det} \rangle + b \langle P_{det} \rangle^2 + d \langle P_{det} \rangle \frac{G_{EDFA} F_{EDFA}}{L} \right], \tag{4.17}$$

where:

$$d = \frac{e\mathcal{R}R_L}{2\mathbb{k}T} \eta. \quad [W^{-1}] \tag{4.18}$$

Recalling (4.15) and (4.14), we can rewrite F as:

$$F = 2 + \frac{1}{G_{RF}^*}\left[\frac{1}{G_{EDFA}^2} + \frac{a\langle P_{det}^*\rangle}{G_{EDFA}} + b\langle P_{det}^*\rangle^2 + d\langle P_{det}^*\rangle\frac{F_{EDFA}}{L}\right]. \tag{4.19}$$

This is the noise factor of the optically amplified link. Note that the optical gain G_{EDFA} decreases the thermal, shot noise and ASE-signal beating noise contributions, and has no effect on the RIN. Equation (4.19) should be compared with the expression of F^*, which is the noise factor of the link with electrical post-amplifier, given by (4.11). The use of an optical amplifier is advantageous in terms of link noise factor if $F^* > F$, that is:

$$F_{RF} + \frac{a\langle P_{opt}\rangle}{L} > \frac{1}{G_{EDFA}^2} + \frac{a\langle P_{opt}\rangle}{LG_{EDFA}} + d\langle P_{opt}\rangle\frac{F_{EDFA}}{L^2}, \tag{4.20}$$

where $\langle P_{opt}\rangle$ is the average power at the modulator output (see Fig. 4.4) and we used the relation:

$$\langle P_{det}^*\rangle = \frac{\langle P_{opt}\rangle}{L}. \tag{4.21}$$

We can further simplify the relation (4.20) by recalling that $G_{EDFA} \gg 1$ and by assuming $\eta = 1$, so that $a = d$. Then, $F^* > F$ if:

$$F_{RF} > d\langle P_{opt}\rangle\left(\frac{F_{EDFA}}{L^2} - \frac{1}{L}\right). \tag{4.22}$$

Note that F_{RF} must clearly be greater than 1. To give some feeling for the behavior of relation (4.22), we calculated $F^* = F$ as a function of F_{EDFA}, F_{RF} and L: this gives the boundary of relation (4.22). We chose $\mathcal{R} = 0.7\,\mathrm{A/W}$, $R_L = 50\,\Omega$, $T = 300\,\mathrm{K}$ and $\langle P_{opt}\rangle = 1.5\,\mathrm{mW}$, giving $d\langle P_{opt}\rangle \simeq 1$. The result is shown in Fig. 4.5: note that the curves shown in this figure do not give the absolute value of the link noise factor, but divide regions where $F^* > F$ and $F^* < F$. If the curves are below 1, the optically amplified link has better noise factor than the electrically amplified link, even if the electrical amplifier is noiseless. This is because, with the parameters chosen in this example, the thermal noise and shot noise contributions are dominant. In these conditions, (4.19) shows that optical amplification can reduce the link noise factor. If the link uses a noisy EDFA with $F_{EDFA} = 7\,\mathrm{dB}$ and there is no optical loss after the amplifier, than an RF amplifier with noise factor lower than 4 (6 dB) will provide better noise figure than the optical amplification.

In lossy links, the optical amplification appears to be particularly advantageous with respect to electrical amplification, as those typically used for distribution of wireless signals in ROF networks, because the NF of such links is dominated by the effect of optical losses. Remember that 1 dB of optical loss corresponds to 2 dB of electrical loss. In this situation, the Friis' formula implies that an electrical amplifier at the link end cannot help in improving the link NF. Instead, an optical amplifier can decrease the link loss and improve the link NF, until its own noise contribution becomes dominant. Also, note that if the EDFA is at the beginning of the link, the input optical signal power is higher, the amplifier is more saturated and the the ASE is lower. Hence, intuitively, the

noise factor improves if the amplification is placed early in the transmission link, that is: in the optical domain at the beginning of the link, before as much optical losses as possible. A similar conclusion is given by Betts in [83], where the author calculates de NF of optically amplified links but makes no comparison with electrical amplification.

Note that an electrical pre-amplifier feeding the modulator RF input would be effective in reducing the link noise figure [84, page 277]. However, this solution is impractical if link performance is limited by distortion from the modulator itself.

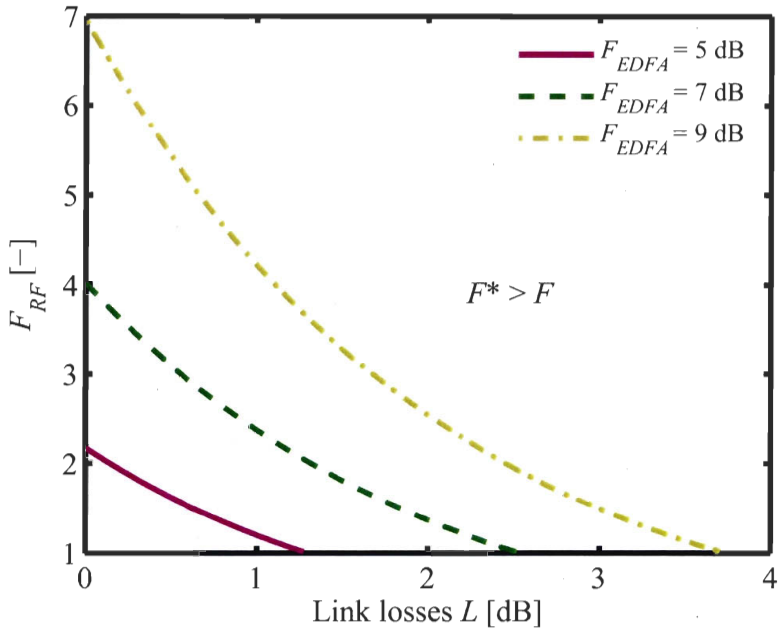

Figure 4.5: Boundaries of relation (4.22) as a function of F_{EDFA}, F_{RF} and link losses L. For values of F_{RF} above the curves: $F^* > F$. Parameters of the simulation: $d\langle P_{opt}\rangle = 1$.

4.2 Some considerations on detected noise in narrowband ROF systems with high optical modulation depth

When optical modulation depth is small, it is possible to calculate the impact of optical noise sources on the total detected electrical noise by considering the optical signal as almost constant in power. This kind of approximation is used, for example, in [122] to calculate the power spectral density RF noise due to EDFA ASE. In systems with high optical modulation depth, this approximation is not valid, and this gives rise to questions on the validity of the noise expressions given in (4.4). In this section, we discuss this problem taking large inspiration from [123], where the authors give a general derivation of photocurrent noise associated with the detection of optically

amplified signals. However, we will adjust the general model to take into account the bandlimited nature of the RF modulating signal. Then, we will extend the analysis to explain some peculiar characteristics of RIN noise and the RF noise generated by the stimulated Brillouin scattering.

The optical signal is band-limited over a band B_0. Hence, it can be treated using the analytical representation:

$$\mathbf{V}(t) = V_s(t) + \mathbf{V}_n(t) \tag{4.23}$$

where $\mathbf{V}(t)$ is a complex stochastic process corresponding to the baseband complex equivalent representation of the optical field on the detector, written as the sum of the optical deterministic signal $V_s(t)$ and optical noise $\mathbf{V}_n(t)$. $\mathbf{V}_n(t)$ is assumed to be a complex, stationary, circularly symmetric [124, 125] gaussian process with zero expected value. The two field quantities are independent and normalized so that $|\mathbf{V}(t)|^2$ represents the instantaneous optical intensity.

The optical signal is detected using a photoelectric detector with responsivity $\mathcal{R}$ and filtered by a filter $h(t)$ with bandwidth B_h, which includes the detector impulse response and any other filter following the detector. For example, in a ROF link followed by a signal receiver, the $h(t)$ would include the channel selection filters at the input of the receiver. Hence, in bandlimited transmission links, the filter $h(t)$ typically has a bandpass response.

The detector is sensitive to instantaneous optical intensity, that is $|\mathbf{V}(t)|^2$. The detected and filtered signal is a non-stationary stochastic process named $\mathbf{i}(t)$:

$$\mathbf{i}(t) = \left[\mathcal{R}|\mathbf{V}(t)|^2 + \mathbf{i}_{shot}(t)\right] * h(t). \tag{4.24}$$

The $\mathbf{i}_{shot}(t)$ term is the shot noise intrinsically generated by the photodetection process, and $*$ indicates convolution. Hence, the variance of $\mathbf{i}$ is ([123] and, for a stationary optical signal, [126, p. 455]):

$$\sigma_{\mathbf{i}}^2(t) = C_{\mathbf{i}}(t,t) = \underbrace{\mathcal{R}^2 \int_{-\infty}^{+\infty}\int C_{|\mathbf{V}|^2}(\alpha,\beta)\, h(t-\alpha)\, h(t-\beta)\; d\alpha\, d\beta}_{\text{(a)}} + \underbrace{\mathcal{R}\, e\left[\left\langle|\mathbf{V}(t)|^2\right\rangle * h^2(t)\right]}_{\text{(b)}}, \tag{4.25}$$

where $C_{|\mathbf{V}|^2}(t_1,t_2)$ is the autocovariance of $|\mathbf{V}(t)|^2$, and $\langle x\rangle$ represents the expected value of the random variable x. The part (b) in (4.25) is due to the shot noise, which is white with zero expected value and autocorrelation:

$$R_{\mathbf{i}_{shot}}(t,\tau) = \mathcal{R}e\left\langle|\mathbf{V}(t)|^2\right\rangle \delta(\tau). \tag{4.26}$$

The $R_{\mathbf{i}_{shot}}(t,\tau)$ is time dependent because the instantaneous intensity is not stationary. The $h(t)$ being a linear filter and the shot noise being white, the filtered noise contribution to $\sigma^2_{\mathbf{i}}(t)$ can be written as $\sigma^2(t)_{\mathbf{i}_{shot}} = \mathcal{R}e\left\langle|\mathbf{V}(t)|^2\right\rangle * h^2(t)$ [127, p. 312]. The part (a) in (4.25) is the general expression of the variance of stochastic process $|\mathbf{V}(t)|^2$ filtered by a linear filter $\mathcal{R}\cdot h(t)$.

Simplification of (4.25) is based on the assumption that $\mathbf{V}_n(t)$ is gaussian. Hence, we can write:

$$\sigma^2_{\mathbf{i}}(t) = \sigma^2_{\mathbf{i},V_s\ shot}(t) + \sigma^2_{\mathbf{i},\mathbf{V}_n\ shot}(t) + \sigma^2_{\mathbf{i},\mathbf{V}_n\mathbf{V}_n\ beat}(t) + \sigma^2_{\mathbf{i},V_s\mathbf{V}_n\ beat}(t) \tag{4.27}$$

In appendix D we show that:

$$\sigma^2_{\mathbf{i},V_s\ shot}(t) = \mathcal{R}e\left[|V_s(t)|^2 * h^2(t)\right] \tag{4.28a}$$

$$\sigma^2_{\mathbf{i},\mathbf{V}_n\ shot}(t) = \mathcal{R}e\left[\left\langle|\mathbf{V}_n(t)|^2\right\rangle * h^2(t)\right] \tag{4.28b}$$

$$\sigma^2_{\mathbf{i},\mathbf{V}_n\mathbf{V}_n\ beat}(t) = \mathcal{R}^2\iint_{-\infty}^{+\infty}\left|\left\langle\mathbf{V}_n(\alpha)\,\mathbf{V}_n^\star(\beta)\right\rangle\right|^2 h(t-\alpha)\,h(t-b)\;d\alpha d\beta \tag{4.28c}$$

$$\sigma^2_{\mathbf{i},V_s\mathbf{V}_n\ beat}(t) = 2\mathcal{R}^2\cdot\mathrm{Re}\left\{\iint_{-\infty}^{+\infty}V_s^\star(\alpha)\,V_s(\beta)\left\langle\mathbf{V}_n(\alpha)\,\mathbf{V}_n^\star(\beta)\right\rangle\times\right.$$
$$\left.\times\;h(t-\alpha)\,h(t-\beta)\;d\alpha d\beta\right\} \tag{4.28d}$$

Note that for a stationary $\mathbf{V}_n(t)$:

$$\left\langle\mathbf{V}_n(\alpha)\,\mathbf{V}_n^\star(\beta)\right\rangle = R_{\mathbf{V}_n}(\alpha-\beta), \tag{4.29}$$

where $R_{\mathbf{x}}(\tau)$ represent the autocorrelation function of the stationary stochastic process $\mathbf{x}(t)$. Let's now examine in detail each noise variance term in (4.28).

Signal shot noise $\sigma^2_{\mathbf{i},V_s\ shot}(t)$

This is the convolution of the deterministic functions $|V_s(t)|^2$ and $h^2(t)$. The latter can be calculated using the convolution of the spectrum of $h(t)$ with itself. The convolution can also be calculated in the spectral domain as multiplication between the spectra of $|V_s(t)|^2$ and $h^2(t)$, as graphically shown in Fig. 4.6. The spectrum of $|V_s(t)|^2$ must reveal its bandlimited nature, so we depicted it as three Dirac delta functions at $\pm f_{RF}$ and at zero frequency, the latter representing the signal average detected optical power P_o. If $h(t)$ has a lowpass response, as it is often the case, the $\sigma^2_{\mathbf{i},V_s\ shot}(t)$ is dependent on time because it follows the modulated instantaneous signal optical power. Hence, a description of $\sigma^2_{\mathbf{i},V_s\ shot}(t)$ as a simple function of average power is not strictly valid. Choosing $B_h < 2f_{RF}$ will average out the fluctuations of the variance, but also the transmitted signal. This problem can be eliminated by choosing a bandpass $h(t)$ with a narrowband spectral response centered around f_{RF}. As shown in Fig. 4.6b, the

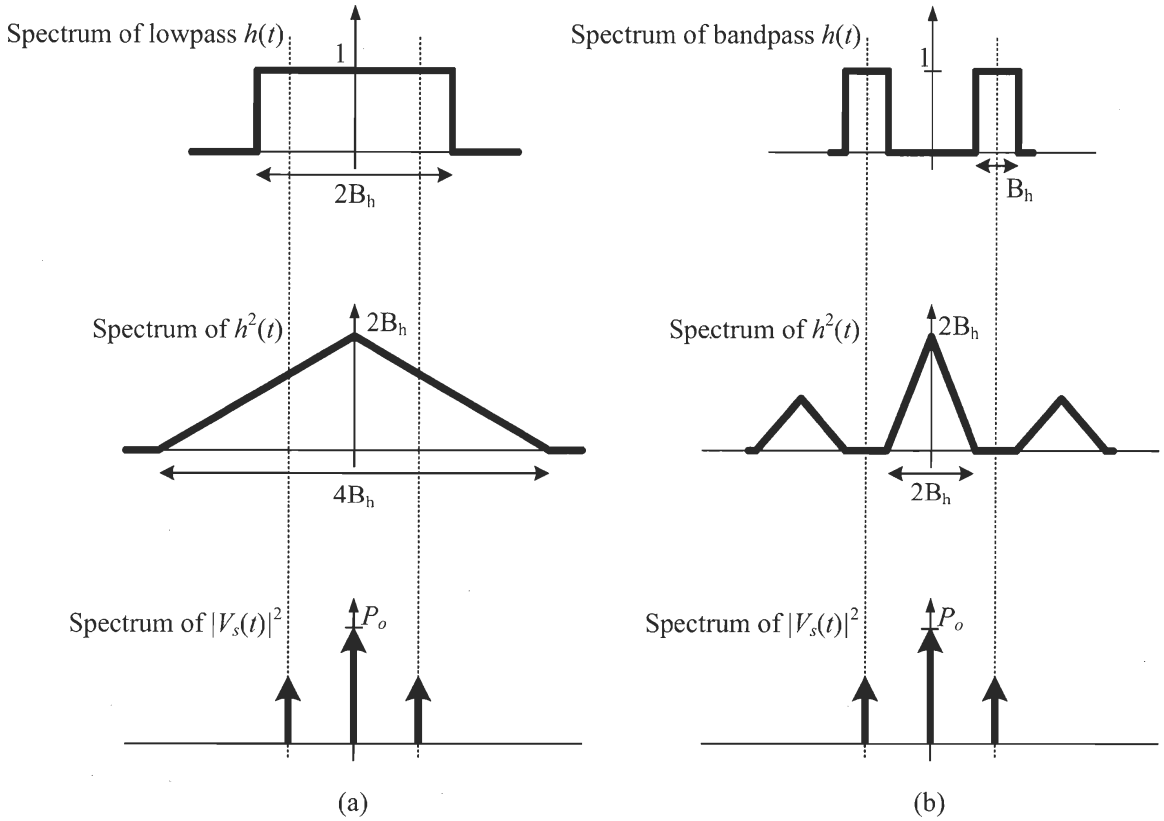

Figure 4.6: Graphical solution for the convolution integral in $\sigma^2_{\mathbf{i},V_s\ shot}(t)$. P_o is the signal average detected optical power.

$h^2(t)$ of such a filter selects only the average signal power P_o, automatically giving a stationary one-sided shot noise variance equal to:

$$\sigma^2_{\mathbf{i},V_s\ shot} = 2\mathcal{R}e\, B_h P_o \tag{4.30}$$

Hence, assuming bandpass filtering, we can correctly use (4.4a) in narrowband ROF systems with high optical modulation depth. The same conclusion for signal shot noise is also exposed in a work by Fernando [128].

ASE shot noise $\sigma^2_{\mathbf{i},\mathbf{V}_n\ shot}(t)$

Let us assume that $\mathbf{V}_n(t)$ represents ASE noise with bandwidth B_o and power spectral density $S_{det,ASE}$. If $B_o \gg B_h$, then $\mathbf{V}_n(t)$ can be treated as white stationary gaussian noise. Hence, (4.28b) loses the dependence on time and can be written as:

$$\begin{aligned}
\sigma^2_{\mathbf{i},\mathbf{V}_n\ shot} &= \mathcal{R}e\left[\left\langle|\mathbf{V}_n|^2\right\rangle * h^2(t)\right] \\
&= \mathcal{R}e\left[\left\langle|\mathbf{V}_n|^2\right\rangle \int_{-\infty}^{+\infty} h^2(t)\, dt\right] \\
&= \mathcal{R}e\left[\left\langle|\mathbf{V}_n|^2\right\rangle \int_{-\infty}^{+\infty} |H(f)|^2\, df\right],
\end{aligned} \tag{4.31}$$

where $H(f)$ is the Fourier transform of $h(t)$, and the latter equation is based on Parseval theorem. This is clearly a stationary variance, equal to (one-sided, considering ASE noise on two polarizations):

$$\sigma^2_{\mathbf{i},\mathbf{V}_n\ shot} = 4\mathcal{R}e\, S_{det,ASE} B_o B_h \tag{4.32}$$

ASE-ASE beat noise $\sigma^2_{\mathbf{i},\mathbf{V}_n\mathbf{V}_n\ beat}(t)$

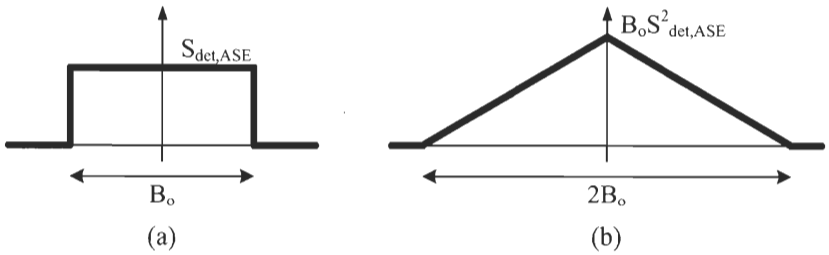

Figure 4.7: (a) ASE power spectral density and (b) its convolution.

From (4.29), the $|\langle \mathbf{V}_n(\alpha)\, \mathbf{V}_n^{\star}(\beta)\rangle|^2$ term in (4.28c) can be written as:

$$|\langle \mathbf{V}_n(\alpha)\, \mathbf{V}_n^{\star}(\beta)\rangle|^2 = R_{\mathbf{V}_n}(\alpha-\beta) \cdot R^{\star}_{\mathbf{V}_n}(\alpha-\beta). \tag{4.33}$$

By using the Wiener-Khinchin theorem, this can be interpreted in the spectral domain as the convolution between the power spectrum of $\mathbf{V}_n(t)$ and the power spectrum of its conjugate. If $\mathbf{V}_n(t)$ represent ASE noise with bandwidth B_o, the power spectrum of $\mathbf{V}_n(t)$ and $\mathbf{V}_n^{\star}(t)$ both have the rectangular shape shown in Fig. 4.7a, which after the convolution gives the two-sided spectrum shown in 4.7b. In a rather simple way, we found the well known ASE-ASE beating spectrum with triangular shape, $2B_o$ bandwidth and $B_o S^2_{det,ASE}$ maximum two-sided power spectral density [122, p. 210]. Since $B_o \gg B_h$, we can assume that the ASE-ASE beating noise is white and calculate the $\sigma^2_{\mathbf{i},\mathbf{V}_n\mathbf{V}_n\ beat}(t)$ in a similar way as for the ASE shot noise in (4.31), giving a one-sided stationary variance:

$$\sigma^2_{\mathbf{i},\mathbf{V}_n\mathbf{V}_n\ beat} = 4\mathcal{R}^2 S^2_{det,ASE} B_o B_h \tag{4.34}$$

The ASE-ASE beating noise and ASE shot noise do not depend on the signal, hence it is not surprising that equations (4.32) and (4.34) are not influenced by the signal OMD.

ASE-signal beat noise $\sigma^2_{\mathbf{i},V_s\mathbf{V}_n\ beat}(t)$

Simplification of the double integral in (4.28d) is based on the assumption of whiteness of ASE noise over B_h. Then, the ASE autocorrelation is a Dirac delta and the one-side detected variance is:

$$\sigma^2_{\mathbf{i},V_s\mathbf{V}_n\ beat}(t) = 2\mathcal{R}^2 S_{det,ASE}\left[|V_s(t)|^2 * h^2(t)\right], \tag{4.35}$$

which is non-stationary. As for signal shot noise, simply taking the average signal power for calculating the $\sigma^2_{\mathbf{i},V_s\mathbf{V}_n\ beat}(t)$ is not strictly correct, unless a bandpass $h(t)$ is chosen. Then:

$$\sigma^2_{\mathbf{i},V_s\mathbf{V}_n\ beat}(t) = 4\mathcal{R}^2 S_{det,ASE} P_o B_h, \tag{4.36}$$

as expected. Note that for a noise which is not white, this simplification is not possible and the integral in (4.28d) should be evaluated. This is the case of Brillouin related noise as described in the next section.

4.3 A special case for $V_n(t)$: noise from Stimulated Brillouin Scattering

In ROF systems, when the optical power launched over a SMF is increased, the SBS is typically the first fibre nonlinear effect that is found to limit the system performance [129]. The SBS can be considered as a power dependent loss mechanism which limits the power injected in the fibre by reflecting part of it in the backward direction. In ROF links, this forbids any improvement of the link gain and NF by increasing the system launched optical power. Furthermore, the backward SBS is noisy [130] and induces noise in the transmitted signal due to the variable and noisy power transfer from the forward propagating signal wave and the backward propagating Brillouin wave. The presence of SBS alters the detected signal noise floor in two ways. First, excess noise appears around 0 Hz and around harmonics of the acoustic wave frequency f_B for both backward and forward propagating fields [131, 132]. Second, the SBS induces a phase change in the optical carrier, which causes a partial conversion of the laser phase noise (and chirp, in the case of direct modulation) into excess intensity noise at low frequencies [131]. SBS induced intensity noise on the transmitted wave has been shown to be the dominant detected signal noise in the frequency band lower than 1 GHz [132].

Most literature about the effects of SBS on ROF links focuses only on baseband SBS noise because it results in substantial CNR degradation in cable TV (CATV) systems [133], which typically employ modulation frequencies below 1 GHz. Little work is reported for Brillouin induced excess noise around a multi-gigahertz RF carrier [134]; the deleterious influence of SBS noise also affects high frequency narrowband ROF links. In the measurement presented in [131], Peral used a directly modulated laser at $f_{RF} = 300\,\text{MHz}$ and the noise contributions at f_{RF} is clearly visible, even if partially hidden by the baseband SBS noise contribution. We measured a similar behavior with external modulation at 5 GHz, as shown in Fig. 4.8. For the moment, let us focus on curve (a) to note the structure of the SBS noise with the baseband noise bell 1 GHz wide, and the much narrower noise peak around the modulation carrier.

The interpretation of the Brillouin induced noise spectrum following the theory of section 4.2 is non-trivial because, as discussed above, SBS noise cannot be considered white but is band limited. We assume that the SBS induced noise can be described as a narrowband (baseband) stochastic complex modulation of the optical carrier. This assumption is justified by the Brillouin backscattering mechanism, which couple some carrier power into a backreflected Stokes wave, thus modulating the carrier itself. We assume also that the spectrum of the signal V_s is such that only the optical carrier has

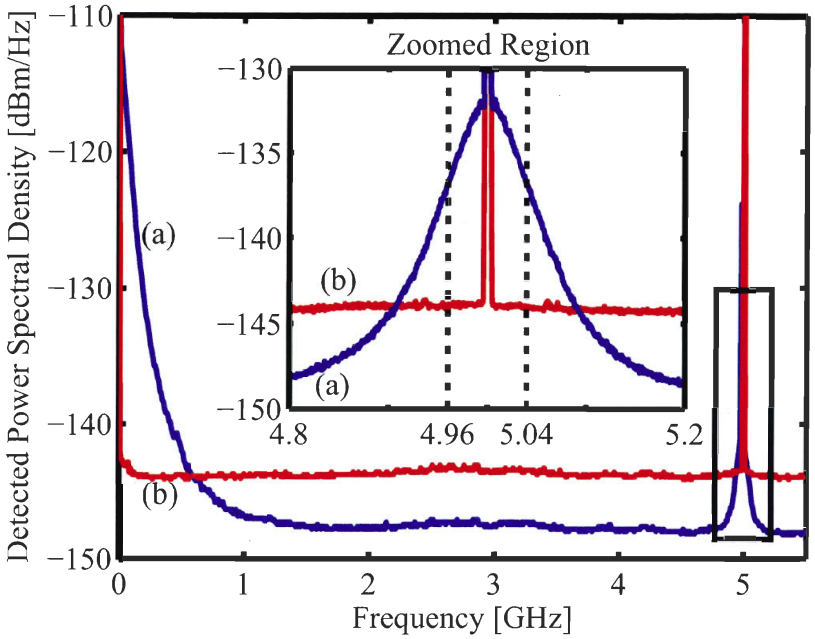

Figure 4.8: Detected RF power spectral density in SBS-impaired ROF link. In (a) the modulator is set at quadrature; 3 dB bandwidth of measured noise peak is 80 MHz. In (b): $|V_{bias}| = V_{bias,Gmax} = 0.083\ V_{\pi}$. Resolution bandwidth: 1 MHz. $P_{RF} = 0$ dBm.

power above the SBS threshold, and not the sidebands. In this case, since the spectrum of the Brillouin gain is very narrow (typically about 15 MHz), it can be assumed that, for modulation frequencies of the order of gigahertz, only the optical carrier is affected by the SBS noise and not the sidebands[2]. Under these assumptions, the SBS noise can be described by a stationary stochastic process $\mathbf{V}_n(t)$ with narrowband (baseband) PSD $S_{\mathbf{V}_n}(f)$. The signal V_s is assumed periodic with fundamental frequency f_{RF}, and can be described by its Fourier series:

$$V_s(t) = \sum_{n \to -\infty}^{+\infty} c_n e^{jn2\pi f_{RF} t}, \tag{4.37}$$

where c_n are complex coefficients. Then, the total SBS-induced detected noise will be composed mainly by two components: a $\mathbf{V}_n - \mathbf{V}_n$ beat noise and a $V_s - \mathbf{V}_n$ beat noise. The former is a baseband contribution whose PSD $S_{\mathbf{V}_n - \mathbf{V}_n}$ can be calculated in a similar way as we did for ASE-ASE beating noise:

$$S_{\mathbf{V}_n - \mathbf{V}_n}(f) = \mathcal{R}^2 \left[S_{\mathbf{V}_n}(f) * S^{\star}_{\mathbf{V}_n}(f) \right] |H(f)|^2 . \tag{4.38}$$

The latter is more complex and can be described by a cyclostationary stochastic process[3] $\mathbf{y}(t) = V_s^{\star}(t) \cdot \mathbf{V}_n(t)$. Rigorous determination of statistics of such a cyclostationary

[2]This condition is typically encountered in low OMD links: for example, Williams in [134] measured no SBS noise around the second harmonic of the RF modulation signal in a low OMD link, even in presence of strong SBS excitation. Noise around the second harmonic is mainly given by beating between optical noise around the upper and lower optical modulation sidebands: in the link studied by Williams the SBS does not contribute significantly to the noise in these bands.

[3]For a definition of cyclostationary stochastic processes see [127, page 373].

process is laborious and beyond our need here, but common practice [135, 136] is to characterize the process by its time averaged autocorrelation over one cyclostationary period. This averaging is equivalent to modeling the time reference or phase of the process as a random variable uniformly distributed over one cycle [136]. By taking this approach, we can express the term $V_s^{\star}(t)\,V_s(t+\tau)\,\langle \mathbf{V}_n(t)\,\mathbf{V}_n^{\star}(t+\tau)\rangle$ in (4.28d) as the product $R_{\mathbf{y}}(\tau) = R_{V_s}(\tau)\,R_{\mathbf{V}_n}(\tau)$ between the autocorrelation of $\mathbf{V}_n(t)$ and the autocorrelation of $V_s^{\star}(t)$. The latter is defined as:

$$R_{V_s}(\tau) = \frac{1}{T}\int_{t_0}^{t_0+T}\sum_{n\to-\infty}^{+\infty} c_n^{\star}e^{-jn\omega_{RF}t}\sum_{m\to-\infty}^{+\infty} c_m e^{jm\omega_{RF}(t+\tau)}dt = \sum_{n\to-\infty}^{+\infty}|c_n|^2\,e^{jn\omega_{RF}\tau}, \quad (4.39)$$

where the two summations collapse into one, because of the averaging integral. Hence, the noise-signal beating term is now stationary and is described by the convolution between the spectrum of $\sum_{n\to-\infty}^{+\infty}|c_n|^2\,e^{jn\omega_{RF}\tau}$ and the power spectrum of $\mathbf{V}_n(t)$, as shown in Fig. 4.9. This latter statement can be easily demonstrated on the basis of the theory of modulation of stochastic processes given by Papoulis in [127, pages 363-365].

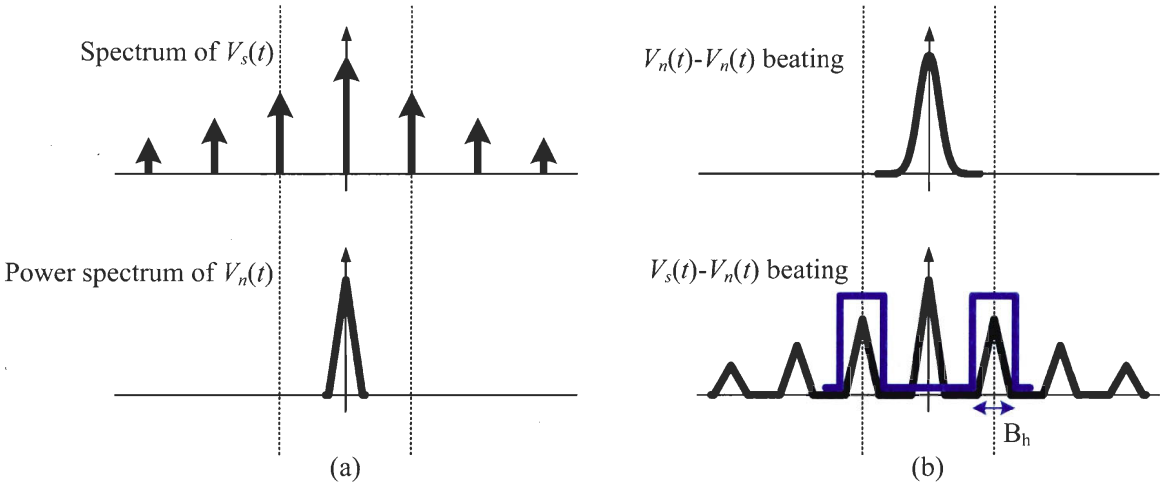

Figure 4.9: SBS noise contributions. In (a): the signal spectrum and the noise PSD. In (b): noise-noise and signal-noise beating for high OMD modulation. In blue, the spectrum of $h(t)$.

In the limit of the assumptions and within the approximation of averaging the statistics of the cyclostationary process, the derivation proposed above justifies the contribution of SBS detected noise around the RF carrier presented in Fig. 4.8: this noise comes from beating between the signal spectrum and the narrowband stochastic modulation of the optical carrier caused by the SBS.

To complete the calculation of the integral in (4.28d), the noise process should be filtered by a narrowband $h(t)$. From (4.28d), the $\sigma^2_{\mathbf{i},V_s\mathbf{V}_n\,beat}$ is equal to:

$$\sigma^2_{\mathbf{i},V_s\mathbf{V}_n\,beat}(t) = 2\mathcal{R}^2\cdot\mathrm{Re}\left\{\iint_{-\infty}^{+\infty} R_{\mathbf{y}}(\alpha-\beta)\,h(t-\alpha)\,h(t-\beta)\,d\alpha d\beta\right\}. \quad (4.40)$$

The double integral represents the variance of $\mathbf{z}(t) = \mathbf{y}(t) * h(t)$, which has been made stationary by the averaging in (4.39). Hence, from standard theory of filtering of stationary stochastic processes:

$$\sigma_{\mathbf{z}}^2 = \int_{-\infty}^{+\infty} S_{\mathbf{yy}}(f) |H(f)|^2 df, \tag{4.41}$$

where $S_{\mathbf{yy}}(f)$ is the Fourier transform of $R_{\mathbf{y}}(\tau)$. The $\sigma_{\mathbf{z}}^2$ is positive and real, and can be also expressed by $R_{\mathbf{z}}(0)$. Remembering that we assumed a bandwidth of $R_{\mathbf{V}_n}$ much lower than f_{RF}, and that $H(f)$ is centered on f_{RF}, $R_{\mathbf{z}}(\tau)$ can be expressed as:

$$R_{\mathbf{z}}(\tau) = \left(|c_{-1}|^2 e^{-j2\pi f_{RF}\tau} + |c_1|^2 e^{j2\pi f_{RF}\tau}\right) * R_{\mathbf{V}_n}(\tau), \tag{4.42}$$

and the $\sigma_{\mathbf{z}}^2$:

$$\sigma_{\mathbf{z}}^2 = \left(|c_{-1}|^2 + |c_1|^2\right) \sigma_{\mathbf{V}_n}^2. \tag{4.43}$$

Assuming $|c_{-1}|^2 = |c_1|^2$, the $\sigma_{\mathbf{i},V_s\mathbf{V}_n\,beat}^2$ variance given in (4.28d) becomes:

$$\sigma_{\mathbf{i},V_s\mathbf{V}_n\,beat}^2 = 4\mathcal{R}^2 |c_1|^2 \sigma_{\mathbf{V}_n}^2. \tag{4.44}$$

Note that equation (4.44) is proportional to $|c_1|^2$, which is related to the power of the modulation sidebands in the optical spectrum. Hence, increasing the modulation sidebands will increase also the variance of the detected noise around the RF carrier.

Unluckily, it is virtually impossible to directly measure the optical spectrum of the $\mathbf{V}_n$ generated by the SBS, because its bandwidth is of the order of tens of megahertz. However, in the following section we will present some experimental work on SBS in ROF links with modulator bias optimization, which well fit the model of SBS noise presented here.

4.3.1 The CNR of SBS-impaired ROF links

Optical phase modulation is often used to counteract the SBS effects in ROF links [137], but the main disadvantages of this technique are the higher bandwidth occupied by the phase modulated signal and the greater complexity of the modulation stage. We show that the bias optimization technique, in addition to link gain improvement, can lead to suppression of the SBS and associated noise, thus significantly improving the CNR of SBS-noise-limited links, without the complexity of an additional phase modulation.

The reference link for this work, first published in [138], is shown in Fig. 4.10. A DFB laser is intensity modulated by a MZ modulator, after polarization control. Then, the signal is amplified by an EDFA, coupled to the fibre using a circulator with 1.5 dB losses, used to observe the backscattered SBS power, and propagated over 10 km of

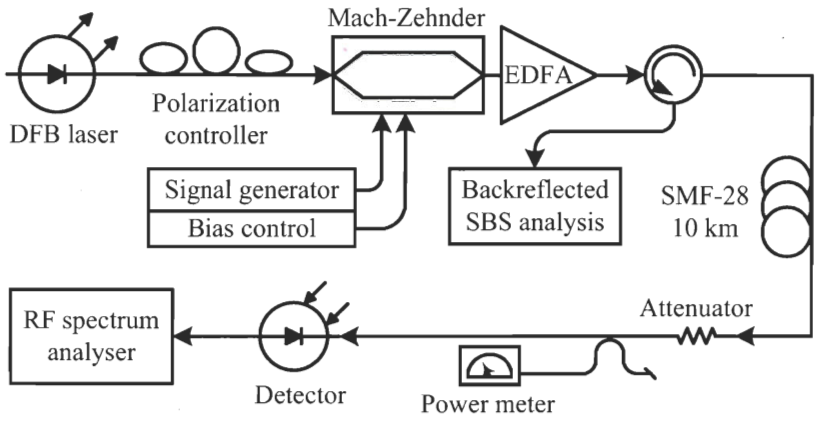

Figure 4.10: Experimental setup for measuring the impact of SBS on ROF links. A DFB laser is intensity modulated by a MZ after polarization control, amplified by an EDFA and propagated over 10 km of standard fibre. An attenuator controls detector saturation. The detector is connected to a HP 8565E RF spectrum analyzer. The backscattered SBS power is monitored using a circulator and a power meter.

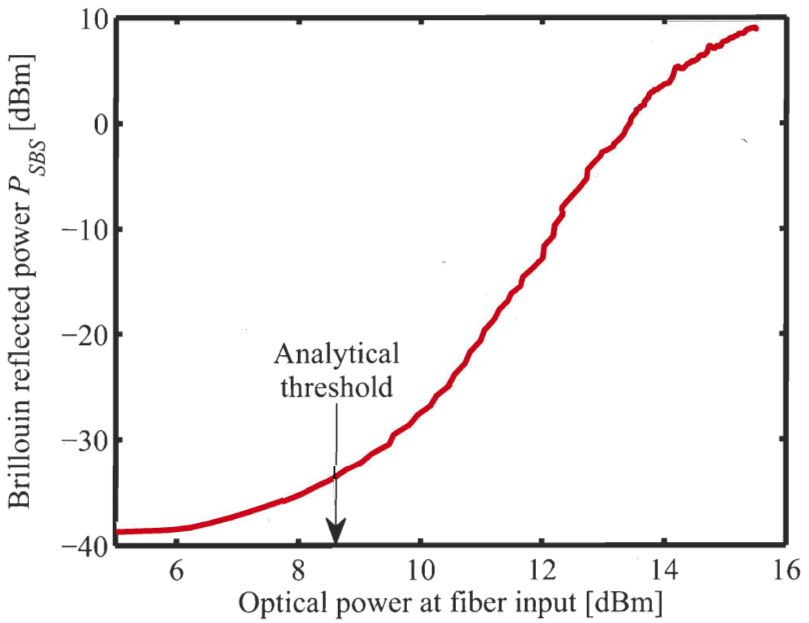

Figure 4.11: The Brillouin reflected power P_{SBS} as a function of the fibre input power. The analytical threshold is given by equation (4.46). For fiber input power below 6 dBm, the measured reflected power is dominated by Rayleigh scattering.

standard SMF. An attenuator helps to control detector saturation. The detector is connected to an RF spectrum analyzer. The modulating signal is a simple tone at f_0 =5 GHz. The link is very similar to the one used in chapter 3 for the link gain study, except for the circulator and SBS analysis setup, constituted by either a power meter or an OSA. Further details on the hardware used in this setup are given in table 4.1. In Fig. 4.11 we report a measurement of the backreflected SBS power versus input fibre power that can be used to identify the SBS threshold for this link. This measure is taken with signal modulation active, but the presence or absence of chirp-less

Table 4.1: Details on the hardware used in Fig. 4.10

Device	Model	Settings and Comments
Laser	DFB HP LSC2500	Pump current: 100 mA Output power: 7 dBm Max. power at EDFA input: -2 dBm
Fibre	SMF-28	Length: 10 km linear losses (α): $6.9 \cdot 10^{-5}\,\mathrm{m}^{-1}$ fibre core area (A): $52.8\mu\mathrm{m}^2$ Brillouin gain coefficient (γ): $2 \cdot 10^{-11}$m/W [133]
Modulator	MZ JDS OC-1	Bandwidth: 10 GHz Extinction ratio: > 35 dB Insertion loss: 5 dB V_π: 3.35 ± 0.07 V
EDFA	JDS OAB1552+1FA0	Small signal gain (G_0): 37 dB Max. saturated output power ($P_{out,max}$): 17 dBm
Detector	Agilent 11982A	Bandwidth: 15 GHz Responsivity: 300 V/W
Circulator	-	Insertion losses: $\simeq 1.5$ dB

modulation does not affect significantly the SBS threshold and the ratio between fibre injected power and backscattered power [133].

A typical detected RF spectrum in the (0-5.5) GHz band is shown in Fig. 4.8. The low frequency noise is clearly visible in curve (a) as an important increase of detected power spectral density for frequencies below 1 GHz. Also, a noise bell with about 80 MHz bandwidth around 5 GHz is shown. Curve (b) shows the same measurement after bias optimization: we observe a reduction of the noise at low frequency and around 5 GHz, with and increase of the noise floor due to the contribution of EDFA amplified spontaneous emission, as seen before.

The SBS-induced noise contribution affects the detected noise floor as shown in Fig. 4.12, which can be compared with Fig. 4.2 measured with the fibre replaced by an attenuator. In Fig. 4.12, SBS-induced noise is dominant for $|V_{bias}| > 0.2V_{pi}$, increasing the received noise floor up to 17 dB with respect to the linear link. For $|V_{bias}| < 0.2V_{pi}$, we observe a decrease in SBS-induced noise. For $|V_{bias}| < 0.1V_{pi}$ the ASE beating noise becomes dominant. Note that the SBS noise contribution actually increases when moving the bias from $0.6V_\pi$ to $0.2V_\pi$, and this cannot be simply explained by the increasing ASE noise contribution because the ASE PSD is always well below the measured noise level. This is rather better explained by observing the evolution of the sideband and carrier optical powers with bias, as shown in Fig. 4.13 along with the measured backscattered Brillouin power P_{SBS}: for bias values in the $0.6V_\pi$-$0.3V_\pi$ range, the optical carrier power at fibre input is almost constant, and so is the Brillouin backscattered power, which decreases only by about 3 dB. Hence, recalling the interpretation of the SBS noise as a narrowband complex random modulation of the optical carrier $\mathbf{V}_n(t)$, we can assume

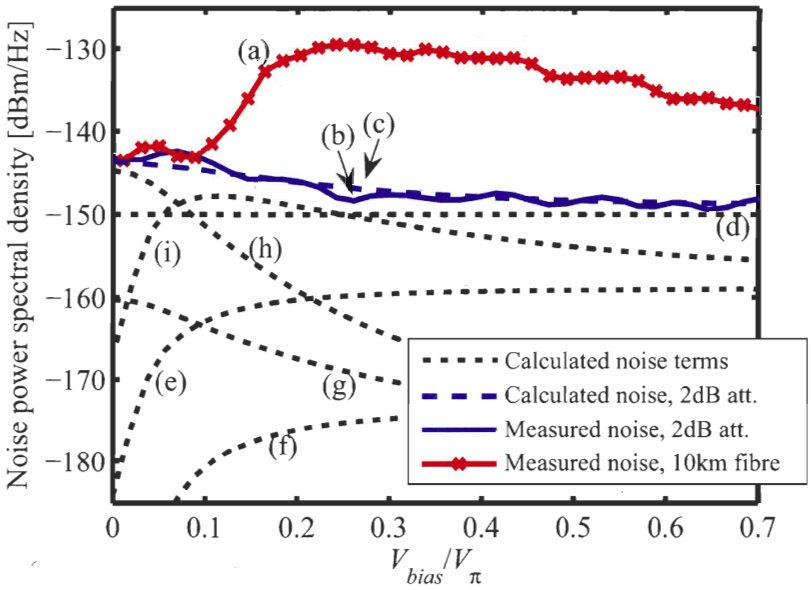

Figure 4.12: Detected Noise PSD in SBS-impaired ROF link, as a function of modulator bias. Curve (a) is the measured noise with 10 km of standard fibre, (b) is the measured noise with the fibre replaced by a 2 dB attenuator, (c) is the sum of all the calculated noise contributions (d-i), (d) is DANL of the spectrum analyzer (RBW= 10 Hz), (e) is signal shot noise, (f) is noise from laser RIN, (g) is ASE shot noise, (h) is ASE-ASE beat noise, (i) is ASE-signal beat noise. As in Fig. 4.2, no optical filtering was used and noise is sampled using an RF spectrum analyzer in noise marker mode, 1 MHz aside the 5 GHz tone with $P_{RF} = 0$ dBm.

that its power spectral density decreases also of about 3 dB. To the contrary, the measured optical modulation sidebands power at fibre end increase by more than 10 dB. Then, the model given by (4.44) predicts an increase of detected noise contribution of about 7 dB, due to the $V_s - \mathbf{V}_n$ beating between the optical modulation sidebands and the SBS-induced noise on the optical carrier. This is in very good agreement with the observed increase in the measured noise within the $0.6V_{\pi}$-$0.2V_{\pi}$ range, thus further confirming the validity of the model proposed in the previous section. Actually, it appears that the variance of the SBS $\mathbf{V}_n$ can be considered proportional to the detected P_{SBS}: this is reasonable because it is a common observation that the more SBS is excited in the fibre, the more noise is observed at the link end. Recalling (4.44), we express the detected link noise PSD limited by the SBS noise, shown in Fig. 4.12 curve a, as:

$$S_{V_s - \mathbf{V}_n} = k\,|c_1|^2\,P_{SBS}, \tag{4.45}$$

where $S_{V_s-\mathbf{V}_n}$ represent the PSD of the $V_s - \mathbf{V}_n$ beating noise and k is a constant value. The comparison between the total received noise at the link end and (4.45) is given in Fig. 4.14: the two curves fit well until the Brillouin noise is dominant. We think that this can be considered another confirmation of the validity of the model and of (4.44).

Note that this model of the Brillouin-induced RF noise is novel and has never been published before. Another experimental demonstration of its validity is reported in appendix E.

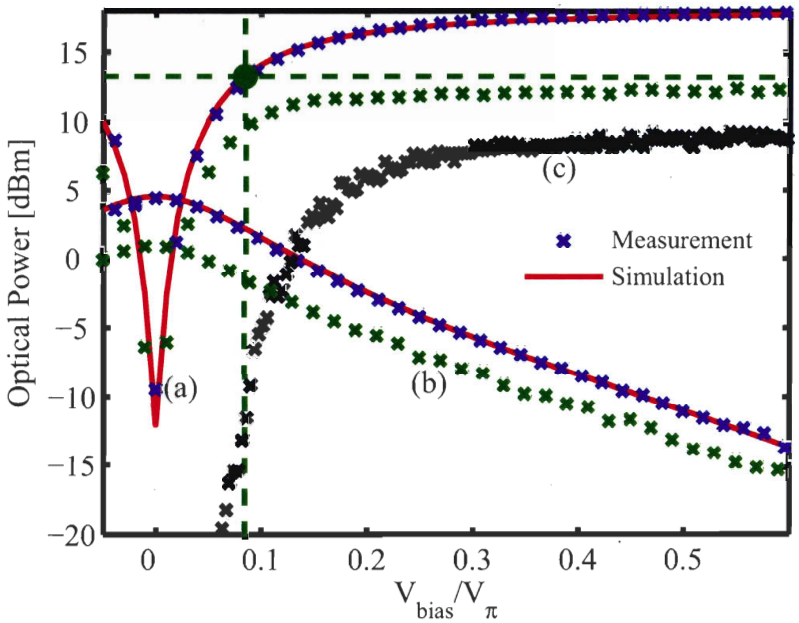

Figure 4.13: Power of the optical carrier, modulation sidebands and backscattered SBS power as a function of MZ bias. Optical carrier power (a) and modulation sidebands power (b): in blue, measured values at EDFA output; in green, measured values at fibre output; (c) measured SBS reflected power P_{SBS}. The spectrum measurement are taken using an ANDO AQ6317B OSA with 0.01 nm RBW. The power of the sidebands is corrected to take into account the fraction of carrier power falling over the sidebands, due to the limited resolution of the OSA. Modulation frequency: 5 GHz.

With bias lower than about $0.2V_\pi$, the carrier power and the Brillouin noise are strongly suppressed. Moving the bias to $V_{bias,Gmax} \simeq 0.083V_\pi$ suppresses the carrier power at EDFA output from about 17 dBm down to 13.8 dBm, and the backscattered SBS power decreases rapidly from about 9 dBm down to -12.6 dBm. Note that the sideband power is always lower than the SBS threshold, usually calculated as[4]:

$$P_{th} = 21A\alpha/\left[\gamma\left(1 - e^{-\alpha L}\right)\right] = 8.85 \text{ dBm}, \tag{4.46}$$

where the parameters are given in table 4.1.

Fig. 4.12 demonstrates that the impact of Brillouin on the link noise can be reduced by optimizing the bias, and we remember from chapter 3 that bias optimization can also lead to optimized link gain. Combining these two effects, we expect to observe a significant improvement in link CNR. The measured CNR for a complete link with 10 km of standard fibre is shown in Fig. 4.15: for bias values near the quadrature point, the CNR is relatively low because the detected RF power is low (curve b) and the noise floor is affected by SBS-induced noise. However, when the bias moves towards $V_{bias,Gmax}$, a steep rise in CNR is observed. At this point, the CNR is more than 20 dB higher than at quadrature. For $|V_{bias}| < V_{bias,Gmax}$, the detected RF power falls due

[4]From [81]; assuming the absence of pump depletion and pump linewidth much smaller than Brillouin gain bandwidth.

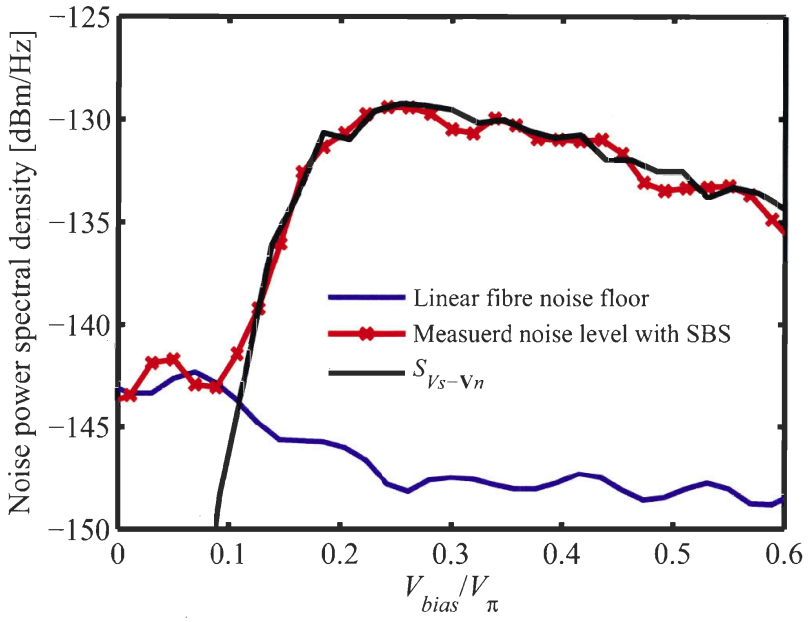

Figure 4.14: Comparison between detected noise limited by SBS and equation (4.45). The linear fibre noise floor and the measured noise level with SBS are a zoom of curves given in Fig. 4.12.

to the lower modulation efficiency of the MZ at such values of bias. Curve (c) is a similar measurement with the fibre replaced by a 2 dB optical attenuator: the CNR is not affected by SBS noise and its shape follows curve (d), calculated from the detected RF power and the noise floor of curve (c) in Fig. 4.12.

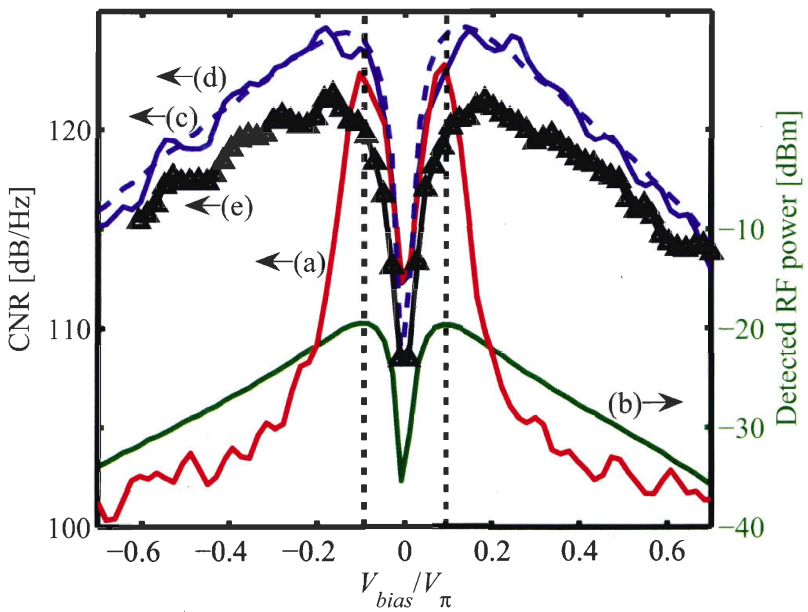

Figure 4.15: CNR and detected RF power versus the modulator bias in SBS-impaired link. Curve (a) is the measured CNR with 10 km of fibre. Curve (b), (c) and (d): detected RF power, calculated and measured CNR with fibre replaced by a 2 dB attenuator. Curve (e) is the measured CNR with complete link and phase modulation to reduce the SBS. Dotted lines identify $V_{bias,Gmax}$.

In order to confirm that the source of CNR degradation is SBS, we added a phase modulator and a polarization controller before the MZ modulator. We applied a sinusoidal phase modulation on the signal (frequency: 80 MHz, amplitude: $10\,V_{\text{p-p}}$) to increase the SBS threshold and reduce the SBS-induced noise. In this case, measured CNR is shown in Fig. 4.15, curve (e): the shape is similar to curve (c) and this confirms that SBS-induced noise causes the observed CNR degradation. For this test, we adjusted the DFB laser power in order to counterbalance the additional losses from the phase modulator and tried to have the same mean power at the EDFA input, as in all other measurements. However, at maximum laser power, the mean power was still too low by 1.5 dB, which explains the difference between curves (e) and (c) in Fig. 4.15.

The measurement shown above demonstrates that the bias optimization technique may be useful in suppressing the SBS, hence improving the received signal CNR. Note however that total SBS suppression with bias optimization is only possible if the SBS threshold is higher than both the minimum optical carrier power and the maximum optical sideband power at the fibre input, which are found when $V_{bias} = 0$. Also, the bias which makes the SBS-induced noise negligible over other sources of noise in the system may not be the bias that gives, for instance, maximum link gain. However, moving the bias towards the zero transmission point is an attractive technique for its simplicity and may surely assist other classical methods for SBS suppression, including:

- Optical phase modulation [137]
- Carrier suppression by filtering [139]
- Link segmentation with different fibre spans [140]

In the system under test, the minimum carrier power is about $-12\,\text{dBm} \ll P_{th}$, as defined by (4.46). Hence, in the system under test, the bias optimization technique leads to SBS control without the need for additional SBS countermeasures, thereby reducing the link complexity.

4.4 Impact of laser RIN on narrowband signals

Another noise contribution that may give unexpected results in high OMD links is RIN, which we omitted in the analysis in section 4.2. In fact, the RIN is much easier to analyze in the instantaneous optical power domain, instead of the electric field domain, as we did in section 4.2. The modulated instantaneous optical power $P(t)$ can be described as:

$$P(t) = [1 + ms(t)]\,[P_0 + \mathbf{P}(t)]\,, \tag{4.47}$$

where $s(t)$ is the modulating signal with frequency f_{RF}, m is the optical modulation index, P_0 is the average optical power and $\mathbf{P}(t)$ is the instantaneous fluctuation of the

optical power related to the RIN. Note that the optical fluctuation $\mathbf{P}(t)$ multiplies with the signal, and thus represents a multiplicative noise term. Following the same approach as in section 4.2, the detected photocurrent can be defined as:

$$i(t) = \mathcal{R}P(t) * h(t), \tag{4.48}$$

where $h(t)$ represents the frequency response of the photodetector and is defined as a passband filter centered around f_{RF}. The variance of the photocurrent is given by an expression similar to (4.25). Then, the variance of the photocurrent due to the RIN is:

$$\sigma_i^2(t) = C_i(t,t) = \mathcal{R}^2 \iint_{-\infty}^{+\infty} C_P(\alpha,\beta)\, h(t-\alpha)\, h(t-\beta)\; d\alpha\, d\beta, \tag{4.49}$$

where $C_P(\alpha,\beta)$ is the autocovariance of $P(t)$. We define $\mathbf{P}(t)$ as a white stationary stochastic process and $s(t)$ as a deterministic periodic signal. Hence, the autocorrelation of $\mathbf{P}$ is a Dirac delta:

$$R_{\Delta P}(\alpha,\beta) = P_0^2 \frac{r}{2}\delta(\alpha-\beta), \tag{4.50}$$

where $\frac{r}{2}$ is the double sided RIN power spectral density. After a few simple steps developing C_P, we get:

$$\sigma_i^2(t) = \mathcal{R}^2 P_0^2 \frac{r}{2} \int_{-\infty}^{+\infty} [1+ms(\tau)]^2 h^2(t-\tau)\; d\tau. \tag{4.51}$$

If we define $s(t) = A\cos(2\pi f_{RF}t)$, assuming $mA < 1$ to avoid clipping, the last equation can be solved in the frequency domain as shown in Fig. 4.16: note that the signal $[1+ms(\tau)]^2$ has some components at $2f_{RF}$ that are not filtered away by $h^2(t)$. Hence, the $\sigma_i^2(t)$ is not stationary but cyclostationary, even if we used a bandpass $h(t)$:

$$\sigma_i^2(t) = \mathcal{R}^2 P_0^2 \frac{r}{2}\left[2B_h\left(1+m^2P_s\right) + m^2P_sB_h\cos(2\pi\cdot 2f_{RF}\cdot t)\right], \tag{4.52}$$

where $P_s = \frac{A^2}{2}$ is the average power of $s(t)$. Again, we can stationarize the variance by taking the average over one period of cyclostationarity [136]. Hence, the stationarized variance is simply:

$$\sigma_i^2 = \mathcal{R}^2 P_0^2 r B_h\left(1+m^2P_s\right), \tag{4.53}$$

and is dependent on the average power of $s(t)$. The same result have been reported by Fernando in [128], with a different demonstration. The importance of (4.53) is twofold: first, it shows that the standard definition of RIN variance being simply proportional to the square of the average detected photocurrent is not valid in high OMD links: (4.53) reduces to (4.4b) only if $m^2P_s \ll 1$. This has been demonstrated experimentally by Fernando in [128]. Second, (4.53) suggests that in RIN limited links increasing the power of the modulation signal will not improve unlimitedly the CNR at detection, even if the modulator is perfectly linear. This important detail will be shown experimentally in the following section.

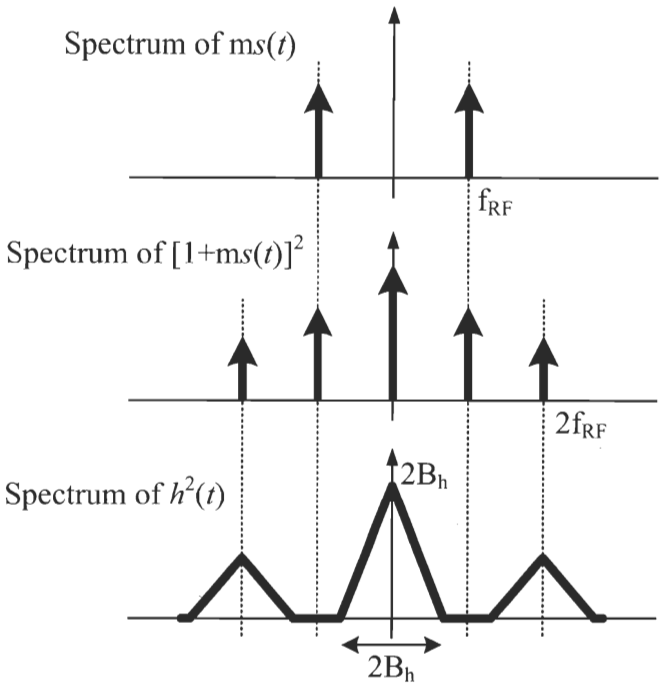

Figure 4.16: Graphical solution of (4.51).

4.4.1 Comparing DFB-SCs and fibre lasers in high OMD narrowband links

In the group where we have had the privilege to work, significant efforts have been spent to develop a new type of multiwavelength fibre laser, based on fibre Bragg gratings written in photosensitive Erbium-Ytterbium codoped fibre (Brochu *et al.* [141], Slavik *et al.* [142]). So there was strong interest in comparing the performance of these lasers to more widely used semiconductor DFB (DFB-SC) lasers in the context of ROF transmission links based on WDM. An example of the potential application of multiwavelength fibre lasers is given in chapter 6: the laser is used as an optical source for an all-optical beam-former, which is designed to address each antenna in an array by using a different laser emission wavelength in a WDM configuration. We will show in chapter 6 that multiwavelength lasers are particularly well adapted for this application because all the wavelengths are modulated by the same RF signal using a single modulator.

One relevant difference between the fibre lasers proposed in COPL and DFB-SC lasers is the RIN PSD: the fibre lasers feature a RIN relaxation frequency on the order of a few megahertz, while typically this is on the order of gigahertz for semiconductor lasers. Also, the RIN peak of multiwavelength fibre lasers is typically higher compared to DFB-SC lasers. In Fig. 4.17 we compare the RIN PSD of a HP LSC2500 DFB-SC laser and a fibre laser fabricated by Brochu [143]. The spectrum of the latter is given in appendix F. Note that, even if the fibre laser tested here has a single emission

wavelength, its RIN is representative of the RIN of single lines of a multiwavelength distributed Fabry-Perot fibre laser [144].

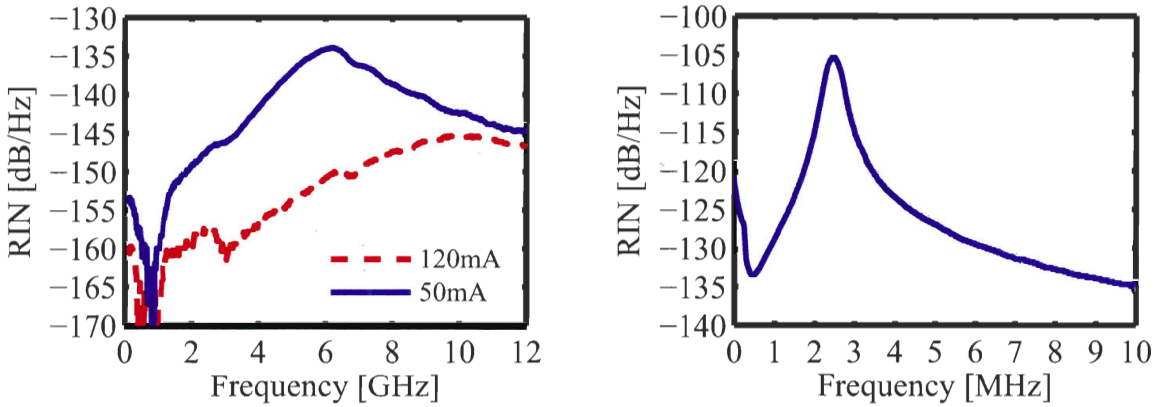

Figure 4.17: Comparison of semiconductor DFB RIN and fibre laser RIN (a) Semiconductor DFB: `HP LSC2500`, for two bias current settings. (b) Brochu's fibre laser RIN. Pump laser: `JDS 27-BCB-794`, 980 nm. Pump bias current: 330 mA. Laser temperature: 17°C (thermistor: 14 kΩ).

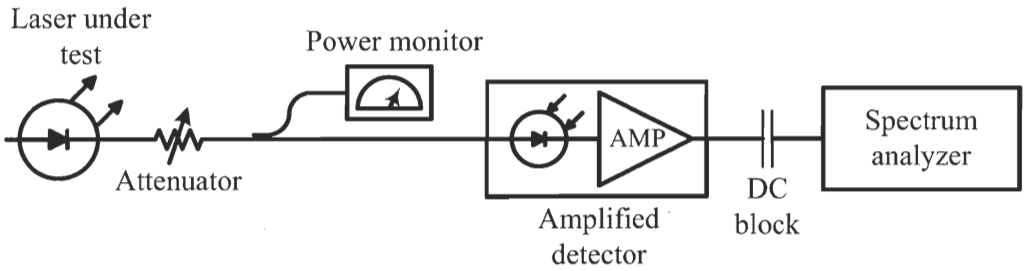

Figure 4.18: RIN measurement setup. The amplified detector is an `Agilent 11982A` optical converter, the DC block is a `MCL BLK-18`, the spectrum analyzer is an `HP 8565E`.

These RIN measurements have been obtained using the setup shown in Fig. 4.18: the laser under test is attenuated to avoid detector saturation and its average power is recorded. Then, we measured the PSD of the signal detected by an amplified photodetector using a spectrum analyzer in noise measurement mode. The thermal noise contribution, read on the analyzer without input optical signal, and shot noise, estimated from received optical power, are subtracted from the total noise PSD to obtain the RIN PSD. The main limitation of this measure is that we estimated the detector responsivity ($\mathcal{R} = 300\,\mathrm{V/W}$) and considered a flat detector bandwidth response. However, the errors on the RIN measurements due to these approximations do not affect the validity of the discussion following here. More precise measurements of RIN of the type of fibre laser used here are shown in [144].

Equation (4.53) raises some questions about the application of fibre lasers in ROF links with narrowband, high OMD signal modulation: intuitively, the laser RIN is modulated along with the average optical power by the signal. In the frequency domain, this corresponds to a convolution of the laser spectrum (with its RIN) with the modulating

signal. Hence, if the modulation RF signal is a simple RF tone at f_{RF}, after detection an image of the low frequency RIN peak of a fibre laser may be observed around f_{RF}. This is pictured in Fig. 4.19.

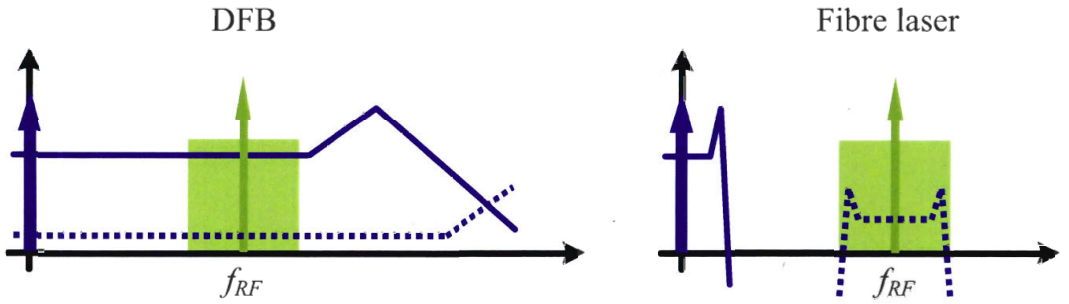

Figure 4.19: Cartoon of the detected noise in a RIN limited link with a fibre laser and a DFB-SC laser.

Indeed, the RIN peaks around the RF carrier are measurable. We modulated the fibre laser with RIN shown in Fig. 4.17b using a MZ modulator and a 2.5 GHz tone; we measured the detected spectrum shown in Fig. 4.20, which clearly exhibit the RIN peaks about ±2.5 MHz aside the carrier. A similar measurement has been presented by Betts in [83, figure 14] using a diode-pumped Nd:YAG laser.

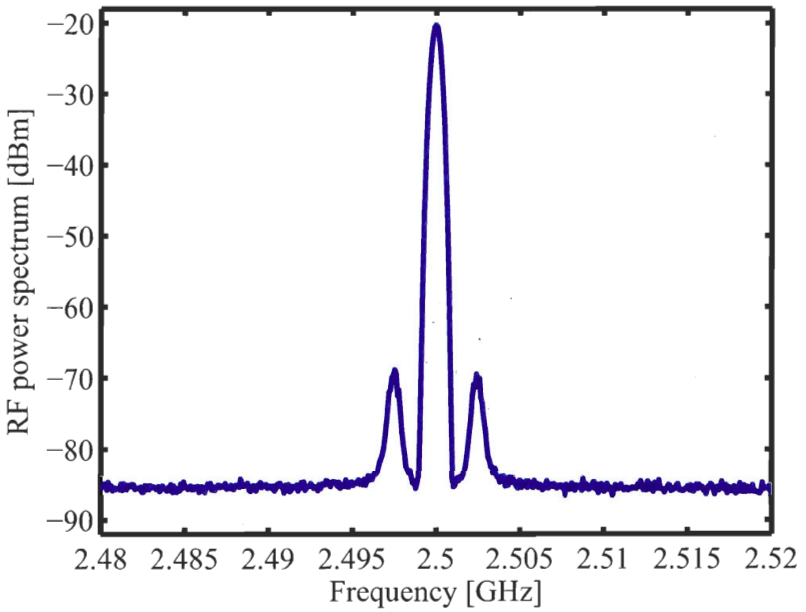

Figure 4.20: Detected RF power spectrum with fibre laser as optical source. The fibre laser signal is externally modulated by a 2.5 GHz tone at 5 dBm. The signal is then attenuated and detected with an `HP 8565E` amplified detector. The spectrum is observed on a `HP 8565E` spectrum analyzer with $RBW = 100$ KHz.

We also simulated the shape of the detected noise floor in a system with a perfectly linear modulator and RIN as the only source of noise. The instantaneous laser power is simulated as a stochastic process with a power spectral density that has the shape given in Fig. 4.17, and an expected value equal to the average laser power. After a linear

modulator driven with a 5 GHz tone, the detected photocurrent exhibit the PSD shown in Fig. 4.21: the PSD using a DFB-SC laser source or a fibre laser source is estimated using an FFT from one realization of the detected stochastic process representing the photocurrent. We properly simulate the RIN peaks around the RF carrier when the source is a fibre laser. In this case, neglecting other sources of noise, the noise floor far from the DC and the RF tone is lower than the noise level given by a DFB-SC laser. However, near the DC and near the RF tone, the noise contribution from the fibre laser RIN is higher than the noise generated by the DFB-SC laser, and noise peaks emerge above the noise level given by the DFB-SC laser RIN. Also, in Fig. 4.21 the DFB-SC laser exhibits a single RIN peak around 10 GHz, as in the measurement shown in Fig. 4.17a for a drive current of 120 mA, which is the maximum allowed for the laser model used here (`HP LSC2500`).

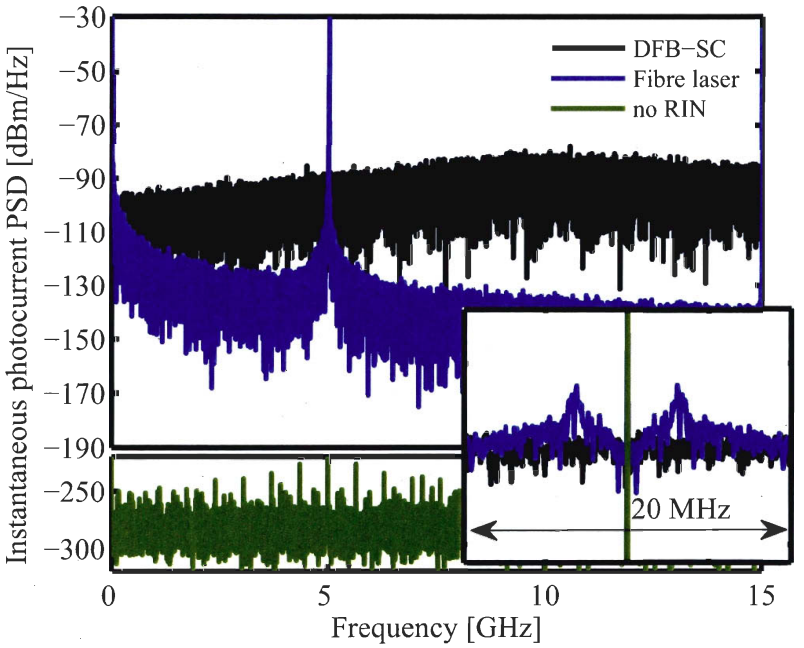

Figure 4.21: Simulated estimation of photocurrent PSD in presence of RIN for a DFB-SC laser and a fibre laser with 5 GHz linear modulation. Estimation is based on FFT (periodogram). Shot noise and thermal noise are neglected. $P_{RF} = 10$ dBm. Average detected optical power: 0.5 mW, optical modulation dept: 50%.

Fig. 4.21 suggests that the fibre lasers are better adapted to the transmission of large bandwidth signals than DFB-SC lasers. In fact, the variance of the detected photocurrent is the estimated noise PSD integrated over the signal bandwidth: for a laser fibre, if the band is large enough, the variance may be lower than for a DFB-SC laser. For example, considering a link bandwidth of 15 GHz, the instantaneous optical power at the laser output assumes the shape shown in Fig. 4.22: the power from the DFB-SC laser exhibits a larger variance, whereas the power from the fibre laser shows a low variance, and a dominant low frequency oscillation pattern due to the RIN peaks. For a narrowband signal the situation is different because within the signal bandwidth, around the RF carrier, the RIN floor from the fibre laser is higher, thus limiting the

detected signal CNR.

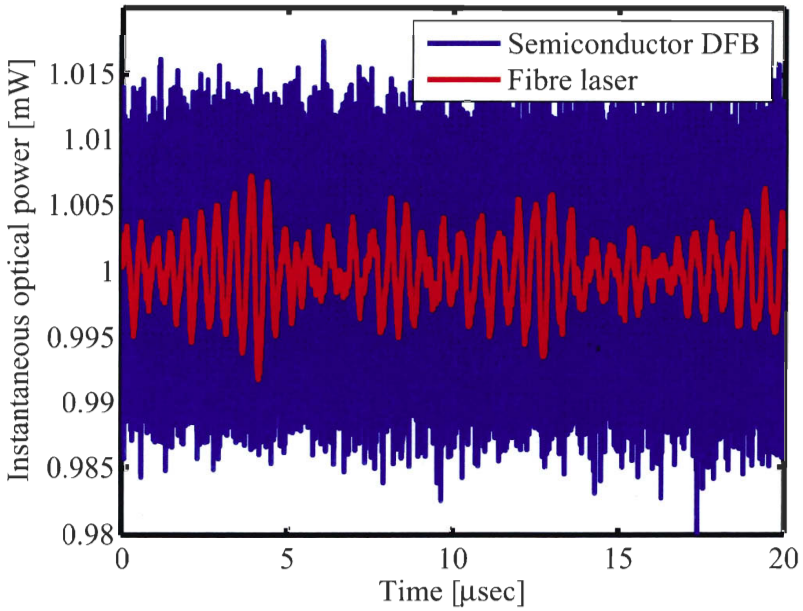

Figure 4.22: Simulated instantaneous optical power emitted by semiconductor and fibre lasers. Simulation over 8 GHz bandwidth. Lasers power: 1 mW.

Now, we can interpret in a new way the meaning of (4.53): the RIN average variance is determined by two terms: one (the 1 factor) is the RIN contribution related to the average power, which in the spectral domain is centered around the DC and it is dominant for low OMD. We will call this term: DC RIN. The second term, called here AC RIN, is proportional to the square of the OMD (that is to m^2A^2) and is related to the contribution of RIN centered on the RF carrier. If the RIN noise floor near the RF carrier was only determined by the average optical power, as it is usually assumed, increasing the modulation power should alleviate the impact of the RIN noise on the detected CNR. But, as we suggested before, (4.53) states that increasing the modulation power does not improve indefinitely the CNR, which is also affected by the AC RIN noise contribution centered around the carrier and proportional to the modulation power itself. Equation (4.53) is strictly valid only for the DFB-SC laser RIN, which can be assumed white over the signal bandwidth. However, the spectral interpretation can be extended to the fibre laser RIN. To prove this fact, we measured and simulated the detected CNR for a 2 GHz modulation as a function of the modulation power. The CNR is calculated and measured integrating the noise floor over 20 MHz bandwidth and calculating the ratio with the detected RF carrier power. We chose a 20 MHz bandwidth to include the RIN peaks of the fibre laser and to match the transmission bandwidth of an IEEE 802.11a OFDM signal. Fig. 4.23 shows two simulations: one with RIN as the only source of noise and the other with RIN, thermal noise and shot noise. The modulator is a MZ at quadrature. The results show that increasing the modulation power actually improves the CNR in as much as this is limited by shot noise, thermal noise and DC RIN. With the fibre laser, above about -5 dBm of modulation power the CNR saturates because it is dominated by the AC RIN peaks around the carrier,

within the 20 MHz bandwidth. If only RIN is considered as source of noise, there is no saturation effect because the AC RIN dominates over DC RIN for all modulation powers: the DC component of the fibre laser RIN is very low around the 2 GHz RF modulation carrier because the RIN decreases as f^{-1} after the relaxation frequency [145], which is at about 2.5 MHz for the fibre laser tested here. The DFB-SC laser CNR only saturates at much higher modulation powers because DC RIN dominates. Note that if a linear modulator were used and $mA < 1$ is respected to avoid clipping, the maximum impact on the CNR due to AC RIN predicted by (4.53) for a perfectly white RIN PSD is about 1.7 dB. At 15 dBm, we measured a CNR degradation of about 3 dB when using the DFB-SC laser, whose RIN can be assumed white: the difference is due to compression from the MZ modulator.

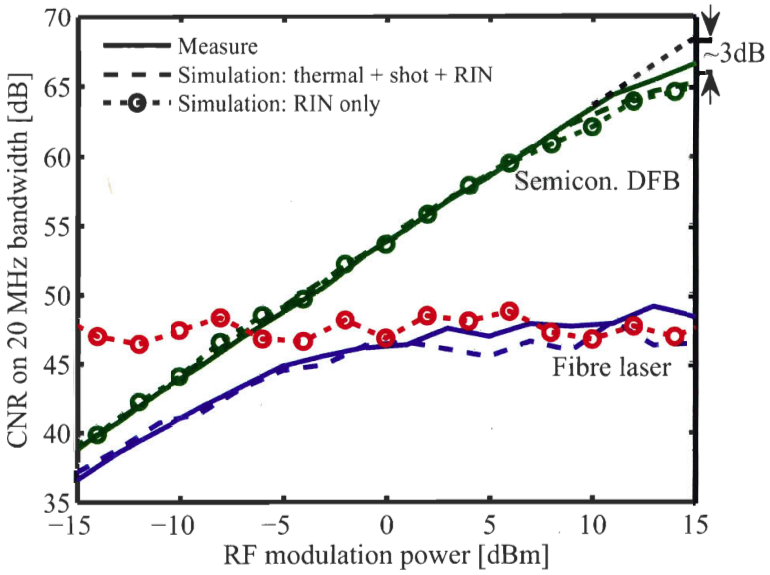

Figure 4.23: Comparison between measured and simulated CNR considering thermal noise, shot noise and RIN. Modulation frequency: 2 GHz. MZ bias at quadrature. With semiconductor DFB: detected average optical power is -0.4 dBm. With fibre laser: detected average optical power is -1.1 dBm: the fibre laser has slightly lower output power than the DFB-SC laser. RF signal source: `HP 83731B`.

We demonstrated that the RIN of fibre lasers may have a significant impact on the CNR of narrowband signals in high OMD links. In the next section we will examine how this affects the EVM of OFDM signals.

4.4.2 DFB-SCs and fibre lasers transmitting OFDM signals

We simulated the impact of RIN on the EVM of 20 MHz wide IEEE 802.11a OFDM signals, with several RF carrier frequencies, using a perfectly linear modulator and considering RIN as the only noise source, so as to isolate its effect. We compared the DFB-SC and fibre laser sources with 10%, 50% and 100% optical modulation depth.

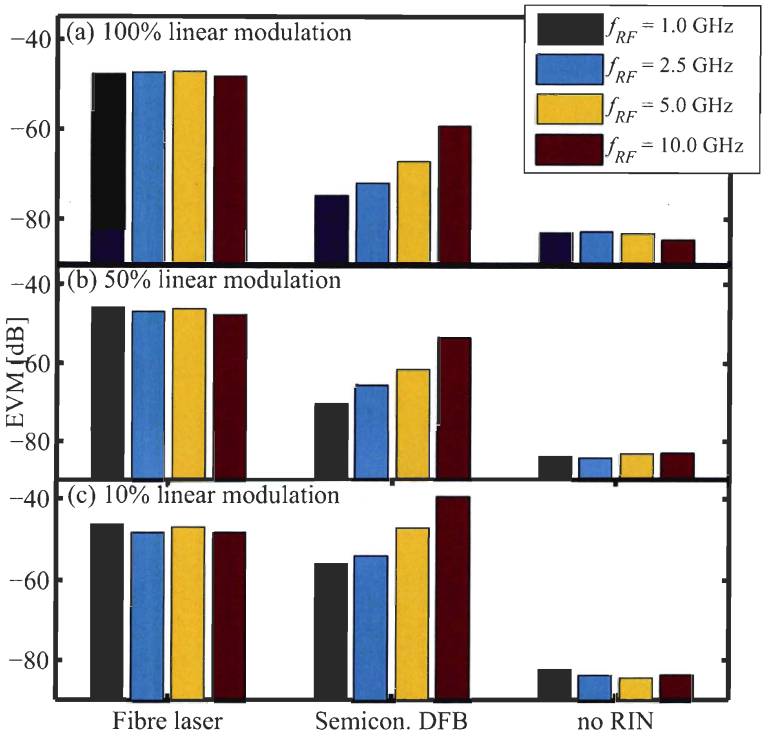

Figure 4.24: RIN-limited EVM. Linear modulation, detected average optical power: 1 mW. Only RIN is considered as source of noise.

As shown in Fig. 4.24, the fibre laser has essentially constant EVM for all frequencies and all optical modulation depths, because AC RIN is always dominant and proportional to the optical modulation depth. Note that, as we described in chapter 2: EVM $\simeq -$CNR, and CNR is given in Fig. 4.23 (simulation with RIN only). This value of EVM is very near to the minimum measurable EVM of the vector signal analyzer `Agilent E4440A`, so we were not able to perform a reliable and trustworthy measurement of EVM to confirm the predictions of Fig. 4.24. Anyway, the fibre laser modeled in the simulation does not appear to be a significant source of EVM and the measurements confirmed that EVM of about -42.9 dB can indeed be reached when using a fibre laser and RF carrier frequency at 2.5 GHz[5]. At the same carrier frequency, the simulation predicts a lower EVM from the DFB-SC laser, and we measured -44.8 dB, limited by the test equipment.

The simulation in Fig. 4.24 also shows that increasing the frequency worsens the EVM given by the DFB-SC laser because the DFB-SC RIN has a peak around 10 GHz. Finally, with a DFB-SC laser, the EVM improves with the OMD following the CNR, as shown before in Fig. 4.23.

In conclusion, the DFB-SC laser RIN noise is lower than the RIN noise from a fibre

[5]Experimental conditions: $P_{RF} = 3$ dBm to avoid distortion form the MZ, MZ at quadrature point, output laser power: 5.7 dBm, pump laser current: 330 mA, Laser temperature: 17°C (thermistor: 14 kΩ).

laser for modulation carrier frequencies far from the RIN peak and for high OMD links. However, both fibre laser RIN and DFB-SC laser RIN can be considered negligible sources of EVM impairment. Multiwavelength distributed Fabry-Perot fibre lasers exhibit a RIN behavior similar to the fibre laser tested in this section [144]. Hence, they can be used as multiwavelength sources for beam-forming applications with OFDM signals.

4.5 Conclusions

In this chapter we described the impact of several optical noise source on the NF and CNR of a link. We introduced a stochastic model to describe the optical noise, which allows to justify the behavior of Brillouin noise contribution in links with modulator bias optimized for maximum link gain. On the basis of this theoretical work, we showed experimentally that the SBS noise can be suppressed by moving the modulator bias towards the minimum transmission point. The noise model is also applicable to the RIN and permits the derivation of the expression of RIN noise variance in links with high OMD. We used these results to evaluate experimentally and numerically the impact of RIN on link CNR. We also evaluated its impact on the EVM of OFDM signals, and we found that it is very low, and almost non measurable. Finally, we compared the NF of optically amplified links and links with an electrical amplifier placed after the detector. We found that optical amplification is typically less noisy than electrical amplification, following the well known rule that low noise figure is obtained if the amplifier is placed as near as possible to the link source. An electrical amplifier placed before the modulator would be even more effective on reducing the noise figure, but it would increase the distortion from the modulator. The effects of link distortion on the OFDM signal are examined in the next chapter.

Chapter 5

Nonlinear effects

As opposed to the wireless transmission channel, the optical channel features a significant nonlinear behavior, which may lead to unacceptable levels of signal distortion in improperly designed ROF links. Nonlinearities may come from all optical link components, as the modulator, the optical amplifier, the fibre and the detector. In our experimental tests with the commercial detectors, conducted in collaboration with Irina Kostko[1] and Mohammad E. Mousa Pasandi, the detector linearity proved to impose a strong limit on how much RF power can be provided by the ROF link [50]. In particular, in [50] we showed no evidence of improvement in the link linearity when comparing an electrically amplified link and an optically amplified link with a commercially available low power photodetector. We chose not to study the design of a linear detection stage: a few other research groups are working on this problem to meet the need for high RF power photodetectors with gigahertz-range bandwidths. Some solutions have been proposed [68, 65, 66, 67]. Noteworthy is the work of Urick and Williams [69], who reported a link employing a high power detector that yields a maximum linear output power of 6 dBm on a 6 GHz bandwidth. Hence, a properly designed detector would be capable of handling high photocurrents and would provide high RF output power without distortion. However, no high power photodetector has reached the market as commercial component yet, and none was available to us for testing. Hence, in this work we assume the detector as linear by properly attenuating the optical power right before detection. This has the only consequence of reducing the output power of the detector but does not limit the validity of the results of this work, in which we focus on the characterization of the impact of the external modulator, optical amplifier and fibre nonlinearities on the transmission of OFDM signals.

A problem rarely discussed in literature is the influence of the modulator bias point on the nonlinear behavior of a ROF link. We focused our attention on this problem, in order to understand if the advantages of bias optimization presented in the previous

[1]Dr. Kostko was with the department of electrical and computer engineering, McGill University, Montreal, QC, Canada.

chapters come with an acceptable link linearity or not. We proceed step by step: first we discuss the distortion introduced by the electro-optical MZ modulator. A detailed understanding of the MZ modulator nonlinearities is important as a reference to which to compare the distortion observed after propagation through other components of the link. Then, we discuss the distortion coming from the EDFA: we show that variations of the average optical power due to bias optimization in the presence of framed or burst-like OFDM signals cause fluctuations of the EDFA gain along the frames, and that results in heavy signal degradation. This problem appears to be the main limit of the bias optimization technique, but we propose two simple and effective methods to circumvent this limitation. Finally, we present a detailed characterization of the distortion at the end of a complete ROF link including the modulator, the amplifier and the fibre. We show that if the modulator bias is properly set out of quadrature, the fibre nonlinearity can partially compensate for the modulator distortion, so that at the link end the total distortion is lower than at the modulator output. We experimentally demonstrate the improvement of IMD3 and EVM, and we quantify them as a function of link parameters like the fibre length, the fibre input power and the modulator bias. We also show that the same value of bias can provide low link losses and low link distortion, thus significantly increasing the link SFDR and maximum output power.

5.1 Methodology, and some considerations on the relations between BER, EVM, HD3 and IMD3

The goal of our study is to identify the link nonlinear effects that most impair the signal EVM and BER, and to find the link operating point that minimizes this impairment. In this section we present our approach to this problem.

Modeling nonlinear systems may be a complicated task, which often requires some simplifications [146, chapter 5]: a common one is to assume a memoryless nonlinearity, as opposed to nonlinearities with memory. The term "memoryless" implies that the output of a device is a function of the input signal at the present instant only, or a function of the input at some fixed delay. This implies also that the transfer characteristics are frequency independent. Memoryless models are very popular and they are fairly accurate to characterize a great variety of devices, generally under the condition that the input signal has a bandwidth sufficiently smaller than the band of operation of the device. Further model simplifications come by recognizing the bandpass nature of the transmitted signal, as opposed to a wide-band system description. Then, the nonlinearity is assumed to be "bandpass": Jeruchim [146, chapter 5] defines a bandpass nonlinearity as one whose output spectrum is concentrated around a carrier frequency if the input spectrum is itself concentrated around a carrier frequency. A standard model for a bandpass nonlinearity is a memoryless nonlinearity followed by a filter centered on the signal RF carrier and wide enough to accommodate for the signal bandwidth.

In presence of a bandpass memoryless nonlinearities, the BER and EVM of OFDM signals can be estimated using analytical or semi-analytical methods. These methods are based on the fact that the OFDM signal is described by a stationary gaussian stochastic process [147]. Then, the received distorted signal can be described as an attenuated replica of the transmitted signal plus a distortion generated noise [148], whose power and PSD are dependent on the specific nonlinear system and on the transmitted signal power. This additional distortion noise is demonstrated to be uncorrelated to the signal [149]. Hence, the receiver BER and EVM can be estimated for a given input signal power as is done for linear system impaired by AWGN. In this case, the EVM and the BER are directly related through the signal to nonlinear noise ratio. This method has been applied by Horváth [150] to calculate analytically the impact of the MZ modulator distortion on OFDM signals. Bo [151] proceeded in a similar way to study the nonlinear response of a laser diode to direct current modulation, which is modeled as a third order polynomial memoryless nonlinearity. In [76], Shi calculates the BER and ACPR for amplitude clipping nonlinearities, and Banelli and Cacopardi [148] calculate the BER stemming from PAs nonlinearities.

These analytical estimations of the signal quality after a nonlinearity are of great interest, but they are hard to extend to more complex nonlinearities that do not respect the memoryless assumption. Hence, the analytical models given above cannot be applied to the nonlinear propagation over a fibre span, whose proper description requires a (bandpass) model with memory, given by the nonlinear Schrödinger propagation equation[2]. Also, the analytical BER estimations are rigorously valid only if the signal has stationary gaussian statistics. In section 5.2, we will show that the analytical model of the MZ distortion underestimates the BER because the IEEE 802.11a frame cannot be assumed to have stationary statistics. For these reasons, in this work we adopted an experimental and numerical Monte Carlo approach to explore the impact of propagation through the nonlinear ROF link on a standard-compliant OFDM signal, and to estimate the EVM and BER as a function of signal power. Indeed, the Monte Carlo approach is known to be time consuming, because a high number of data frames should be transmitted over the link to ensure a good level of confidence on low level of BER. Measurement and simulation times are even greater in the presence of nonlinearities because the data frames transmitted during the test must all be unique and not repeated: the nonlinear noise is waveform dependent and its statistics are biased if a reduced set of test frames is used for the BER and EVM tests. For this reason, the estimation of BER by simulation and measurement becomes impractical for a low amount of distortion. In this case, we preferred the estimation of EVM, which is faster because it does not require the counting of rare error events but evaluates the distortion of the received signal constellation. This is also common practice in the literature, so that our results are readily comparable to other works.

In addition to BER and EVM estimations, useful information on the linearity of

[2]The coupling between dispersion and nonlinearity produces memory in the optical channel, so that the received optical power in a given instant depends on the evolution of optical power before that instant. An optical channel with low dispersion can be assumed memoryless [152].

a link can be extracted by observing the third order harmonic distortion (HD3) and third order intermodulation distortion (IMD3). The test signals for HD3 and IMD3 measurements are much easier to treat analytically, numerically and experimentally than the complete OFDM frame needed for EVM and BER estimation. Still, the HD3 and IMD3 help in revealing the nature of the nonlinearity under test: intuitively, in a nonlinear link, a deterioration in BER and EVM and an increase in HD3 and IMD3 are just different manifestations of the same nonlinear behavior. Indeed, the relation between BER, EVM, HD3 and IMD3 is strictly dependent on the specific nonlinearity under test, and may be very hard to quantify precisely. Hence, in general, a simple HD3 or IMD3 test cannot give the full information on the EVM behavior. Nevertheless, some useful trends on EVM can always be pointed out by observing the IMD3, as supported by the fact that, in a memoryless bandpass nonlinear system, the EVM is impaired by the total in-band noise power contribution from the odd-order nonlinear beating of the signal spectrum with itself. This is shown by Blachman [153], Shi [76], Banelli and Cacopardi [148], and Rodrigues [154]. Hence, odd-order distortion affects the EVM, and the IMD3 is a measure of odd-order in-band distortion generated when the system is driven with two RF tones. Indeed, the IMD3 test gives no information on the statistics of the received signal, but if the IMD3 is low we can reasonably expect to find low EVM also (if the system is distortion limited). As a confirmation, in the simple case of memoryless bandpass nonlinearities, Ku reports a technique that attempts to estimate the EVM using two-tone IMD3 measurements [155]. Throughout this work, we often take advantage of the information derived from simple IMD3 testing as hints to the behavior with complex OFDM signal. For example, IMD3 tests first revealed the possible compensation of MZ third order distortion when the modulator is properly biased and followed by a nonlinear fibre, as explained in section 5.4.

The works of Blachman *et al.* cited above are the basis of a very important observation: the EVM of a narrowband OFDM signal is not affected by even-order distortion beating terms because they fall out of the OFDM bandwidth and are suppressed by the filter included in the bandpass nonlinearity[3]. This is the basis for the whole idea of bias optimization of a MZ modulator, along with the fact that the IMD3 generated by a MZ modulator is not dependent on the modulator bias. This was first reported by Kolner [89], and in the next section we present an experimental verification. Hence, the EVM is not dependent on the modulator bias, in as much as the signal is distortion limited. We repeat and verify this statement in the next section: moving the bias out of quadrature does not affects the signal quality at the output of the modulator, so the bias is a free parameter that can be used, for instance, to increase the link gain, as we showed in chapter 3.

[3]In a real system, this filter is physically included in the receiver.

5.2 Distortions from a Mach-Zehnder modulator

5.2.1 Harmonic and intermodulation distortions

The baseband equivalent of the bandpass memoryless model of a MZ modulator is given in appendix B, equation (B.1). This MZ model is relatively simple and allowed Hilt [156] and Kolner [89] to calculate analytically the harmonic and intermodulation distortion generated by the modulator as a function of driving signal amplitude and bias. In appendix B, we also calculate the harmonic distortion in a more general case than Hilt's work. Odd-order distortion terms (harmonic and intermodulation) from the modulator are well understood to be constant with bias and only dependent on the driving signal amplitude. From equation (B.20b) and from [89], we have the following expressions for HD3 and IMD3:

$$\mathrm{HD3} = \frac{J_3\left(\frac{\pi}{V_\pi}V_v\right)}{J_1\left(\frac{\pi}{V_\pi}V_v\right)} \tag{5.1a}$$

$$\mathrm{IMD3} = \frac{J_2\left(\frac{\pi}{V_\pi}V_v\right)}{J_0\left(\frac{\pi}{V_\pi}V_v\right)}. \tag{5.1b}$$

The IMD3 formula is valid for a driving signal with two tones of equal amplitude. These formulas are easily confirmed by measurements, in as much as the system is modulator distortion limited, and they can be used to calculate the minimum distortion levels exhibited by a system employing a MZ modulator, unless some distortion compensation occurs, as we will show later. Note that figures 3.19, reported in chapter 3 (page 62) demonstrate that HD3 is constant with bias, and Fig. 5.1 demonstrates the same for IMD3. The measurement setup used in this experiment is shown in Fig. 5.2. All simulations and testing with high power signals presented in this section have been performed with an RF carrier frequency of 1 GHz, because the PA available for the experimental setup had limited bandwidth and could not operate at 5 GHz. However, the bandwidth of the modulator was about 10 GHz so we do not expect any difference in the modulator nonlinear behavior between 1 GHz and 5 GHz, both frequencies being well within its bandwidth. This is confirmed by later tests at RF power up to 10 dBm, which can be reached without PA.

In Fig. 5.3, we show the simulated and measured harmonic and intermodulation distortions as a function of modulation power: it is interesting to note that the difference between IMD3 and HD3 is almost constant for all practical values of modulation power and only diverges for very high distortion values, as also shown in Fig. 5.4. Hence, in the range of practical values of modulation power, for which IMD3 and HD3 are much lower than 0 dB, the IMD3 can be calculated from the HD3 by adding 4.77 dB. Also, note that both IMD3 and HD3 increase twice as fast as the input RF power, as

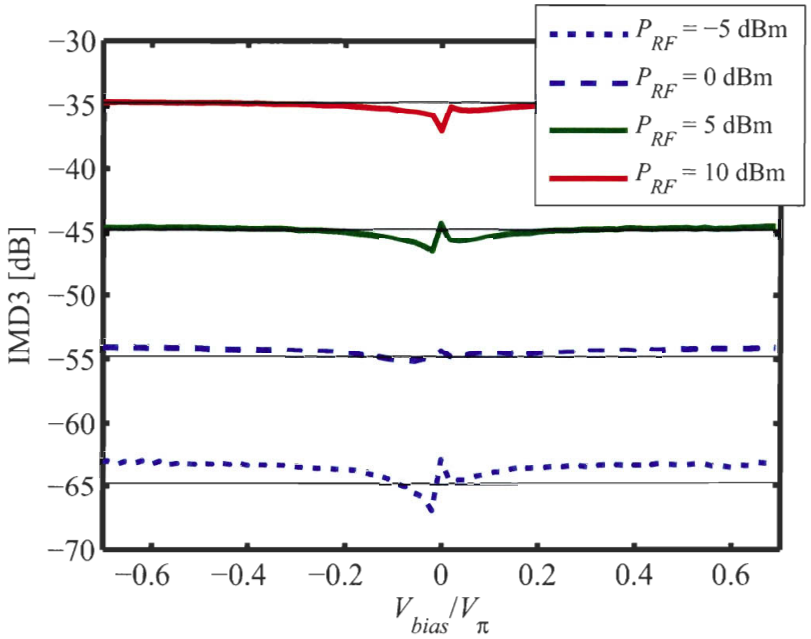

Figure 5.1: Measured IMD3 as a function of the modulator driving power and bias. Modulator efficiency factor $G_{TM} = -5.2\,\text{dB}$, signal frequency 1 GHz. Black horizontal lines are predicted values from equation (5.1b).

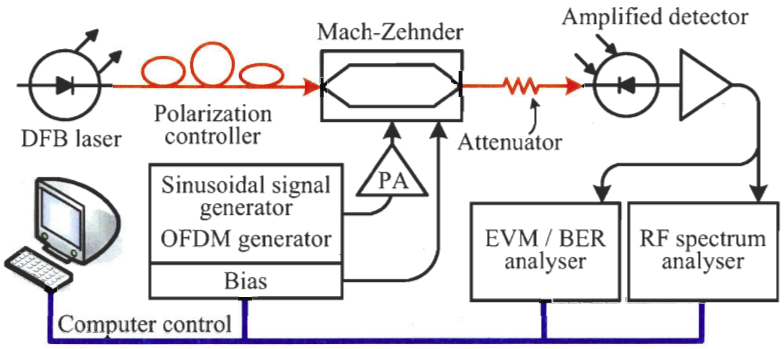

Figure 5.2: Experimental setup for the measurement of the HD3, IMD3 and EVM at the output of a MZ modulator. Orange lines: optical connections; black lines: electrical connections; blue lines: general purpose interface bus (GPIB) connections. Laser: DFB `EXFO`; PA: `Minicircuits ZHL-1000-3W`; amplified detector: `Agilent 11982A`; EVM/BER analyzer and RF spectrum analyzer: VSA `Agilent E4440A`; sinusoidal and OFDM signal generator:VSG `Agilent E4438C`.

expected from their definition.

The curves in figures 5.3 and 5.4 are not dependent on the specific MZ measured in our tests, but can be extended to any $LiNbO_3$-based MZ by referring to the axis scale reported on the top of the graphs, labeled $\langle V_{RF}\rangle/V_{\pi}$. This scale represents the ratio between the average effective voltage amplitude $\langle V_{RF}\rangle$ on the modulator arms and the modulator V_{π}. The former is defined as the amplitude of a sinusoidal signal with the same average power of the OFDM signal, reported on the arm of the modulator to take into account its electrical losses.

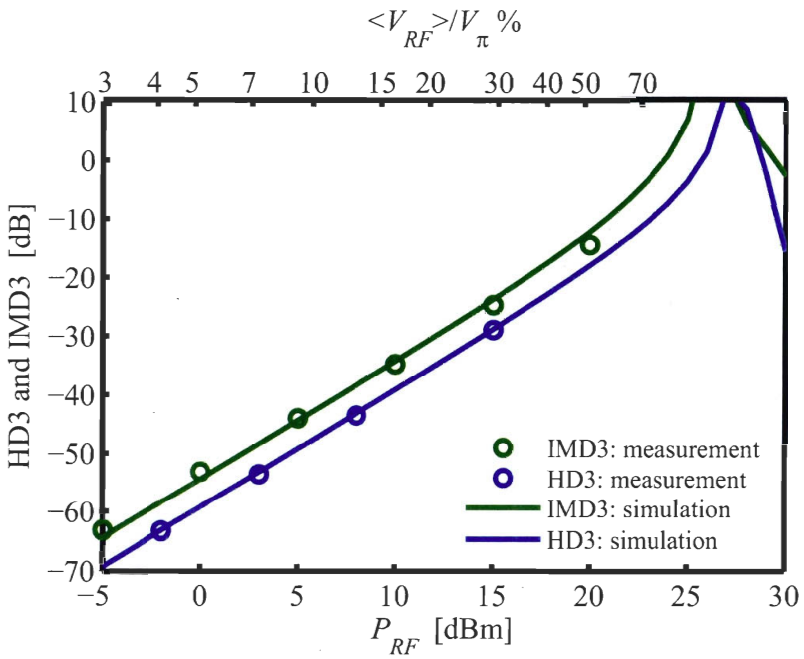

Figure 5.3: Measured and simulated HD3 and IMD3 as a function of the RF modulation power P_{RF} at the output of a MZ modulator biased at quadrature. Modulator RF losses: 5.2 dB.

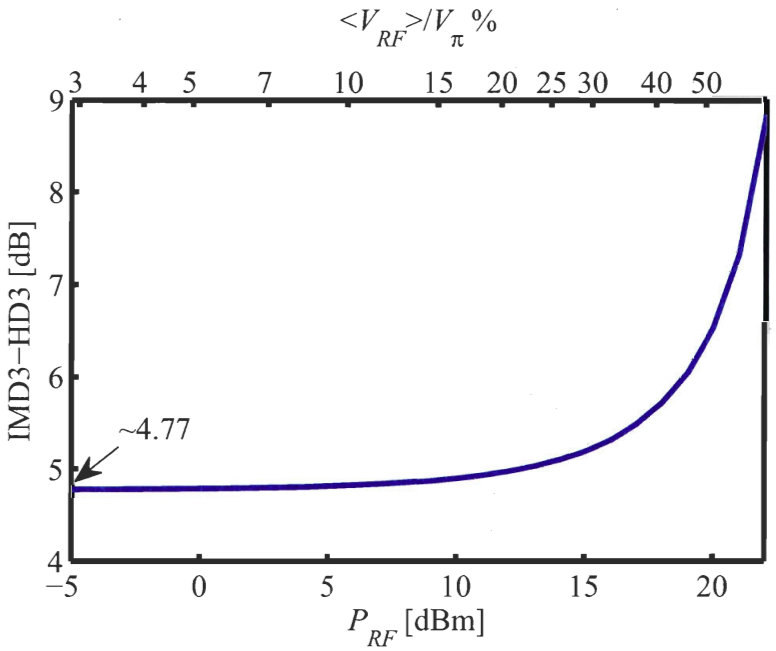

Figure 5.4: Difference between IMD3 and HD3 as a function of the modulation power.

5.2.2 BER characterization

The impact of the MZ distortion on the OFDM BER has been studied theoretically by Horváth [150]. His work is an application of the more general theory developed by

Blachman [153], which allows the calculation of the signal and distortion noise PSD at the output of a bandpass memoryless nonlinearity, assuming a stationary gaussian distribution of the input stochastic process. In bandpass systems, Blachman's theory confirms that the distortion noise within the signal bandwidth is generated only by odd-order intermodulation terms. Blachman's works have been applied to OFDM by Banelli and Cacopardi [148], who first calculated the SNR and BER at the output of a PA modeled with Bessel functions series. Since the MZ output is also described by Bessel functions, it is possible to apply the same theory to estimate the modulator performance with OFDM signals, as is done by Horváth in [150].

Horvath's technique is indeed powerful and noteworthy, but we found some significant discrepancies between its predictions and the BER measured using IEEE 802.11a compliant test signals. We characterized experimentally the MZ distortion limited EVM and BER in the link shown in Fig. 5.2. The source signal was synthesized by a computer controlled vector signal generator (VSG) (`Agilent E4438C`), programmed to generate sequences of standard compliant OFDM frames with random data. The frames were fed to a quadrature biased MZ modulating a 7 dBm DFB laser (by `EXFO`). Some attenuation was added before the detector to avoid saturation and the detected signal was fed to a computer controlled VSA. For each frame, the computer was programmed to compare the sent and received signal constellations and data bits, so to estimate EVM and BER. The measurement results for BER are shown in Fig. 5.5, compared to numerical simulations and theoretical predictions for 64-QAM constellation data distributed on 48 OFDM subcarriers. Note that we were able to predict the BER performance by numerical simulation, whereas the theoretical predictions from [150] underestimate the BER. This is explained by the structure of a standard compliant OFDM stream, which cannot be fully described by a gaussian stationary stochastic process: each frame starts with a training symbol, which is not stochastic and does not have the same PAPR as the data symbols. Also, any distortion noise generated by the training symbol affects the channel compensation algorithm in a way that may increase the probability of error detection along the frame (depending on the performance of the algorithm in presence of noise). Unlike our numerical simulator, Horvath's theoretical predictions do not take into account this effect, and give results similar to a system without training-symbol-based channel compensation. This assertion is supported in Fig. 5.5 by comparing the theoretical BER curve with the numerical simulation of a transmission link where the training symbol is not used to compensate for the channel response but only signal delay and average power loss are compensated (black curve).

To complete the experimental characterization of the MZ limited BER, we report in Fig. 5.6 the measured BER for 64-QAM, 16-QAM and 4-QAM OFDM frames as a function of the modulation power P_{RF}. For each constellation, we report two curves, named coded and uncoded: the former is the BER of an OFDM link employing the convolutional code (rate 3/4) supported by the IEEE 802.11a protocol; the latter is the BER calculated for an uncoded sequence of bits. We take this last as reference because we seek the conditions that allow the optical link to be transparent to OFDM transmission, without exploiting any error correction algorithm.

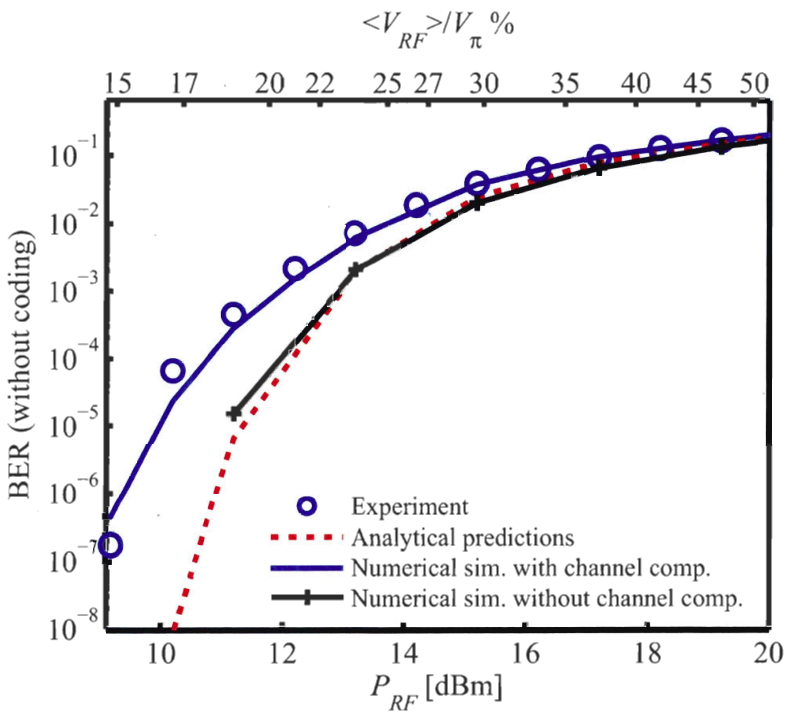

Figure 5.5: Comparison of the measured BER at the output of a MZ with: (1) a numerical simulation of a standard compliant OFDM signal and training symbol based transmission channel compensation; (2) a numerical simulation of an OFDM signal without training symbol, and channel compensation limited to delay and losses; (3) the analytical predictions from Horvath's theory.

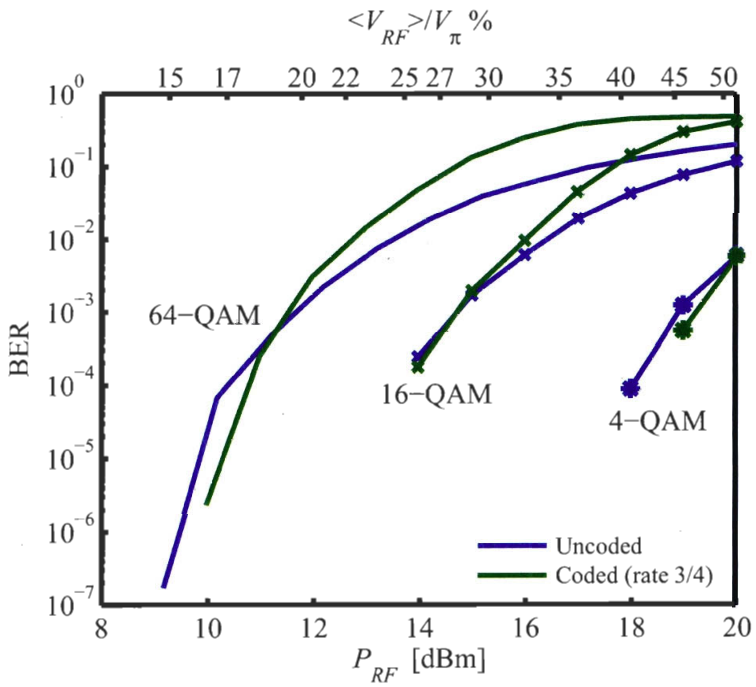

Figure 5.6: Measured coded and uncoded BER at the MZ output as a function of the modulation power P_{RF}. Bias is at quadrature.

The curves in figures 5.6 can be extended to any $LiNbO_3$-based MZ by referring to the $\langle V_{RF} \rangle / V_\pi$ axis. The $\langle V_{RF} \rangle / V_\pi$ must be lower than about 16% to ensure an uncoded BER lower than 10^{-6}, for the most demanding 64-QAM constellation. Note that this result is not dependent on modulator bias, in as much as the system is limited by modulator distortion.

5.2.3 EVM characterization

We measured and simulated the EVM as a function of the modulator bias and input RF power. As we discussed before, one important feature of the MZ nonlinear behavior is that the EVM is constant with bias, in as much as it is distortion limited. This is confirmed by Fig. 5.7: EVM is constant over a large range of bias values. However, at the minimum and maximum transmission points, the signal becomes noise limited because it is suppressed by the modulator.

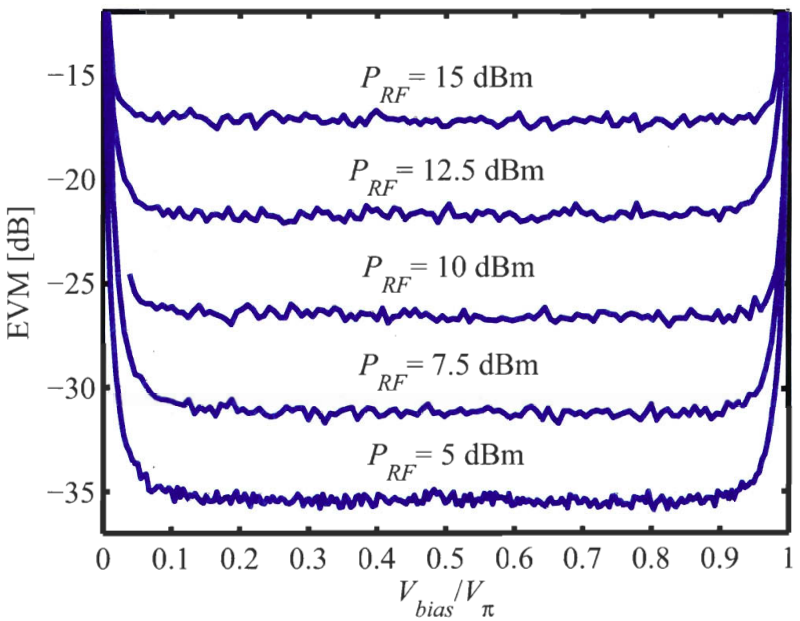

Figure 5.7: Measure of EVM at the MZ output as a function of bias and modulation power P_{RF}.

Measured and simulated EVM as a function of modulation power are shown in Fig. 5.8: note that EVM is not dependent on the order of QAM modulation adopted by the signal. The most important result given in this graph is the maximum $\langle V_{RF} \rangle / V_\pi$ that allows to respect the maximum EVM imposed by the IEEE 802.11a protocol: for 64-QAM OFDM modulation, the maximum acceptable EVM is -25 dB: reached for about 10 dBm of average power at the input of the tested modulator, corresponding to about $\langle V_{RF} \rangle / V_\pi = 16\%$: the same value providing uncoded BER lower than 10^{-6}.

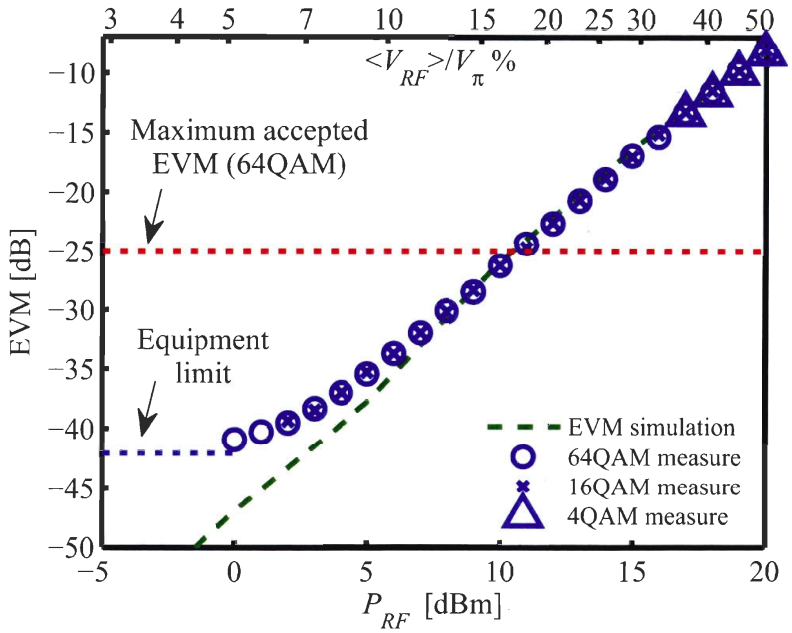

Figure 5.8: Measure and simulation of the EVM as a function of the modulation power P_{RF}.

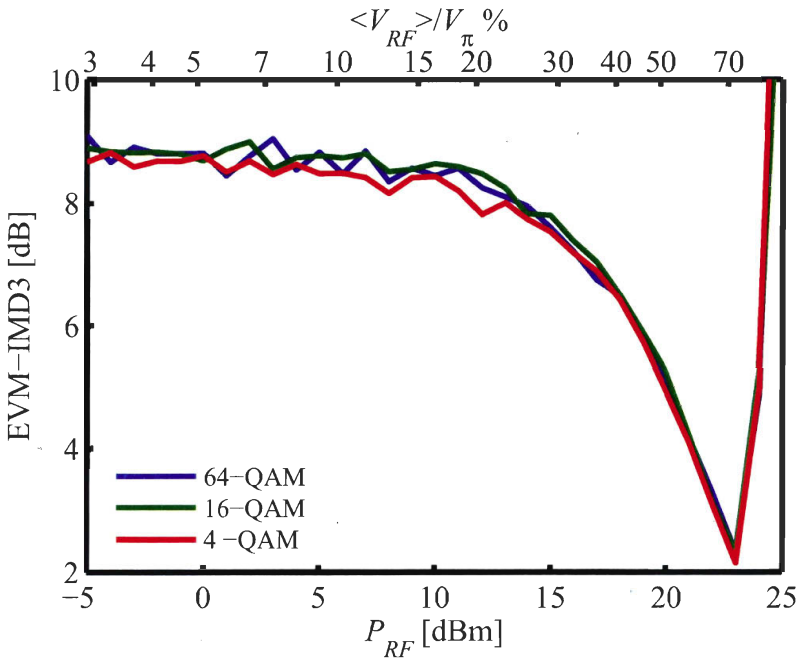

Figure 5.9: Difference between EVM and IMD3 values as a function of the modulation power P_{RF} and the constellation type.

We already discussed that EVM and IMD3 are related, so that a decrease in IMD3 can be taken as a hint that EVM is also decreasing. Quantitatively, this relation depends on the nonlinearity and on the signal power. For a $LiNbO_3$-based MZ, the EVM-IMD3 difference is reported in Fig. 5.9 as a function of signal power and QAM order. For all practical modulation powers, the EVM is about 9 dB higher than the IMD3. This

graph, along with Fig. 5.4 is useful for the link designer to estimate the MZ-limited EVM from the HD3 or IMD3 values, which may be easier to measure if the OFDM signal generation and analysis equipment is not available.

To our knowledge, a complete experimental characterization of the impact of a MZ modulator on EVM and BER of a IEEE 802.11a compliant OFDM signal has never been reported in the literature. Kurt [157] gives curves of BER for QPSK OFDM in a system with a MZ modulator, multimode fibre and additive phase noise on the signal, but does not extend his work to 64-QAM signals. Islam [158] and Singh [159] both give a simulated curve of EVM versus MZ modulation index, but their results are not exactly coincident and are underestimated with respect to our measurements; and they do not report BER measurements. Mitchell [34] also gives one measured EVM curve at quadrature for 16QAM OFDM signals, but the curve is given as a function of modulator input power and not as a function of $\langle V_{RF} \rangle / V_\pi$, so that it is not easily comparable with other results. Hence, to our knowledge the measurements reported in this section are the first complete characterization of the performance of 802.11a compliant OFDM signals limited by MZ modulator distortion.

In appendix G, we briefly report on the behavior of electroabsorption modulators (EAMs) and SOA used as modulators: we focus on the dependence of their behavior on voltage (or current) bias to understand if a bias optimization technique can be used with these modulators.

5.3 Distortions from the erbium-doped fibre amplifier

In the experimental links presented in chapter 3 and 4, the MZ modulator is followed by an EDFA. We have already discussed that EDFAs may be used in ROF links to increase the RF gain and to improve the noise figure. We have also shown that the performance of amplified ROF links used with narrowband RF signals take advantage of the optimization of the modulator bias. In this section, we give details on the impact of the EDFA on the link linearity, particularly if the modulator bias is shifted out of quadrature to optimize the link gain.

In the literature, the EDFAs are a known source of second order distortion when fed by a chirped optical signal [160, 161, 162]. This is explained by the fact that the EDFA features a gain that varies with wavelength, i.e., a gain tilt. When the EDFA is fed by a chirped signal, the combination of chirp and gain-tilt causes generation of second-order distortion. Third order nonlinearities form the EDFA are rarely discussed in the literature, and found to be negligible in [160]. In the absence of signal chirp, the other possible source of EDFA nonlinearity is gain variation as a function of the input power. However, the gain does not respond to input signal variations at speeds faster than a few hundreds of kilohertz because of the long EDFA gain saturation time and

gain recovery time (100 µs–350 µs) [163, 164]. Hence, no impact of the EDFA on the link third order distortion is expected when using unchirped modulators and transmitting analog optical signals with carrier frequency in the gigahertz range. Indeed, this is confirmed by our experimental tests, whenever the power of the modulating signal is kept constant. However, in this section we will show that the bias optimization may couple power fluctuations of the RF modulating signal to the mean optical power at the MZ output. Slow variations in optical power interacts with the gain dynamics of the EDFA and degrades the quality of the transmitted signal. We illustrate this effect for 802.11a/g signals, whose framed or burst transmission strategy implies a difference between the power levels used when transmitting a frame versus waiting in the idle state. It is shown that, in an amplified ROF link used for transmission of such signals to a remote antenna, the bias optimization may cause a heavy signal quality penalty due to the dynamic response of the EDFA. We also show that the penalty is significant even if the idle time between frames is much shorter than typical gain saturation/recovery time of EDFAs. This appear to be a serious disadvantage of the bias optimization technique. However, we propose and verify experimentally two simple electrical and optical compensation schemes, based on mean power clamping at the modulator output, which are capable of restoring the transmission quality. This work has been published in [165].

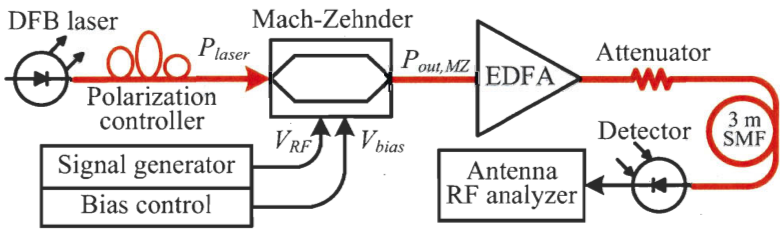

Figure 5.10: Setup of the experimental link for the measurement of distortion at the output of an EDFA. Orange lines: optical connections. EDFA: `JDS OAB1552+1FAO`.

The experimental link used in this work is shown in Fig. 5.10, where the output of a DFB laser is intensity modulated by a MZ and amplified by an EDFA. As it was not our goal to study the effects of fibre dispersion or nonlinear response, the signal was propagated over only 3 m of SMF. A detector is connected to an RF VSA (`Agilent E4440A`). The received optical power is fixed at -6 dBm by an attenuator to avoid detector saturation. The modulating signal is a 64-QAM OFDM modulated carrier at 1 GHz. The carrier frequency is limited by the amplifiers used in the signal generation setup, but we do not expect any difference in the link behavior for higher carrier frequencies, as long as we stay within the modulator bandwidth. Apart from the carrier frequency, the signal complies with IEEE 802.11a protocol, and its structure is shown in Fig. 5.11: it is divided in frames with a synchronization symbol, a training symbol, and an OFDM payload. Between two frames, the transmitter is in idle state and the RF carrier is suppressed. In this work, the idle time t_{idle} between the frames is varied between 0 µs and 500 µs.

We measured the EVM and RF power after detection versus modulation power P_{RF}, with bias optimized for maximum RF gain and $t_{idle} = 0$ µs, as shown in Fig. 5.12.

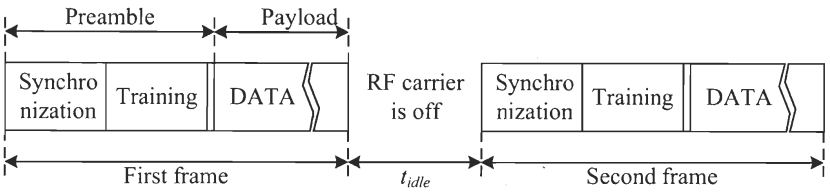

Figure 5.11: Structure of an OFDM sequence with idle time t_{idle} between frames.

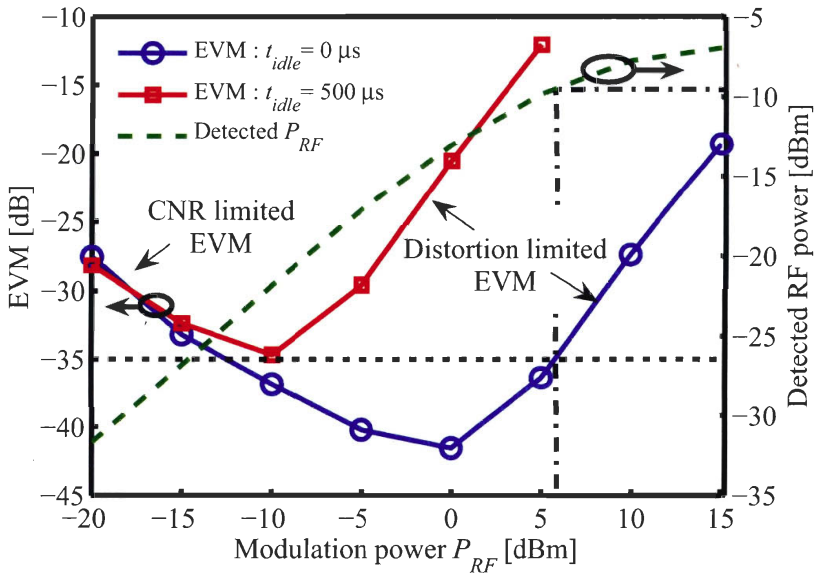

Figure 5.12: Variation of EVM and detected RF power versus modulation power P_{RF}. EVM is measured for $t_{idle} = 0\,\mu s$ and $t_{idle} = 500\,\mu s$. Frames are 500 µs-long. Bias is optimized at each point in order to maximize the detected RF power. Dotted line represents the EVM target value at -35 dB, and dash-dotted line indicates the maximum detected RF power at target EVM. $P_{laser} = 4\,dBm$. Other link parameters are given in table 4.1, page 92.

At low modulation powers, the EVM is limited by the CNR at the receiver, which is kept constant by fixing the received optical power. At high modulation powers, the EVM is limited by the third order distortion from the MZ. This is confirmed by the observation that EVM increases two times faster than P_{RF}, and that for $P_{RF} > 0\,dBm$ the EVM follows the curve given by Fig. 5.8. While the 802.11a protocol fixes the maximum EVM at -25 dB, a 10 dB margin is desirable and an EVM of -35 dB is chosen as a target. Thus, if $t_{idle} = 0\,\mu s$, Fig. 5.12 suggests an acceptable modulation power range from -12 dBm to 5 dBm, with a maximum detected RF power of -10 dBm. If $t_{idle} = 500\,\mu s$, the EVM target is only approached at much lower received RF power levels, and the benefits of bias optimization and optical amplification on the link RF gain are greatly reduced.

The EVM penalty with long t_{idle} is a result of the interaction between the framed nature of the 802.11a/g signal and the MZ bias optimization, and does not occur if modulator bias is fixed at quadrature. In order to demonstrate that no penalty is observed at quadrature, we show in Fig. 5.13 the measured EVM as a function of the

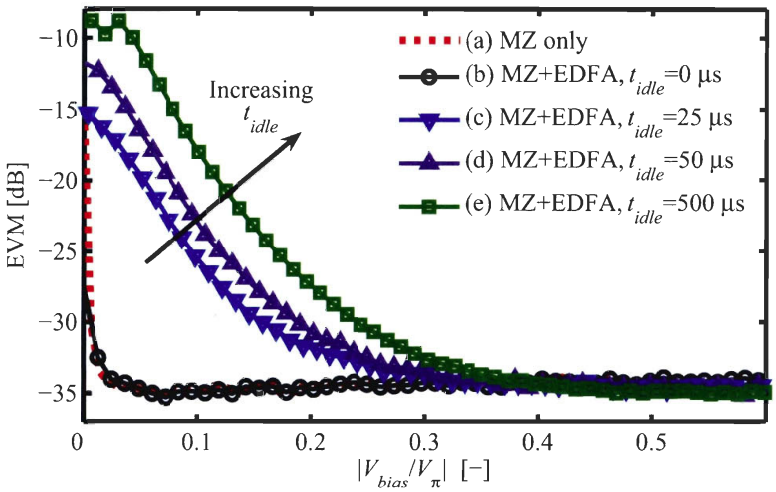

Figure 5.13: EVM versus bias for increasing idle time. Curve (a) is without EDFA and it is the reference for minimum measurable EVM with $P_{RF} = 5\,\text{dBm}$.

modulator V_{bias} at $P_{RF} = 5\,\text{dBm}$. The curve (a) in Fig. 5.13 represents the EVM measured after the MZ without EDFA. This is a reference level because the EVM is fixed by the third-order distortion from the modulator itself, and we already discussed that only odd-order terms can affect narrowband signals such as those used by IEEE 802.11a. Odd-order nonlinearities are constant with bias, and so is the EVM. Curve (b) in Fig. 5.13, measured using the EDFA and $t_{idle} = 0\,\mu\text{s}$, is indistinguishable from curve (a), thereby confirming that EDFAs do not add signal distortion. With $t_{idle} > 0\,\mu\text{s}$ we obtain curves (c)-(e), for which the EVM at quadrature stays around 35 dB. With bias approaching zero, the EVM grows up rapidly due to the high optical carrier attenuation from the low biased MZ, which degrades the link CNR. At $V_{bias} = 0.08V\pi$, which in this test is the optimum bias for maximum link RF gain, the EVM reaches the maximum value accepted by 802.11a/g (-25 dB) with a t_{idle} as low as 25 µs. This is at least four times lower than typical gain saturation time for EDFAs (100 µs–350 µs). This phenomenon is explained by the dynamic response of the EDFA to slow variations of the mean optical power at its input. This is a known source of errors in packet-based and WDM digital optical networks [166].

In a ROF link with bias optimization, the mean optical power $< P_{out,MZ} >$ at the EDFA input depends on the modulating voltage V_{RF} as given by equation (3.18), reported here for convenience of the reader:

$$\langle P_{out,MZ} \rangle = \frac{P_{laser}}{2}\left[1 - J_0\left(\frac{\pi V_{RF}}{V_\pi}\right)\cos\left(\frac{\pi V_{bias}}{V_\pi}\right)\right], \tag{5.2}$$

where P_{laser} is the power at MZ input and J_0 is the zero-order Bessel function of the first kind. Thus, the EDFA gain depends on the presence of a frame, when V_{RF} is fixed by the modulation power P_{RF}, or absence of a frame, when $V_{RF} = 0$. Note that in chapter 3 we showed that bias optimization is most effective when the laser power heavily saturates the amplifier at quadrature bias. Then, the link gain is optimized for a relatively narrow range of bias values, far from quadrature. In these conditions,

the negative impact of gain dynamics is also most evident because the dependence of $\langle P_{out,MZ} \rangle$ on P_{RF}, modeled by the $J_0\left(\frac{\pi V_{RF}}{V_\pi}\right)$ term in equation (5.2), are amplified by $\cos\left(\frac{\pi V_{bias}}{V_\pi}\right)$ approaching the unity.

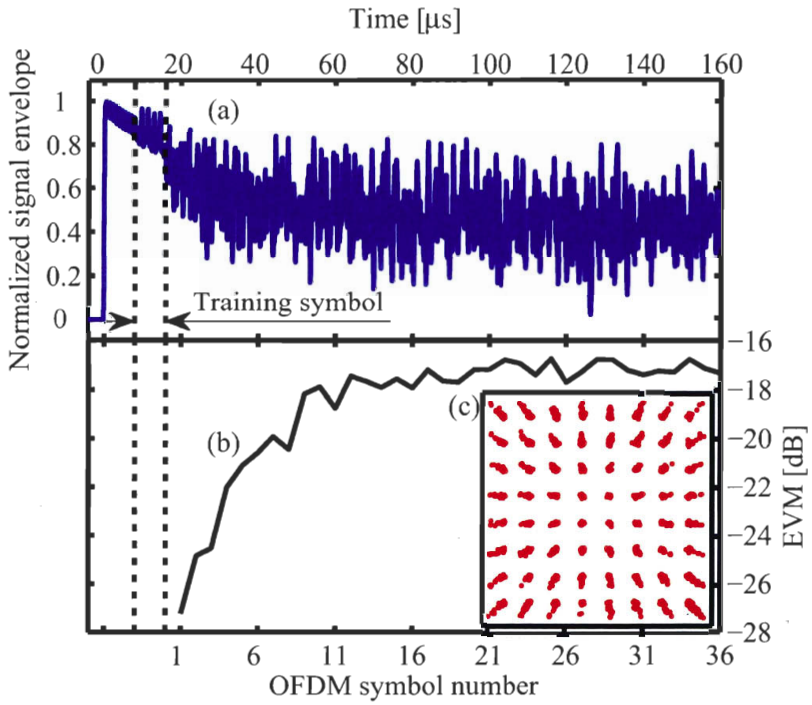

Figure 5.14: (a) Normalized envelope of the detected OFDM signal at the beginning of a frame. (b) Evolution of EVM along the frame. (c) Detected constellation for the whole frame. The location of the 8 µs-long training symbol is identified by dotted lines.Time and OFDM symbol number are in scale. OFDM symbols are 4µs-long.

The influence of the dynamic response of the EDFA at the beginning of a frame is shown by Fig. 5.14, curve(a), where the envelope of the detected RF signal is plotted for $V_{bias} = 0.1V_\pi$ and $t_{idle} = 500\,\mu s$. With such a long idle time, the beginning of the OFDM frame is amplified by an unsaturated EDFA with high available gain. As the frame progresses, the gain is depleted and the power of the received signal decreases, leading to an EVM dominated by amplitude (not phase) noise. Note that with $t_{idle} = 0\,\mu s$, the EDFA is always saturated because the modulation signal has constant nonzero power. Hence, the signal sees constant gain. The EDFA gain variations at the beginning of each frame cause high EVM penalty because the 802.11a/g protocol uses the training symbol to calibrate the decoding process and to remove the transmission channel phase and amplitude response, which is assumed to be constant along the frame. In this case, this assumption is not valid, so that the amplitude error on the training symbol is spread all along the frame and affects the entire payload. This explains the high EVM penalty observed in Fig. 5.13 for relatively low values of idle time. The evolution of EVM with the OFDM symbols along the frame (Fig. 5.14, curve b) confirms this interpretation. The dotted lines in Fig. 5.14 identify the position of the training symbol, which appears 8 µs after the beginning of the frame. The detected constellation also shows that

there is no significant error on the symbols phase (Fig. 5.14, inset c). Mitchell [34] first observed the distortion caused by the optical amplifier dynamic response in an experimental analysis of the propagation of 802.11a signals on a 23 km ROF link with external modulation and optical amplification. In his experiment, the constellation at the link end presents an amplitude distortion similar to Fig. 5.14, inset (c). However, he attributed the measured BER degradation to the amplifier noise: we think this is not correct because EDFA noise would rather spread the received constellation points uniformly around the optimal value and not compress their amplitude. A comparison of the effects of AWGN and amplitude compression on the constellation is given in Fig. 5.15.

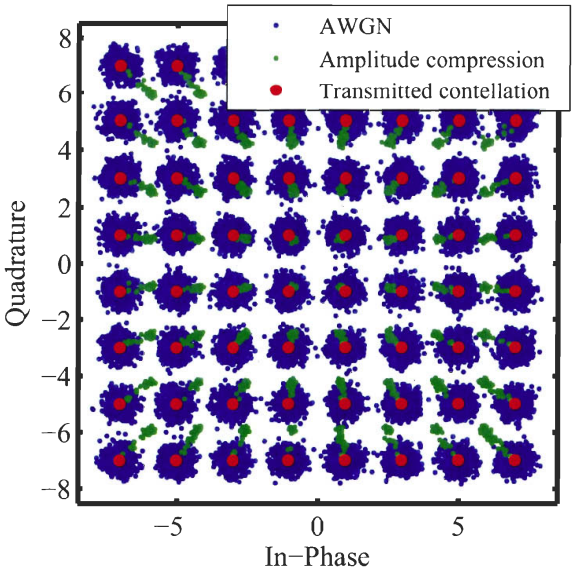

Figure 5.15: Example of the effect of AWGN and amplitude compression on the constellation.

Standard gain clamping of the EDFA could be used to counteract the EVM penalty. However, less optical gain would be available and the effectiveness of bias optimization would be greatly reduced because gain clamping keeps constant the EDFA saturation level: from chapter 3, we remember that higher RF gain and detected RF power are achievable when the bias optimization reduces the EDFA saturation level.

As the signal generator knows when a frame is active, this knowledge can be used to clamp the optical power at the EDFA input instead of clamping the EDFA gain. This is implemented by modifying the experimental link as shown in Fig. 5.16a: an optical switch, controlled by a "frame off" signal from the generator, is used to provide a saturating signal to the EDFA when the frame is not active. The power to be added can be calculated using (5.2) for an infinite extinction ratio MZ. In Fig. 5.17a we show the calculated variation of the optical power at EDFA input with and without an active frame. The power difference between these two states is the "correction power" to be coupled into the EDFA input. In Fig. 5.17b we show that the power correction can cancel the EVM penalty, thus confirming that penalty comes from modulation of the optical power at the EDFA input. Note that the system is sensitive to relatively

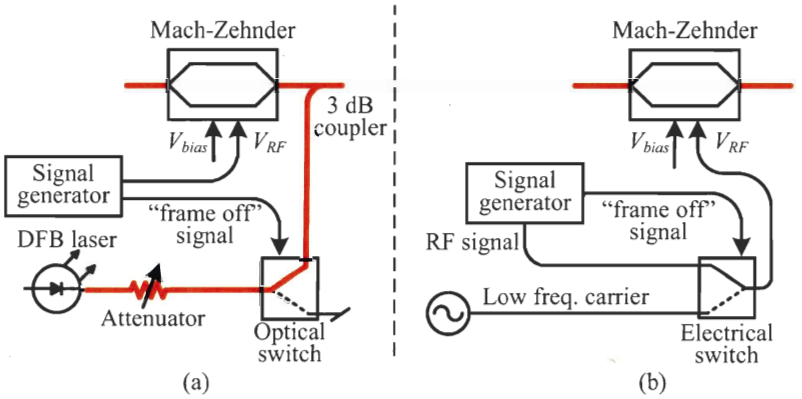

Figure 5.16: Modifications of the experimental link of Fig. 5.10 to clamp the optical power at EDFA input. (a) A second laser is switched into the EDFA when the packet is inactive. (b) A low frequency signal is used to modulate the optical power when the packet is inactive. Orange lines: optical connections. Optical switch: `Dicon GP700`; electrical switch: `Hittite HMC347LP3` on evaluation board; Low frequency carrier generator: `Agilent 33120A`.

small variations of optical power: for $V_{bias} = 0.1V_{\pi}$ and $t_{idle} = 25\,\mu s$, a power difference between the "frame active" and "frame inactive" states of 1.4 dB is sufficient to give an EVM penalty of about 20 dB.

The same results can be obtained without the additional cost of a second laser by clamping the optical power electronically. We modified the link as shown in Fig. 5.16b: when the frame is inactive, a low frequency RF carrier is routed to the MZ RF input. We tested this solution for a carrier frequency as low as 1 MHz: if the RF power of the carrier is equal to the average power of the 802.11 signal, the EDFA does not sense any variation of optical power at its input and the EVM penalty is also canceled. The low frequency carrier can be easily filtered out at the receiver. In Fig. 5.17b we compare the optical and the electrical methods, showing that both are equally effective in suppressing the EVM penalty.

In conclusion, we proved that dynamic response of the EDFA is a source of EVM penalty when bias optimization is used. Power clamping at EDFA input by optical or electrical means can avoid this penalty.

The results presented above suggest that the use of a bias feedback circuit to clamp the MZ bias at a desired value may cause distortion. In fact, the bias feedback circuits are usually based on a low frequency (f_{bias}) amplitude modulation of the optical carrier. The harmonics of f_{bias} are sensed and locked to a fixed value by the feedback circuit in order to stabilize the desired bias point. If f_{bias} is on the order of a tenth of a kilohertz or less, the EDFA gain may react to the amplitude modulation and cause some distortion to the detected signal. Hence, care must be taken to select f_{bias} high enough to avoid interaction with the EDFA. The amplitude of the modulation must also be kept as low as possible to avoid an increase in link distortion [167]. In our measurements, we did not use a bias feedback circuit.

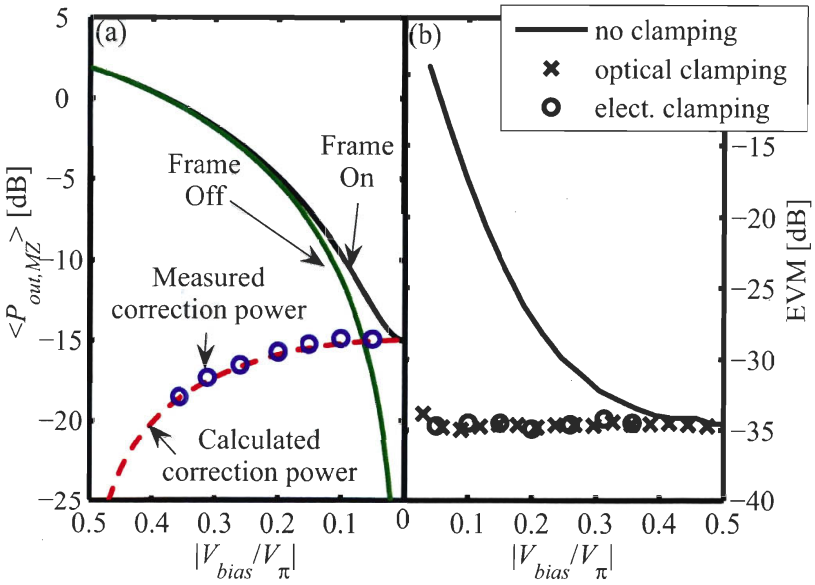

Figure 5.17: (a) Calculated (dashed lines) and measured (circles) correction power needed to null the EVM penalty. Solid lines: Optical power at EDFA input with frame on and off. (b) Variation of EVM with respect to MZ bias for $t_{idle} = 500\,\mu s$, with and without correction by optical power clamping.

5.3.1 Simulation of EDFA dynamic response with $t_{idle} = 0\,\mu s$

We said that, when the bias is out of quadrature, the envelope of the OFDM signal is coupled to the average power. Any fluctuation of the average power can cause variations of the EDFA gain and, consequently, signal distortion. This is true throughout the OFDM frame and, in principle, could cause some increase of the detected EVM even when there is no separation between the transmitted frames, i.e., t_{idle} is equal to $0\,\mu s$. Indeed, we never observed experimentally such an increase of EVM at the output of the EDFA, but we decided to explore this topic by simulating the dynamic behavior of the EDFA with low biased OFDM signals. The EDFA dynamic simulator is based on the reservoir model published by Bononi and Rusch in [168]. We adapted the model parameters to simulate an amplifier with the same steady-state saturation output power and small signal gain as the one used in our experimental tests. Then, we simulated the EVM at the output of the EDFA as a function of the modulator bias and OFDM signal power. In Fig. 5.18 we show the difference in EVM with and without the EDFA. The results confirm that some worsening of the EVM is observed for low bias, but the EVM is dominated by distortion from the MZ at all bias values for modulation powers higher than 5 dBm. In particular, the EVM is MZ distortion limited for the values of bias that give maximum RF gain in our system, unless very low modulation power are used. However, note that the minimum measurable EVM is limited by the VSA and VSG, and so it is not possible to properly measure the EVM for very low modulation powers.

This simulation confirms that the EDFA amplifier has no impact on the link EVM

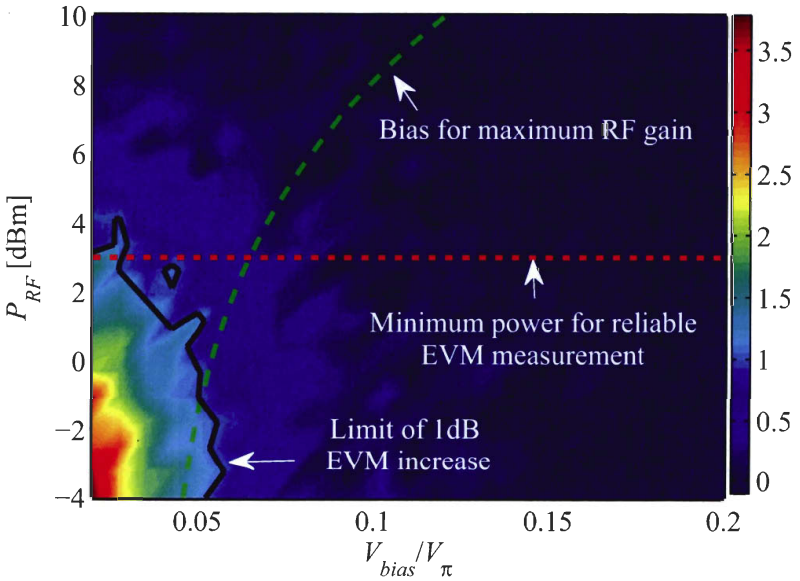

Figure 5.18: Difference between EVM after the EDFA and EVM before the EDFA, taking into account the EDFA dynamic response to fluctuations of the input power. Modulation frequency 1 GHz; modulator RF losses: 5.2 dB; maximum EDFA input power: 4 dBm; EDFA model parameters: pump wavelength 980 nm, signal wavelength 1550 nm, pump power 18.4 dBm, fluorescence time 10.5 msec, EDFA length 40 m.

for all practical values of modulation power and bias. However, it also raises interesting questions about the use of SOAs for amplification in systems with bias optimization. SOAs exhibit a faster dynamic response then EDFAs, and may react to power variations which occur along a frame, giving a significant EVM penalty. We did not explore this topic, but it is indeed open for future work.

In the next section we present original results on the distortion of a complete link with modulator, amplifier and fibre.

5.4 Distortion from the single mode fibre

The propagation over a dispersive and nonlinear optical fiber is an important source of signal distortion in ROF links. The early literature on this topic focused mainly on CATV ROF links, which are sensitive to second order distortion stemming from the interplay between dispersion, fibre self-phase modulation (SPM) and laser chirp [169, 170, 171, 172]. In the same context, Phillips [173] gives analytic expressions for second and third order harmonic distortion, assuming chirped direct modulation of a laser and a dispersive nonlinear fibre. Externally modulated links with a MZ modulator have been studied by several authors. For such links, the analytical expression of the electric field at the output of the modulator allows the calculation of the impact of fibre dispersion on the link harmonic distortion, including also the modulator bias as

a parameter (Corral [174], Cheng [114] and Fuster [113]). Cho extended the analysis to IMD3, giving analytical expressions of the power of the intermodulation distortion terms from a dispersive MZ-modulated link [175]. Some works also include the fibre nonlinear effects, but typically assume linear modulation or fixed modulator bias. For example, Gopalakrishnan [176] reports that fibre distortion limits the linearity of externally modulated analog CATV links at propagation distances greater than 90 km, but he uses a linearized optical modulator. Ramos studies the impact of fibre SPM on the signal power fading associated to dispersion (described in chapter 3), reporting a decrease in power penalty if the appropriate amount of power is launched on the fibre [177]. However, he also assumes linear modulation. Again assuming a linear modulator, Ramos studies the impact of fiber SPM on system second order harmonic distortion, and he suggests that optical phase conjugation can improve the link linearity [178, 179]. Willems reports measurements of the second order distortion of a CATV 50 km-long link, but the modulator is biased at quadrature [180].

To our knowledge, the impact of modulator biasing in conjunction with both fibre nonlinearities and dispersion is still an unexplored topic in the literature. In this section, we report our theoretical and experimental work on the linearity of short length (< 50 km) ROF optical links employing a zero-chirp MZ modulator, an optical amplifier and standard SMF. We focus on the effect of modulator bias on the link IMD3. We also report numerical and experimental results on the link EVM when an IEEE 802.11a signal is transmitted. Part of this work has been published in [181]. We start by presenting a simple analytical model that can be used to calculate the harmonic and intermodulation distortion at the link end from the shape of the received optical spectrum. Based on this model, we discuss our experimental results on IMD3 minimization after a 10 km fibre link, observed when the modulator bias is moved off quadrature. Finally, we report simulation and experimental results to prove that this technique leads to improved link EVM with respect to a standard quadrature biased link.

5.4.1 Analytical calculation of link HD3 and IMD3 from the received optical spectrum

Let us assume that the modulation signal is a pure sinusoidal signal with pulsation ω_{RF}. Then, in the most general form, the baseband equivalent of the electric field at the detector can be described as the sum of infinite spectral elements at $\pm n \cdot \omega_{RF}$:

$$E(t) = Ce^{i\varphi_C} + \sum_{n=1}^{\infty} \left[S_{L,n} e^{i\left(-n\cdot\omega_{RF}t+\varphi_{S_{L,n}}\right)} + S_{U,n} e^{i\left(n\cdot\omega_{RF}t+\varphi_{S_{U,n}}\right)} \right], \qquad (5.3)$$

where C and φ_C are the amplitude and the phase of the optical carrier, $S_{U,n}$ and $\varphi_{S_{U,n}}$ are the amplitude and phase of the n order upper sideband, and $S_{L,n}$ and $\varphi_{S_{L,n}}$ are amplitude and phase of the n order lower sideband, as defined in Fig. 5.19. The photodetector output current $i(t)$ is equal to:

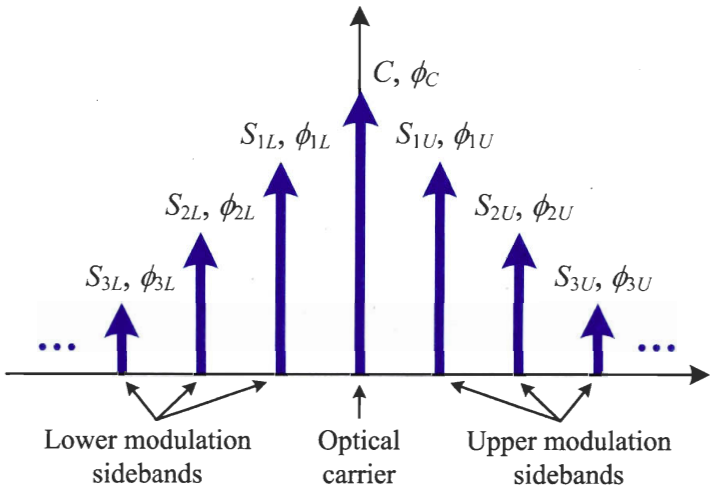

Figure 5.19: Definition of C, φ_C, $S_{U,n}$, $\varphi_{S_{U,n}}$, $S_{L,n}$ and $\varphi_{S_{L,n}}$.

$$i(t) = \mathcal{R} \cdot \frac{1}{2} |E(t)|^2, \tag{5.4}$$

where $\mathcal{R}$ is the detector responsivity and the $\frac{1}{2}$ factor is due to the baseband representation of the electric field [80, page 152]. When $|E(t)|^2 = E(t) \cdot E^{\star}(t)$ is calculated from equation (5.3), we find that the detected signal is the superposition of a large number of sinusoidal terms at frequency $n \cdot \omega_{RF}$, with $n \geq 0$. Each term at $n \cdot \omega_{RF}$ is determined by the beating of two elements of the spectrum of $E(t)$, spaced apart by $n \cdot \omega_{RF}$. The total detected amplitude of a given frequency is then the coherent sum of all the terms at this frequency. For example, in Fig. 5.20, we show the first three terms that add up to generate the detected third order harmonic, resulting from the beating of 6 elements of the optical spectrum. Note that we will maintain consistently this terminology throughout the text, to avoid confusion: the optical spectrum is composed of "elements", whose beating generates "terms", or contributions to the total detected signal power at a given frequency.

Typically, in a DSB system we can assume a symmetry in the amplitude of the electric field spectrum: $S_{L,n} = S_{U,n} = S_n$, which holds in as much as any optical filtering is symmetrical in amplitude with respect to the optical carrier. Then, if we develop the (5.4) for the fundamental frequency ω_{RF}, we find [4]:

$$\begin{aligned} f_{\omega_{RF}}(t) \propto & 2CS_1 \cos(\varphi_c - \alpha_1) \cos(\omega_{RF} t + \beta_1) + \\ & + 2 \sum_{n=1}^{\infty} S_n S_{n+1} \cos(\alpha_n - \alpha_{n+1}) \cos(\omega_{RF} t - \beta_n + \beta_{n+1}), \end{aligned} \tag{5.5}$$

[4] As a verification, we applied this equation to the expression of the spectrum of a MZ modulator given in appendix B, equation (B.15), and we found the first harmonic of the instantaneous optical power, given by equation (B.16). The proof is reported in appendix B.

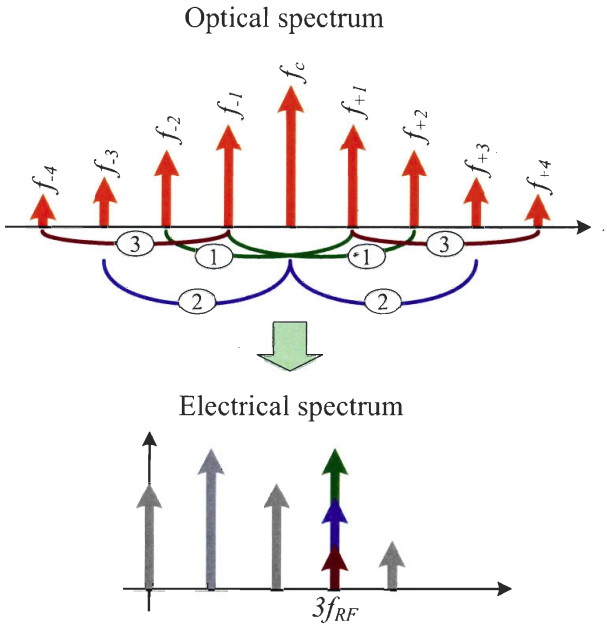

Figure 5.20: The detected RF third order harmonic is determined by the sum of a number of terms stemming from the beating of elements of the optical spectrum separated by $3 \cdot \omega_{RF}$. If the optical spectrum amplitude is symmetrical with respect to the carrier, some beating terms can be regrouped to ease the analytical calculation of the total power at the RF third harmonic. In the example, 6 beating elements of the optical spectrum are grouped in three terms contributing to the amplitude detected RF third harmonic.

where:

$$\alpha_n = \frac{\varphi_{L,n} + \varphi_{U,n}}{2} \tag{5.6a}$$

$$\beta_n = \frac{-\varphi_{L,n} + \varphi_{U,n}}{2}. \tag{5.6b}$$

A similar equation for the third order harmonic can be found by summing all the terms at $3\omega_{RF}$, and we find:

$$\begin{aligned} f_{3\omega_{RF}}(t) \propto & 2CS_3 \cos(\varphi_c - \alpha_3) \cos(3\omega_{RF}t + \beta_3) + \\ & + 2S_1 S_2 \cos(\alpha_1 - \alpha_2) \cos(3\omega_{RF}t + \beta_1 + \beta_2) \\ & + 2\sum_{n=1}^{\infty} S_n S_{n+3} \cos(\alpha_n - \alpha_{n+3}) \cos(3\omega_{RF}t - \beta_n + \beta_{n+3}). \end{aligned} \tag{5.7}$$

These equations reveal that the detected power at the fundamental and third order harmonic, and so the HD3, are changed manipulating the amplitude and the phase of the electric field spectrum. To clarify this concept, let us consider a simple linear link with an ideal laser source, a linear optical modulator driven by a pure sinusoidal RF tone at ω_{RF}, and no optical filtering. An ideal modulator modulates linearly the instantaneous optical power, which is proportional to the $|E(t)|^2$. Because of the square module operator, the optical field $E(t)$ has an infinite number of spectral elements, even

if the RF modulating signal is a pure RF tone at ω_{RF}. All these optical spectral elements of $E(t)$ beat at the detector generating RF tones at all the harmonics of ω_{RF}. The total detected photocurrent is proportional to the instantaneous optical power so that, with no optical filtering or distortion on the link, it must be an undistorted image of the RF modulating sinusoid. Hence, the RF tones generated at the detector by the beating of the spectral elements of $E(t)$ sum up in such a way that destructive interference nulls the power at the harmonics of ω_{RF}, and constructive interference occurs only for the tone at ω_{RF}. However, any filtering of the amplitude or the phase of the electric field would affect the amplitude and phase of the detected RF tones and prevent a perfect destructive interference at the harmonics of ω_{RF}, so that the total detected photocurrent would be affected by harmonic distortion. We will show that the opposite is also true: if the modulator is not linear, a modification of the spectrum can compensate for its nonlinear response and minimize the detected distortion.

This kind of reasoning has been used, for example, by Corral [174] and Cheng [114] to calculate the harmonic distortion in a dispersive link with a MZ modulator. Cho extended the model to intermodulation distortion, at the expense of an increased analytical complexity [175]. In this case, the number of beating elements in the optical spectrum is much higher because the spectrum is more complex. For IMD3 measurements and simulations, in the RF domain we assume a modulating signal composed of two tones f_1 and f_2, with $|f_1 - f_2| \ll f_1$. The IMD3 signals are found at $2f_2 - f_1$ et $2f_1 - f_2$. If f_1 and f_2 have the same amplitude, the IMD3 signals also have the same amplitude. In Fig. 5.21 we identify some of the beating elements giving rise to IMD3 terms. The sum of all the IMD3 terms gives the total detected RF power at the IMD3 frequencies.

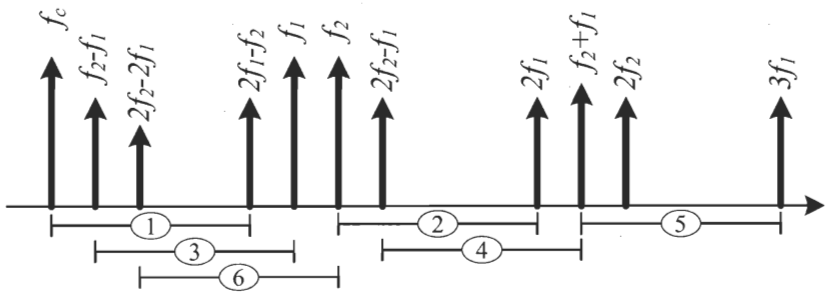

Figure 5.21: Beating elements of the optical spectrum that generate signal contributions (we name them "terms") at $2f_1 - f_2$. The sum of all these terms gives the total detected RF power at $2f_1 - f_2$. Only one side of the spectrum is shown, but the spectral elements placed symmetrically with respect to the carrier also contribute to the power at $2f_1 - f_2$.

In case of the IMD3, it is more difficult to write close forms for the detected fundamental power and distortion, as given by the equations (5.5) and (5.7) for harmonic distortion. However, if the optical spectrum is symmetric in amplitude with respect to the carrier, we can still calculate each beating term separately. For example, the first

three terms identified in Fig. 5.21 can be written as:

$$y_1 = 2CS_{2f_1-f_2}\cos\left(\varphi_c - \frac{\varphi_{2f_1-f_2}+\varphi_{f_2-2f_1}}{2}\right)\times \\ \times\cos\left[2\pi\left(2f_1-f_2\right)t+\frac{\varphi_{2f_1-f_2}-\varphi_{f_2-2f_1}}{2}\right] \tag{5.8a}$$

$$y_2 = 2S_{f_2}S_{2f_1}\cos\left(\frac{\varphi_{f_2}+\varphi_{-f_2}}{2}-\frac{\varphi_{2f_1}+\varphi_{-2f_1}}{2}\right)\times \\ \times\cos\left[2\pi\left(2f_1-f_2\right)t+\frac{\varphi_{2f_1}-\varphi_{-2f_1}}{2}-\frac{\varphi_{f_2}-\varphi_{-f_2}}{2}\right] \tag{5.8b}$$

$$y_3 = 2S_{f_1}S_{f_2-f_1}\cos\left(\frac{\phi_{f_1}+\phi_{-f_1}}{2}-\frac{\phi_{f_1-f_2}+\phi_{f_2-f_1}}{2}\right)\times \\ \times\cos\left[2\pi\left(2f_1-f_2\right)t+\frac{\phi_{f_1}-\phi_{-f_1}}{2}-\frac{\phi_{f_2-f_1}-\phi_{f_1-f_2}}{2}\right]. \tag{5.8c}$$

The strongest detected power at f_1 can be written as:

$$y_1 = 4CS_{f_1}\cos\left(\varphi_c-\frac{\varphi_{f_1}+\varphi_{-f_1}}{2}\right)\cdot\cos\left[2\pi f_1 t+\frac{\varphi_{f_1}-\varphi_{-f_1}}{2}\right]. \tag{5.9}$$

Below, we apply these models to interpret the behavior of both harmonic and intermodulation distortion in a link with dispersive and nonlinear fibre (10 km of SMF), as a function of the MZ modulator bias.

5.4.2 HD3 in links with dispersive fibre

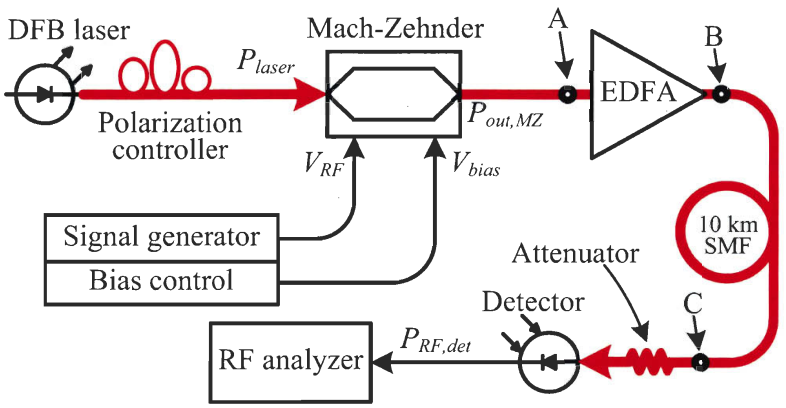

Figure 5.22: Reference ROF link. A polarization controlled DFB laser is fed to a balanced MZ modulator with adjustable DC bias. The modulator output is then amplified by an EDFA and propagated over 10 km of standard SMF. Before detection, the signal is attenuated to avoid detector saturation. Orange lines: optical connections.

In this section, we refer to the link shown in Fig. 5.22. In order to understand the role of fibre dispersion and $\chi^{(3)}$ nonlinearities, we first consider the case of a link

with low optical power transmitted over the fibre (i.e., without an EDFA before the fibre), so that we can model it as a linear dispersive waveguide. In this case, the HD3 is described by the simple formula given by Cheng [114]:

$$HD3 = \frac{P_{3\omega_{RF}}}{P_{\omega_{RF}}} = \frac{J_3\left[\pi \frac{V_{RF}}{V_\pi} \cos\left(3\frac{\varphi}{2}\right)\right]}{J_1\left[\pi \frac{V_{RF}}{V_\pi} \cos\left(\frac{\varphi}{2}\right)\right]} \tag{5.10a}$$

$$\varphi = \frac{D\lambda^2\omega_{RF}^2}{2\pi c}, \tag{5.10b}$$

where $P_{3\omega_{RF}}$ and $P_{\omega_{RF}}$ are respectively the power of the detected fundamental and third harmonic, D is the fibre dispersion, λ is the optical carrier wavelength, ω_{RF} is the RF carrier pulsation, and c is the speed of light. It is important to remember that all the optical spectral elements whose beating contributes to the detected third harmonic are separated in frequency by $3\omega_{RF}$. For this reason, with increasing accumulated dispersion along the link, the power fading of the detected third harmonic is three-fold accelerated with respect to the power at fundamental frequency, and the HD3 has a first null before the first null of the fundamental power. However, for higher dispersion the HD3 may increase above the value at zero dispersion, as shown in Fig. 5.23, which compares (5.10a) with a numerical simulation of the HD3 and the power of fundamental and third harmonic.

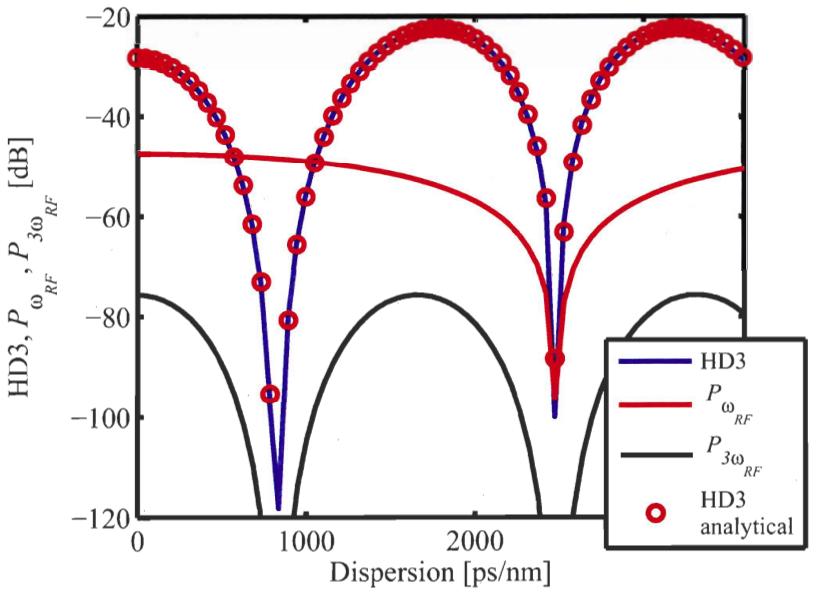

Figure 5.23: Numerical simulation of the HD3 at the end of a link with dispersive fibre, compared with the prediction of (5.10a). $P_{RF} = 10\,\text{dBm}$, i.e., $\frac{V_{RF}}{V_\pi} = 0.17$.

From (5.10a), we note that for all practical modulation amplitudes ($\frac{V_{RF}}{V_\pi} < 0.586$, corresponding to $P_{RF} < 21\,\text{dBm}$), the HD3 nulls occour when the fundamental power is somewhat attenuated. In Fig. 5.23 the maximum fundamental power attenuation at HD3 nulls is about 1 dB. For very high modulation amplitudes, the fundamental power is actually increased at HD3 nulls with respect to the zero dispersion value, as shown

in Fig. 5.24 where $\frac{V_{RF}}{V_\pi} \simeq 1$. Equation (5.10a) also confirms that, even in the presence of dispersion, the HD3 is not influenced by the modulator bias.

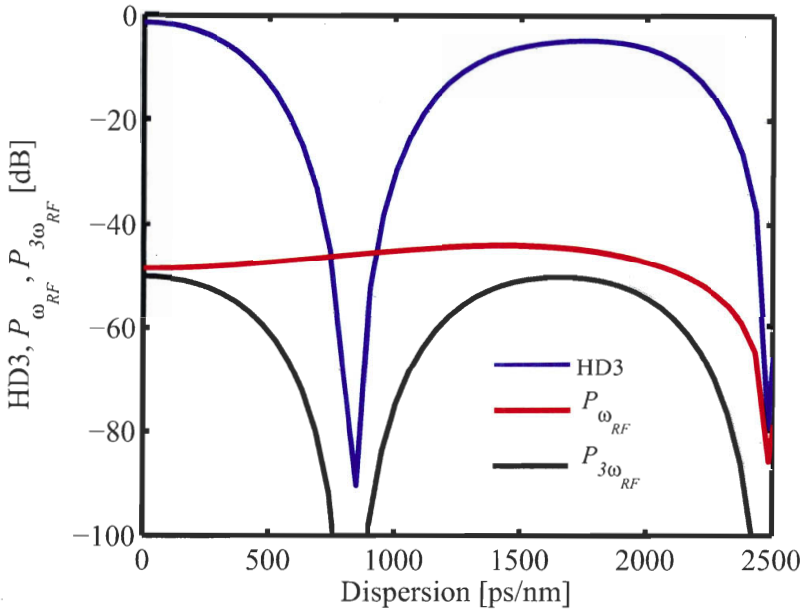

Figure 5.24: Numerical simulation of the HD3 at the end of a link with dispersive fibre and $\frac{V_{RF}}{V_\pi} \simeq 1$.

Before moving to the more complex case of a nonlinear fibre, it is useful to interpret the dependence of HD3 on dispersion on the basis of (5.5) and (5.7). We start by noting that the two strongest contributions to the detected third harmonic are given, as shown in Fig. 5.20, by:

1. the beating of the element of the optical spectrum at $f_{-\omega_{RF}} = f_c - \omega_{RF}$ with the element at $f_{2\omega_{RF}} = f_c + 2\omega_{RF}$, and the beating of $f_{\omega_{RF}} = f_c + \omega_{RF}$ with $f_{-2\omega_{RF}} = f_c - 2\omega_{RF}$.
2. the beating of the optical carrier (at frequency f_c) with the elements of the optical spectrum at $f_{+3\omega_{RF}} = f_c + 3\omega_{RF}$ and $f_{-3\omega_{RF}} = f_c - 3\omega_{RF}$.

If the optical spectrum has the same amplitude at $f_{+n\omega_{RF}}$ and $f_{-n\omega_{RF}}$, the contributions to the detected third harmonic are, from equation (5.7):

$$y_1 = 2S_1S_2 \cos(\alpha_1 - \alpha_2) \cos(3\omega_{RF}t + \beta_1 + \beta_2) \tag{5.11a}$$
$$y_2 = 2CS_3 \cos(\varphi_c - \alpha_3) \cos(3\omega_{RF}t + \beta_3) \tag{5.11b}$$
$$y_3 = 2S_1S_4 \cos(\alpha_1 - \alpha_4) \cos(3\omega_{RF}t - \beta_1 + \beta_4), \tag{5.11c}$$

where the coefficients are defined on page 127. The amplitude of y_1, y_2 and y_3 are dependent on the total accumulated dispersion through the $\cos(\alpha_1 - \alpha_2)$, $\cos(\varphi_c - \alpha_3)$ and $\cos(\alpha_1 - \alpha_4)$ terms. If we assume a linear dispersion, the net phase difference

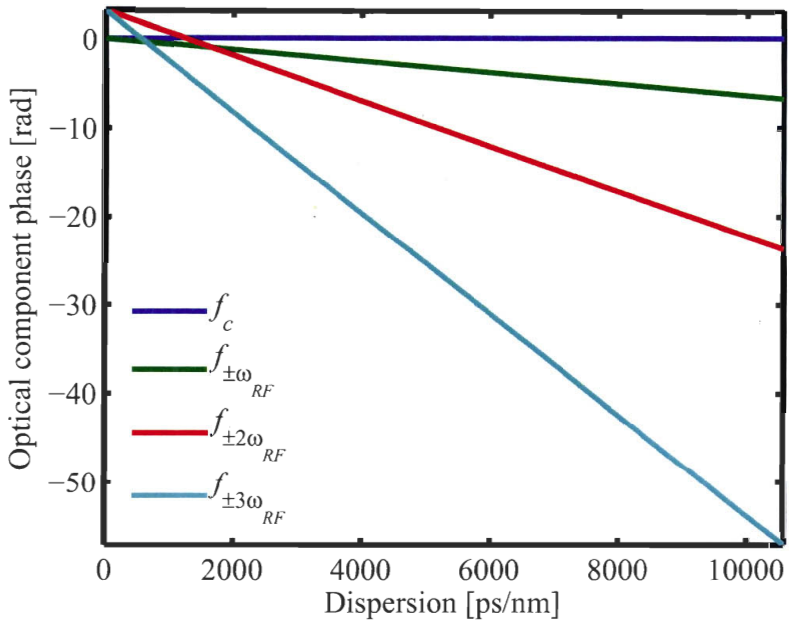

Figure 5.25: Numerical simulation of the evolution of the phases of the optical spectrum elements as a function of the accumulated dispersion. $\frac{V_{RF}}{V_\pi} = 0.17$.

between the optical carrier at f_c and the other elements of the optical spectrum at $f_{\pm n\omega_{RF}}$ is described by a parabola, centered on f_c. Hence, $\varphi_{L,n} = \varphi_{U,n} = \varphi_n$ and we can write: $\beta_n = 0$ and $\alpha_n = \varphi_n$, with $\varphi_c = 0$. Also, from the quadratic evolution of the phase as a function of the frequency we know that φ_2 increases with dispersion four times as fast as φ_1, and φ_3 nine times as fast. This is confirmed by Fig. 5.25, where we show a simulation of the phases of the optical spectrum elements at f_c, $f_{\pm\omega_{RF}}$, $f_{\pm2\omega_{RF}}$ and $f_{\pm3\omega_{RF}}$ as a function of the accumulated dispersion. Then, $\varphi_1 - \varphi_2$, which affects the amplitude of y_1, varies three times as fast as φ_1, and $\varphi_c - \alpha_3$, which affects y_2, varies nine times as fast. Hence, if we calculate y_1 and y_2, and we compare their sum with the amplitude of the detected fundamental frequency, we see that the amplitude of the third harmonic vanishes three times more often than the fundamental, as shown in Fig. 5.26. This justifies the behavior of the HD3 as a function of dispersion as determined by the evolution of the phase of the optical spectral elements along the dispersive fibre.

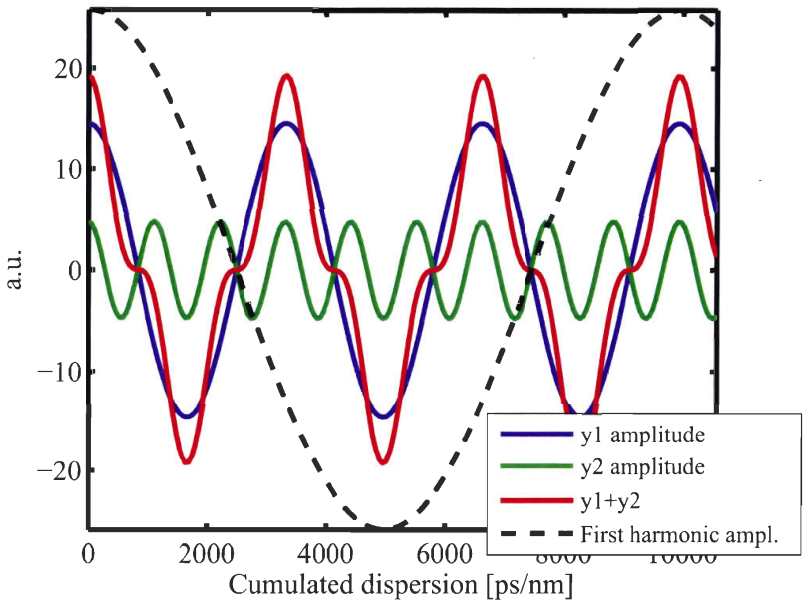

Figure 5.26: The amplitude of the detected RF first harmonic compared with the amplitude of the first two terms y_1 and y_2, which sum up to give the amplitude of the detected RF third harmonic.

5.4.3 IMD3 in links with dispersive fibre

In dispersive links, the IMD3 is described analytically by Cho [175]:

$$\mathrm{ID3} = \frac{P_{2f1-f2}}{P_{f1}} \propto \frac{\cos^6\left[\pi L D \lambda_c^2 f_{RF}^2/c\right]}{\cos^2\left[\pi L D \lambda_c^2 f_{RF}^2/c\right]}. \tag{5.12}$$

One important difference between the IMD3 and the HD3 seen before is that the beating elements in the optical spectrum contributing to the distortion power are spaced by $2f_1 - f_2$ and $2f_2 - f_1$. Since $|f_1 - f_2| \ll f_1$, the dispersion causes a similar power fading to the beating terms contributing to the detected RF distortion and useful signal. Hence, both detected power at $2f_1 - f_2$ and f_1, named P_{3L} and P_1 in Fig. 5.27, have nulls for the same values of accumulated dispersion, as suggested by (5.12). The same equations show that the total detected RF distortion fades out more rapidly than the useful signal with increasing dispersion, and so the IMD3 decreases. However, for each dB of attenuation of the detected IMD3, the signal power is attenuated by about 0.5 dB.

Adding dispersion appears to be an interesting method to improve the link linearity. However, while the HD3 is decreased with minimum power penalty on fundamental frequency, the IMD3 can be reduced only at the expense of a significant fading of the detected signal power. If signal fading is excessive, power RF amplifiers must be added to compensate, potentially causing further signal distortion, systems complexity and cost. Also, the amount of HD3 and IMD3 reduction depends only on the accumulated dispersion and RF carrier frequency. The carrier frequency is usually fixed by the RF transmission protocol, i.e., at 5 GHz for IEEE 802.11a. Dispersion in standard

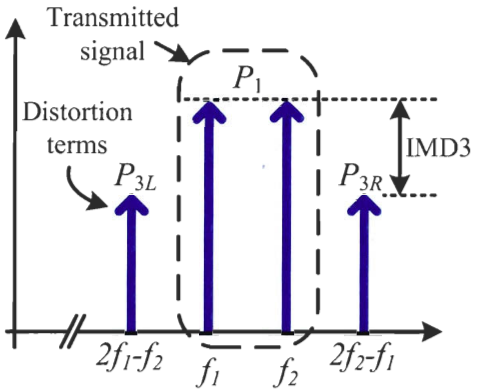

Figure 5.27: Definition of IMD3 in the electrical domain.

SMF is also fixed at 17 ps/nm-km, so only the transmission distance is a parameter for optimizing the HD3. This is impractical for most links for indoor or campus networks, which are not likely to use very long fibre spans: a reasonable order of magnitude for the maximum fibre length used to cover a building is about 10 km. In a ROF system employing standard SMF after 10 km of propagation of a 5 GHz, the dispersion alone can improve the HD3 by only about 1 dB, and IMD3 improvement is negligible.

5.4.4 HD3 and IMD3 in links with nonlinear fibre

In this work, we study the HD3 and IMD3 in analog optical links employing a MZ modulator, an EDFA and 10 km of standard fibre, and we include fibre nonlinearities in the analysis.

In high modulation power narrowband ROF links, the dynamic range and signal quality are limited by the modulator nonlinear response. As a solution, linearized modulators have been proposed, but these devices are usually complex and expensive. As a cheaper alternative, we show that, by controlling the modulator bias, the fibre $\chi^{(3)}$ nonlinearities can help in reducing the link HD3 and IMD3 below the level imposed by the MZ modulator, effectively providing compensation for the modulator distortion. This is due to the interaction between the distortion caused by the MZ and the fibre nonlinearities. First, we apply a 5 GHz sinusoidal test signal to the link and we show measurements and simulations proving simultaneous HD3 improvement and received power maximization. Then, we extend the measurements and simulations to the IMD3. The results for both HD3 and IMD3 are interpreted by studying the evolution of the optical spectrum elements and beating terms contributing to distortion, as a function of bias and propagation length of the fibre. In this work, we avoid SBS by adding proper attenuation at fibre input or by phase modulating the optical signal before amplification. This work is novel and the results on IMD3 have been published in [181].

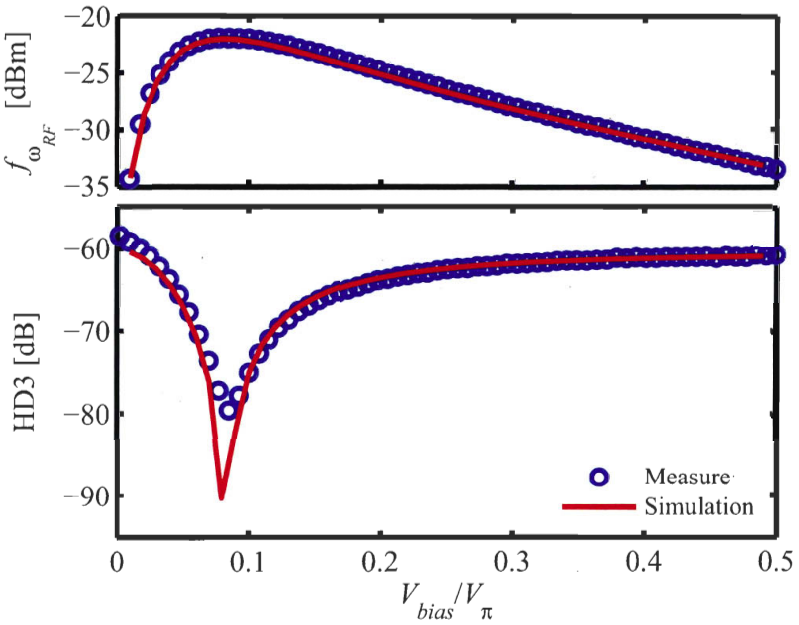

Figure 5.28: Measurement and simulation of the HD3 and the detected RF power at the fundamental frequency in a link with 10 km of fibre. The simulation includes the fibre $\chi^{(3)}$ nonlinearities. Modulation frequency: 1.51 GHz; modulation power: 0 dBm; modulator RF input losses: 8 dB; Laser power at EDFA input (bias at quadrature): -6 dBm; attenuation at fibre input: 2.5 dB; optical power launched on the fibre (bias at quadrature): 14.2 dBm.

We saw before that the HD3 is only slightly improved by dispersion over 10 km of a linear SMF, for any modulator bias. However, when fibre nonlinearities are take into account, even for such short fibre length the HD3 can be improved by moving the bias off quadrature. We measured the HD3 curves using a link as sketched by Fig. 5.22. The modulation frequency was 1.51 GHz, the modulation power 0 dBm, and there was about 2.5 dB additional optical loss at fibre input. The fibre roll has been characterized to measure its length, dispersion, losses and nonlinear coefficient as given in table 5.1[5]. With bias at quadrature, the laser power at the EDFA input is -6 dBm. The other link parameters are the same as table 3.1, page 46.

Table 5.1: Parameters of nonlinear fibre roll used in the experiments.

Fibre type	SMF-28
Length	10.56 km
Losses	0.2 dB/km
Dispersion	17.4 ps/nm·km
Nonlinear coefficient γ	1 $W^{-1}km^{-1}$

We show in Fig. 5.28 the measurement of detected HD3 and RF power on the fundamental frequency as a function of bias in a link with 10 km of SMF fibre, along

[5]The nonlinear coefficient was characterized by coupling to the fibre two lasers with equal polarization and measuring the four-wave mixing (FWM) at the fibre output for various combinations of laser powers. The same setup was simulated with increasing values of nonlinear coefficient, until the simulated FWM levels showed a good fitting with the measured data.

with a simulation including a nonlinear split-step fibre model. The HD3 clearly shows a minimum for values of bias that is, interestingly, near to the maximum value of received RF power. The physical reason for the presence of a minimum in HD3 can be understood by observing the amplitude and phases of the elements of the optical spectrum, as we did for the linear dispersive case. In Fig. 5.29 we report the simulated amplitude of the spectrum elements as a function of the bias. The solid lines are amplitudes before the fibre, and the dashed lines are after the fibre. Moving the bias towards the minimum transmission point changes the ratio of power transmitted in the optical carrier and modulation sidebands: the carrier at the even sidebands are suppressed and the odd sidebands are amplified, as suggested by the analytical expression of the MZ spectrum given in appendix B. Throughout the propagation over the fibre, both the amplitude and the phases of the optical spectrum elements are affected by $\chi^{(3)}$ nonlinearities: the four-wave mixing (FWM) transfers power from the optical carrier and the first modulation sidebands (at $f_{\pm\omega_{RF}}$) to the second and third modulation sidebands (at $f_{\pm 2\omega_{RF}}$ and $f_{\pm 3\omega_{RF}}$). Note that the FWM effect is more important when the bias setting is such that the carrier and the first modulation sidebands have similar power values. The nonlinear self- and cross-phase modulations (SPM and XPM) also change the phases of the optical spectrum elements, as shown in Fig. 5.30. Then, at the detector, the beating terms generating the third order harmonic vary with the bias. The first three beating terms, namely y_1, y_2 and y_3, are given by (5.11), and vary with bias as shown in Fig. 5.31. Note that the higher amplitude of the optical elements at $f_{\pm 2\omega_{RF}}$ and $f_{\pm 3\omega_{RF}}$ for low bias greatly increases the absolute amplitude of y_1 and y_2, with respect to quadrature biasing, where FWM has less effect because most of the optical power is concentrated in the optical carrier. Also, the SPM and cross-phase modulation (XPM) contribute in changing the sign of y_1 at low bias. Then, the sum of y_1, y_2 and y_3 is nulled for $V_{bias} \simeq 0.09V\pi$, and the third harmonic power fades out at this bias. Under the conditions of this simulation, which fits with the experimental measurements shown in Fig. 5.28, the nonlinear modulation of the amplitudes and phases of the optical spectrum elements affects mostly the received RF third order harmonic, and have negligible impact on the received RF fundamental. The detected RF fundamental and third harmonic normalized powers as a function of bias before and after the fibre are shown in Fig. 5.32. Note that the normalized powers of fundamental and third harmonic superimpose at the modulator output, so that the HD3 is constant with bias. After the fibre, the fundamental power still has the same dependence on bias, but the third harmonic has a minimum, which explains the measured minimum in HD3.

It is interesting to compare the evolution of HD3 along the fibre with bias at quadrature and $V_{bias} = 0.09V\pi$. As shown in Fig. 5.33, at quadrature the HD3 increases slightly with fibre length, whereas at lower bias there is a distortion minimum around 10 km. In Fig. 5.34 we also compare the amplitudes of the optical carrier and the optical spectrum elements at $f_{\pm\omega_{RF}}$, $f_{\pm 2\omega_{RF}}$ and $f_{\pm 3\omega_{RF}}$, for the two same values of bias. At quadrature, the shape of the spectrum at the modulator output is such that the FWM is inefficient in amplifying the second and third optical modulation sidebands. Hence, no HD3 null is observed. For $V_{bias} = 0.09V\pi$, the relative power of the first

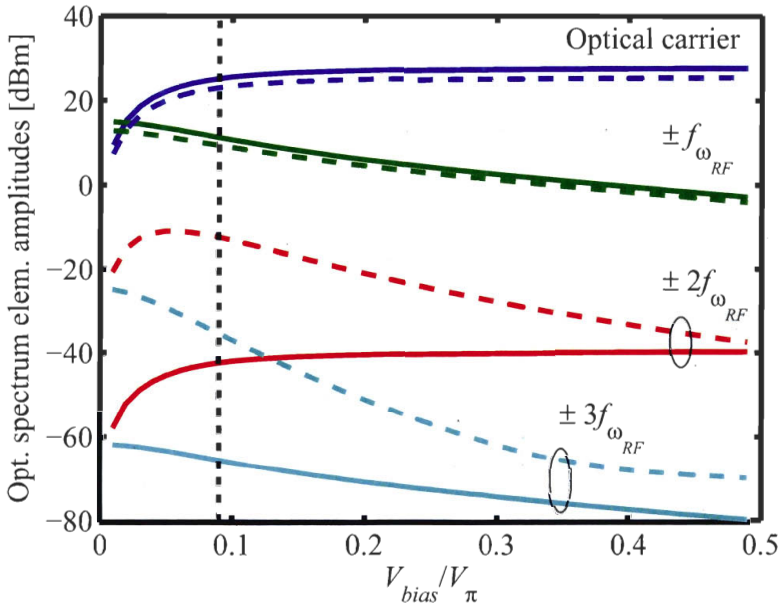

Figure 5.29: Simulated amplitude of the spectrum elements as a function of the bias. Solid lines: amplitudes before the fibre; Dashed lines: after the fibre. Total attenuation due to propagation: 2 dB; modulation frequency: 1.51 GHz; modulation power 0 dBm; modulator RF input losses: 8 dB; attenuation at fibre input: 2.5 dB.

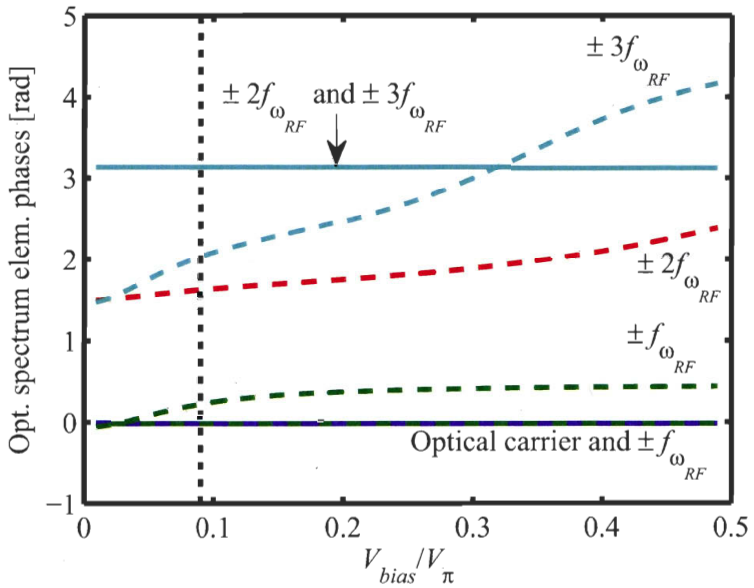

Figure 5.30: Simulated phase of the spectrum elements as a function of the bias. Same conditions as Fig. 5.29.

modulation sideband with respect to the optical carrier is higher, so that the FWM efficiently transfers power to the other sidebands. Note that the power transfer mostly occurs in the first kilometers of fibre, where the propagated power is higher because the accumulated propagation loss is low, and where accumulated dephasing of the optical

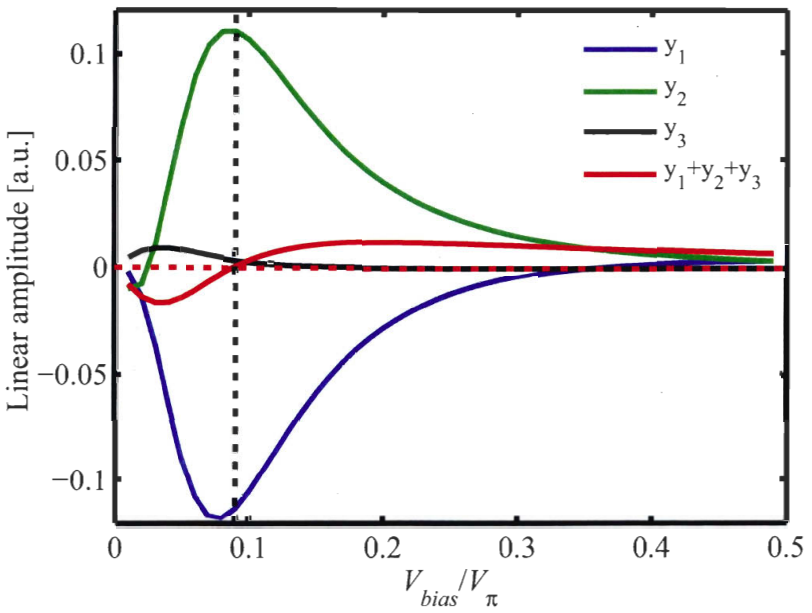

Figure 5.31: Amplitudes of the three strongest beating terms contributing to the total detected power at $3\omega_{RF}$ as a function of bias. Same conditions as Fig. 5.29.

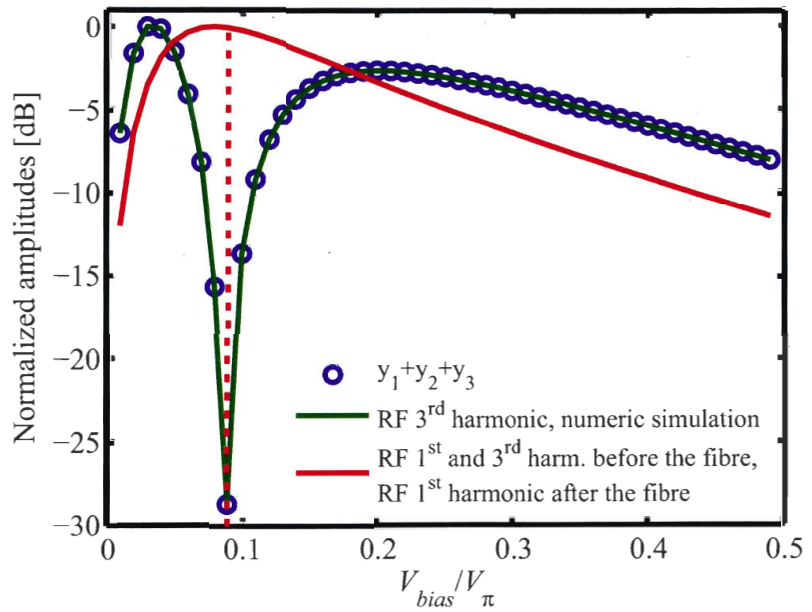

Figure 5.32: Detected RF first and third harmonics normalized powers as a function of bias before and after the fibre, compared to the sum of the beating terms shown in Fig. 5.31. The RF first and third harmonics before the fibre and the RF first harmonic after the fibre have all the same behavior, so the normalized curves are superimposed. Same conditions as Fig. 5.29.

sidebands due to dispersion is also low.

The optimum bias value for minimizing the HD3 at link end is dependent on the fibre length, the power launched at fibre input, and the shape of the optical spectrum

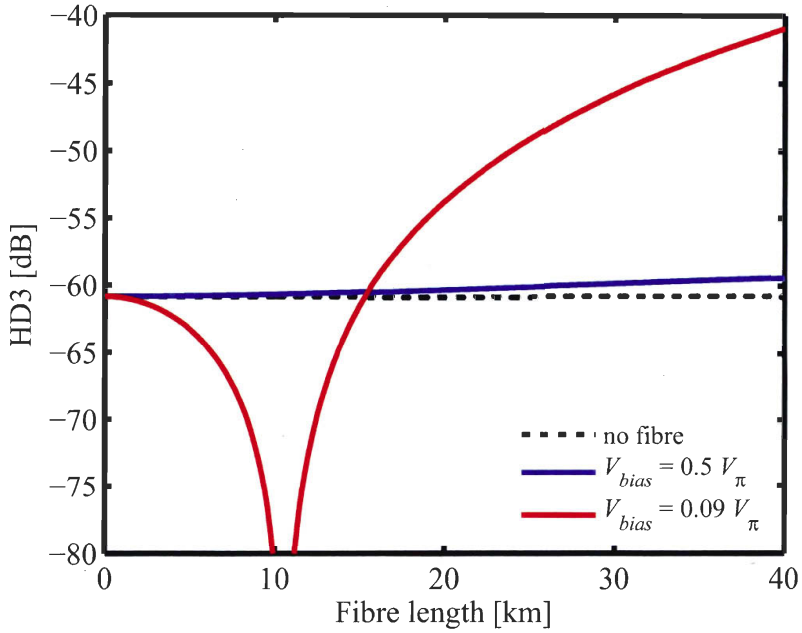

Figure 5.33: Evolution along the fibre of the detected HD3 for two values of bias: $V_{bias} = 0.5V\pi$ (quadrature) and $V_{bias} = 0.09V\pi$. Same conditions as Fig. 5.29.

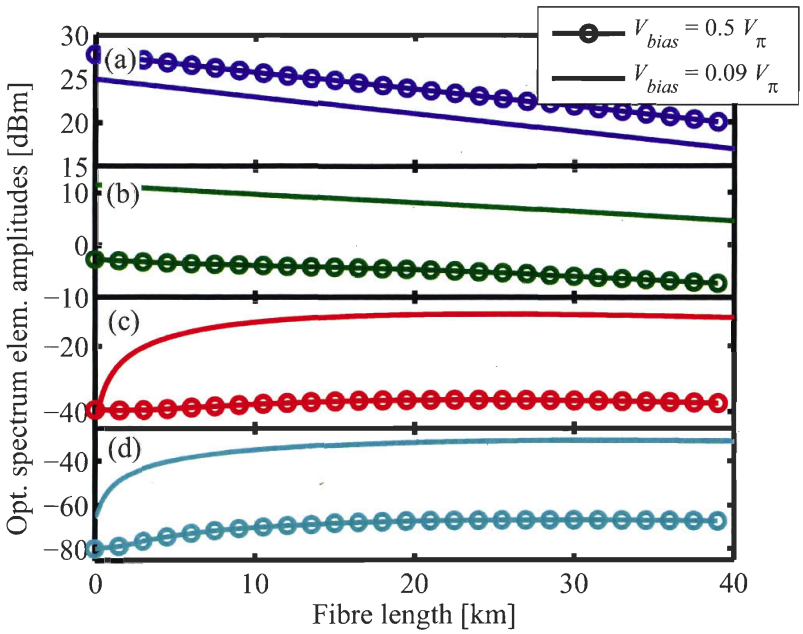

Figure 5.34: Evolution of the amplitudes of the elements of the optical spectrum along the fibre for $V_{bias} = 0.5V\pi$ (quadrature) and $V_{bias} = 0.09V\pi$. Same conditions as Fig. 5.29.

at fibre input. However, we stop here the study of the harmonic distortion and we proceed with the IMD3 and EVM, which are more relevant to the behavior of a link with complex multicarrier signals like OFDM. In the following text we show that, as the HD3, the IMD3 and EVM can be minimized by moving the bias off quadrature in the presence of fibre nonlinearities. We will also discuss under which conditions the IMD3

is achievable simultaneously with detected RF power maximization. For the EVM, we will present the dependence of optimum bias on fibre length and launched power.

The reference link is the same as used for HD3 measurements but, for IMD3 measurement, the RF modulation signal is composed of two tones of equal amplitude at frequencies 5 GHz±10 MHz, for a total signal bandwidth of 20 Mhz: the same as that of an OFDM signal. The signal generator is an `Agilent E4438C`, which provides both tones on the same RF output and that can be calibrated to generate very low IMD3 (< -80 dB) even for RF powers as high as 10 dBm.

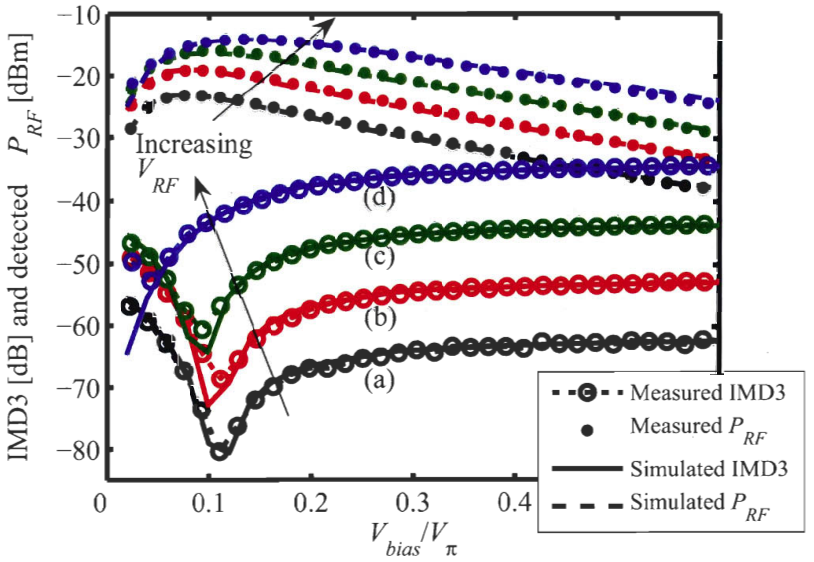

Figure 5.35: Comparison between measured and simulated IMD3 and detected P_{RF}. (a) $P_{RF} = -5$ dBm, (b) $P_{RF} = 0$ dBm, (c) $P_{RF} = 5$ dBm. Other link parameters: $G_0 = 37$ dBm, $P_{out,max} = 17$ dBm, $P_{laser} = 2$ dBm, fibre length: 10.56 km, dispersion: 17 ps/nm·km, nonlinear coefficient γ: 1 $W^{-1}km^{-1}$, fibre losses: 0.2 dB/km. For (d) $P_{RF} = 10$ dBm and $P_{laser} = 4$ dBm. At the output of the EDFA we added about 2.5 dB of losses.

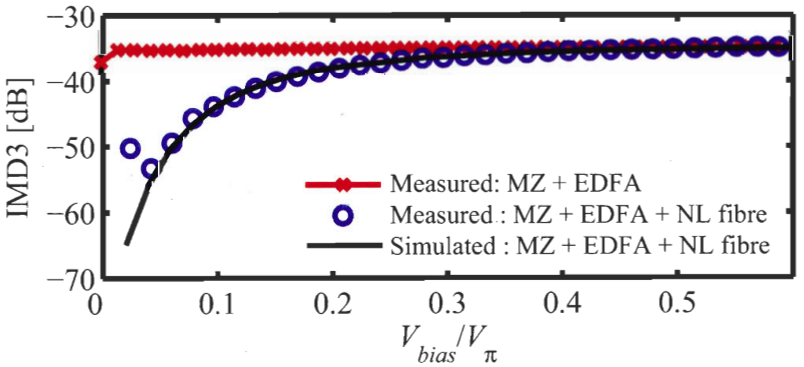

Figure 5.36: Comparison measured and simulated IMD3 at test points B and C in the experimental conditions of Fig. 5.35, curve (d).

We measured the IMD3 at the end of the link shown in Fig. 5.22. Results of measurement and simulation are shown in Fig. 5.35: unlike the case of a dispersive

linear link, the IMD3 is now bias dependent and very low values are reached even for only 10 km of fibre. For the sake of clarity, in Fig. 5.36 we compare the curve (d) of Fig. 5.35, measured at test point C (see the link setup in Fig. 5.22), with the detected IMD3 after the amplifier, at test point B: in the same experimental conditions, we clearly observe a reduction of detected IMD3 at test point C with respect to test point B. In Fig. 5.35, and in chapter 3, we show that by changing the bias we can improve the link RF gain: as long as the optical detector is maintained out of saturation, we can have simultaneous improvement of the link gain and linearity.

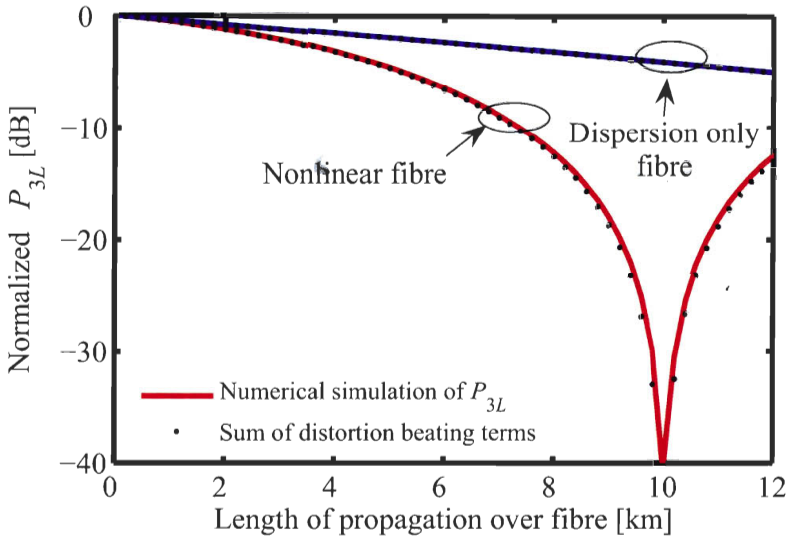

Figure 5.37: Comparison between numerically simulated P_{3L} along the fibre and sum of the beating terms calculated from the received optical spectrum. Simulation parameters as in Fig. 5.35, curve (a). V_{bias} is set to bias that gives minimum IMD3 in Fig. 5.35, curve (a).

Like the HD3, the detected IMD3 is the result of the beating of many elements in the optical spectrum. The stronger the system nonlinearity, the higher is the number of elements that must be considered to precisely calculate the received IMD3. In the case of curve (a) of Fig. 5.35, the IMD3 is well approximated by summing the 3 terms, stemming from the beating of 6 optical elements and given by (5.8). As we discussed before for the HD3, the amplitude of the beating terms varies along the fibre under the effect of dispersion and $\chi^{(3)}$ fibre nonlinearities: this is shown in Fig. 5.38, where we compare the evolution of the three beating terms described by equations (5.8) in a nonlinear fibre (graph a) and dispersive fibre (graph b). For the V_{bias} that minimizes the IMD3 after 10 km of propagation, the FWM, SPM and XPM modify the amplitude and phase of the optical spectrum in such a way that at link end the beating terms adds up in total destructive interference, and the power detected on P_{3L} fades out. At the same time, the power of P_1 does not suffer from significant fading, as showed in Fig. 5.37 where we compare the detected P_1 and P_{3L} in a nonlinear fibre link and dispersive link: dispersion alone cannot improve significantly the IMD3 over only 10 km of standard SMF, but nonlinear effects can compensate for nonlinearity from the MZ and provide very low IMD3. Note that if the modulator was perfectly linear, the fibre would create distortion.

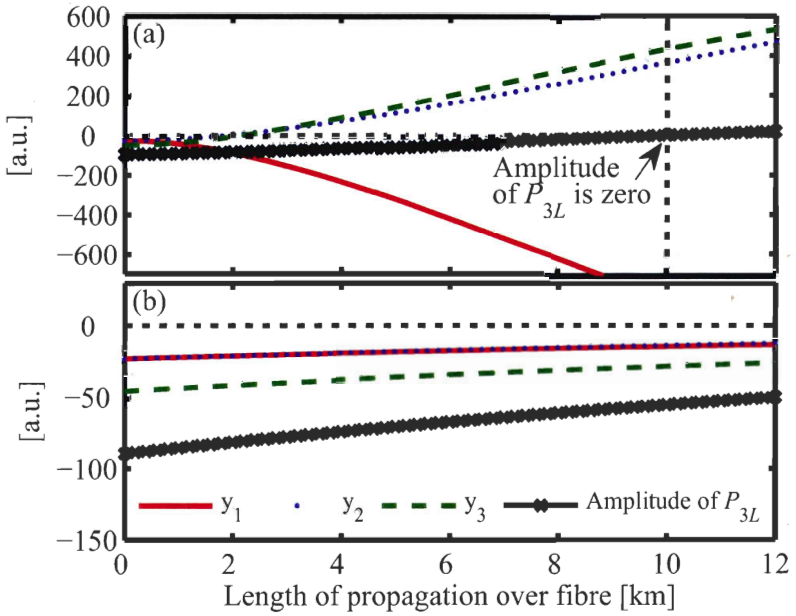

Figure 5.38: Evolution along the fibre of the amplitude of the beating terms described by equations (5.8). (a) nonlinear fibre and (b) dispersive linear fibre. When the beating terms are in opposition of phase and sum up to zero, the amplitude of P_{3L} is zero. $V_{bias}/V_\pi = 0.11$.

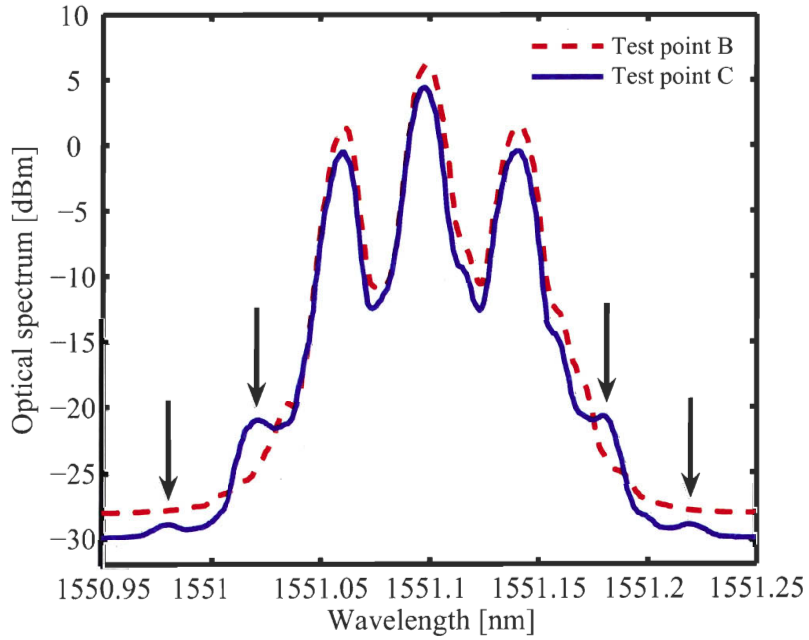

Figure 5.39: Measured optical spectrum at test points B and C. Experimental conditions as in curve (d), Fig. 5.35. Modulator bias optimized for minimum distortion. The arrows point to FWM peaks generated by the fibre.

The FWM contributing to distortion compensation can be observed on the optical spectrum measured at the minimum distortion bias of Fig. 5.35, curve (d): Fig. 5.39 shows the spectrum at test points B and C and confirms an increase in the modulation sideband at two and three times the two-tones modulation frequencies, which are

separated by 20 MHz and are not resolved by the spectrum analyzer.

5.4.5 Bias for minimum IMD3 and maximum gain

The bias value which gives minimum IMD3, named V_{IMD3}, depends on the power launched over the fibre, which is affected by the EDFA saturation and other parameters that also have an influence on the link gain. Thus, it is interesting to find whether it is actually possible to have maximum link gain and minimum distortion for the same MZ bias value. We performed this study by varying four parameters, one at a time: the RF modulation power P_{RF}, the laser power P_{laser}, EDFA saturation output power $P_{out,max}$ and attenuation at test point B. In Fig. 5.40 on page 145, we show the optimum bias for RF gain and minimum distortion as a function of these four parameters. Note that the RF gain does not vary rapidly with bias, so in Fig. 5.40 we show gray regions representing the range of bias which gives a gain within 0.5 dB from the maximum.

As we could expect, in Fig. 5.40A V_{IMD3} appears to be heavily dependent on the power launched in the fibre: a higher power at the fibre input moves the minimum distortion bias towards the quadrature point. With the amplifier parameters used in these simulations, a small attenuation as low as 2 dB before the fibre input makes the V_{IMD3} go below $0.05V_{\pi}$: an extremely low value that would cause an RF power penalty of about 4 dB. The received RF power decreases more rapidly for a bias below the optimum value than above (see chapter 3); hence, for 10 km of propagation, an EDFA with high saturation output power should be chosen, which would give also high RF gain. Note also in Fig. 5.40C that increasing the EDFA saturation makes the $V_{bias,Gmax}$ (bias for maximum RF gain) and the V_{IMD3} both move towards the quadrature. The V_{IMD3} is also heavily influenced by the modulation signal amplitude, as shown by Fig. 5.40B, because it influences the mean power and the power distribution over the elements of the electric field propagating on the fibre: the modulation power should be chosen as a function of the EDFA parameters (and link length, as we will see for the EVM), so that the minimum distortion is found for the same bias as the maximum link RF gain. The laser power influence on V_{IMD3} is relatively low, as shown by Fig. 5.40D, especially if the EDFA is saturated. However, it goes in opposite direction than the $V_{bias,Gmax}$: for high laser power the V_{IMD3} is decreased and the $V_{bias,Gmax}$ is increased.

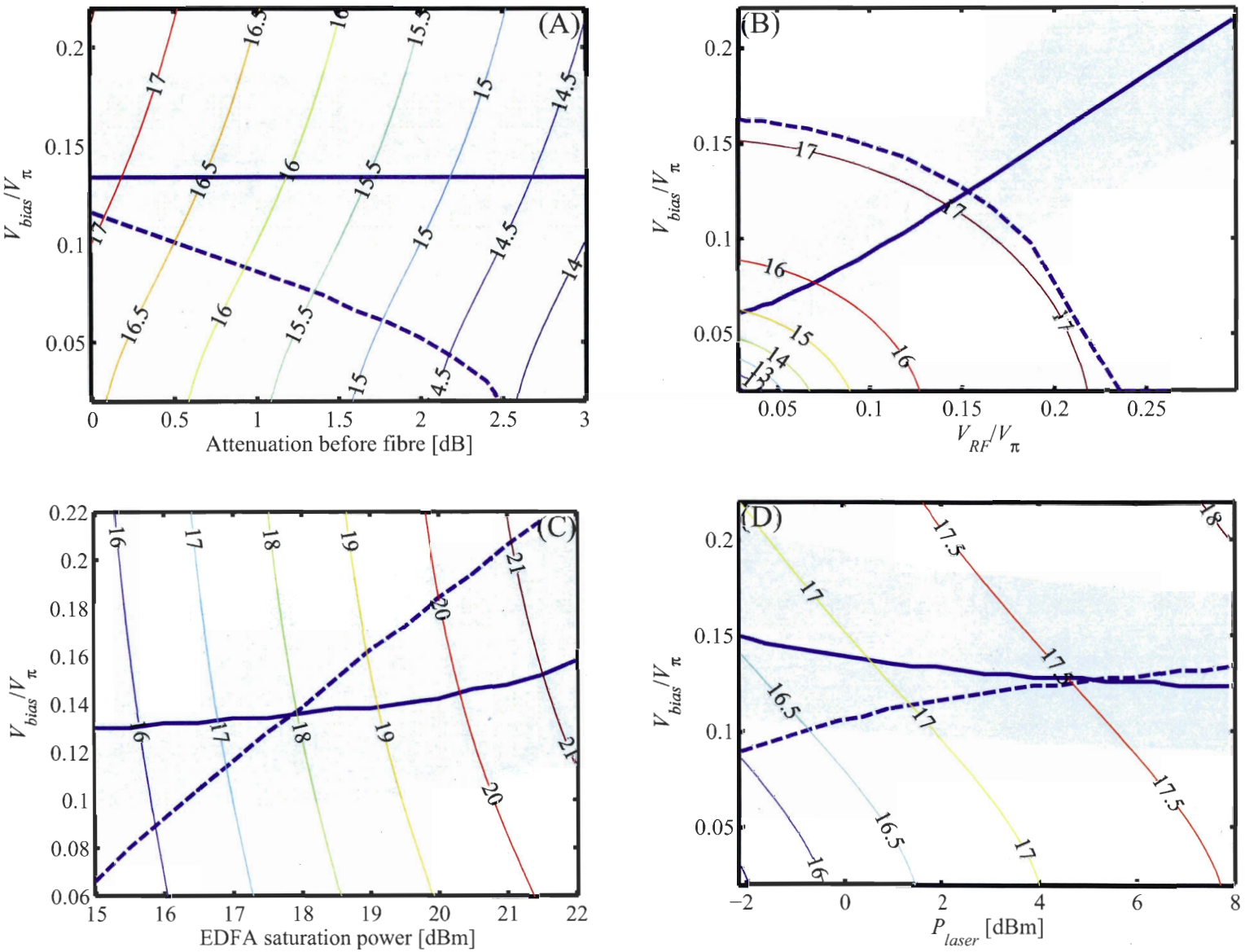

Figure 5.40: Simulation of the V_{bias}/V_π that gives maximum gain (solid bold lines) and minimum ID3 (dashed bold lines) as a function of the attenuation at fibre input, V_{RF}/V_π, $P_{out,max}$ and P_{laser}. Isolines represent the mean optical power at fibre input. (A): $P_{out,max} = 17\,\text{dBm}$, $V_{RF}/V_\pi = 0.17$ ($P_{RF} = 10\,\text{dBm}$), $P_{laser} = 2\,\text{dBm}$, an attenuator at fibre input is used to limit the launched optical power. (B): $P_{out,max} = 17\,\text{dBm}$, $P_{laser} = 2\,\text{dBm}$, P_{RF} from -10 dBm to 10 dBm. (C): $P_{laser} = 2\,\text{dBm}$, $V_{RF}/V_\pi = 0.17$. (D): $P_{out,max} = 17\,\text{dBm}$, $V_{RF}/V_\pi = 0.17$. For all simulations: $G_0 = 37\,\text{dB}$, fibre length 10 km, $D = 17\text{ps/nm-km}$, losses 0.2 dB/km, nonlinear coefficient $1\,\text{W}^{-1}\text{km}^{-1}$, modulation frequency 5 ± 0.01 GHz, modulator RF losses: 5.4 dB.

5.4.6 EVM improvement with bias

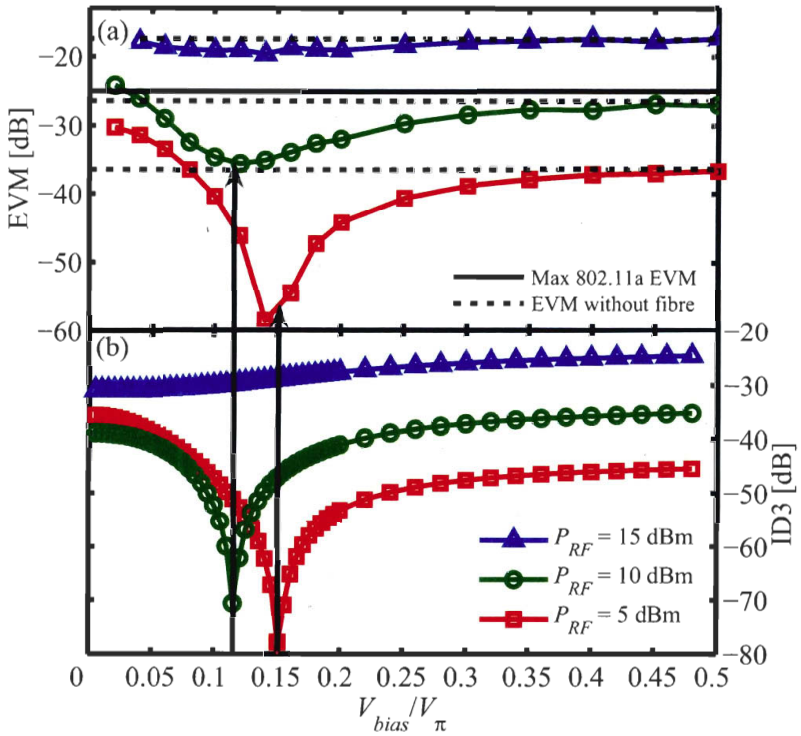

Figure 5.41: Simulation of EVM and IMD3 as a function of MZ bias for 3 values of modulation P_{RF}. $G_0 = 37\,\text{dBm}$, $P_{out,max} = 17\,\text{dBm}$, $P_{laser} = 2\,\text{dBm}$. Dotted lines are EVM at test point B and solid horizontal line is maximum EVM accepted by IEEE 802.11a protocol (-25 dB).

If the link linearity is improved by moving the bias off quadrature, we may reasonably expect to observe an improvement in detected EVM of an OFDM frame. To confirm this, we simulated the transmission of an 802.11a compliant signal over the reference link of Fig. 5.22. The simulation is performed for each MZ bias point by averaging the EVM of several signal frames, in order to ensure the statistical validity of the results. Laser RIN, shot, thermal and ASE-related noises are neglected in the simulation, while distortion from the MZ and the fibre are included. The resulting EVM curves are shown in Fig. 5.41, along with the IMD3 calculated for a two-tone signal with the same mean RF power of the OFDM signal. The EVM indeed shows a minimum in correspondence of the IMD3 minimum, even if the EVM minima are not as spiked. This in a consequence of the high signal PAPR: along a given OFDM frame, the instantaneous RF power can vary over a range of several decibels. The bias which gives minimum EVM is RF power dependent, which explains the smoothed shape of the EVM curves. The curve corresponding to the highest modulation power ($P_{RF} = 10\,\text{dBm}$) is particularly interesting because at this modulation power, without fibre propagation, the distortion from the MZ modulator is high enough to make the EVM of the received OFDM signal only about 3 dB lower than the maximum value accepted by the IEEE 802.11a protocol: -25 dBm. In this case, by adjusting the bias, the EVM can be much improved and made

lower than -35 dB, which allows for high quality transmission.

In the following, we experimentally demonstrate that a significant improvement of EVM is indeed possible through modulator bias optimization. The experimental

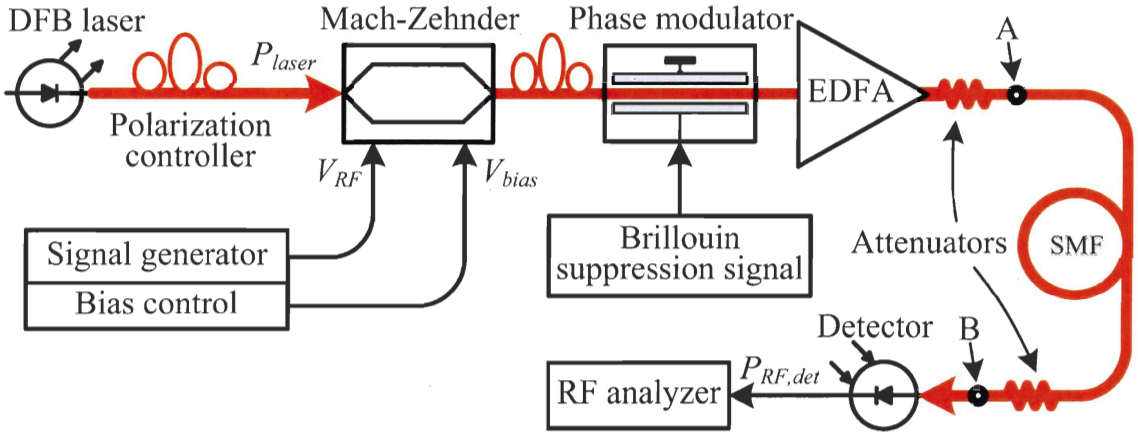

Figure 5.42: The experimental setup for measuring received EVM after propagation over an optical link with 10 km, 20 km or 40 km of standard SMF. Maximum optical power at fibre input: 11 dBm; Brillouin suppression signal: 80 MHz, 10 V_{p-p}, sinusoidal; laser: `Phonetics TUNICS-BT`; laser output power: 7 dBm; laser output wavelength: 1550 nm; modulator insertion losses: 5.1 dB; modulator RF losses: 5.4 dB; MZ modulator: `JDS OC-1`; phase modulator: `UTP APE PM-1.5-8.0-1-1-C`; EDFA: `JDS OAB1552+1FA0`, maximum saturated output power: 17 dBm, small signal gain 37 dB; fibre: SMF; detector: `Agilent 11982A`; RF signal generator: VSG `Agilent E4438C`; RF signal analyzer: VSA `Agilent E4440A`.

setup is shown in Fig. 5.42: the optical signal from a polarization controlled DFB laser is fed to the MZ modulator, modulated by an IEEE 802.11a compliant OFDM signal with average power P_{RF}. Then, the signal is phase modulated using an 80 MHz, 10 V_{p-p} sinusoidal signal to suppress the SBS. The signal is amplified with an EDFA, attenuated by 6.8 dB to set the maximum power at test point A to about 11 dBm, and propagated over 10 km, 20 km or 40 km of standard SMF. A second attenuator ensures that the received optical power (at test point B) is lower than -3 dBm to avoid distortion from the detector. The detected signal is analyzed using a vector signal analyzer (`Agilent E4440A`). SBS suppression is included in the system to ensure that the signal analysis at link end is not affected by SBS-generated noise. Bias control can help to suppress SBS-generated noise by reducing the optical carrier power, as shown in chapter 4. However, with more than 10 km of fibre the bias optimization alone was not sufficient to fully suppress the SBS-generated noise, which was completely eliminated by phase modulating the optical signal.

In our tests, the EDFA and the phase modulation did not add additional distortion noise, so the distortion limited behavior of the EVM at test point A was fully determined by the MZ modulator. After propagation over the fibre link, the measurements shown in figures 5.43, 5.44 and 5.45 clearly confirms the EVM improvement suggested by Fig. 5.41. The results are presented for the modulation power of 5 dBm (effective $V_{RF}/V_{\pi} = 0.1$), 7.5 dBm ($V_{RF}/V_{\pi} = 0.12$) and 10 dBm ($V_{RF}/V_{\pi} = 0.17$). Also shown in

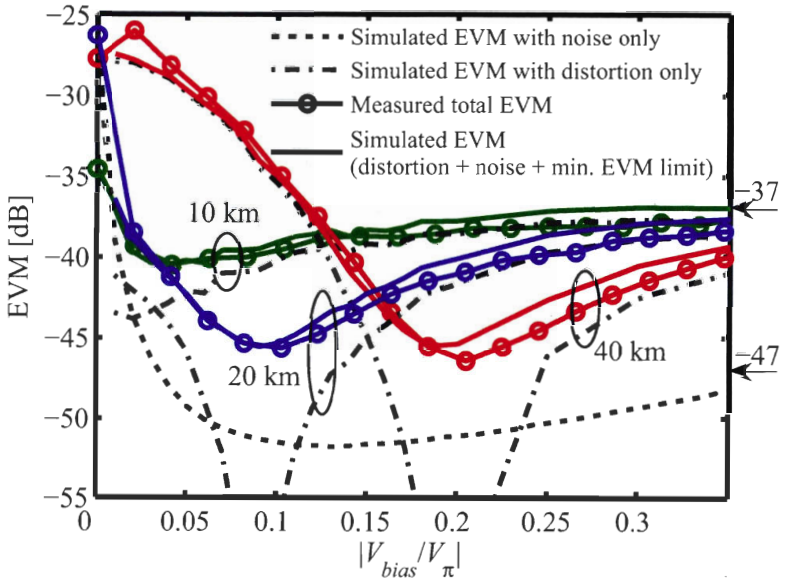

Figure 5.43: Measured and simulated EVM versus bias for a modulation power $P_{RF} = 5\,\text{dBm}$. On the right side of the figures, the lower arrow represent the minimum measurable EVM and the higher arrow indicated the EVM measured at test point A.

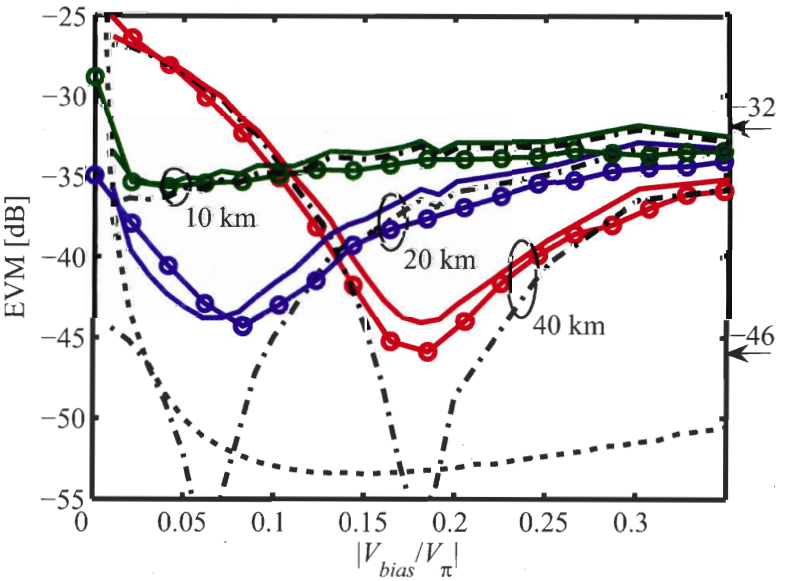

Figure 5.44: The same as Fig. 5.43, with $P_{RF} = 7.5\,\text{dBm}$.

figures 5.43, 5.44 and 5.45 are the numerical simulations for all theses cases and good agreement is obtained when taking into account the EVM degradation due to the low received CNR near $V_{bias} = 0$, and the minimum measurable EVM due to the limitations of the vector analyzer (right bottom arrow on graphs). For $|V_{bias}/V_\pi| < 0.05$, ASE-ASE and ASE-signal beating noise dominate (as shown in chapter 4), and EVM rises rapidly. In all cases, the EVM tends to the value fixed by the MZ distortion when the bias is near

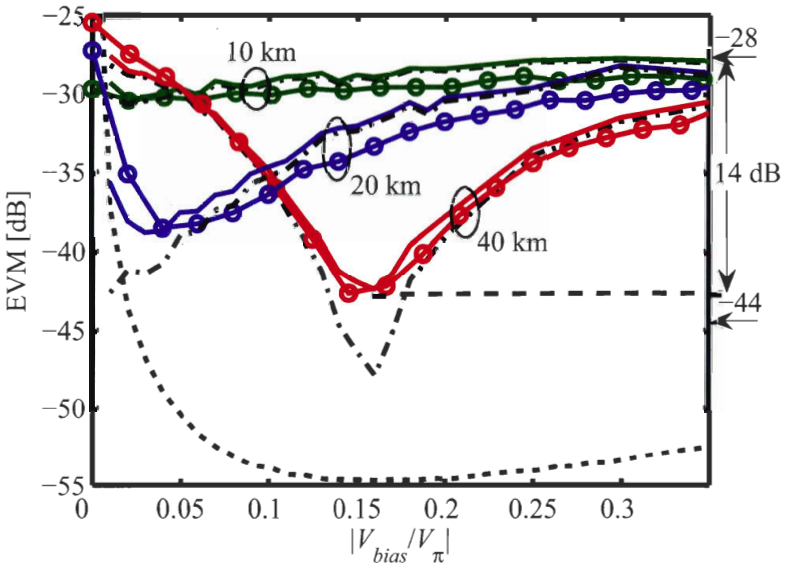

Figure 5.45: The same as Fig. 5.43, with $P_{RF} = 10\,\text{dBm}$.

quadrature. In the case of a MZ modulation power of 10 dBm (Fig. 5.45), the EVM improvement at optimum bias versus quadrature is as high as 14 dB, being -28 dB at quadrature (near the minimum accepted by the IEEE 802.11a specification of -25 dBm for 64-QAM constellation) and as low as -42 dB (signal analyzer limited) at optimum bias.

To our knowledge, this is the first experimental demonstration of distortion-free transmission of IEEE 802.11a over a 40 km-long optically amplified ROF link. In [34], Mitchell reports experimental measurements of EVM with a 40 km-long optically amplified link, modulator bias at quadrature, and modulation P_{RF} lower than 0 dBm: he finds a distortion limited EVM as high as -26 dB.

We simulated the attainable EVM improvement (considering only the effect of distortion), and the corresponding optimum $V_{bias} = V_{minEVM}$ as functions of the attenuation (or power level) in test point A and fibre length, for $P_{RF} = 10\,\text{dBm}$. The amount of EVM improvement due to interplay of MZ and fibre nonlinear effects, shown in Fig. 5.46, is very sensitive to peak power levels on the fibre: depending on the fibre length, an optimum launch power exists to maximize EVM improvement via the V_{bias}. The best launch power decreases with fibre length and is as low as 8 dBm for 50 km of fibre, corresponding to about 10 dB of attenuation after the EDFA. If a too high power is launched, the fibre link does not improve the EVM but, on the contrary, makes it worse. Hence, in long haul transmission, the bias will not help in improving the EVM. Also, note that very high attenuation will greatly reduce the link gain, nulling the gain improvement that low bias can offer by decreasing the EDFA saturation level. The V_{minEVM} as a function of attenuation before the fibre and fibre length is shown in Fig. 5.47: good improvement in EVM is obtained if $|V_{minEVM}| < V_\pi/2$, and V_{minEVM} de-

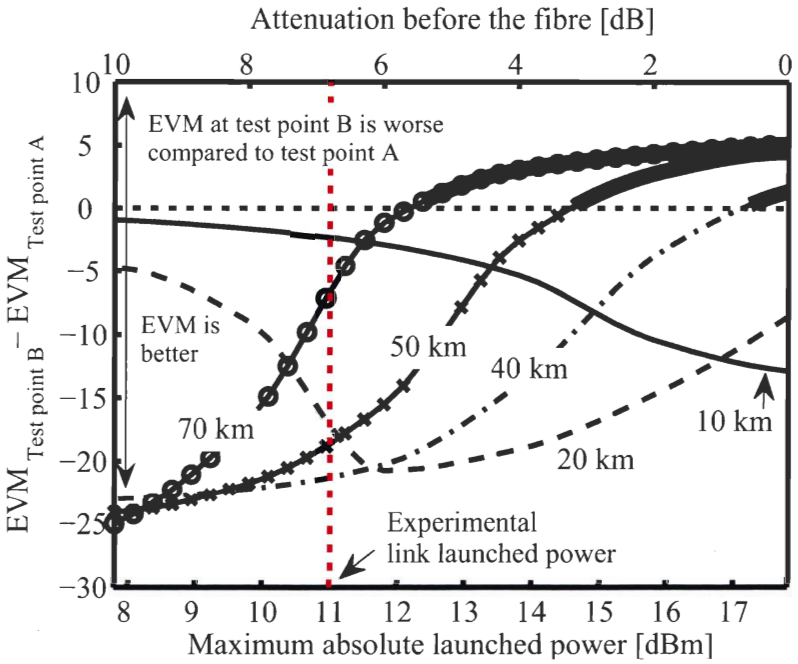

Figure 5.46: Simulation of maximum EVM improvement for fibre lengths between 10 km and 70 km. $P_{RF} = 10\,\text{dBm}$.

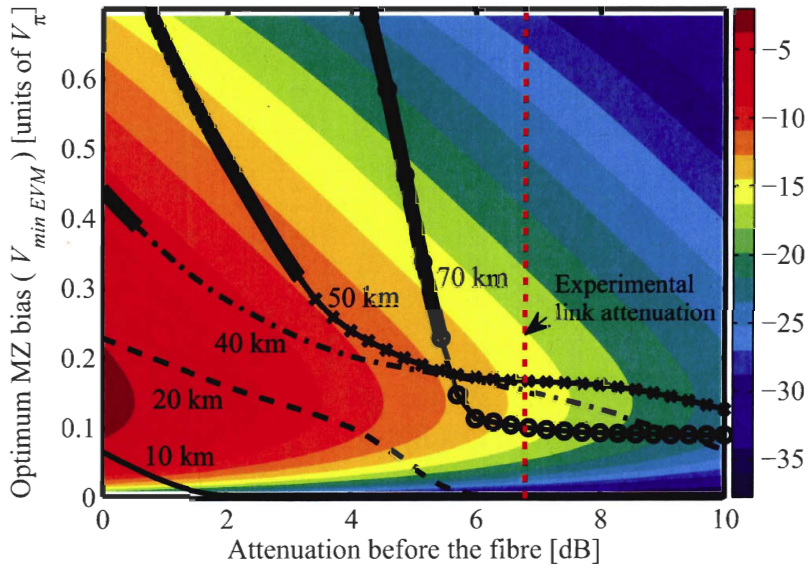

Figure 5.47: Simulation of V_{bias} that minimizes the EVM (V_{minEVM}) for fibre lengths between 10 km and 70 km. The bold sections identify the values of V_{minEVM} for which the EVM at test point B is worse compared to the EVM at test point A. The color shading represents the RF gain penalty as a function of bias and attenuation. $P_{RF} = 10\,\text{dBm}$.

creases with the power launched on the fibre. For short links, the V_{minEVM} can be very near to 0, which is a disadvantage because the link gain for such bias values is low. The link gain penalty with bias and attenuation is also shown in Fig. 5.47. Maximum gain is for $V_{bias} = 0.12V_{\pi}$.

In conclusion, we explored numerically and experimentally the improvement in IEEE 802.11a EVM that can be observed at the end of an analog optical link with external modulation and optical amplification. We showed that modulator bias optimization can greatly improve the EVM in distortion limited links. Simulations show that, depending on link length, there is a trade off between EVM improvement and link gain when choosing the bias point and optical power on the fibre. Bias optimization for narrowband linearization of a ROF link is an attractive technique for its low cost and ease of implementation for link lengths ($< 40\,\text{km}$) of common use in ROF systems. At the time of writing, the results reported in this section are being submitted for publication.

5.5 Conclusions

In this chapter we presented the results of our study on the nonlinear behavior of the main components of a ROF link: the MZ, the amplifier and the fibre, and its impact on the IEEE 802.11a OFDM signal quality. We showed that the MZ is a significant source of distortion, and imposes a limit on the minimum EVM measurable at the end of a linear lossy link. However, the MZ distortion can be partially compensated by the dispersion and fibre nonlinear effects. We interpreted this compensation by observing the optical spectrum at the detector, and linking its amplitude and phase characteristics to the RF harmonic and intermodulation distortion. We showed that the distortion compensation can effectively improve the detected EVM in links with length lower than 40 km. We also studied the distortion stemming from the EDFA, showing that if the MZ bias is out of quadrature, the envelope of RF modulating signal is coupled to the average optical power. Then, the EDFA dynamic response to variations of the average optical power may cause signal distortion. The impact on a continuous OFDM signal is negligible, but if the signal is divided into frames and transmitted in bursts separated by few tens of microseconds, the dynamic response of the EDFA severely degrades the signal EVM. This is a serious limit for the implementation of the bias optimization technique, but it may be overcome with simple modification of the modulation stage. This concludes our investigation of the modulator bias optimization technique.

In this chapter we showed that the spectrum of the electric field propagating over the link can be manipulated to decrease the detected distortion. This concept can be extended noting that properly designed optical filters can manipulate the optical spectrum in order to perform all optical RF signal processing. An example is given in the next chapter, where we present a novel all-optical beam-former based on optical filters and capable of controlling the amplitude and the phase of the RF signals fed to an antenna array.

Chapter 6

An example of all optical manipulation of RF signals: the beam-former

One advantage of optical distribution links for wireless networks is the possibility of integration with optical signal processing functions. One notable example is the optical beam-former (BF). In this chapter we present a novel solution for an all-optical BF based on FBGs. This BF allows for remote centralized independent control of both amplitude and phase of each antenna in an array. It is designed to best integrate in WDM ROF links based on DSB modulation with 25 GHz-spaced wavelengths, and it is optimized for IEEE 802.11a 5 GHz signals with 20 MHz bandwidth. The amplitude control offered by this BF also permits to compensate for dispersion of the ROF link, which otherwise would cause DSB signal fading. The BF can be controlled by stretching or by adjusting the temperature of the FBGs. The former method allows for faster adjustment of the array radiation pattern. This is not a true time delay BF, so one of the limiting factors on the RF useful bandwidth is the "beam squint" effect. We will call this new device: two-stages beam-former (TS-BF) because it is constituted by an arrangement of two cascaded filters.

6.1 Interest of the proposed optical TS-BF and related literature works

Antenna arrays are becoming increasingly important in mobile communications because they allow for dynamic and fast shaping of the antenna radiation pattern without the use of mechanical parts. As described in the introduction to this thesis, page 12, radiation pattern shaping finds applications in both indoor and outdoor wireless networks.

Drawbacks for widespread application of all-electronic control of antennas amplitude and phase include cost, bandwidth limitations, size, weight, loss, and sensitivity to electromagnetic interference. Optical signal processing holds a great promise for alleviating these problems. For example, the so-called optical true time delay beam-formers (TTD-BF) feature wideband operation with flat frequency response, potentially limited only by the bandwidth of photodetectors and modulators. True wideband operation is respected because the TTD-BF acts on the relative delay, and not the phase, of each antenna signal in the array. Otherwise, the radiation pattern has different shape for different frequencies over the signal band: this is referred to as "beam squint" and is a serious problem for wideband systems like radars. However, many modern communication systems use narrowband signals and do not need a TTD-BF: for example, we remember that the bandwidth of IEEE 802.11a signals is only 20 MHz. For such narrowband signals, the beam squint can often be neglected, especially for indoor applications, and the control of signal phase instead of delay is acceptable. This assumption is confirmed in [182, page 31], where the 3 dB bandwidth of a phased array is calculated as:

$$\Delta f = 0.886B \cdot \frac{c}{L \sin \varphi}. \tag{6.1}$$

B is the beam broadening factor, typically valued between 1 and 2, and equal to 1 for uniformly illuminated arrays; L is the largest characteristic array dimension and φ is the steering angle. For linear arrays, L can be calculated from the number of antennas and their maximum separation d, defined by the condition $d \leq \lambda/2$, where λ is the radiation wavelength. This limit on the antenna separation is needed to avoid aliasing effects and strong secondary lobes in the radiation pattern [109, page 657]. Hence, for an 8 element array transmitting a 5 GHz signal ($\lambda = 6$ cm), the maximum L is equal to 21 cm and the maximum array bandwidth, considering $\varphi = 90°$, is about 1.2 GHz: much wider than the bandwidth of interest for wireless communications.

On the basis of these considerations, we proposed for the first time in [183] a novel optical FBG-based BF (named here TS-BF) that acts on signal phase instead of delay and is well suited for integration in ROF links for wireless communication systems. For this application, it offers several advantages over other BFs proposed in the literature, including simultaneous and independent control over amplitude and phase for each antenna in the array, high RF carrier frequency operation and compatibility with DSB modulation systems, good performance/complexity compromise and easy integration with antenna remoting links. In the following, we describe these features in detail.

Simultaneous and independent control over amplitude and phase for each antenna in the array

The flexibility in designing the shape of the radiation pattern depends on the number of degrees of freedom available in the array: simultaneous control of amplitude and phase of the signal of each antenna in the array (referred to as beam-forming) offers better flexibility in designing the radiation pattern than phase only control (beam-steering). Applications of interest for wireless communications like interferer nulling [43, 184], null steering [185], and array sidelobe minimization require complete amplitude and phase

array control. The TS-BF offers this functionality.

Most literature works based on FBGs allow only for beam-steering [186, 187, 188] by controlling the signals phase/delay. A few works describe independent control [189, 190, 191] of signals phases for each antenna. Simultaneous and independent control of amplitude and phase have been presented in [192] using a network of amplitude and phase modulators integrated on a silicon-based photonic circuit.

High RF carrier frequency operation and compatibility with DSB modulation systems

An important feature of the TS-BF is that it is designed to support DSB modulation, and can be adapted to operate with a broad range of RF carrier frequencies: from IEEE 802.11a 5 GHz to 10 GHz (for some flavors of IEEE 802.16), and even 40 GHz and 60 GHz wireless communication systems. Such high frequencies are attracting some attention for picocell indoor networks [193, 29], because interference from adjacent cells is reduced by high propagation losses [194]. Beam-steering is proposed in 40 GHz-60 GHz frequency systems to implement SDMA [195, 196].

Some optical BFs proposed in literature cannot reach very high RF carrier frequency in DSB modulation systems because they add chromatic dispersion to the signal. As we saw in chapter 3, fibre and optical components dispersion cause increasing RF signal fading at higher RF frequency. For example, RF signal fading has been observed in BFs based on chirped FBGs, due to the chirp-induced dispersion within the modulation sidebands [186, 197]. Several authors have proposed to solve this issue by using SSB modulation instead of DSB, but the former requires a more complex modulation stage. For example, SSB modulation is generated using sideband filtering [116], which is a conceptually simple technique but it requires the filter to be carefully tuned to sideband frequency. Other techniques for generating SSB signals include those based on a dual electrode MZ modulator [117], a Sagnac structure [198], or hybrid modulator structure [199]: all require non standard devices such as the dual electrode MZ, or elaborated arrangements of components. Also, the SSB modulation format does not allow the use of potentially low cost modulators, such as those based on the electro-absorption effect. Finally, the DSB modulation has a 3 dB advantage in both gain and NF over SSB modulation [60]. The TS-BF is not only compatible with DSB modulation, but can also be used to compensate for fibre dispersion and reduce the consequent DSB signal fading.

Another interesting BF solution is proposed by Roeloffzen [200], based on an assembly of ring resonators with periodic spectral response. This is a TTD-BF and it is dispersion-free, but its operation bandwidth is only a few hundred megahertz and it is not compatible with wireless network frequency ranges.

Good performance/complexity compromise

The TS-BF offers a good compromise between scalability with the number of anten-

nas and the number of components or beam-former complexity. It employs few optical components: $2N$ cascaded FBGs (that can be seen as two long FBGs) and a 4-port circulator (or two 3-port) for independent complex control of N antennas. In [190], independent control of signal phase only is obtained with N FBGs and N circulators for N antennas. In [188] and in [191], the beam-former is simpler (one FBG and one circulator) but the signal phases are not adjusted independently or there is no control over signal amplitudes.

Another advantage of the TS-BF is that it can potentially offer fast radiation pattern adjustment as needed for best multipath fading suppression [40] in indoor or campus mobile environment, where the antenna array points and follows an user moving at walking speed. The TS-BF can be controlled by stretching or by adjusting the temperature of FBGs. When the former method is used, the speed of reaction of the TS-BF is limited only by the speed of the stretcher. Piezoelectric stretchers can adjust the radiation pattern in a fraction of millisecond.

Easy integration with antenna remoting links

Optical beamforming in ROF links is most advantageous if the BF is designed to be localized and controlled at the central station (CS), in order to simplify the wireless termination points (WTPs). However, if the ROF link antenna addressing is based on WDM, the BF must operate with constant optical wavelengths and must not rely on tuneable sources: the operation wavelengths are fixed by the WDM filters which route the optical signals form the CS to the WTPs. Previously published works often rely on tunable lasers [201, 202] or thermal adjustment of the emission wavelength of DFB lasers [191]. The work presented in [190] uses fixed wavelengths but one FBG for each antenna in the array.

6.2 System level description of the TS-BF

Typically, a BF can be described by the sketch shown in Fig. 6.1a: a source signal is split into N branches, one for each antenna. Each branch is weighted by a coefficient a, complex in the most general case. The weighted signals are launched in air by the antennas and interfere constructively or destructively depending on the direction and the a coefficients, determining the array radiation pattern. The same concept is applicable in reception but, for simplicity, we limit our discussion here to the transmission case.

The TS-BF system level pattern is shown in Fig. 6.1b: the signal is imprinted on N wavelengths from a multi-wavelength source using a single optical modulator. Then, the wavelengths are filtered by the TS-BF, which changes phase and amplitude of the RF signal transmitted on each wavelength. This is equivalent to weighting each signal by a complex coefficient a. After filtering, the wavelengths are separated by an AWG and fed to an array of photodetectors and antennas. This solution allows to integrate

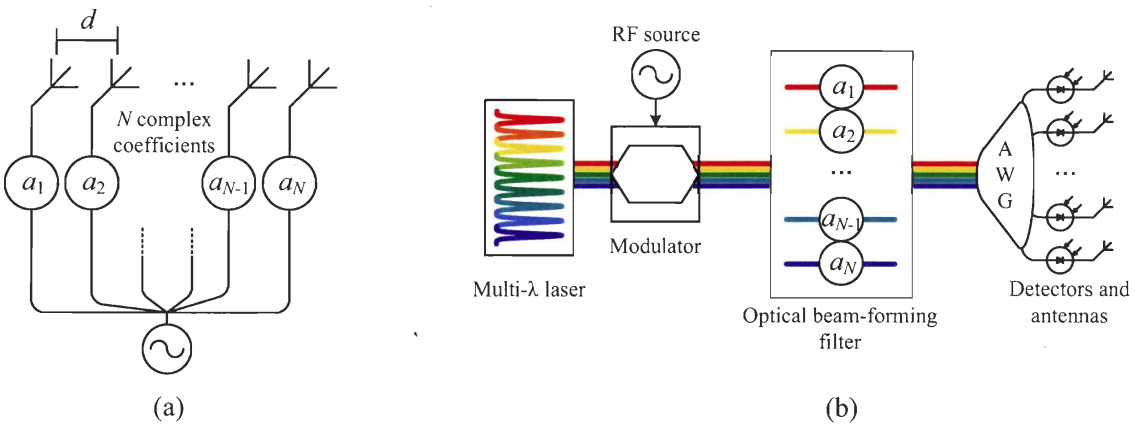

Figure 6.1: System level sketch of the TS-BF. (a) schematic of an RF BF. (b) Schematic of the TS-BF in a WDM-based ROF link.

efficiently the BF into a WDM-based ROF distribution link, and also permits to install the BF at the CS. In fact, the TS-BF is decoupled from the WTP and can be placed before the fibre span connecting the CS to the WTP.

In the following sections, we first describe the basic element of the TS-BF, which is the device that generates a single complex coefficient in optical domain for a single wavelength, or channel. After, we complete the description of the TS-BF by extending the single-channel solution to a multi-channel solution, ready for beam-forming applications.

6.3 Theory of operation of a single channel TS-BF

For low modulation depths, the baseband equivalent description of the optical field $E(t)$ of a DSB modulated optical signal can be approximated by the sum of three spectral components. After filtering the signal with an optical filter, we can write the spectrum as:

$$E(t) = A_C e^{j\varphi_C} + A_{SL} e^{j(-2\pi f_{RF} t + \varphi_{SL})} + A_{SU} e^{j(+2\pi f_{RF} t + \varphi_{SU})}, \tag{6.2}$$

where f_{RF} is the modulation RF frequency, A_C and φ_C are amplitude and phase of the optical carrier, A_{SL}, φ_{SL}, A_{SU} and φ_{SL} are the amplitudes and phases of the lower and upper modulation sidebands. In the most general case: $A_{SL} \neq A_{SU}$, but if the filter amplitude is constant over the spectrum band, we can take $A_{SL} = A_{SU} = A_S$. Thus, after beating onto a photo-detector, the detected RF voltage signal at f_{RF} is proportional to:

$$V_{RF} \propto A_C A_S \cos(\varphi_L - \varphi_U) \cdot \cos(\omega_{RF} t + \varphi_L + \varphi_U), \tag{6.3}$$

where $\varphi_U = \frac{\varphi_{SU} - \varphi_C}{2}$ and $\varphi_L = \frac{\varphi_C - \varphi_{SL}}{2}$ represent half the accumulated phase difference between the sidebands and the carrier due to the filter phase response. As shown by

(6.3), it is possible to independently set the amplitude and phase of the received signal by controlling φ_U and φ_L. Note that φ_U and φ_L can be written as:

$$\varphi_L = \frac{1}{2} \int_{-\omega_{RF}}^{0} D(\omega)\, d\omega \qquad \varphi_U = \frac{1}{2} \int_{0}^{\omega_{RF}} D(\omega)\, d\omega, \tag{6.4}$$

where $\omega_{RF} = 2\pi f_{RF}$ and $D(\omega)$ is the group delay response of the optical filter. Also, note that the RF signal phase is defined by the average value between $\varphi_{SU} - \varphi_C$ and $\varphi_C - \varphi_{SL}$. With fibre dispersion, equation (6.3) transforms into:

$$V_{RF} \propto \cos\left(\varphi_L - \varphi_U + \frac{L_f \mathrm{D}_f}{4\pi c}\lambda_0^2 \omega_{RF}^2\right) \cdot \cos\left(\omega_{RF} t + \varphi_L + \varphi_U\right), \tag{6.5}$$

where D_f is the fibre dispersion, L_f the fibre length, c the speed of light and λ_0 the optical carrier wavelength. Thus, by controlling $\varphi_L - \varphi_U$ it is possible to compensate for dispersion induced signal fading: signal amplitude manipulation by acting on $\varphi_L - \varphi_U$ is indeed equivalent to adding a controlled amount of negative or positive dispersion to the DSB optical signal.

The central question is how to gain simultaneous and independent control over φ_L and φ_U, leading to the original idea of the proposed TS-BF. For a single channel, its structure is sketched in Fig. 6.2.

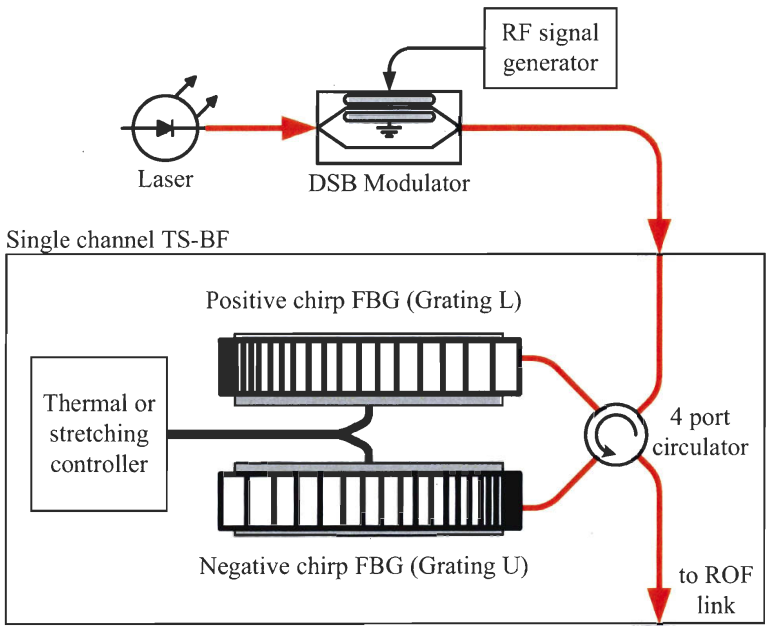

Figure 6.2: The proposed novel optical BF. The signal from a laser source is modulated by a DSB modulator and filtered. The laser wavelength is filtered twice by separated FBGs, one with positive chirp $+C$, the other with negative chirp $-C$. By adjusting the temperature or by stretching each FBG, phase and amplitude of the RF signal which modulates the laser can be controlled independently.

The BF is physically formed by two FBGs, one with positive chirp $+C$ and the other with negative chirp $-C$. We will refer to the gratings as FBG_L and FBG_U, because

their delay response is designed to have a peak-like structure centered respectively onto the lower and upper modulation sidebands of the optical spectrum, as shown in Fig. 6.3. The FBG_L and FBG_U are designed as all pass filters with flat amplitude response. Amplitude and delay responses of the gratings are important only in the zones described by solid lines in Fig. 6.3, as will be clearer later, because the responses outside these zones (dotted sections) do not influence the performance of the beam-former. The total TS-BF group delay for one channel is the sum of the group delay of FBG_L and FBG_U, whose opposite chirp ensures that the total chirp, and corresponding dispersion, are zero.

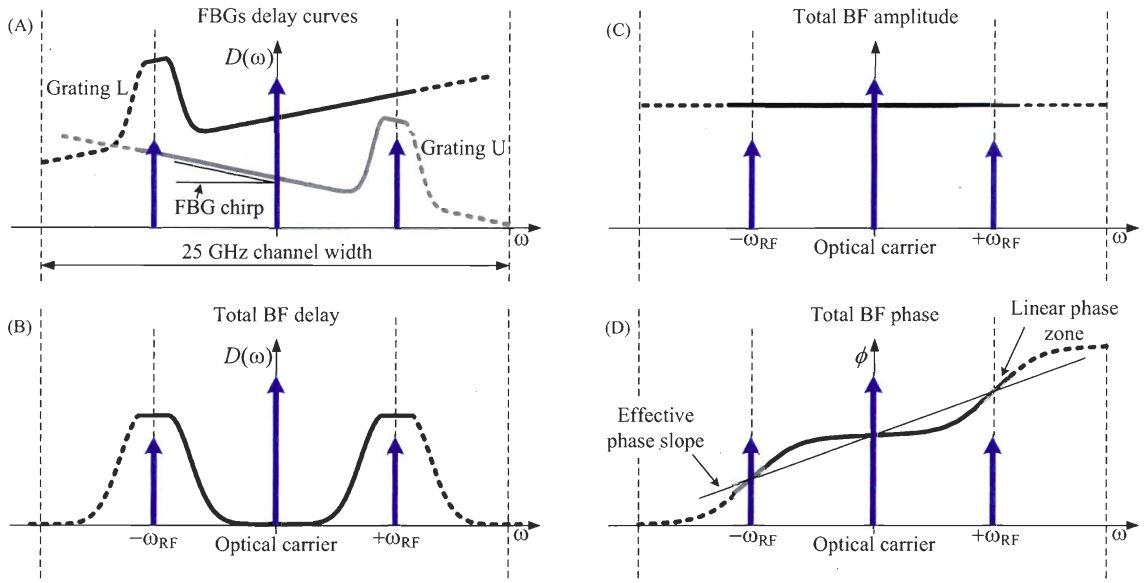

Figure 6.3: Sketch of the amplitude and delay response of the gratings for the TS-BF. (A) delay response of FBG_L and FBG_U. (B) the total delay response after cascading the FBG_L and FBG_U. (C) Total amplitude response and (D) total phase response. The dotted lines represent zones of the filters response which do not affect the behavior of the beam-former. In blue: the optical carrier and 5 GHz modulation sidebands.

Recalling (6.4), we note that the values of φ_L and φ_U are each defined by the total accumulated delay integrated respectively in the lower and upper portion of the spectrum, between the modulation sidebands and the optical carrier. By stretching or controlling the temperature of the gratings, their delay response can be shifted, thus affecting the values of φ_L and φ_U. The grating design ensures that, for small amounts of shift, φ_L is affected only by the position of FBG_L, and φ_U by FBG_U. Also, small shifts ensures that the dotted zones of the filter response in Fig. 6.3 always stay outside the spectrum region comprised between the two modulation sidebands, and do not affect φ_L and φ_U.

The values of φ_L and φ_U, from their definition, represent the accumulated phases of the modulation sidebands with respect to the optical carrier. The phase φ_c of the optical carrier itself can be assumed as a fixed zero phase reference that does not change when FBG_U and FBG_L are shifted. If the gratings are shifted symmetrically with respect to

the optical carrier (Fig. 6.4, A and C), φ_L and φ_U have the same value: $\varphi_L - \varphi_U = 0$, and the RF signal is phase shifted with constant amplitude. This is sketched in Fig. 6.4C, where the phases of the carrier and modulation sidebands are represented by small red circles. With symmetrical grating shift, the three phases are always aligned on a straight line with changing slope, which is equivalent to a dispersion-free total delay response. With asymmetrical grating shift, $\varphi_L - \varphi_U \neq 0$ and the RF signal amplitude is attenuated. We showed in (6.5) that the signal attenuation is obtained by adding a controlled amount of dispersion to the optical signal, which can also counterbalance link dispersion from fibre and other devices. This is shown by 6.4D: because of the asymmetrical grating shift, the phase of the modulation sidebands and optical carrier are no longer aligned on a straight line but can be connected by a parabolic curve of positive or negative curvature, which is equivalent to a positive or negative group delay dispersion. Note in (6.3) that the RF signal amplitude A and phase ϕ are set respectively by $A = \cos(\varphi_L - \varphi_U)$ and $\phi = \varphi_L + \varphi_U$: two independent equations in two independent variables. Hence, we can have independent and simultaneous control over both A and ϕ.

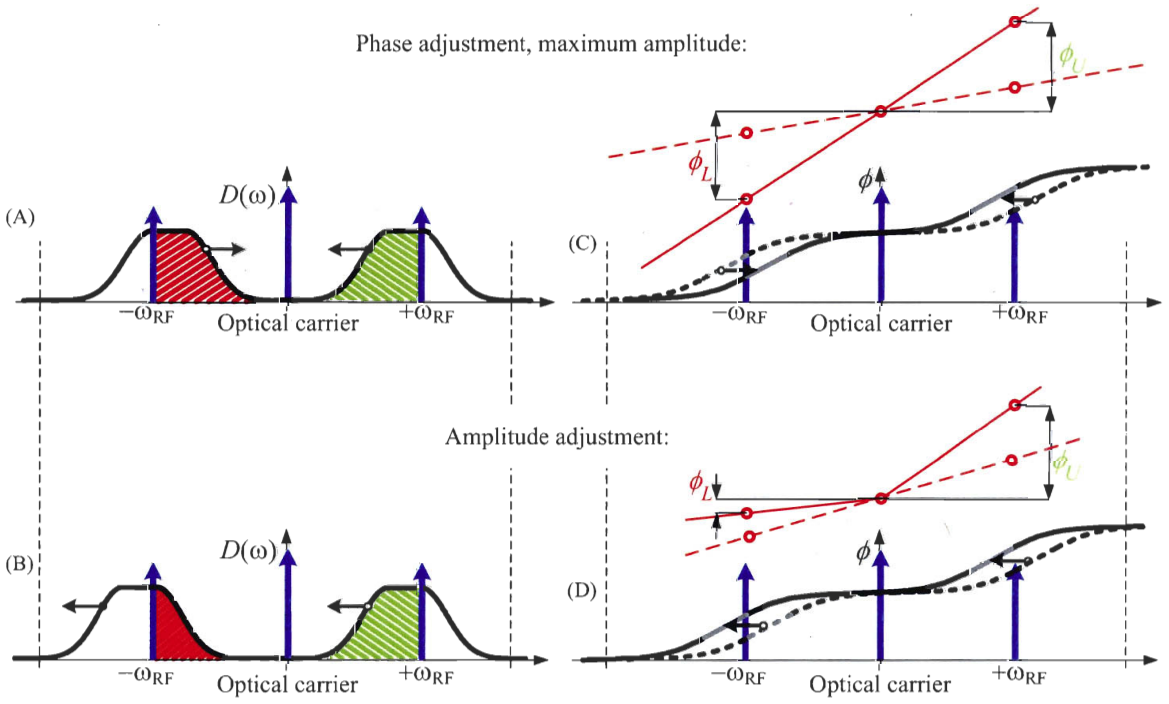

Figure 6.4: Theory of operation of the TS-BF. A and C: symmetrical grating displacement; B and D: asymmetric grating displacement. In C and D, the black lines represent the accumulated phase in the optical signal spectrum before (dotted black line) and after (solid black line) the grating displacement. The red lines are used to highlight the variations of φ_L and φ_U when the grating are moved from a reference position (red dotted lines, $\varphi_L = \varphi_U$) to a new position (solid red line). After a symmetric grating displacement φ_L is still equal to φ_U, while after asymmetric displacement $\varphi_L \neq \varphi_U$.

6.3.1 Operation with narrowband modulated RF signals

As we anticipated in the introduction to this chapter, the TS-BF is not a TTD-BF. This can be understood by comparing the effect of a true time delay and the operation of the TS-BF, as shown in Fig. 6.5. A true time delay corresponds to a flat delay line covering the entire signal spectrum, which is a constant slope phase response: increasing the delay will increase the phase slope for all signal frequencies. Note that the phase retardation ϕ due to the increase in the phase slope is not constant over the signal bandwidth, but increases linearly with frequency. Instead, the TS-BF phase response in a narrow bandwidth around the carrier never changes slope with FBG_U and FBG_L positions, which corresponds to imposing the same phase retardation ϕ over all the signal (baseband) bandwidth[1].

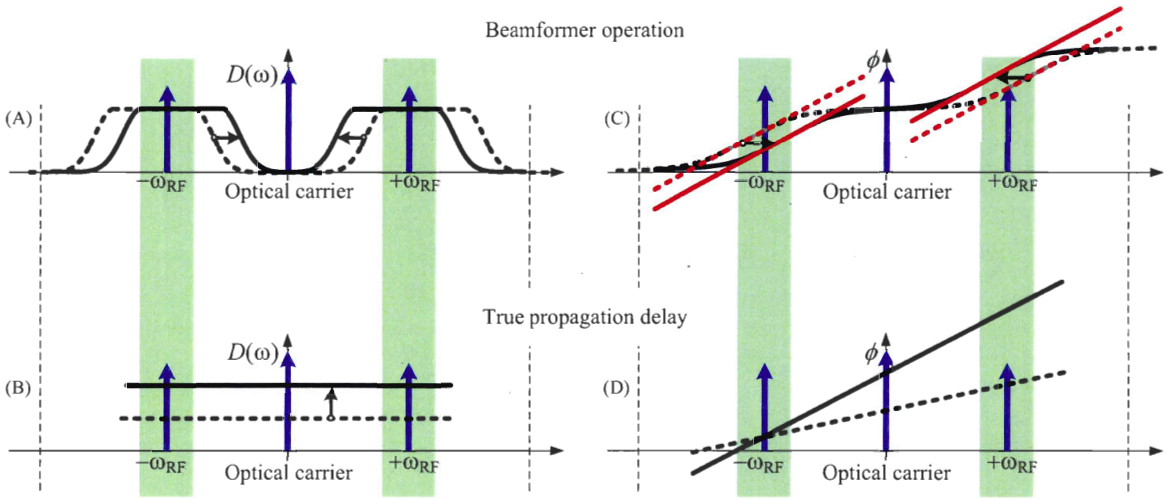

Figure 6.5: The beam squint effect in the TS-BF. A and C: symmetric grating displacement changes the signal phase ϕ, but the phase slope over the signal bandwidth remains unchanged. B and D: On the contrary, a true delay changes the inband phase slope.

6.3.2 Required amounts of amplitude and phase control

For a linear antenna array with constant element spacing d, the beam pointing direction is defined by:

$$\sin(\alpha) = \frac{c}{d}\Delta\tau, \tag{6.6}$$

where α is the beam steering angle and $\alpha = 0$ when the beam main lobe points in the direction normal to the array, c is the speed of light and $\Delta\tau$ is the time delay difference

[1]We refer here to the bandwidth of the baseband signal, which modulates the RF carrier in the RF domain. This bandwidth must be small with respect to the frequency of the RF carrier in order to respect the narrowband modulation condition. This is not to be confused with the bandwidth of the optical signal.

between signals fed to adjacent antennas. For a steering angle $\alpha = \frac{\pi}{2}$ and an element spacing $d = \frac{\lambda_{RF}}{2}$, $\Delta\tau = \frac{T_{RF}}{2}$. In normalized units $T_{RF} = 2\pi$ and $\Delta\tau = \pi$. If the array has 8 antennas, the last antennas must be able to accumulate a delay up to $\pm 3.5\pi$ to ensure a 180° steering range. For a 5 GHz RF carrier, this means that the beam-former must be able to offer a maximum of 700 ps of signal delay tunability range. This is quite a difficult value to reach with the proposed TS-BF because it requires the design of FBGs with an exceedingly large peak delay response. However, the TS-BF is designed to be used with narrowband RF signals which have a slowly varying carrier envelope. Hence, the phase retardation of the signals fed to each antenna can be wrapped in within the $[-\pi, \pi]$ range. This causes a perturbation on the radiation pattern, which adds up with the beam squint effect discussed before. In the special case of simple beam steering, we simulated the maximum error on the beam pointing direction and on the half power beam width as a function of the signal frequency and steering angle, taking into account both the beam squint effect and the phase wrapping. The phase wrapping is a source of error on the radiation pattern because far-field interference of the antenna patterns does not occur on the same wavefront for all the antennas, and the signal envelope varies (slowly) between adjacent carrier periods. The results of the simulations are shown in Fig. 6.6: the radiation pattern for a 20 MHz bandwidth signal is affected by a maximum pointing error of less than 0.4°, which is only 1.3% of the 3 dB angular beam width. The simulations considered an 8 antennas uniform linear array with $\frac{\lambda_{RF}}{2}$ spacing, $f_{RF} = 5$ GHz and a maximum steering angle of 75°.

For beam-steering, the amplitude apodization of the signals driving the array antennas can be designed using a number of techniques. All try to minimize both the radiation pattern sidelobes and main lobe angular width. One method that provides very low sidelobes (but large main lobe) is the binomial design technique, which is interesting to us here because it uses very aggressive amplitude apodization [109, page 680]. For example, an 8 element array with binomial design requires a maximum amplitude attenuation (on the first and last antennas) of about 30 dB. More common radiation pattern designs often use attenuation levels of the order of 6 dB. However, from (6.5) we also know that the proposed TS-BF can be used to compensate for dispersion induced signal attenuation: the higher the attenuation that the TS-BF can reach in a dispersion-free link, the higher the dispersion that the TS-BF can compensate. For this reason, we take 30 dB as the maximum amount of amplitude control that the TS-BF must be able to achieve.

In conclusion, for the TS-BF we target a 2π range phase retardation and up to 30 dB amplitude attenuation for each signal in the antenna array.

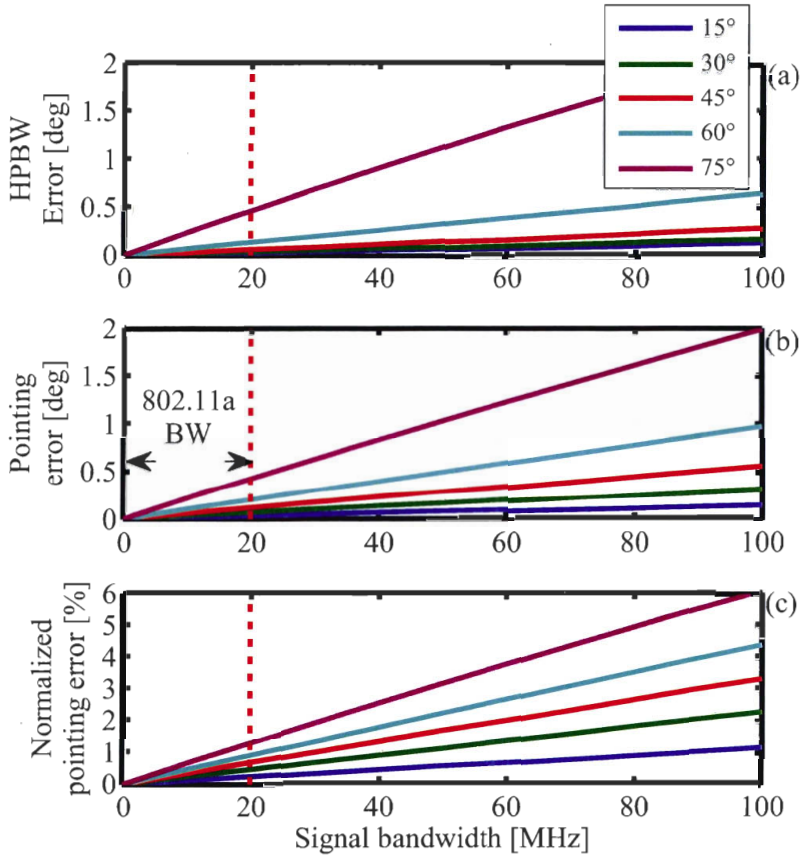

Figure 6.6: Errors in definition of a linear beam-former radiation pattern as a function of RF baseband signal bandwidth and pointing angle with respect to the direction normal to the array. (a) Error on the half power beam width; (b) Error on the pointing direction; (c) Error on the pointing direction normalized by the beam width. The simulation takes into account the beam squint due to signal phase control instead of delay, and the error on phase and amplitude phase wrapping to keep signals phase retardation in within the $[-\pi, \pi]$ range. Phase wrapping causes some amplitude error because the envelope is (slowly) varying between carrier periods. The curves are calculated for a 8 antennas array (antennas spacing: $\lambda_{RF}/2$), $f_{RF} = 5\,\text{GHz}$.

6.4 The Gires-Tournois single channel design solution

The experience gained in our laboratory on the design and manipulation of FBG-based coupled cavities periodic filters suggested an initial grating design with the amplitude and delay responses needed by this application.

In this first design, published in [183], the FBG_U and FBG_L are realized using two Gires-Tournois FBG coupled cavities (GT-CCs). A Gires-Tournois cavity is a Fabry-Perot etalon with a 100% backreflector. This is an all pass filter operating in reflection, and it has spectrally periodic group delay variations with free spectral range (FSR) fixed by the cavity length. In order to tailor the shape of the group delay

response of the filter, lattice coupled cavities [203] might be implemented by adding more reflectors with the same relative spacing and conveniently designed reflectivities. In the following, we assume that the reflectors are made by superimposed chirped FBGs, so two sets of superimposed FBGs form the two Gires-Tournois with coupled cavitiess (GT-CCs), which are cascaded through the four port circulator to form the TS-BF. As explained in section 6.3, the amplitude and phase responses of the TS-BF are controlled by shifting the frequency response of the superimposed chirped gratings by controlling their temperature or by imposing a strain. However, note that in this section we do not simulate the temperature or stretching control of actual gratings. Instead, we base our design on the Madsen's lattice coupled cavities theory, which assumes the gratings to be like lumped or discrete reflectors. The main advantage of this approximation is that it allows a rapid design of the most important TS-BF parameters, such as the number of gratings per GT-CCs and the grating reflectivities.

Let m be the number of coupled cavities forming each Gires-Tournois: the higher the m, the easier it is to tailor the GT-CCs delay and amplitude response. The theoretical delay response of an m cavities Gires-Tournois limits the values of φ_L and φ_U over a maximum range of $m\pi$, which corresponds to a maximum signal phase retardation of $2m\pi$. However, covering all the phase retardation range demands very large shifts of the delay peaks, which is impractical for a single cavity design. So, $m > 1$ is needed for $[0, 2\pi]$ phase retardation range. By increasing m, the phase retardation range can be covered with a smaller peak delay shift. Furthermore, the delay peak must feature a flat top large enough to ensure a flat filter delay response for all values of phase retardation. For high m and small peak shifts, it is easier to respect this design constraint. The maximum m is fixed by practical limitation in the feasibility of the GT-CCs with several superimposed gratings and by the maximum grating length.

We designed the GT-CCs using 3 coupled cavities (4 reflectors, or superimposed chirped FBGs in the discrete reflectors approximation). The delay response of each GT-CC over one FSR, neglecting the grating chirp, is shown in Fig. 6.7. The design is accomplished in three steps: first we define a target group delay response for a cavity FSR of 25 GHz and a 5 GHz RF modulation signal with a maximum of 100 MHz bandwidth. The FSR fixes the separation between the reflectors. After, we describe the amplitude and delay responses of the GT-CCs using a polynomial autoregressive moving average (ARMA) model [203]. The polynomial coefficients are calculated from the FBGs reflectivities using a step-up algorithm [203]. Then, we can apply an optimization algorithm on the reflectivity values in order to best approximate the target delay response. This, for the GT-CC centered on the lower modulation sideband, is defined as shown by the green bold lines in Fig. 6.7. The width of the flat top region in the delay response must be narrower than 5 GHz to ensure that φ_L and φ_U can be controlled independently by the position of the lower and upper sideband delay peak, respectively. However, the resolution on the position of the peaks is finite and fixed by the temperature or stretching controller resolution. Thus, a large flat zone allows for better phase shift resolution. We define the target delay curve with a flat zone width of 2.5 GHz and a minimum value in the region between the optical carrier and the

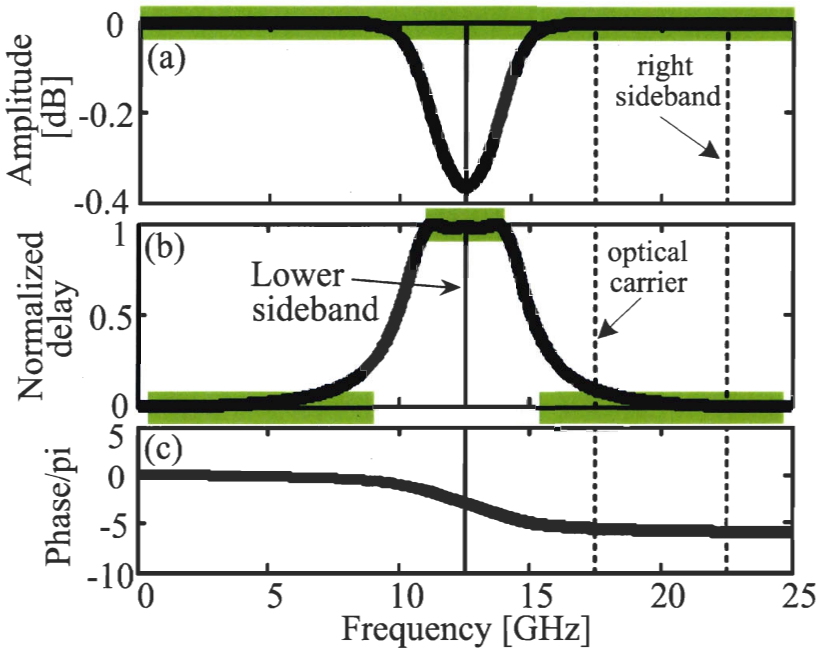

Figure 6.7: Design of a three-cavity GT-CC for the lower sideband. Grey lines represent the design target. (a) Amplitude response. (b) Normalized delay response. (c) phase response: the total phase difference between FSR edges is 6π, i.e., 2π for each cavity.

right sideband to ensure maximum decoupling between φ_L and φ_U. Also, we impose a maximally flat GT-CC amplitude response.

The design process provides the reflectivity values of the GT-CC gratings (in the discrete reflector approximation) and the coefficients of the polynomial ARMA model, which describe the amplitude and delay responses of the two GT-CCs. We used the ARMA model to simulate the phase and amplitude response of the one channel TS-BF. The results are shown in Fig. 6.8 as bidimensional maps as a function of the GT-CCs delay peak positions with respect to the signal modulation sidebands. Remember that the GT-CCs are one possible way of designing the gratings that we previously named FBG_U and FBG_L. Hence, in Fig. 6.8 we refer to "GT-CC U" and "GT-CC L" to designate the GT-CCs corresponding to FBG_U and FBG_L respectively. Moving the GT-CCs delay peaks position along the secondary diagonal of these maps, from (-1.2, -1.2) GHz to (1.2, 1.2) GHz along the A-B path, the BF gives 2.3π phase shift of the RF signal with variations on amplitude lower than 0.5 dB. To get exactly constant amplitude, the working point can be moved on the amplitude isolines shown in Fig. 6.8. The phase is constant and amplitude varies when moving the delay peaks along the main diagonal, identified by the C-D path.

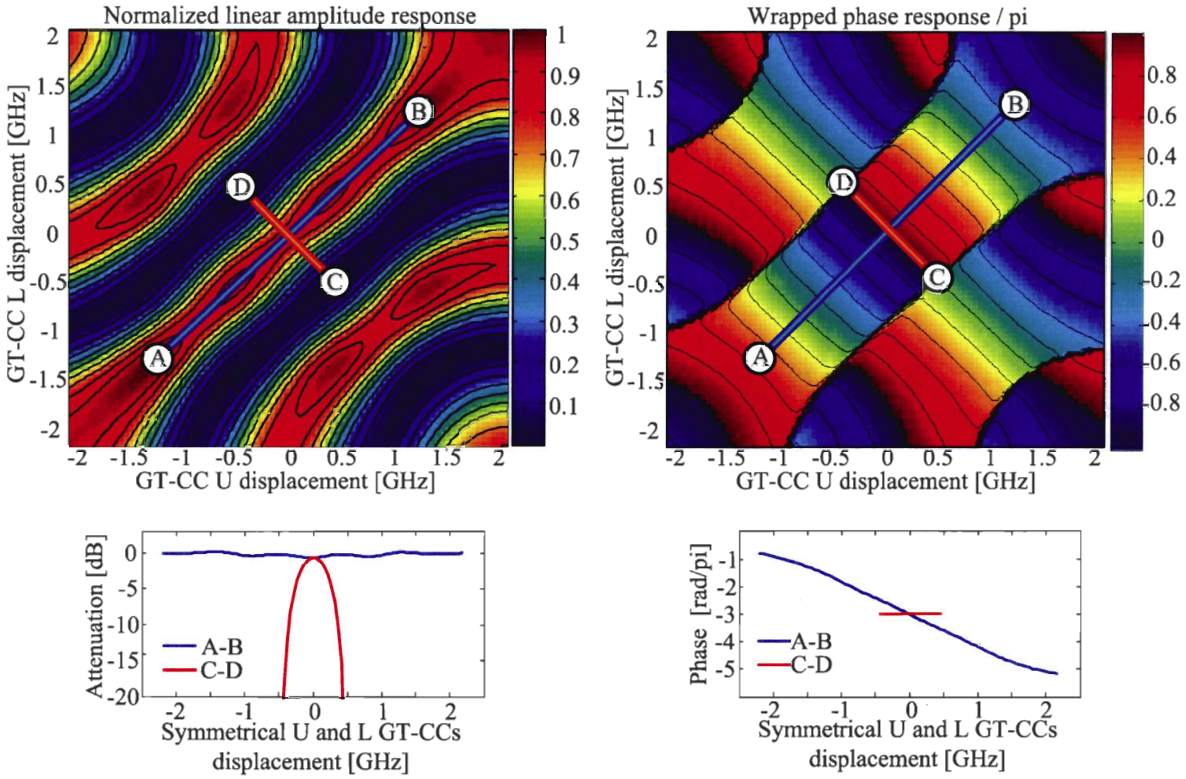

Figure 6.8: Phase and amplitude maps for the BF based on Gires-Tournois coupled cavities. If the GT-CCs frequency responses are shifted along the A-B path, or the secondary diagonal of the maps, the amplitude of the RF signal detected after the TS-BF is constant, while the phase changes by more than 2π. A shift on the C-D path, or the main diagonal of the maps, keeps the phase constant and changes the amplitude.

6.5 Experimental verification with a simplified design

Note that the GT-CCs design algorithm described previously outputs the reflectivities of the chirped superimposed FBGs and their relative positions, as determined by the FSR. However, this design technique models the FBGs as localized (lumped) reflectors, which is a rather poor assumption: the FBGs are distributed reflectors and, in order to ensure the correct phase relation among the coupled cavities in the GT-CC, the relative position between the gratings must be corrected to take into account for nonzero interaction or penetration length of the signal in the FBGs. Furthermore, the amount of the correction depends on the gratings strength. Thus, if we calculate the modulation index obtained by superimposing the gratings with positions and reflectivities given by the optimization algorithm, we obtain a GT-CC with very different phase and amplitude response. The problem of adjusting the relative position of the four gratings to obtain the right GT-CC response is quite complex and we solved it by using a genetic optimization algorithm, which provides the modulation index design of the GT-CC. Even with a proper modulation index design, a physical realization of the GT-CCs is complex. Superimposed chirped FBGs can be written in fibres by successive

exposures of the fibres to ultraviolet light through a chirped phase mask. However, this method is not practical for more than two superimposed FBGs, because, among other problems, it is hard to precisely and simultaneously control the phase of the coupled cavities and the reflectivities of the cavity reflectors: these two critical parameters are coupled and depend on the grating strengths, which are nonlinear function of the fibre photosensitivity, number of superimposed gratings and other experimental parameters of the writing process. An alternative solution is based on the use of phase sampled phase masks, which allow to write the GT-CC in a single UV scan: in this method the complexity of the GT-CC modulation index is implemented into the mask itself. However, a different phase sampled phase mask must be calculated and fabricated for each GT-CC design, and this is an expensive procedure. So, we decided to test the validity of our model and simulations with a simpler one cavity Gires-Tournois (GT) design, which can be realized easily with the facilities available in COPL.

The simulated and measured delay curves of a single cavity GT over several FSR are shown in Fig. 6.9.

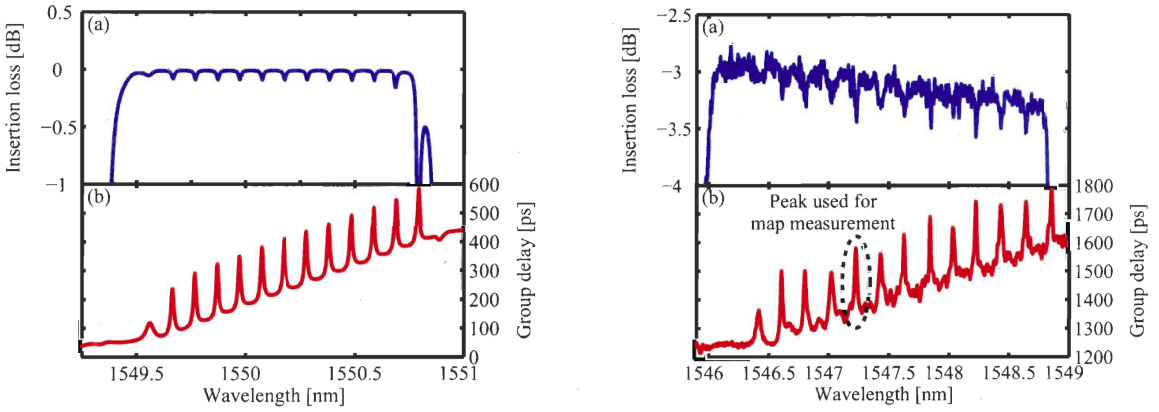

Figure 6.9: (a) simulated and (b) measured spectrum and delay response of a single cavity GT. GT-CC simulation parameters: grating length: 50mm; number of transfer matrix segments: 1000; modulation index amplitude of first grating: $1.1\exp^{-4}$; modulation index amplitude of second grating: $3.5\exp^{-4}$; chirp 0.5 nm/cm. Experimental GT-CC parameters: fibre: H_2-loaded `UVS-INT`; UV laser power: 40 mW; chirp $\pm$0.5 nm/cm; mask scanning speed for first grating: 0.09 mm/s; mask scanning speed for second grating: 0.3 mm/s; grating relative shift: 3.9 mm; grating length 50 mm.

Two single cavity GTs filters with opposite chirp have been mounted in the TS-BF setup shown in Fig. 6.10. The signal from a tunable laser is modulated with a 5 GHz tone by a MZ with bias fixed at quadrature by a feedback circuit. The optical signal is then amplified and filtered by the TS-BF. Note that the tunable laser is used to have more freedom in selecting one specific peak pair in the TS-BF response, but its wavelength is fixed for all measurements. The delay peaks are aligned with the modulation sidebands by controlling the temperature of both gratings and by stretching slightly one of them. We programmed in the LabView environment to automatically control the entire setup: the software sends commands to the thermal controller to fix the temperature of the gratings. After a few seconds for thermal stabilization, the

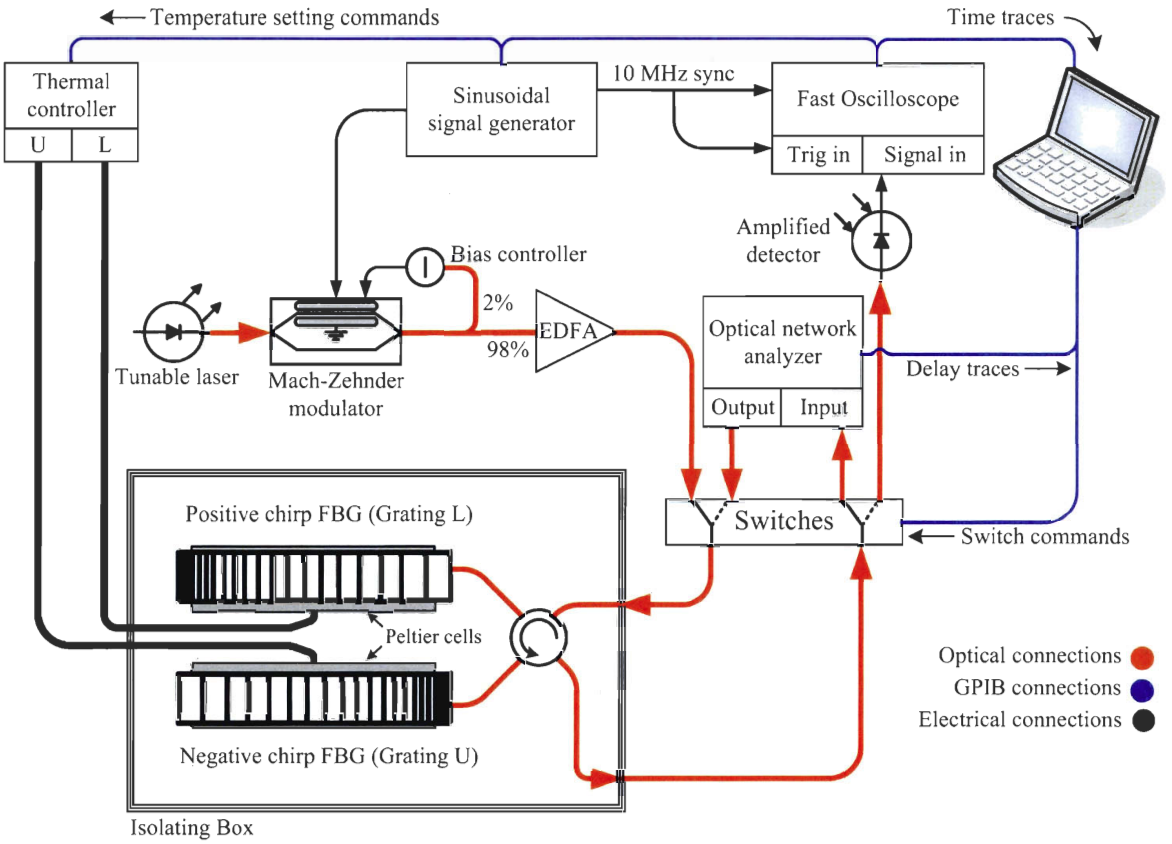

Figure 6.10: Setup for measurement of the amplitude and phase of a single channel TS-BF. Tunable laser: `Phonetics Tunics-BT`; modulator: `JDS OC-1`; EDFA: `JDS OAB1552+1FA0`; switch: `JDS SB series`; Thermal controller: `ILX LDT 5910B`; signal generator: `Agilent E4438C`; fast oscilloscope: `Agilent DSO81004B Infiniium`, real time, 10 GHz bandwidth; EVM analyzer: `Agilent E4440A`; optical network analyzer: `Advantest Q7750`.

fast oscilloscope is used to acquire an image of the filtered and detected sinusoidal signal. The oscilloscope is synchronized with the RF signal generator and triggered on a 10 MHz reference clock, also given by the RF signal generator and in a fixed relation of phase with the 5 GHz tone. On the oscilloscope, the 5 GHz trace appears stable, it is averaged over 16 traces, acquired and saved on the computer. After, the switches are set to exclude the laser and the detector from the circuit and, instead, feed the TS-BF with a test signal coming from the optical network analyzer (ONA), which is used to measure the optical delay of the TS-BF. With this second measurement, we can ensure to properly map the temperature settings to values of shifts of the delay peaks, so that we can calculate amplitude and phase maps as a function of the actual frequency shifts of the delay peaks. All the data is saved on a computer and post-processed using MatLab code to calculate the amplitude and phase maps shown in Fig. 6.11, where they are compared with the simulation maps.

The simulation of the amplitude and phase maps is based on the response of ideal gratings. As anticipated, one cavity does not allow for 2π RF signal phase retardation: the maximum simulated and measured retardation is about 1.6π. Also, the control over

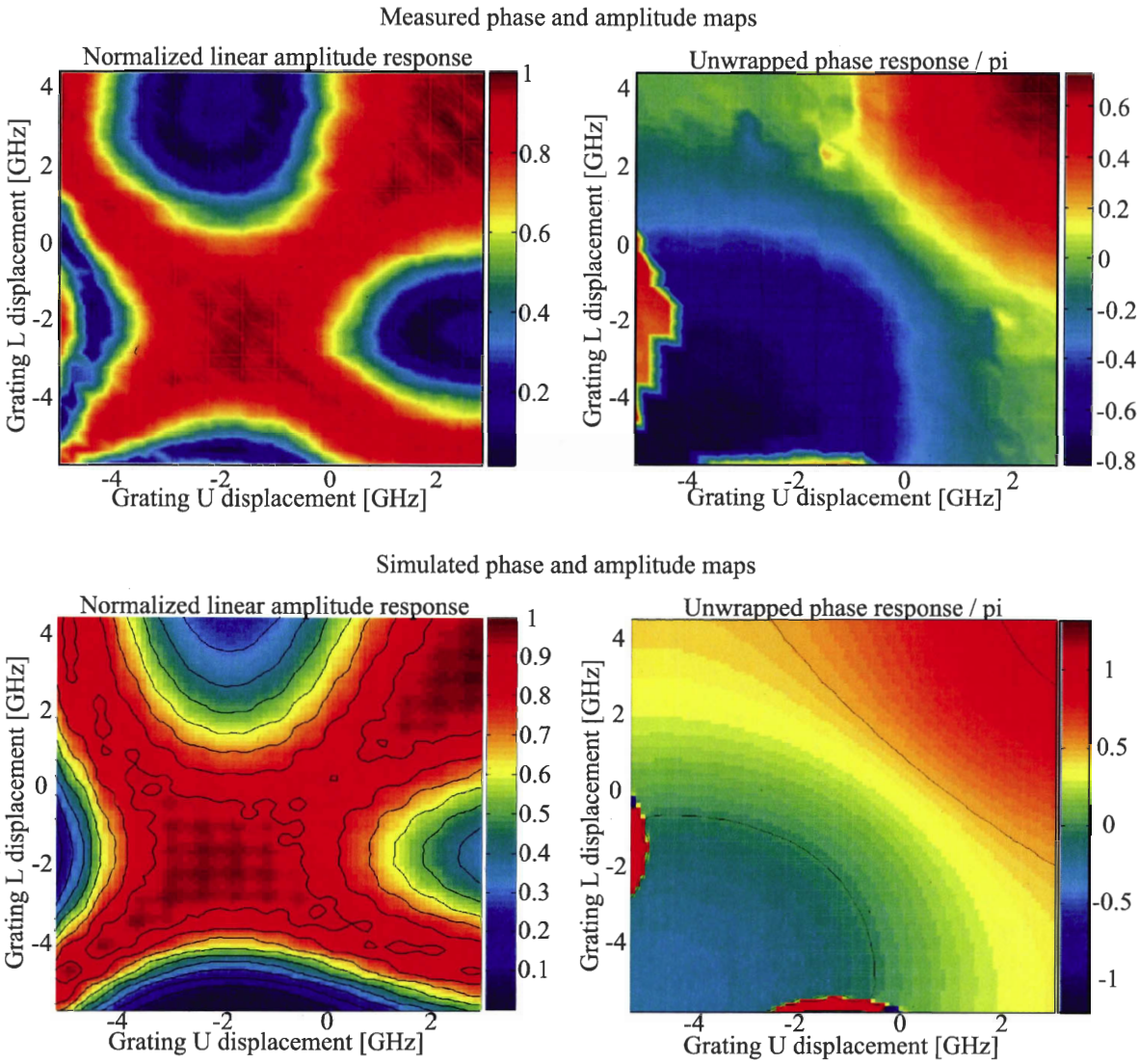

Figure 6.11: Measurement and simulation of the GT amplitude and phase maps.

the amplitude is possible only for a limited range of phase values, confirming that a single cavity design is not the best solution for beamforming applications. However, the good match between measurements and simulations demonstrates that we model properly the TS-BF.

6.6 Moving towards a multichannel solution

A single channel optical filter that can act on the amplitude and phase of an RF signal finds applications by itself as complex tap generator in RF photonic multi-tap filters or optical signal processors, in a configuration similar to the one shown in Fig. 6.12. Complex taps offer the highest flexibility in designing the filters [204, 205]. Clearly, the

limitation here is the narrow bandwidth of operation of the filter.

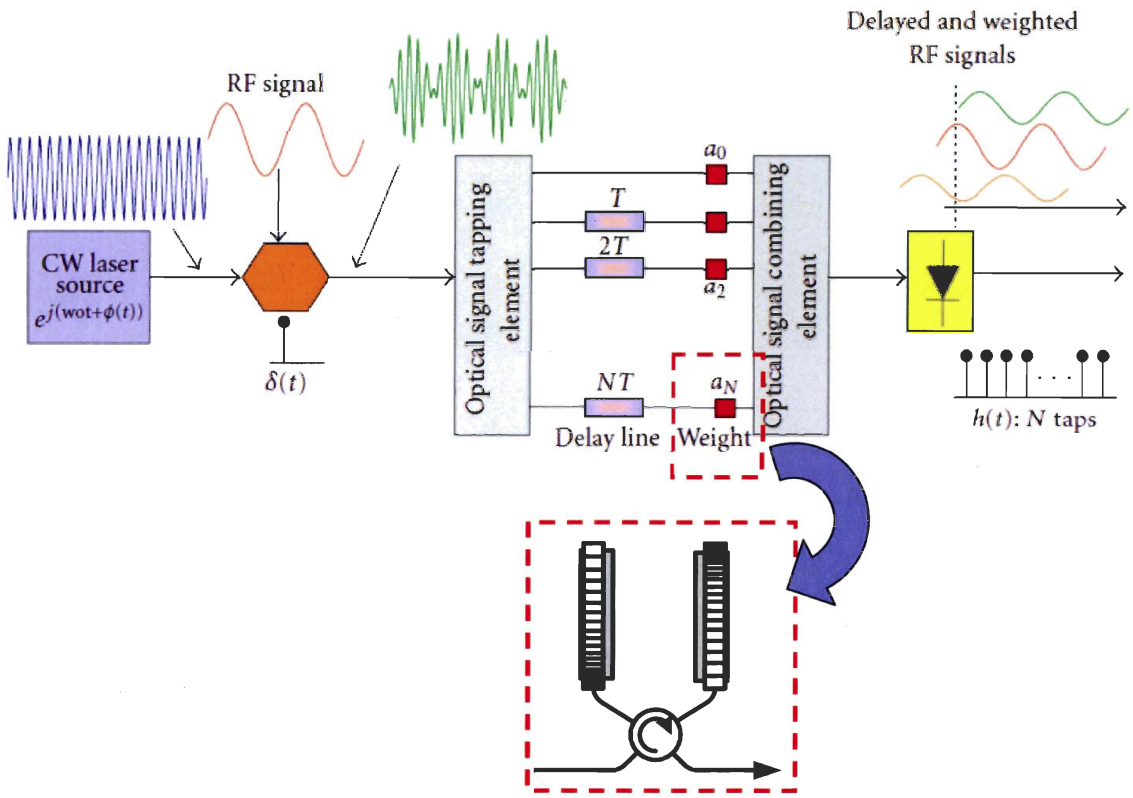

Figure 6.12: Sketch of an optical multi-tap filter. Adapted from [204].

For beam-forming it is fundamental to be able to extend the single channel TS-BF to a multi-channel TS-BF. When we first proposed the Gires-Tournois coupled cavities solution, we thought that it would have been possible to easily extend it to multiple channels. The idea was to use a structure similar to the distributed GT filter for multichannel dispersion compensation proposed by Doucet *et al.* [206]: we thought that, with the right GT-CCs design, it would be possible to control all the RF signals for all the antennas in the array by associating each signal to a different resonance of the periodic response of the GT-CCs. We assumed that it would be possible to map each resonance to a different physical section of the GT-CC gratings and to control these sections independently one from an other. This was suggested by the fact that the minimum physical length of a series of N coupled cavities with a given resonance is, from the well known Fabry-Pérot relation:

$$L_{TOT} = NL_{cavity} = N\frac{c}{2n_g \mathrm{FSR}}, \tag{6.7}$$

where c is the speed of light, n_g is the fibre group index, and FSR is the GT-CC free spectral range. For a three-cavity design with 25 GHz FSR: $L_{TOT} \simeq 1.2\,\mathrm{cm}$. From the gratings chirp C, it is also possible to calculate the physical spacing d_{FSR} between two

consecutive group delay peaks, which is the cavity spacing:

$$d_{FSR} = \frac{\text{FSR}}{C}. \tag{6.8}$$

We were aware that (6.7) was a simplification of a more complex reality because it considers the gratings as localized reflectors. This is indeed a poor assumption: the cavities extend much more than L_{TOT} because the gratings have non-zero length of interaction with the optical signal. However, we thought that by choosing $d_{FSR} \gg L_{TOT}$ it would have been possible to effectively separate the FSRs in such a way that each FSR, and signal wavelength, was mapped to a different portion of the GT-CC gratings. Then, temperature or stretching control of each section of the gratings would have affected the signal wavelengths separately and independently.

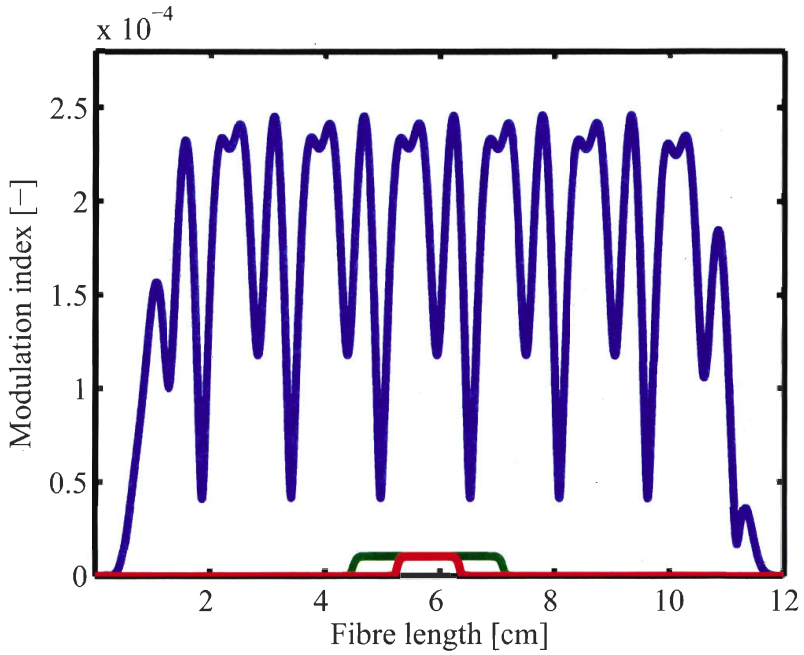

Figure 6.13: Modulation of the refractive index of a three-cavity GT-CC. In blue is the modulation index. Red and green curves represent a thermal perturbation of the modulation index over 1 cm and 2.5 cm respectively. The average index of the perturbed zone is increased by $1 \cdot 10^{-5}$, which correspond to about 1°C of temperature variation and 1 GHz of local Bragg wavelength shift. The theoretical cavity spacing d_{FSR} is 2.2 cm.

To test these ideas, we designed a three-cavity GT-CC grating, and we simulated a local variation of temperature, which causes a variation of the average index of a specific location along the GT-CC grating. We tried to optimize the width and position of the perturbed zone to observe the shifting of a delay peak while the adjacent peaks stay unchanged. Examples of the results are shown in figures 6.13 and 6.14. The simulation was performed with a chirp of 0.09 nm/cm, which gives $d_{FSR} = 2.2$ cm; the GT-CC grating is 12 cm long and has four central peaks with flat delay shape, as required by the TS-BF design. We have never been able to shift a delay peak while keeping its shape and leaving unchanged the adjacent peaks: the shape of the delay peaks appear

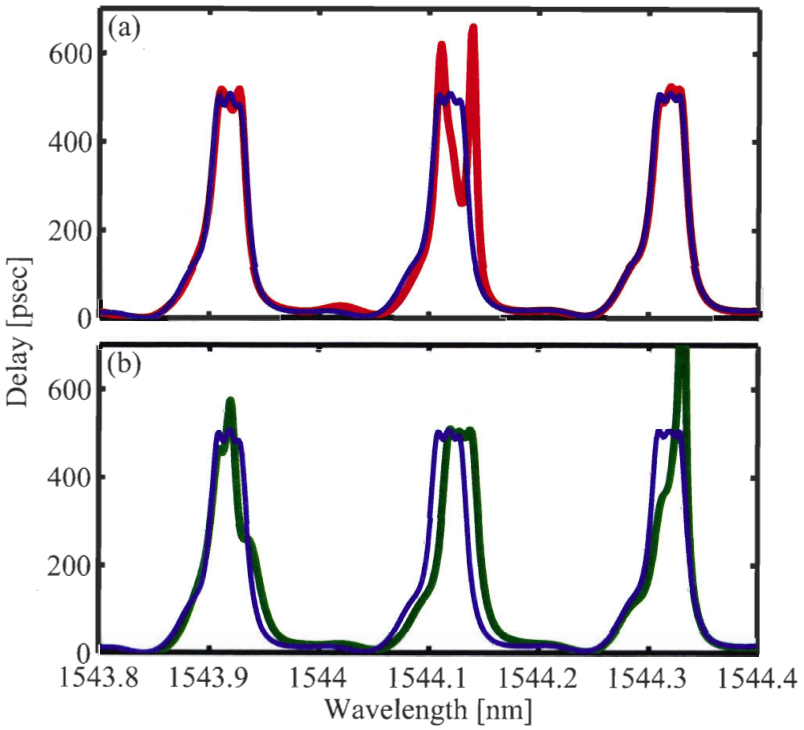

Figure 6.14: Simulated GT-CC delay with and without the local index perturbations given in Fig. 6.13. In (a), the effect of the red perturbation curve: the perturbation is smaller than d_{FSR} and the central delay peak has completely lost its shape while the adjacent peaks are slightly affected by the perturbation. In (b), the effect of the green perturbation curve: the larger perturbation zone allows to shift the central peak without distortion, but affects much more the adjacent peaks. The slope due to the grating chirp is subtracted from the delay curves.

to be sensitive to very small perturbations of the relative phases of the cavities. In the design of Fig. 6.13, the delay shape is conserved only if the average index perturbation extends over more than 2.5 cm, but the adjacent peaks are heavily distorted. On the other hand, a perturbation extending over a short grating region leaves the adjacent channels unchanged but strongly perturb the shape of the tuned channel (see Fig. 6.14). We tried other chirp values for the grating design, but gratings with very low chirp must be very long to cover a useful number of FSR. The limit on the grating length is fixed by the maximum length of the phase mask, which is 14 cm. Within this grating length, we did not find a satisfying design.

In the following, we propose an alternative solution that is well adapted to multi-channel applications.

6.6.1 A new design of the TS-BF for multichannel applications

Again, we first describe the single channel design to move later to the multichannel configuration. The new design for the FBG_L and FBG_U are shown respectively in figures

6.15 and 6.16 and is not based any more on coupled cavities. The gratings are designed to have a flat pass-band amplitude response with a bandwidth of 20 GHz, and a step-like delay response centered respectively onto the lower and upper modulation sideband of the optical spectrum. The step is 400 ps, the gratings chirp $C = \pm 0.25$ nm/cm. The gratings reflectivity must be lower than -20 dB in the out-of-band region, where the adjacent channels are transmitted: the modulation sidebands of the nearest channels are 20 GHz aside the carrier frequency of the reference channel. The requirement is even more stringent because the TS-BF is tuned by shifting the gratings through a thermal or mechanical stress. Hence, we have to take into account that the grating can be shifted near to one of the adjacent channel: we imposed a -20 dB reflectivity 17 GHz aside the optical carrier frequency of the reference channel. The gratings are 89 mm long. Their modulation index is first calculated using a layer peeling algorithm [207]. Then, the gratings are multiplied by an apodization window, which is designed to minimize the grating lengths while maintaining the inband amplitude root mean square (RMS) ripple and RMS phase ripple (as defined in section 6.7) respectively below 0.1% and 0.02°. All the simulations described later include the window function. The gratings modulation index is shown in Fig. 6.17.

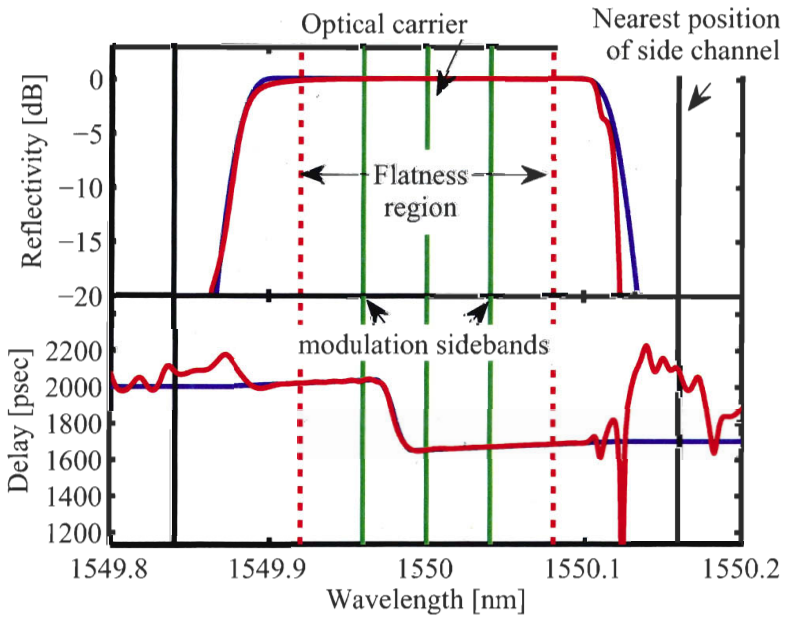

Figure 6.15: Reflectivity and delay of the FBG_L. In blue: design goal; in red: actual grating. Green vertical lines represent the position of the optical carrier and modulation sidebands. Red dotted lines limit the region of maximum flat response. Black lines are the nearest position of the sidebands of the adjacent channels.

We can simulate the amplitude and phase maps for this solution, in a similar way as we did for the GT-CC design, by shifting the gratings delay and amplitude response shown in figures 6.15 and 6.16. The results are presented in figures 6.18 and 6.19, where a black line gives the zone of operation of the TS-BF.

The maximum phase retardation range along the secondary diagonal of the map in

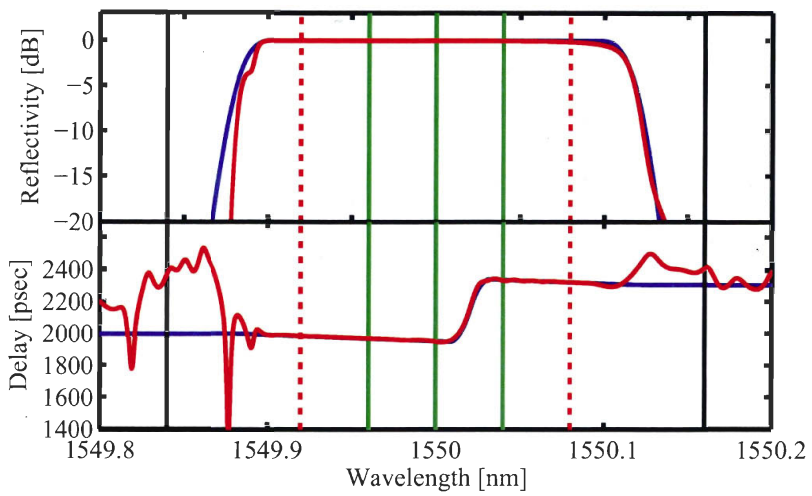

Figure 6.16: Reflectivity and delay of the FBG_U. Colors defined as Fig. 6.15.

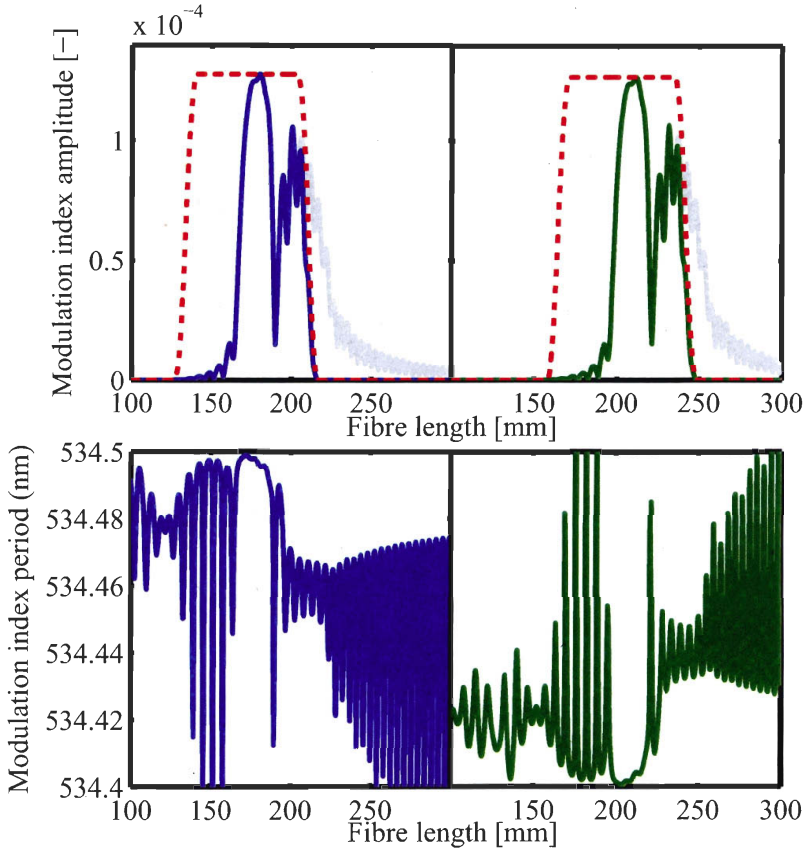

Figure 6.17: Simulated modulation index for the FBG_L (blue) and FBG_U (green). Gray line is the layer peeling algorithm design, before the application of a window function used to shorten the gratings.

Fig. 6.19 reach 2.5π, as shown in Fig. 6.20.

We tested the design experimentally. Serge Doucet prepared the FBG_L and FBG_U

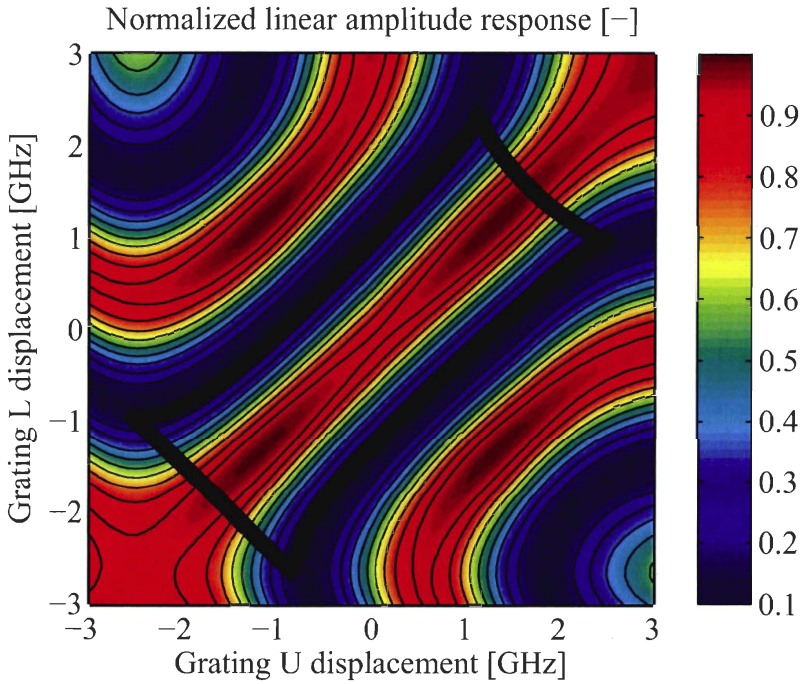

Figure 6.18: Simulated amplitude map of the TS-BF.

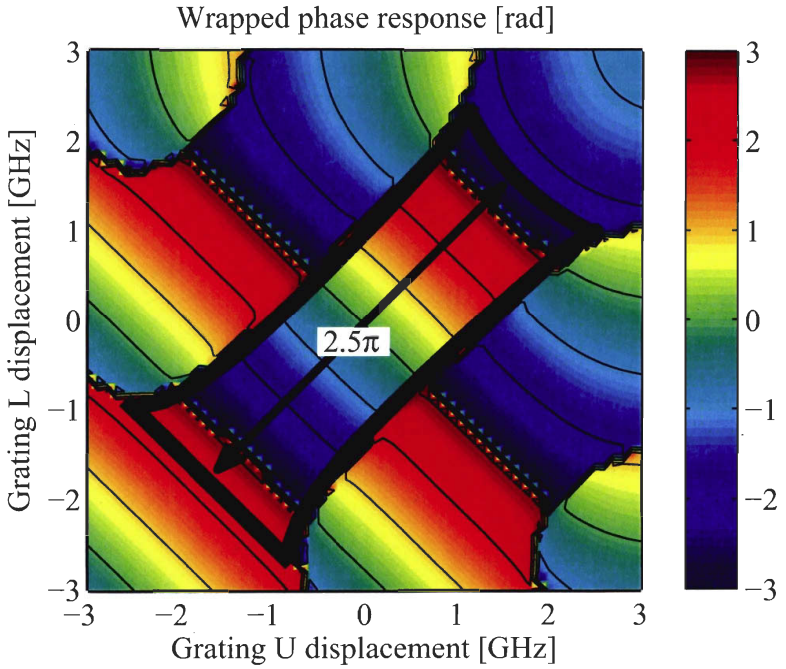

Figure 6.19: Simulated phase map of the TS-BF.

using two phase sampled phase masks from TeraXion. For the amplitude and phase map measurements, the gratings were installed in the setup shown in Fig. 6.10: the grating temperatures were controlled by the means of computer-controlled Peltier cells, and the control software spanned a two-dimensional matrix of gratings temperature

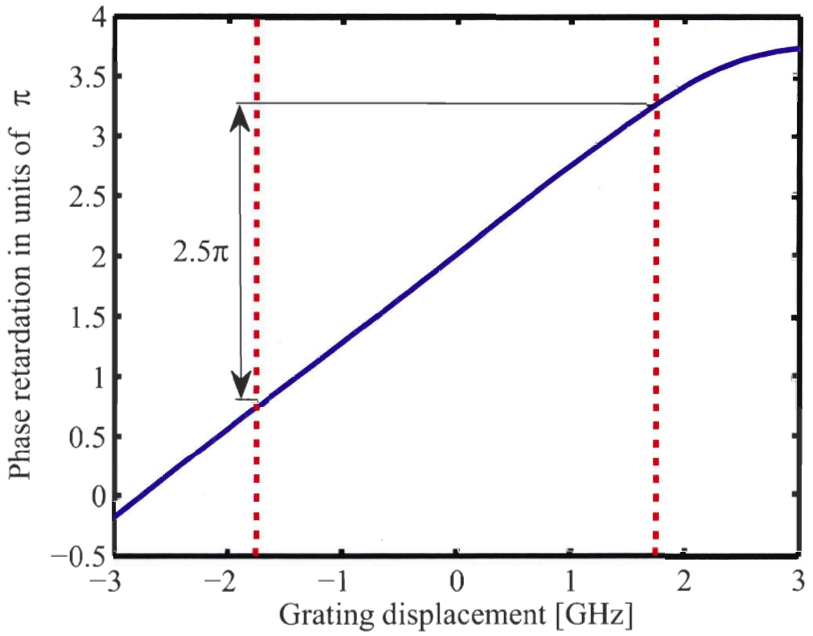

Figure 6.20: Phase retardation on the secondary diagonal of Fig. 6.19.

settings. For each setting, the software collected a measurement of the amplitude of the RF signal carrier at 5 GHz, its phase and a measurement of the TS-BF delay response. The latter is used to relate the temperature values to grating response shift in frequency. The measured amplitude and phase maps are shown in figures 6.21 and 6.22: there is good agreement with amplitude and phase maps given in figures 6.18 and 6.19. In Fig. 6.23 we show phase retardation that can be reached moving the gratings along the secondary diagonal of the phase map: the experimental TS-BF under test allows a maximum retardation of 2π within the same operational region defined by the red dotted lines in Fig. 6.20. This is due to the imperfect delay response of the gratings under tests, whose amplitude and delay responses are shown in appendix H. In Fig. 6.23 we show amplitude response on the main diagonal of 6.22 and 6.21, around a phase retardation of about 0. In the limit of the spatial resolution of the measurement, the phase is kept in a range of $\pm 5°$ while the amplitude is attenuated over a range of more than 6 dB. Moving the grating on the phase map isolines instead of the diagonal would correct for the effects of grating imperfections and allows a more constant phase over the amplitude setting range.

The results on this improved design of the TS-BF for multichannel applications are original and, at the time of writing, they are being submitted for publication.

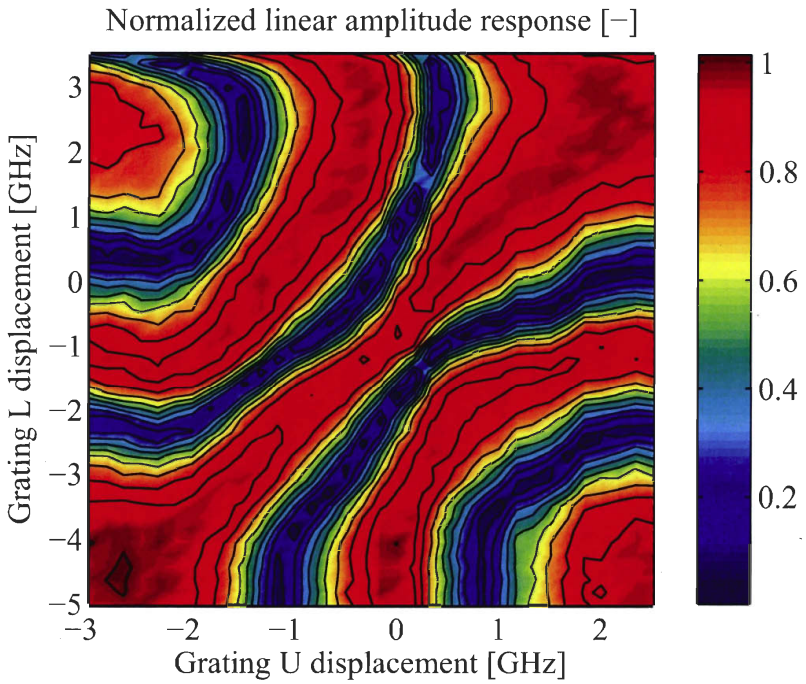

Figure 6.21: Experimental measurement of the amplitude map of the TS-BF.

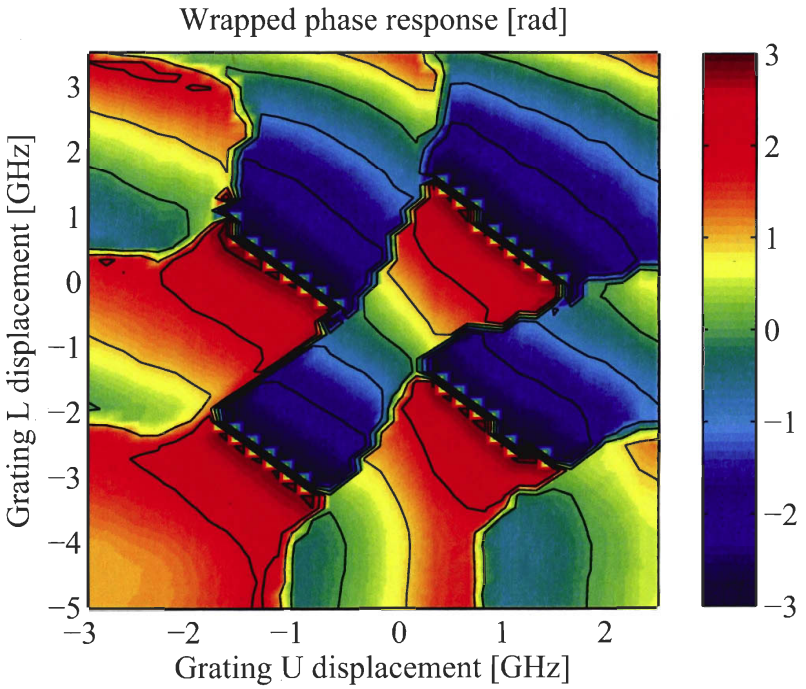

Figure 6.22: Experimental measurement of the phase map of the TS-BF.

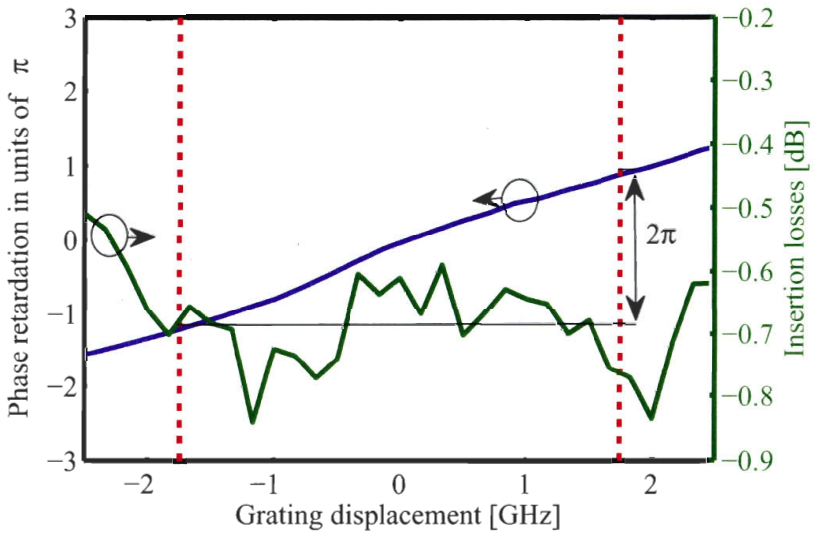

Figure 6.23: Phase retardation and amplitude response on the secondary diagonal of figures 6.22 and 6.21.

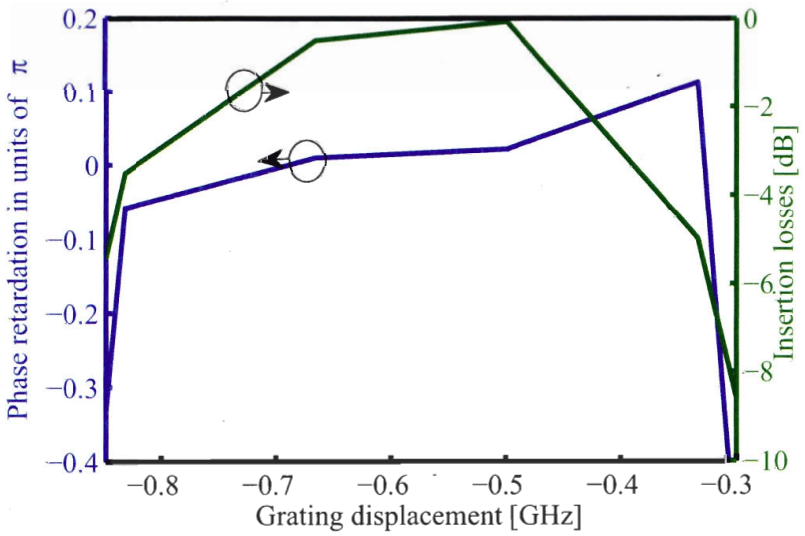

Figure 6.24: Phase retardation and amplitude response on the primary diagonal of figures 6.22 and 6.21.

6.6.2 The multichannel configuration

The multichannel TS-BF has the structure shown in Fig. 6.25: the FBG_U and FBG_L are formed by a chain of independent gratings, one for each channel or antenna in the array. This solution ensures that the channels are independent.

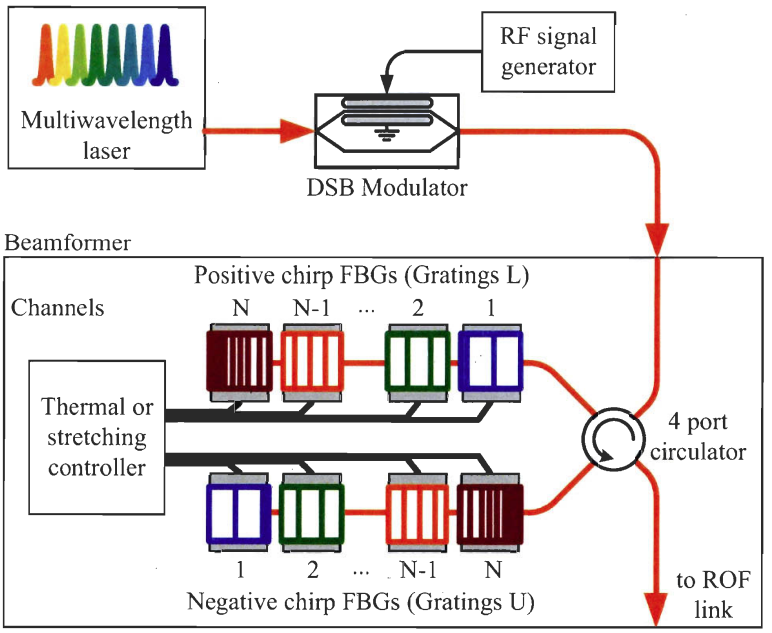

Figure 6.25: The multichannel TS-BF. The signal from a multi-wavelength source is modulated by a single DSB modulator and filtered. Each wavelength is filtered twice by separated FBGs, which are part of two chains of concatenated gratings. By adjusting the temperature or by stretching each FBG, phase and amplitude of the signal on each wavelength can be controlled independently. The TS-BF is designed to feed a dense WDM ROF system with 25 GHz wavelength spacing, each wavelength addressing a different element of an array.

The distance between the gratings in the chains does not have to be controlled very precisely. If the gratings are uniformly spaced, all the channels will accumulate the same propagation delay while traversing the TS-BF. If the spacing is non-uniform, some channels will have a higher propagation delay, which corresponds to an excess phase retardation. However, it is relatively easy to control the positions of the gratings in the chain with a precision of 5 mm, corresponding to an excess phase retardation of 0.24π (43°), which can be easily compensated by conveniently off-setting the TS-BF zero phase calibration.

Note that the optical signal can be generated by a multi-wavelength source as the multi-wavelength fibre lasers proposed by Brochu *et al.* [141] and Slavik *et al.* [142]. All the wavelengths are modulated at the same time by a single modulator. Hence, a multiwavelength laser avoids the need for multiplexing of separated sources, decreasing the setup complexity.

The beam-former can be placed at the CS before the ROF link: this allows for remote

control of the array radiation pattern and for minimization of the WTP complexity.

The main disadvantage of the configuration proposed in Fig. 6.25 is that the minimum length of the chain is N times the length of a single grating (9 cm), which is as much as 72 cm for 8 channels! Such long chains of gratings, along with the actuators needed for controlling the TS-BF, are surely not easy to package. Shorter gratings can be designed by reducing the chirp and decreasing the delay step. However, decreasing the step reduces the phase retardation tunability range: in this design the minimum step height needed for a phase tunability range of 2π is about 370 ps. Also, the windowing function used to limit the length of the gratings can be made tighter, trading-off the smoothness of the delay response and the flatness of the amplitude response. In order to have an idea of the minimum possible gratings length, we pushed the design to its limits by making some compromises on performance (especially the amplitude and phase ripples as defined in the next section) and we obtained gratings of about 7 cm. We did not investigate further this problem.

A four channel complete beam-former setup based on the TS-BF in the configuration given in Fig. 6.25 is currently under test and will be reported by M. E. Mousa Pasandi in his Master's degree thesis.

6.7 Phase and amplitude ripples of the TS-BF

As we discussed briefly before, many signal formats used in wireless communications systems, like wideband code division multiple access (CDMA) (W-CDMA), have strict requirements on filter phase and amplitude ripples, which must be minimized [208, 209]. In [208], Weigel defines the ripples as root-mean-square values:

$$\Delta a_{rms} = \sqrt{\frac{1}{B}\int_B \left[\frac{a(f) - a_{rms}}{a_{rms}}\right]^2 df}, \tag{6.9}$$

$$\Delta \phi_{rms} = \sqrt{\frac{1}{B}\int_B \left[\phi(f) - \phi_{lin}(f)\right]^2 df}, \tag{6.10}$$

where B is the filter bandwidth, a_{rms} is the root-mean-square value of the inband filter amplitude response, Δa_{rms} is unitless, ϕ_{lin} is the linearized (for a minimum root-mean-square error) inband phase, $\Delta\phi_{rms}$ has angular units. With these definitions, for an I/Q modulated signal Weigel calculates the magnitude of the constellation error vector (the EVM) caused by the phase and amplitude ripple of the filter:

$$\mathrm{EVM} \approx 10 \cdot \log_{10}\left\{\Delta a_{rms}^2 + \left[\tan\left(\Delta\varphi_{rms}\right)\right]^2\right\}. \tag{6.11}$$

We calculated (6.9) and (6.10) for our filter, and the results are reported in Fig. 6.26.

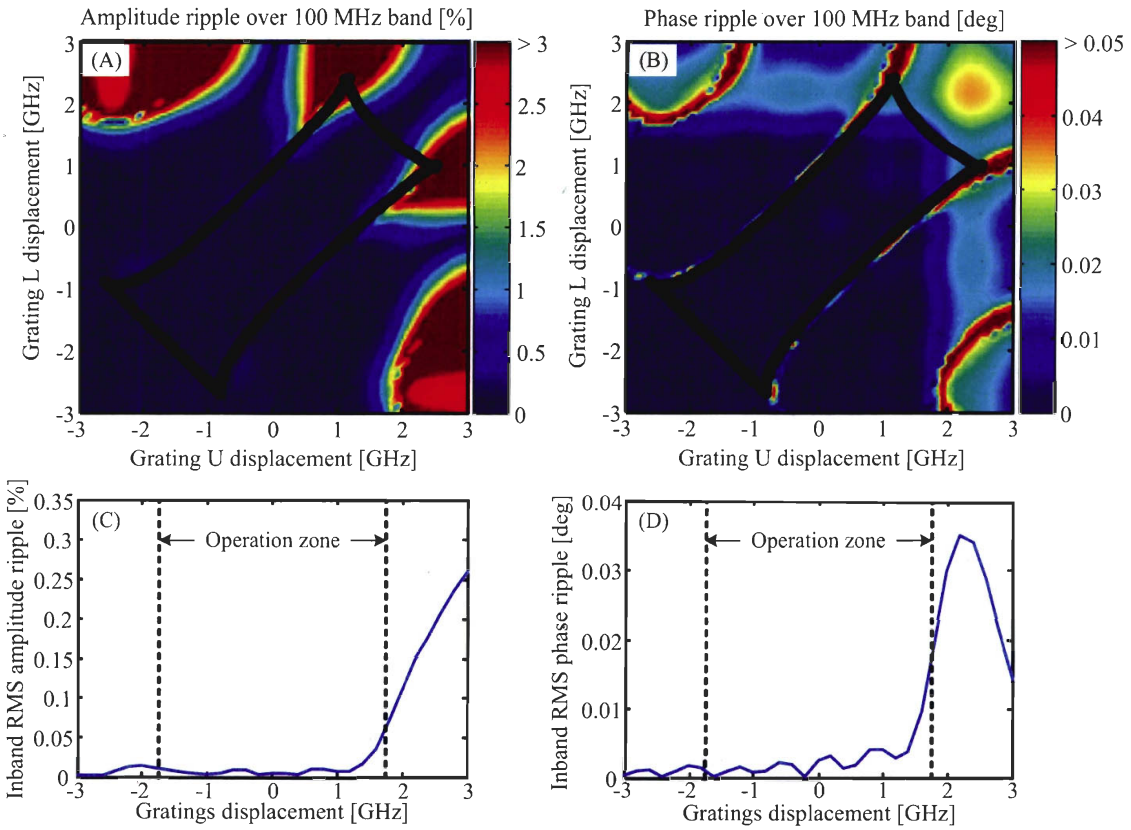

Figure 6.26: Amplitude and phase ripple. A: amplitude ripple map; B: phase ripple map; C: amplitude ripple along the secondary diagonal; D: phase ripple along the secondary diagonal.

The amplitude ripples along the diagonal, in the operation zone, is always below 0.07%, and the phase ripple below 0.02°: such values of ripple have a negligible impact on the EVM, which stays below -60 dB. Note that the ripples worsen around 2 GHz-3 GHz of displacement: in this region, the delay step knees are almost superimposed with the modulation sidebands, and the amplitude and phase are affected by the curvature of the knees.

It is interesting to check if the TS-BF performance is conserved even if the gratings have some imperfections in the modulation index, which could stem from slow variation of the fibre photosensitivity along the gratings, from a poor control over the grating fabrication process, variations of laser power during the fabrication, imperfections of the phase mask, and so on. These problems can affect the envelope of the index modulation, named $n_{AC}(x)$, as well as the local average index, $n_{DC}(x)$, in a way that can be expressed by:

$$\begin{aligned} n_{AC,perturbed}(x) &= n_{AC}[1+\eta(x)] \\ n_{DC,perturbed}(x) &= n_{DC}(x) + \eta(x) \cdot \max\{n_{AC}\} \end{aligned} \tag{6.12}$$

where η is a random process describing the perturbation along the gratings. These definitions of the perturbation come from the experimental experience accumulated in

our research group[2]. Assuming η to have a uniform distribution in a range of $\pm 5\%$ and a maximum spatial period of about 1 mm, we simulated the impact of the index imperfections on the amplitude and phase ripple. We calculated the ripple values for 100 independent realizations of η: the results are reported in figures 6.27 and 6.28 where, for each grating displacement, we show a column of color shaded points representing the histogram of the values of ripples calculated for all the realizations of η. We fitted

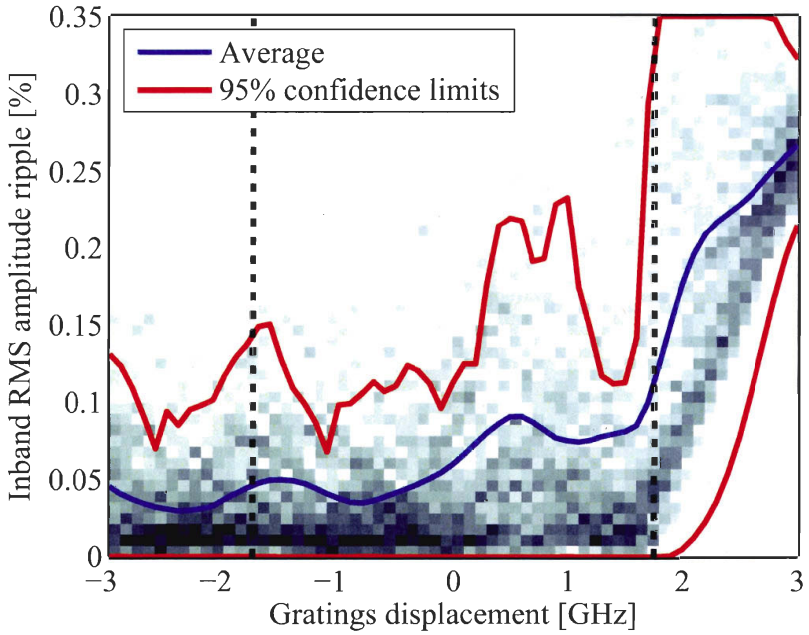

Figure 6.27: Amplitude ripple in presence of random errors in the modulation index of FBG_U and FBG_L.

the ripple histogram for each grating displacement value using a Chi distribution and we inferred a 95% interval of confidence, which can be considered an estimate of the maximum ripple. From figures 6.27 and 6.28, we see that the maximum value for the 95% confidence interval is about 0.35% for the amplitude and 0.04° for the phase. From (6.11), with such ripple values, the EVM is about -47 dB, still a very low value. The W-CDMA standard requires an EVM below -15 dB.

In conclusion, this proposed design for the TS-BF appears to be robust to fabrication imperfections. We did not measured the phase and amplitude ripples of the experimental TS-BF.

[2]Serge Doucet, private communication, and [210].

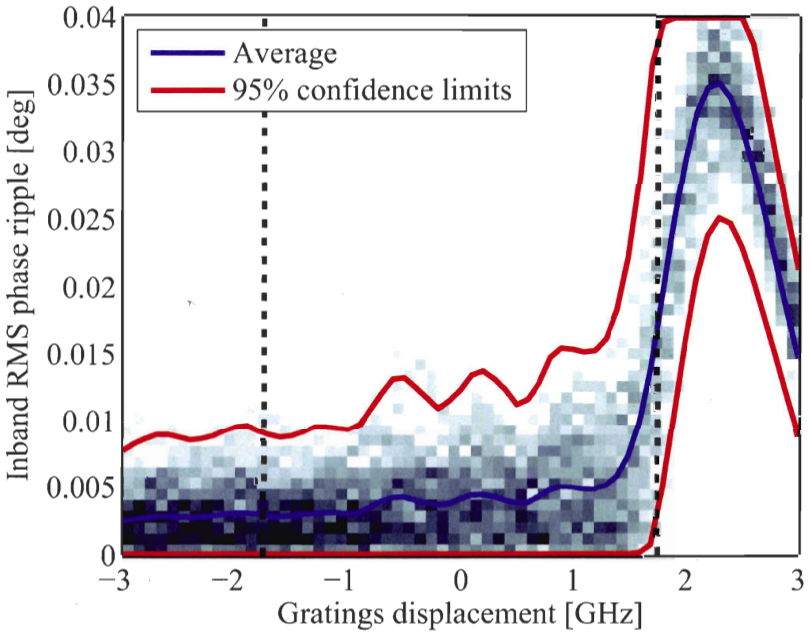

Figure 6.28: Phase ripple in presence of random errors in the modulation index of FBG_U and FBG_L.

6.8 Conclusions

In this chapter we presented a novel all-optical beam-former, which allows for independent adjustment of both amplitude and phase of the signals fed to each antenna in an array. We presented an embodiment of this beam-former based on FBGs, but other technologies can be used for realizing the same device, as for example a set of ring resonators.

This device is not a TTD-BF, and it is designed for controlling narrowband signals. Hence, this device is not adapted to wideband applications like radar. However, it is well adapted to be used in beam-forming array for communication applications: it offers simultaneous and independent control over amplitude and phase for each antenna in the array, high RF carrier frequency operation and compatibility with DSB modulation systems, good performance/complexity compromise and easy integration with antenna remoting links based on WDM for antenna addressing. Finally, the beam-former can be placed at the CS opening the way to remote control of the array radiation pattern and decreasing the complexity of the WTP.

We designed the the beam-former to be used with 5 GHz RF signals. However, it can be easily adapted to work with much higher frequencies, as for example 60 GHz. Note that the grating design to support such high frequencies appear to be much easier than at 5 GHz, because the 2π retardation is obtained with much lower optical delay variations.

The beam-former is a good example of all-optical signal processing functions that can be embedded in a ROF link designed for optical distribution of wireless networks signals.

Chapter 7

Conclusions

In this thesis, we presented our work on ROF distribution links for wireless networks employing OFDM-based communication protocols. Our main objective was to identify the most important limitations and sources of impairment on the OFDM signal stemming from the optical link, and to find a link configuration that was capable of supporting the propagation of such signals with very low impact on the transmission error probability. An additional objective was the study of ROF links with optical amplification and high power RF output, so to evaluate the possibility of driving an antenna at the link end without the need for RF amplification after a detector. Finally, we wanted to explore the potentialities of all-optical manipulation and filtering of RF signals, in order to integrate high level functions, such as signal phase and amplitude control for beam-forming in the optical link itself.

To fulfill these aims, we focused on a specific type of link employing a DFB laser, external modulation with an electro-optic Mach-Zehnder modulator, and an EDFA for optical amplification. While experimenting on the link gain, we observed that moving the modulator bias lead to a significant gain improvement, and we decided to push the study of this effect into more depth. Eventually, bias optimized links became the center of our work when we discovered their potential advantages by a deep investigation of the link gain, noise and distortion properties. For example, the link gain is examined in chapter 3 considering several link parameters, such as the amplifier saturation level, the dispersion, and the degree of impedance matching at the detector. Also, the link noise study presented in chapter 4 is based on a very general model, which led to original results when applied to SBS-related noise. In this way, most of the results of our work can be generalized to other type of ROF link and transmitted signals. For example, throughout all the thesis we focused on signals compliant to the IEEE 802.11a protocol, but all our results can be generalized to other OFDM-based protocols, as 802.11g or the upcoming 802.11n or even to other narrowband or sub-octave type of signals.

This work led to several original contributions, which are presented in this thesis. First of all, we conducted a thorough analysis of externally modulated links employ-

ing a Mach-Zehnder modulator with bias out of quadrature. Notably, we studied the improvement of link RF gain that is made accessible by bias optimization in optically amplified links (published in [88]). We also explored the impact of bias on detected noise and CNR, especially in the presence of SBS-induced noise (published in [138]). The noise analysis was based on a general model of noise in optical links, leading to a novel model of the noise on the RF detected carrier induced by the SBS (to be submitted for publication). Then, we explored several sources of signal distortion in ROF links, and their impact on OFDM signals. First, we studied the impact of nonlinearities of MZ modulators (unpublished) and the signal distortion caused by EDFA gain dynamics and bias shifting out of quadrature in framed OFDM signals (published in [165]). We also conducted a brief study of performance of SOAs used as modulators (published in [64], in collaboration with Vacondio et Mathlouthi). Then, we concentrated on the impact of fibre nonlinearities on link distortion, and its improvement by moving the modulator bias off quadrature (published in [181]). Notably, we studied numerically and experimentally the EVM and its improvement in presence of fibre nonlinearities and off-quadrature modulator bias (to be submitted for publication). An additional noteworthy contribution is the conception of a novel all-optical beam-former capable of controlling simultaneously and independently the amplitude and the phase of the signals fed to each antenna is an array (published in [183] in collaboration with Mousa Pasandi and Doucet; some last results are being submitted for publication)

We discussed in the introduction (chapter 1) the motivations for this work: essentially, the ROF distribution links are an enabling technology for the implementation of centralized network management. This should open the way to the application of several advanced techniques aimed to increase the wireless communication rate and the number of simultaneous users supported by the wireless network, while dealing with problems like the mutual interference between users and dynamic resources management. Also, ROF links should enable an extensive use of antenna arrays in MIMO or beam-former configuration. However, the ROF links will never be more than a niche technology unless the research on this topic makes it possible to improve its cost/performance ratio, compared to the common all-electrical non-centralized networks.

The cost of a technology is a delicate topic because it depends on several factors, often more related to marketing strategies than to research. However, we can recognize that the cost of DFB lasers, EDFAs and Mach-Zehnder modulators is indeed a constraint on the wide diffusion of the kind of ROF links we studied in this thesis, but for very high end applications. This is particularly true for links supporting a high number of separate WTPs. We think that the integration of several optical devices on a so-called photonic chip could be a solution to this problem: it is time for optical components to undergo the same evolution from discrete components to integrated circuits that already allowed the diffusion of electronics in every aspect of our life. This is in our opinion an open and exciting topic of research that would greatly benefit the improvement of ROF technology: it would allow, for example, to integrate all the lasers, modulators and amplifiers feeding the network on a single chip, drastically reducing the costs. Many research group are working on integration of the basic optical devices

on a chip, for example in Intel, IBM and Cornell university, to name a few. Indeed, a simple way to reduce the costs would be to abandon the external modulator and directly modulate the current of a laser diode. We did not explore this topic, but it is surely the next logic step to continue our work. Also, it would be very interesting to test the new SOI-based Mach-Zehnder proposed recently by Intel: in the future, this device may be a low cost alternative for external modulation.

On the performance side of the cost/performance ratio: the ROF link must be as transparent as possible to the OFDM signal. The basic idea of network centralization is that the wireless signal is created in a CS and than distributed to low cost WTPs. The distribution must affect the signal quality as little as possible and should not add significant noise or distortion. One problem is that a badly designed ROF optical link typically has large RF losses, and must be followed by a chain of RF amplifiers to compensate for this loss and to feed the antennas with a convenient signal. However, these amplifiers are known to be a significant source of noise and nonlinear distortion. In particular, to ensure error free OFDM transmission, the amplifiers must operate far from saturation, with an output average power much lower than their 1 dB compression limit. Also, the amplifiers must be placed near the antenna, increasing the WTP complexity and cost. An alternative explored in this thesis is to amplify the signal in the optical domain using EDFAs, which present some advantages in terms of noise and linearity, and allow to place the amplification stage far from the WTP. Also, EDFAs can be shared among the antennas, as discussed in chapter 3. With optical amplification, the antenna is directly driven by the detector, so that the WTP is greatly simplified. However, we recognize that this solution has a great limitation: the nonlinear response of the detector, which must be able to feed the antenna with a high power signal. With commercially available detectors, we were not able to reach the power level of 7 dBm on a single antenna with good signal linearity. This power level was fixed as a target in chapter 1. In our opinion, the design of high power photo detectors is a second important research topic that would benefit the improvement of ROF technology. Several research groups are working on this problem and several types of detectors are emerging that promise high saturation current and large bandwidth: traveling wave detectors, uni-traveling carrier detectors, partially depleted absorber detectors among others, but none is commercially available yet. An interesting continuation of our work would be to test one of those detectors to prove experimentally the transmission of high power OFDM signals with good linearity.

A last topic that is left somewhat incomplete in this thesis is the experimental verification of the operation of the beam-former proposed in chapter 6: we simulated and tested the single channel filter, which is the basic element of the beam-former and act on the amplitude and phase fed to a single antenna, but we did not test the whole beam-former with multiples antennas. At the time of writing, this test is being performed by other students, and we are looking forward to see the results.

This is the first doctoral research on ROF links at the Université Laval, and we hope that our pioneering work will open the way to further development of this line of

research within the *Centre d'optique, photonique et laser* (COPL).

Appendices

Appendix A

Analytical form of the OFDM spectrum

In this appendix we calculate the baseband spectrum of an OFDM symbol sequence. Let us consider the baseband equivalent $\breve{x}(t)$ of $x(t)$ as defined by 2.2:

$$\breve{x}(t) = \frac{1}{\sqrt{N_{subc}}} \sum_{n\to-\infty}^{+\infty} \sum_{k=0}^{N_{subc}-1} a_k^n \cdot w(t - nT_{OFDM}) \times \\ \times \exp\left[i\, 2\pi\, k\Delta f_{OFDM}\,(t - nT_{OFDM})\right]. \tag{A.1}$$

This is a stochastic process derived form the summation of uncorrelated stochastic processes over time and subcarrier number k. If we fix k, for a single subcarrier the A.1 can be simplified into:

$$\breve{x}_k(t) = \sum_{n\to-\infty}^{+\infty} a_k^n \cdot \frac{w(t - nT_{OFDM}) \cdot \exp\left[i\, 2\pi\, k\Delta f_{OFDM}\,(t - nT_{OFDM})\right]}{\sqrt{N_{subc}}}. \tag{A.2}$$

This simplified form can be written as:

$$\breve{x}_k(t) = \sum_{n\to-\infty}^{+\infty} a_k^n \cdot h(t - nT_{OFDM}), \tag{A.3}$$

where:

$$h(t) = \frac{w(t) \cdot \exp\left[i\, 2\pi\, k\Delta f_{OFDM} t\right]}{\sqrt{N_{subc}}}. \tag{A.4}$$

Equation A.3 describes a cyclostationary process [127] where a_k^n is a discrete time complex stationary process with zero mean value. We recall that a_k^n represents the random M-QAM values assigned to the k subcarrier over the OFDM symbols, spanned by n. Hence, in a general case there is no correlation between different values of a_k^n for different n, and the a_k^n process behaves like discrete time white noise with autocorrelation:

$$r_{aa}(\tau) = \sigma_a^2 \delta(\tau), \tag{A.5}$$

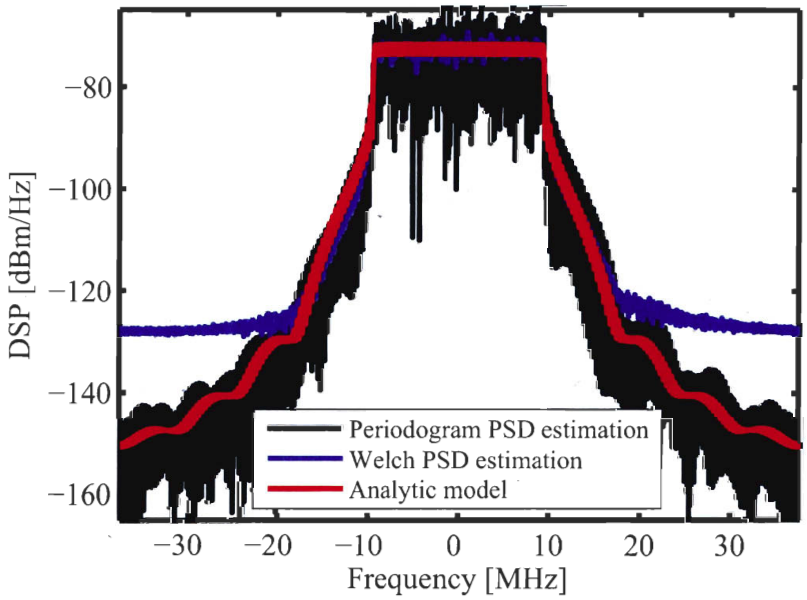

Figure A.1: Comparison between numerical and analytical estimation of an OFDM spectrum. Parameters: 64-QAM coding, 48 data subcarriers, pulse windowing as defined by the 802.11a protocol.

and power spectrum:

$$S_a = \sigma_a^2. \tag{A.6}$$

From the definition of the power spectrum of a_k^n we can now go back step by step and calculate the power spectrum for the sequence of OFDM symbols. The power spectrum is only defined for stationary processes and not for cyclostationary processes like $\breve{x}_k(t)$. However, we can modify this process by adding a random phase ϕ with uniform distribution in the range $(0, T_{OFDM})$, independent of $\breve{x}_k$. The process:

$$\breve{x}_k(t+\phi) \quad \phi \in (0, T_{OFDM}) \tag{A.7}$$

is now wide sense stationary [211] and its power spectrum is [211]:

$$S_{\breve{x}_k}(\omega) = \frac{1}{T_{OFDM}} S_a |H(\omega)|^2. \tag{A.8}$$

The term $H(\omega)$ is the fourier transform of $h(t)$ defined in A.4. Hence, it is:

$$|H(\omega)|^2 = \frac{|W(\omega - k\Delta\omega_{OFDM})|^2}{N_{subc}}, \tag{A.9}$$

were $W(\omega)$ is the Fourier transform of the windowing function. We can now calculate the power spectrum for each subcarrier k, by inserting the A.9 into the A.8. We have:

$$S_{\breve{x}_k}(\omega) = \frac{\sigma_a^2}{T_{OFDM}} \frac{|W(\omega - k\Delta\omega_{OFDM})|^2}{N_{subc}}. \tag{A.10}$$

Now we have to generalize the A.10 to the case of a multicarrier spectrum. Note that for different value of k, the $\breve{x}_k(t+\phi)$ processes are uncorrelated because the a_k^n are

uncorrelated. Hence, we can write [212, page 80]:

$$S_{\breve{x}}(\omega) = \frac{\sigma_a^2}{T_{OFDM}} \sum_{k=0}^{N_{subc}-1} \frac{|W(\omega - k\Delta\omega_{OFDM})|^2}{N_{subc}}. \tag{A.11}$$

A similar formula is given in [213] without demonstration. If the windowing function is a simple rectangle, its fourier transform can be written as:

$$W(\omega) = T_{OFDM} \operatorname{sinc}(\pi f T_{OFDM}), \tag{A.12}$$

where the operator "sinc" represent the cardinal sine function. In this case, the base-band spectrum of the OFDM sequence becomes:

$$S_{\breve{x}}(\omega) = \sigma_a^2 \frac{T_{OFDM}}{N_{subc}} \sum_{k=0}^{N_{subc}-1} |\operatorname{sinc}[\pi(f \cdot T_{OFDM} - k)]|^2. \tag{A.13}$$

This is a sum of N_{subc} sinc functions with central value equal to a M-QAM symbol. Also, for each subcarrier, the sinc function nulls occur at the central frequencies of all other subcarriers, which ensures data transmission without ICI.

In Fig. A.1 we compare a numerically simulated OFDM spectrum with the analytical model. The PSD of the numerical spectrum is estimated using both Welch [212] and periodogram (FFT) techniques, the former giving less noisy inband estimation and the latter being more accurate in the out-of-band region.

Appendix B

General Bessel expansion of Mach-Zehnder modulator transfer function

In this appendix, we develop Bessel function expansions for both the electric field and the instantaneous optical power at the output of a MZ modulator. These expansions allow to easily calculate the spectral components of the electric field propagating over the fibre, and the spectrum of the received RF signal after a photodetector.

The baseband equivalent of the electric field at the output of a balanced MZ modulator with infinite extinction ratio can be written as [214]:

$$\begin{aligned} E_{out,MZ} &= \sqrt{2P_{laser}}\left(\frac{1}{2}e^{i\,\phi}+\frac{1}{2}e^{-i\,\phi}\right)=\sqrt{2P_{laser}}\cos\left(\phi\right) \\ \phi &= \frac{1}{2}\left[\pi-\Gamma-\frac{\pi}{V_\pi}v\left(t\right)\right], \end{aligned} \tag{B.1}$$

where P_{laser} is the available power from the laser source, V_π is the modulator halfwave switching voltage, $v\left(t\right)$ is the modulation voltage on the interferometer arms and Γ defined as:

$$\Gamma=\frac{\pi}{V_\pi}V_{bias}, \tag{B.2}$$

where V_{bias} is a DC bias voltage. With $\Gamma_E=\frac{\pi-\Gamma}{2}$, $E_{out,MZ}$ can be written in the form:

$$E_{out,MZ}=\sqrt{2P_{laser}}\cos\left(\Gamma_E-\frac{\pi}{2V_\pi}v\left(t\right)\right). \tag{B.3}$$

If $v\left(t\right)$ is a real narrowband bandpass RF signal with carrier frequency f_{RF}, it can be written as:

$$v\left(t\right)=V_v\left(t\right)\cos\left[2\pi f_{RF}t+\varphi\left(t\right)\right], \tag{B.4}$$

where $V_v(t)$ and $\varphi(t)$ are respectively the slowly varying envelope and phase of $v(t)$. We assume $V_v(t) = V_v$ and $\varphi(t) = \varphi$ constant in time.

The instantaneous optical power at the MZ output is equal to:

$$P_{out,MZ} = \frac{1}{2} |E_{out,MZ}|^2 , \tag{B.5}$$

where the $\frac{1}{2}$ factor is due to the baseband description of the electric field [80, page 152]. Then, with some simple transformations we have the well known formula [89]:

$$P_{out,MZ} = \frac{P_{laser}}{2} \left\{ 1 - \cos \left[\Gamma + \frac{\pi}{V_\pi} v(t) \right] \right\} . \tag{B.6}$$

By examining the (B.6) and the (B.3), we see that the Bessel expansion of both the instantaneous optical power and the electric field can be derived from the expansion of $\cos[A\cos(2\pi f_{RF} t + \varphi) + B]$, with:

$$E_{out,MZ}: \qquad A = -\frac{\pi}{2V_\pi} V_v \qquad B = \Gamma_E \tag{B.7a}$$

$$P_{out,MZ}: \qquad A = \frac{\pi}{V_\pi} V_v \qquad B = \Gamma \tag{B.7b}$$

Developing the expansion:

$$\cos[A\cos(2\pi f_{RF} t + \varphi) + B] = \underbrace{\frac{1}{2} e^{i[A\cos(2\pi f_{RF} t + \varphi) + B]}}_{\odot} + \underbrace{\frac{1}{2} e^{-i[A\cos(2\pi f_{RF} t + \varphi) + B]}}_{\boxdot} . \tag{B.8}$$

By recalling some trigonometric identities:

$$\begin{aligned} \odot: &\ \tfrac{1}{2} e^{i[A\cos(\varphi)]\cos(2\pi f_{RF} t)} e^{i[-A\sin(\varphi)]\sin(2\pi f_{RF} t)} e^{i B} \\ \boxdot: &\ \tfrac{1}{2} e^{i[-A\cos(\varphi)]\cos(2\pi f_{RF} t)} e^{i[A\sin(\varphi)]\sin(2\pi f_{RF} t)} e^{-i B} \end{aligned} \tag{B.9}$$

The exponentials can be expanded in series of Bessel functions of the first kind and order n (Jacobi-Anger expansions):

$$\begin{aligned} e^{i Z \sin\phi} &= \sum_{n \to -\infty}^{+\infty} J_n(Z) e^{i n\phi} \\ &= J_0(Z) + 2 \sum_{n=1}^{+\infty} \{ J_{2n}(Z) \cos(2n\varphi) + i\, J_{2n-1}(Z) \sin[(2n-1)\varphi] \} \end{aligned} \tag{B.10a}$$

$$e^{i Z \cos\phi} = \sum_{n \to -\infty}^{+\infty} i^n J_n(Z) e^{i n\phi} = J_0(Z) + 2 \sum_{n=1}^{+\infty} i^n J_n(Z) \cos(n\varphi). \tag{B.10b}$$

Also, we recall that:

$$J_n(-Z\sin\varphi) = (-1)^n J_n(Z\sin\varphi) , \tag{B.11}$$

and:

$$J_{-n}(Z) = (-1)^n J_n(Z). \tag{B.12}$$

Hence:

$$\begin{aligned} \odot: \ & \frac{e^{i\,B}}{2}\left[\sum_{n\to-\infty}^{+\infty}\sum_{m\to-\infty}^{+\infty}(-1)^m\, i^n J_n(A\cos\varphi)\, J_m(A\sin\varphi)\right] e^{i\,(n+m)2\pi f_{RF}t} \\ \boxdot: \ & \frac{e^{-i\,B}}{2}\left[\sum_{n\to-\infty}^{+\infty}\sum_{m\to-\infty}^{+\infty}(-1)^n\, i^n J_n(A\cos\varphi)\, J_m(A\sin\varphi)\right] e^{i\,(n+m)2\pi f_{RF}t}, \end{aligned} \tag{B.13}$$

and the (B.8) can be written in a compact Bessel series:

$$\sum_{n\to-\infty}^{+\infty}\sum_{m\to-\infty}^{+\infty}\left[\frac{e^{i\,B}}{2}(-1)^m + \frac{e^{-i\,B}}{2}(-1)^n\right] i^n \times \\ \times J_n(A\cos\varphi)\, J_m(A\sin\varphi)\, e^{i\,(n+m)2\pi f_{RF}t}. \tag{B.14}$$

This Bessel expansion describes both the spectrum of the electric field and the spectrum of the instantaneous optical power (i.e., the detected signal in linear non-dispersive links), by substituting A and B with the values given in (B.7). We have:

$$E_{out,MZ}(t) = \sqrt{2P_{laser}}\sum_{n\to-\infty}^{+\infty}\sum_{m\to-\infty}^{+\infty}\left[\frac{e^{i\,\Gamma_E}}{2}(-1)^m + \frac{e^{-i\,\Gamma_E}}{2}(-1)^n\right] i^n \times \\ \times J_n\left(-\frac{\pi}{2V_\pi}V_v\cos\varphi\right) J_m\left(-\frac{\pi}{2V_\pi}V_v\sin\varphi\right) e^{i\,(n+m)2\pi f_{RF}t}, \tag{B.15}$$

and

$$P_{out,MZ}(t) = \frac{P_{laser}}{2} - \frac{P_{laser}}{2}\sum_{n\to-\infty}^{+\infty}\sum_{m\to-\infty}^{+\infty}\left[\frac{e^{i\,\Gamma}}{2}(-1)^m + \frac{e^{-i\,\Gamma}}{2}(-1)^n\right] i^n \times \\ \times J_n\left(\frac{\pi}{V_\pi}V_v\cos\varphi\right) J_m\left(\frac{\pi}{V_\pi}V_v\sin\varphi\right) e^{i\,(n+m)2\pi f_{RF}t}. \tag{B.16}$$

If the $v(t)$ is a simple sinusoidal signal (i.e., $\varphi = -\frac{\pi}{2}$), the double sum in (B.16) can be reduced to:

$$\begin{cases} \cos\Gamma\cdot J_0\left(\frac{\pi}{V_\pi}V_v\right) & n=0 \\ 2\cos\Gamma\sum_{n=2}^{+\infty} J_n\left(\frac{\pi}{V_\pi}V_v\right)\cos(2\pi\, nf_{RF}\, t) & n \text{ even} \\ -2\sin\Gamma\sum_{n=1}^{+\infty} J_n\left(\frac{\pi}{V_\pi}V_v\right)\sin(2\pi\, nf_{RF}\, t) & n \text{ odd} \end{cases}, \tag{B.17}$$

with $n \geq 0$. This is equivalent to the result given in [89], confirming the validity of (B.16). Note that the (B.17) is not valid if $v(t)$ is a cosine signal or a signal with generic carrier phase. To our knowledge, only Corral in [174] gives a generic Bessel expansion of

the spectrum at the output of a MZ like (B.14). A partial and less compact description of the spectrum is given in [117], which only considers spectrum terms for $n = 0$ and $n = 1$. In [89] and [156], only the spectrum of the received photocurrent is given, and only for $\varphi = -\frac{\pi}{2}$ and $\varphi = 0$, respectively. In [215], only $\varphi = 0$ is considered.

Equation (B.14) can also be verified experimentally by measuring the optical spectrum at the modulator output using an OSA. Fig. B.1 shows that the analytical calculation of the power of the optical carrier and upper modulation sideband is very near to the measured values.

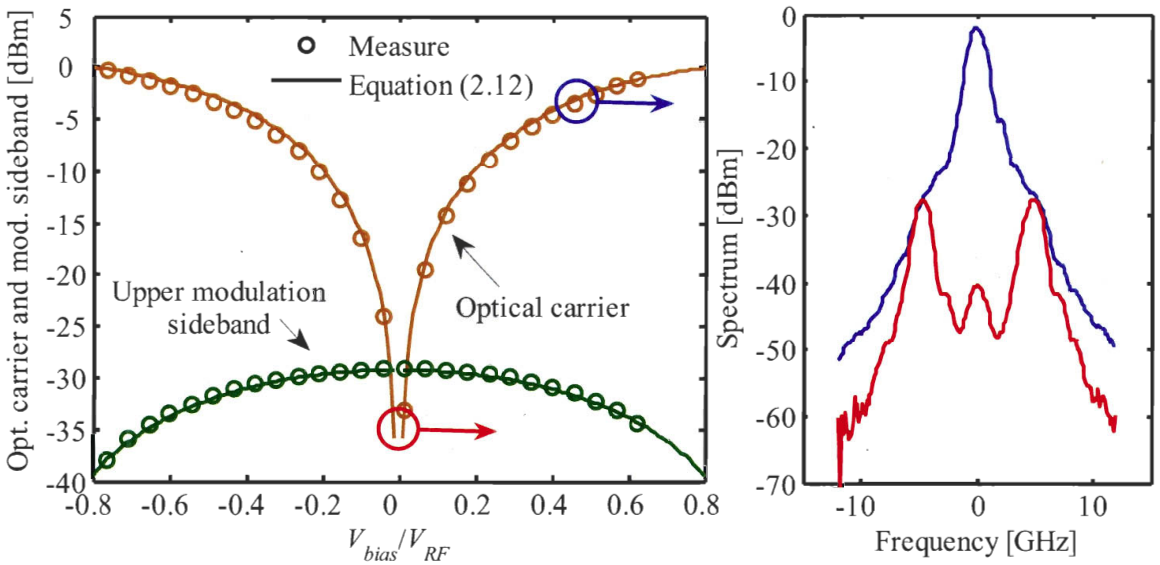

Figure B.1: Comparison of measure and analytical calculation of MZ optical spectrum Measurement: resolution bandwidth = 10 pm, The power of the sidebands is measured by sampling the optical spectrum at ±5 GHz aside the carrier. The value is then corrected by a factor (not bias dependent) to take into account for the fraction of carrier power falling over the sidebands. OSA `ANDO AQ6317B`, $P_{RF} = 0$ dBm

For convenience of the reader, we make explicit here some expression used throughout this text.

Power of the received RF signal at the fundamental frequency f_{RF}, in a linear link, for (a): $\varphi = -\frac{\pi}{2}$, (b): $\varphi = 0$.

$$P_{RF} = \frac{R_{jD}G_{TD}}{8} i_{det}^2 = \frac{R_{jD}G_{TD}}{8} \cdot \begin{cases} \left[k\mathcal{R}P_{laser} \sin(\Gamma)\, J_1\left(\frac{\pi}{V_\pi}V_v\right) \sin(2\pi f_{RF}t)\right]^2 & \text{(a)} \\ \left[k\mathcal{R}P_{laser} \sin(\Gamma)\, J_1\left(\frac{\pi}{V_\pi}V_v\right) \cos(2\pi f_{RF}t)\right]^2 & \text{(b)} \end{cases}, \tag{B.18}$$

where R_{jD} is detector junction resistance, G_{TD} is the detector transducer gain, i_{det} is the detected photocurrent, k is a factor related to link optical losses and gain, V_v is the effective signal amplitude applied to the MZ arms, $\mathcal{R}$ is the detector responsivity, P_{laser}

is the modulated laser power, V_π is the modulator halfwave switching voltage, Γ is the modulator bias point.

Average optical power at MZ output:

$$\langle P_{out,MZ} \rangle = \frac{P_{laser}}{2} \left[1 - J_0 \left(\frac{\pi V_{RF}}{V_\pi} \right) \cos \left(\frac{\pi V_{bias}}{V_\pi} \right) \right] \tag{B.19}$$

Second order and third order harmonic distortion of detected photocurrent at MZ output:

$$\text{HD2} = \frac{1}{\tan(\Gamma)} \frac{J_2 \left(\frac{\pi}{V_\pi} V_v \right)}{J_1 \left(\frac{\pi}{V_\pi} V_v \right)} \tag{B.20a}$$

$$\text{HD3} = \frac{J_3 \left(\frac{\pi}{V_\pi} V_v \right)}{J_1 \left(\frac{\pi}{V_\pi} V_v \right)} \tag{B.20b}$$

These expressions are in linear units.

B.1 Verification of equation (5.5) of chapter 5

Let us assume that the modulation signal is a simple sinusoidal signal (i.e., $\varphi = -\frac{\pi}{2}$). Then, from equation (B.15) we can calculate the spectrum at the MZ output:

$$E_{out,MZ}(t) = \sqrt{2P_{laser}} \cdot \begin{cases} \cos\left(\frac{\pi-\Gamma}{2}\right) \cdot J_0 \left(\frac{\pi}{2V_\pi} V_v \right) & n = 0 \\ 2\cos\left(\frac{\pi-\Gamma}{2}\right) \sum_{n=2}^{+\infty} J_n \left(\frac{\pi}{2V_\pi} V_v \right) \cos(2\pi\, n f_{RF}\, t) & n \text{ even} \\ 2\sin\left(\frac{\pi-\Gamma}{2}\right) \sum_{n=1}^{+\infty} J_n \left(\frac{\pi}{2V_\pi} V_v \right) \sin(2\pi\, n f_{RF}\, t) & n \text{ odd} \end{cases} . \tag{B.21}$$

If the carrier has zero reference phase, the upper odd sidebands have all phase equal to $-\frac{\pi}{2}$, the lower odd sidebands have all phase equal to $+\frac{\pi}{2}$, and all the even order sidebands have zero phase. Then, (5.5) of chapter 5, representing the fundamental harmonic of the instantaneous optical power, can be written as:

$$f_{\omega_{RF}}(t) = 2P_{laser} \cdot \Big\{ 2\cos(a)\sin(a)\, J_0(b)\, J_1(b) \sin(\omega_{RF} t) + 2\sum_{n=1}^{\infty} \cos(a)\sin(a) J_n(b)\, J_{n+1}(b)\, (-1)^n \sin(\omega_{RF} t) \Big\} \tag{B.22}$$

where:

$$a = \frac{\pi - \Gamma}{2} \tag{B.23}$$

$$b = \frac{\pi}{2V_\pi} V_v. \tag{B.24}$$

Collecting the common terms, equation (B.22) becomes:

$$f_{\omega_{RF}}(t) = 2P_{laser}\left\{2\cos(a)\sin(a)\sin(\omega_{RF}t) \times \right.$$
$$\left. \times \left[J_0(b) J_1(b) + \sum_{n=1}^{\infty} J_n(b) J_{n+1}(b) (-1)^n \right] \right\}. \tag{B.25}$$

One property of Bessel function of the first order is[1]:

$$\frac{J_1(2b)}{2} = J_0(b) J_1(b) + \sum_{n=1}^{\infty} J_n(b) J_{n+1}(b) (-1)^n. \tag{B.26}$$

Also, remember that:

$$\cos(a)\sin(a) = \frac{\sin(2a)}{2}. \tag{B.27}$$

Hence:

$$f_{\omega_{RF}}(t) = P_{laser}\sin(2a)\sin(\omega_{RF}t) J_1(2b) \tag{B.28}$$

$$= P_{laser}\sin(\Gamma)\sin(\omega_{RF}t) J_1\left(\frac{\pi}{V_\pi}V_v\right). \tag{B.29}$$

This is the same result as given by (B.16).

[1]From http://mathworld.wolfram.com/BesselFunctionoftheFirstKind.html.

Appendix C

Impedance matching of a lossy network

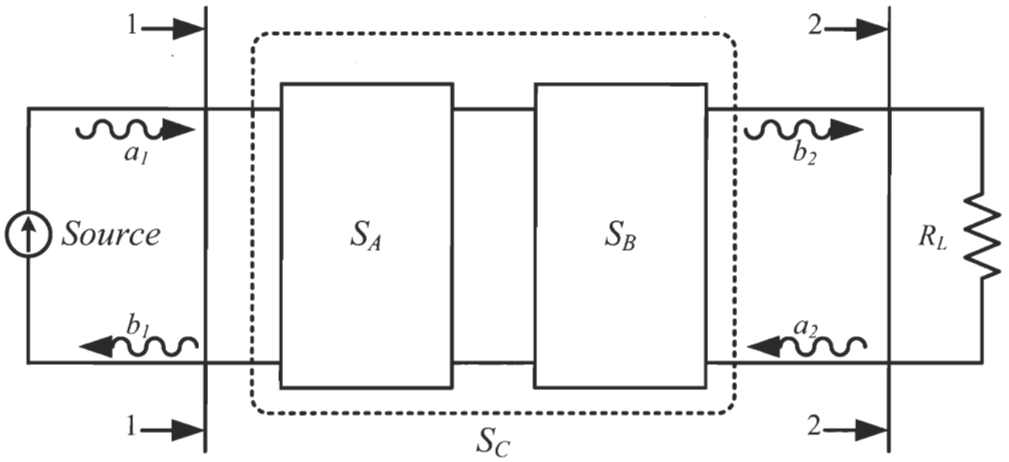

Figure C.1: Chain of networks.

Let us focus on a chain of networks like shown in Fig. C.1. Such a chain can model both the detection and the modulation stages of a link: for the detection stage, the source is a photocurrent generator, S_A would represent the detector circuit model and S_B would be a matching circuit to transfer power to a load R_L. For the modulation stage, the source is a voltage generator (or its Norton equivalent), S_A would represent a matching circuit interfacing the source with the modulator circuit model S_B. We call S_C the scattering matrix representing the chain of S_A and S_B. The calculation of S_C from S_A and S_B is easily completed transforming the scattering matrix descriptions of the A and B networks into the so called T matrices, which are more adapted to treat chains of networks. Such matrices and their relations with scattering parameters are defined, for example, in [216].

By using the T matrices, we can easily show that the scattering matrix S_C of the

chain of networks has:

$$|S_{21,C}|^2 = \frac{|S_{21,A}|^2 |S_{21,B}|^2}{|1 - S_{22,A}S_{11,B}|^2} \tag{C.1}$$

If any of the networks is lossy: $|S_{21,C}|^2 < 1$.

Also, we can show that lossy networks can not be perfectly matched at both sides by using a matching network on one side only. This can easily be demonstrated by examining the properties of a lossless chain S_C, which has the following properties [217]:

$$|S_{11,C}|^2 + |S_{21,C}|^2 = 1 \tag{C.2a}$$

$$|S_{22,C}|^2 + |S_{12,C}|^2 = 1 \tag{C.2b}$$

$$S^\star_{11,C}S_{12,C} + S^\star_{21,C}S_{22,C} = 0. \tag{C.2c}$$

Then, impedance matching on one side would give $S_{11,C} = 0$, and so: $S_{22,C} = 0$, $|S_{21,C}|^2 = |S_{12,C}|^2 = 1$. Hence, if (C.2) are not valid, in general we cannot say that $S_{11,C} = 0$ implies $S_{22,C} = 0$. For lossy networks inserted between a source and a load, optimum power transfer from the source to the load is only obtained with two matching networks: one before and one after the lossy section [217, page 331], in order to impose separately the two conditions $S_{11,C} = 0$ and $S_{22,C} = 0$. This is important for the impedance matching of modulator and detector because we only have physical access to one side of the scattering matrix that describes these devices.

From the point of view of the power transfer in the detector stage, losses within a matrix S_A as well as in the chained matching network S_B, have a double impact:

- Some power is dissipated on the loss, decreasing the $|S_{21,C}|^2$.
- The loss prevents perfect matching of the device on both sides of S_C, because the matching network is applied on one side only.

Both conditions decrease the transducer gain associated to the chain of networks S_C, decreasing the efficiency of the power transfer for a source applied to S_A to a load connected to S_B.

Many detectors and modulators are wideband impedance matched using lossy resistive networks. For the reason described above, lossy matching networks are well known to be a significant source of losses in ROF links. Hence, in narrowband links, lossless reactive impedance matching should be preferred to improve the link RF gain.

Appendix D

Variance of detected photocurrent in presence of additive optical noise

In this appendix we develop equation (4.25) to prove (4.28). Let us recall (4.25):

$$\sigma_{\mathbf{i}}^2(t) = C_{\mathbf{i}}(t,t) = \mathcal{R}^2 \iint_{-\infty}^{+\infty} C_{|\mathbf{V}|^2}(\alpha,\beta)\, h(t-\alpha)\, h(t-\beta)\; d\alpha\, d\beta + \\ + \mathcal{R}\, e \left[\left\langle |\mathbf{V}(t)|^2 \right\rangle * h^2(t)\right], \quad \text{(D.1)}$$

where $\mathbf{V}(t) = V_s(t) + \mathbf{V}_n(t)$ is a stochastic process, baseband complex equivalent representation of the optical field, sum of a deterministic signal $V_s(t)$ and a complex noise process $\mathbf{V}_n(t)$, stationary, gaussian, circularly symmetric, and with zero expected value. $C_{|\mathbf{V}|^2}(t_1,t_2)$ is the autocovariance of $|\mathbf{V}(t)|^2$, $\mathcal{R}$ is the detector responsivity, e is the elementary charge and $h(t)$ is an electric filter.

The autocovariance $C_{|\mathbf{V}|^2}(\alpha,\beta)$ can be written as:

$$C_{|\mathbf{V}|^2}(\alpha,\beta) = \left\langle |\mathbf{V}(\alpha)|^2 |\mathbf{V}(\beta)|^2 \right\rangle - \left\langle |\mathbf{V}(\alpha)|^2 \right\rangle \left\langle |\mathbf{V}(\beta)|^2 \right\rangle, \quad \text{(D.2)}$$

and:

$$\left\langle |\mathbf{V}(t)|^2 \right\rangle = \left\langle \mathbf{V}(t)\, \mathbf{V}^\star(t) \right\rangle \quad \text{(D.3)}$$

$$= V_s(t)\, V_s^\star(t) + \left\langle \mathbf{V}_n(t)\, \mathbf{V}_n^\star(t) \right\rangle + V_s(t) \left\langle \mathbf{V}_n^\star(t) \right\rangle + \left\langle \mathbf{V}_n(t) \right\rangle V_s^\star(t) \quad \text{(D.4)}$$

$$= |V_s(t)|^2 + \left\langle |\mathbf{V}_n(t)|^2 \right\rangle, \quad \text{(D.5)}$$

where the last passage stems from the zero expected value of $\mathbf{V}_n(t)$.

The other term of $C_{|\mathbf{V}|^2}(\alpha,\beta)$ is more complex:

$$\begin{aligned}\left\langle |\mathbf{V}(\alpha)|^2 |\mathbf{V}(\beta)|^2 \right\rangle &= \langle [V_s(\alpha)+\mathbf{V}_n(\alpha)]\,[V_s^\star(\alpha)+\mathbf{V}_n^\star(\alpha)] \\ &\quad \times [V_s(\beta)+\mathbf{V}_n(\beta)]\,[V_s^\star(\beta)+\mathbf{V}_n^\star(\beta)]\rangle \\ &= |V_s(\alpha)|^2 |V_s(\beta)|^2 + |V_s(\alpha)|^2 V_s(\beta)\langle \mathbf{V}_n^\star(\beta)\rangle \\ &\quad + |V_s(\alpha)|^2 V_s^\star(\beta)\langle \mathbf{V}_n(\beta)\rangle + |V_s(\alpha)|^2 \langle \mathbf{V}_n(\beta)\,\mathbf{V}_n^\star(\beta)\rangle \\ &\quad + |V_s(\beta)|^2 V_s(\alpha)\langle \mathbf{V}_n^\star(\alpha)\rangle + V_s(\alpha)V_s(\beta)\langle \mathbf{V}_n^\star(\alpha)\,\mathbf{V}_n^\star(\beta)\rangle \\ &\quad + V_s(\alpha)V_s^\star(\beta)\langle \mathbf{V}_n^\star(\alpha)\,\mathbf{V}_n(\beta)\rangle + V_s(\alpha)\langle \mathbf{V}_n^\star(\alpha)\,\mathbf{V}_n(\beta)\,\mathbf{V}_n^\star(\beta)\rangle \\ &\quad + V_s^\star(\alpha)V_s(\beta)V_s^\star(\beta)\langle \mathbf{V}_n(\alpha)\rangle + V_s^\star(\alpha)V_s(\beta)\langle \mathbf{V}_n(\alpha)\,\mathbf{V}_n^\star(\beta)\rangle \\ &\quad + V_s^\star(\alpha)V_s^\star(\beta)\langle \mathbf{V}_n(\alpha)\,\mathbf{V}_n(\beta)\rangle + V_s^\star(\alpha)\langle \mathbf{V}_n(\alpha)\,\mathbf{V}_n(\beta)\,\mathbf{V}_n^\star(\beta)\rangle \\ &\quad + V_s(\beta)V_s^\star(\beta)\langle \mathbf{V}_n(\alpha)\,\mathbf{V}_n^\star(\alpha)\rangle + V_s(\beta)\langle \mathbf{V}_n(\alpha)\,\mathbf{V}_n^\star(\alpha)\,\mathbf{V}_n^\star(\beta)\rangle \\ &\quad + V_s^\star(\beta)\langle \mathbf{V}_n(\alpha)\,\mathbf{V}_n^\star(\alpha)\,\mathbf{V}_n(\beta)\rangle + \langle \mathbf{V}_n(\alpha)\,\mathbf{V}_n^\star(\alpha)\,\mathbf{V}_n(\beta)\,\mathbf{V}_n^\star(\beta)\rangle\,. \end{aligned} \tag{D.6}$$

Simplification of equation (D.6) is obtained by exploiting the gaussian nature of $\mathbf{V}_n(t)$ and the moment theorem for complex gaussian processes [218], which states that:

$$\begin{aligned}\langle \mathbf{V}_n(\alpha)\,\mathbf{V}_n^\star(\alpha)\,\mathbf{V}_n(\beta)\,\mathbf{V}_n^\star(\beta)\rangle &= \left\langle |\mathbf{V}_n(\alpha)|^2 \right\rangle \left\langle |\mathbf{V}_n(\beta)|^2 \right\rangle + \\ &\quad + \langle \mathbf{V}_n(\alpha)\,\mathbf{V}_n^\star(\beta)\rangle \langle \mathbf{V}_n^\star(\alpha)\,\mathbf{V}_n(\beta)\rangle\,, \end{aligned} \tag{D.7}$$

and:

$$x = \{\alpha,\beta\} : \langle \mathbf{V}_n(x)\,\mathbf{V}_n^\star(x)\,\mathbf{V}_n(x)\rangle = \langle \mathbf{V}_n(x)\,\mathbf{V}_n^\star(x)\,\mathbf{V}_n^\star(x)\rangle = 0. \tag{D.8}$$

Also, from the circularity of $\mathbf{V}_n(t)$ [124, 125]:

$$\langle \mathbf{V}_n^\star(\alpha)\,\mathbf{V}_n^\star(\beta)\rangle = \langle \mathbf{V}_n(\alpha)\,\mathbf{V}_n(\beta)\rangle = 0. \tag{D.9}$$

Recalling that $\mathbf{V}_n(t)$ has zero expected value, (D.6) simplifies to:

$$\begin{aligned}\left\langle |\mathbf{V}(\alpha)|^2 |\mathbf{V}(\beta)|^2 \right\rangle &= |V_s(\alpha)|^2 |V_s(\beta)|^2 + |V_s(\alpha)|^2 \left\langle |\mathbf{V}_n(\beta)|^2 \right\rangle + |V_s(\beta)|^2 \left\langle |\mathbf{V}_n(\alpha)|^2 \right\rangle \\ &\quad + V_s(\alpha)V_s^\star(\beta)\langle \mathbf{V}_n^\star(\alpha)\,\mathbf{V}_n(\beta)\rangle + V_s^\star(\alpha)V_s(\beta)\langle \mathbf{V}_n(\alpha)\,\mathbf{V}_n^\star(\beta)\rangle \\ &\quad + \left\langle |\mathbf{V}_n(\alpha)|^2 \right\rangle \left\langle |\mathbf{V}_n(\beta)|^2 \right\rangle + \langle \mathbf{V}_n(\alpha)\,\mathbf{V}_n^\star(\beta)\rangle \langle \mathbf{V}_n^\star(\alpha)\,\mathbf{V}_n(\beta)\rangle \end{aligned} \tag{D.10}$$

Finally, from (D.10), (D.2) and (D.5):

$$\begin{aligned} C_{|\mathbf{V}|^2}(\alpha,\beta) &= V_s(\alpha)V_s^\star(\beta)\langle \mathbf{V}_n^\star(\alpha)\,\mathbf{V}_n(\beta)\rangle + V_s^\star(\alpha)V_s(\beta)\langle \mathbf{V}_n(\alpha)\,\mathbf{V}_n^\star(\beta)\rangle \\ &\quad + \langle \mathbf{V}_n(\alpha)\,\mathbf{V}_n^\star(\beta)\rangle \langle \mathbf{V}_n^\star(\alpha)\,\mathbf{V}_n(\beta)\rangle \\ &= 2\cdot \mathrm{Re}\left\{V_s^\star(\alpha)V_s(\beta)\langle \mathbf{V}_n(\alpha)\,\mathbf{V}_n^\star(\beta)\rangle\right\} + \left|\langle \mathbf{V}_n(\alpha)\,\mathbf{V}_n^\star(\beta)\rangle\right|^2 \end{aligned} \tag{D.11}$$

Hence:

$$\sigma_{\mathbf{i}}^2(t) = \sigma_{\mathbf{i},V_s\ shot}^2(t) + \sigma_{\mathbf{i},V_n\ shot}^2(t) + \sigma_{\mathbf{i},V_nV_n\ beat}^2(t) + \sigma_{\mathbf{i},V_sV_n\ beat}^2(t)\,, \tag{D.12}$$

where:

$$\sigma^2_{\mathbf{i},V_s\ shot}(t) = \mathcal{R}e\left[|V_s(t)|^2 * h^2(t)\right] \tag{D.13a}$$

$$\sigma^2_{\mathbf{i},V_n\ shot}(t) = \mathcal{R}e\left[\left\langle|V_n(t)|^2\right\rangle * h^2(t)\right] \tag{D.13b}$$

$$\sigma^2_{\mathbf{i},V_nV_n\ beat}(t) = \mathcal{R}^2 \iint_{-\infty}^{+\infty} \left|\langle \mathbf{V}_n(\alpha)\, \mathbf{V}_n^\star(\beta)\rangle\right|^2 h(t-\alpha)\, h(t-b)\ d\alpha d\beta \tag{D.13c}$$

$$\sigma^2_{\mathbf{i},V_sV_n\ beat}(t) = 2\mathcal{R}^2 \cdot \mathrm{Re}\Bigg\{ \iint_{-\infty}^{+\infty} V_s^\star(\alpha)\, V_s(\beta)\, \langle \mathbf{V}_n(\alpha)\, \mathbf{V}_n^\star(\beta)\rangle \times \times\ h(t-\alpha)\, h(t-\beta)\ d\alpha d\beta \Bigg\} \tag{D.13d}$$

Appendix E

An experimental verification of the Brillouin-induced RF noise model

In chapter 4 we modeled the RF noise caused by SBS as a stochastic cyclostationary process. After stationarization, we described its power spectral density as the convolution between $R_{V_n}(\tau)$ and $R_{V_s}(\tau)$: the former was the autocorrelation of a stationary stochastic process representing a narrowband SBS-induced noise on the optical carrier, and the latter was the autocorrelation of the modulation signal (in the optical field domain), written as:

$$R_{V_s}(\tau) = \sum_{n \to -\infty}^{+\infty} |c_n|^2 e^{jn\omega_{RF}\tau}. \tag{E.1}$$

Now, let us examine a particular type of modulation: a perfectly linear sinusoidal modulation of the instantaneous optical power at frequency f_{RF}, with 100% OMD. If such a modulation were possible experimentally, and if the link were dispersion and distortion free (apart for the SBS), after detection we would observe a perfect sinusoid, with no harmonic components at nf_{RF}, with $n > 1$. It would be:

$$|V_s(t)|^2 = 1 + \cos(2\pi f_{RF} t), \tag{E.2}$$

and the spectrum of the received photocurrent, proportional to $|V_s(t)|^2$ through the detector responsivity, would have the simple shape picture in Fig. E.1a. Instead, the signal $V_s(t)$ would have a more complex spectrum, with infinite harmonics (Fig. E.1b). Hence, the $V_s - V_n$ beating component of the SBS noise, whose PSD is the convolution between the Fourier transform of $R_{V_s}(\tau)$ given above and the PSD of V_n, would have a spectrum with power around all the harmonics of f_{RF}. The total detected signal would have the spectrum given in Fig. E.1d: there would be detected noise in regions of spectrum where there is no signal power.

This may appear surprising, but it can be understood by recalling that the detection process generates infinite beating terms between spectral components of $V_s(t)$. In the

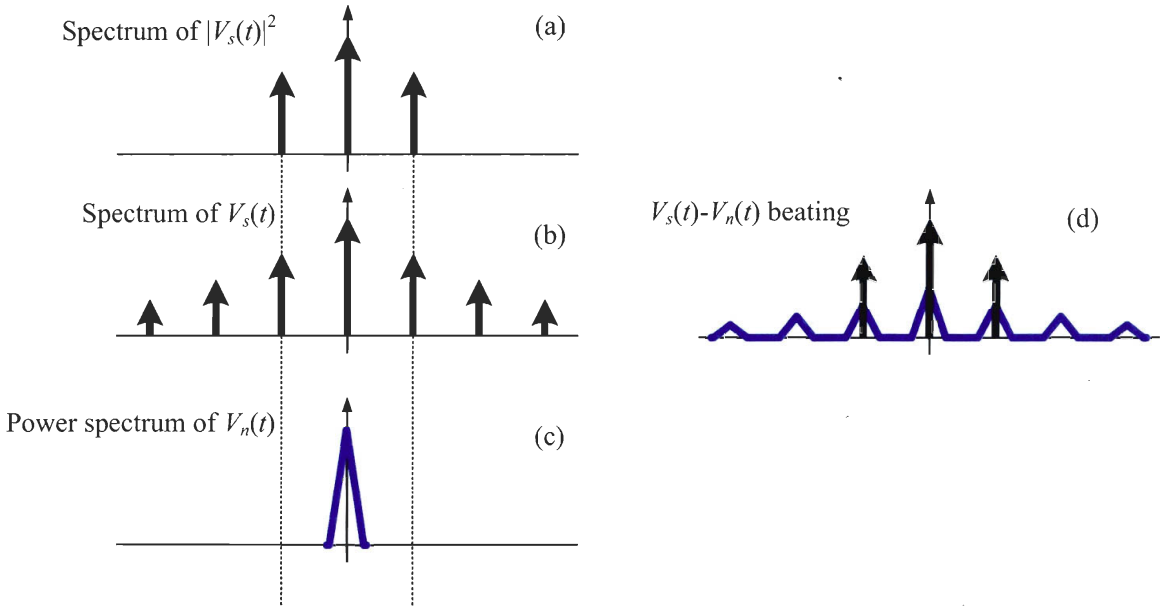

Figure E.1: Graphical calculation of the SBS noise contribution on the detected RF spectrum.

detected photocurrent, those beating terms contributing to harmonics of order $n > 1$ add up in conditions of total destructive interference, and so the harmonics are nulled. This destructive interference is not possible for the beating terms between V_n and V_s because V_n is bandlimited around the optical carrier.

Unluckily, a perfectly linear modulation is not practically achievable, especially with high OMD. However, in a link with a MZ modulator it is possible to null the second harmonic of the detected photocurrent. This is done usually by fixing the bias at quadrature[1]. Then, if the model is correct, we should detect strong noise around $2f_{RF}$, even if the second harmonic is suppressed.

To test this hypothesis, we set up an experimental link shown in Fig. E.2: a `Tunics` laser with output power of 7 dBm was followed by a MZ modulator and an amplifier, an isolator (`Global Opticom IL16DBAB00`) and 20 km of standard fibre. We fed the modulator with a 3 GHz, 19 dBm sinusoidal signal. We optimized the MZ bias to minimize the detected second order harmonic. At this bias, the average power at fibre input was 14.6 dB. At fibre output, an attenuator was used to avoid detector saturation. The optical spectrum at fibre input (point A) and output (point B) are shown in Fig. E.3: at fibre input only the carrier was strong enough to excite SBS (the SBS threshold is about 5 dBm and the modulation sidebands have about 3.5 dBm).

At the fibre output the carrier appear suppressed by the SBS. Note that the spectrum has been measured with an OSA `ANDO AQ6317B` with 10 pm resolution, which is

[1]The propagation over a nonlinear fibre can modify the received spectrum so that the minimum second order harmonic distortion is obtained for a bias slightly off quadrature, but this does not modify the experiment and conclusions presented here.

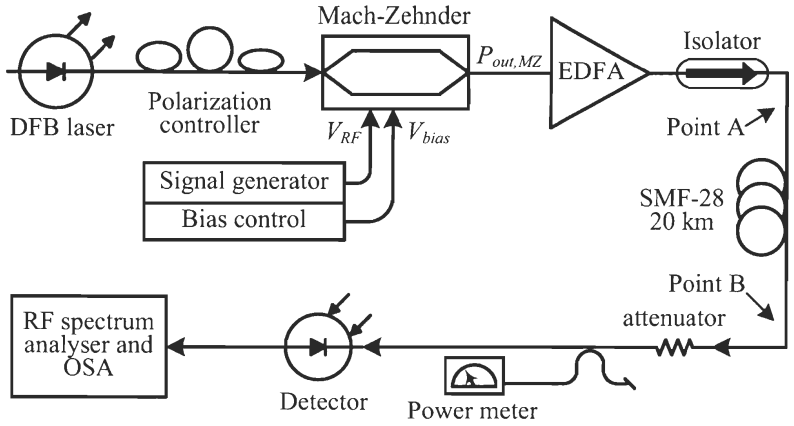

Figure E.2: Experimental link to test the Brillouin noise model.

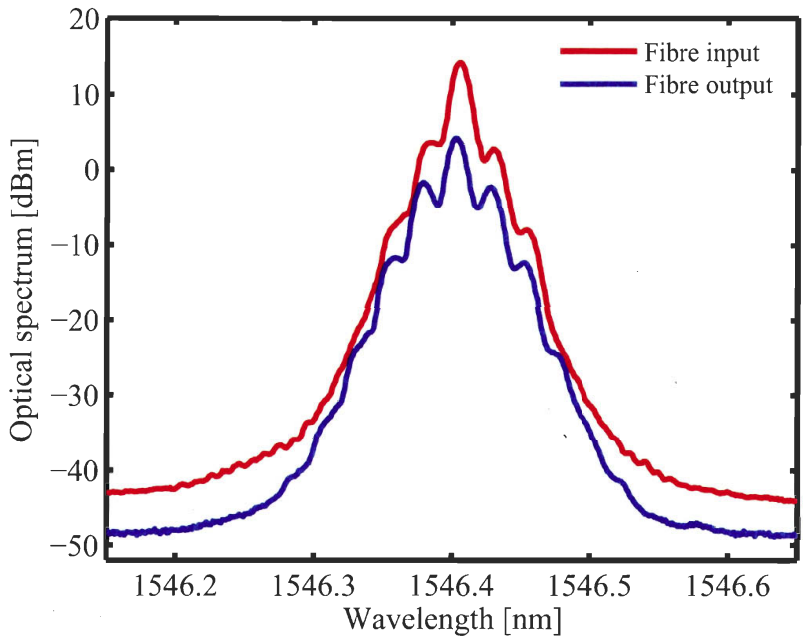

Figure E.3: Optical spectrum at fibre input and output: modulator bias that minimizes the detected second harmonic.

enough to clearly see the second harmonic in the optical spectrum at fibre end.

In Fig. E.4 we show the detected spectrum around the first harmonic at 3 Ghz and the second harmonic at 6 GHz, the latter shifted to superimpose it with the first harmonic. The second harmonic is suppressed, but the SBS noise is clearly visible, with the same bandwidth as the noise around the first harmonic, as predicted by the model. Also, note that the noise level around the second harmonic is about 10 dB below the noise around the first harmonic. This well agrees with the power of the second harmonic in the optical spectrum shown in Fig. E.3, which is also about 10 dB below the first modulation sideband. We think that this is a very good proof of the model.

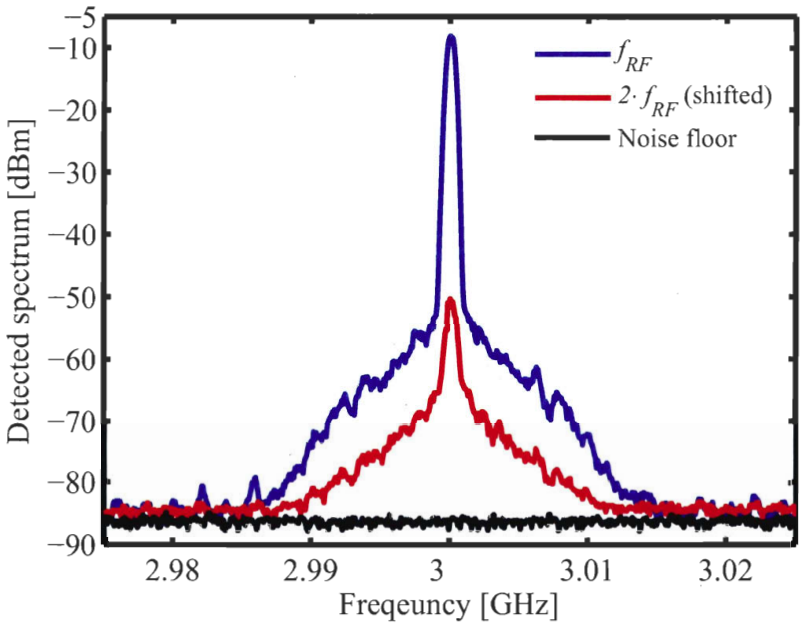

Figure E.4: Detected RF spectrum: first harmonic and second harmonic, shifted in frequency for clarity. Modulator bias set to minimize the second harmonic.

Another proof can be obtained by setting the MZ at the maximum transmission point: the first harmonics of both the optical spectrum and the electrical detected spectrum are suppressed. In Fig. E.5 we show the optical spectrum at fibre input and output: again, only the carrier can excite the SBS and the second harmonic is well below the SBS threshold. The detected RF spectrum, in Fig. E.6, shows a strong SBS noise around the second harmonic, while there is no noise around the first harmonic because the first optical modulation sideband is also suppressed. This confirms that SBS-induced noise is found only at frequencies that correspond to strong components in the optical spectrum, as predicted by the model.

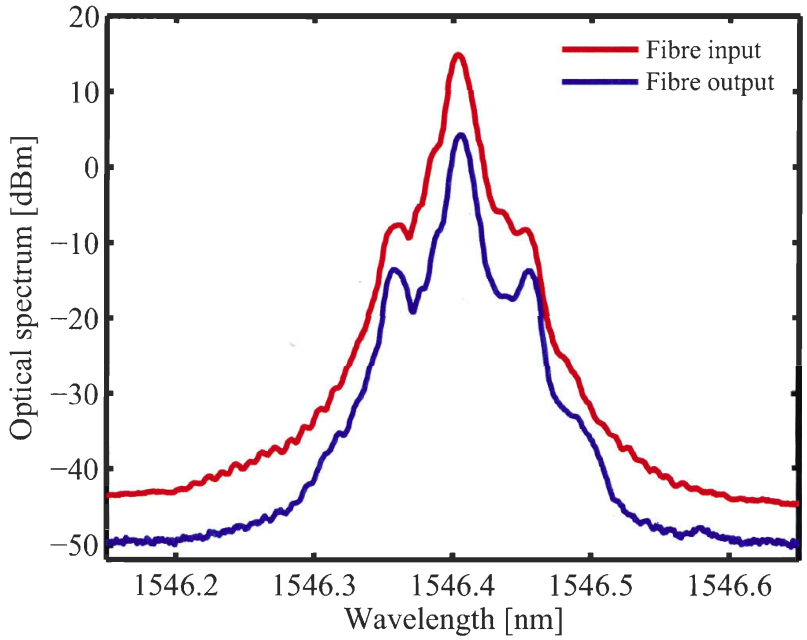

Figure E.5: Optical spectrum at fibre input and output: modulator bias that minimizes the detected first harmonic.

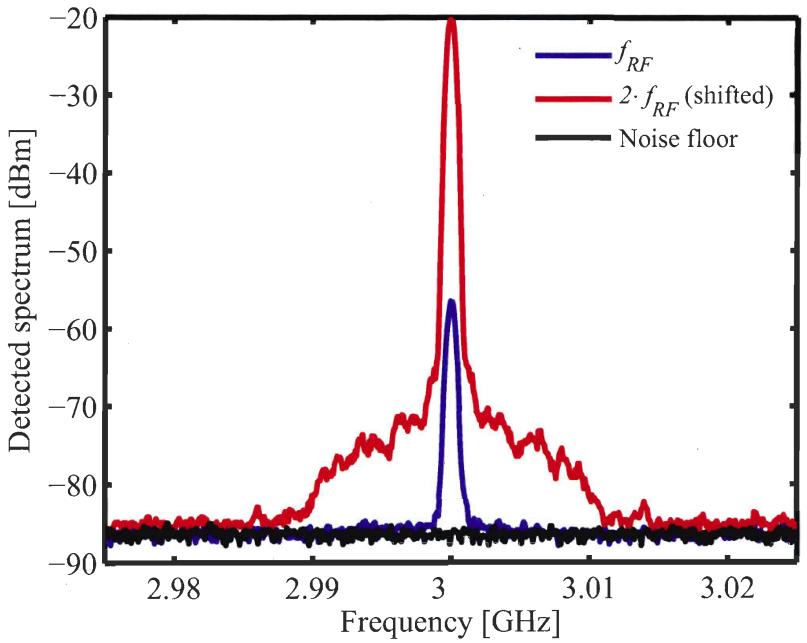

Figure E.6: Detected RF spectrum: first harmonic and second harmonic, shifted in frequency for clarity. Modulator bias set to minimize the first harmonic.

Appendix F

Spectrum of Brochu's fibre laser

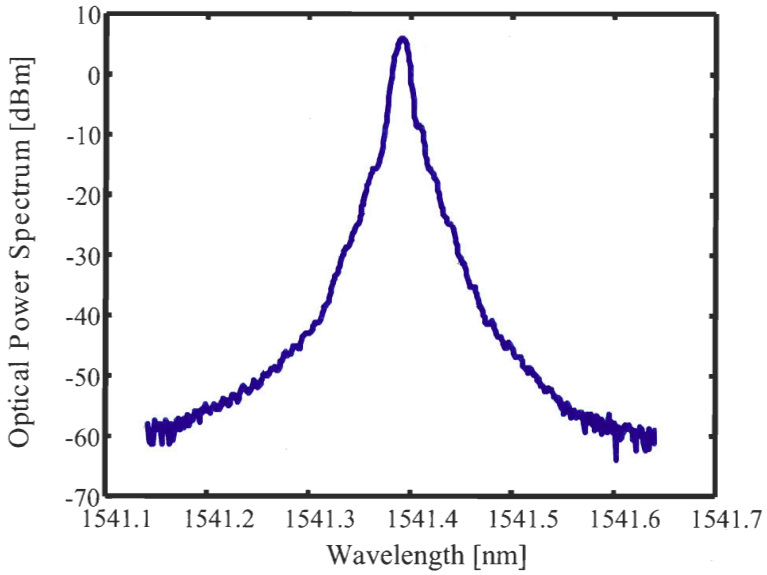

Figure F.1: Spectrum of Brochu's fibre laser. Pump laser: JDS 27-BCB-794, 980 nm. Pump bias current: 330 mA. Laser temperature: 17°C (thermistor: 14 kΩ). Output power: 6.8 dBm.

This is a DFB fibre laser based on a chirped FBG written in erbium-ytterbium codoped fibre. In the center of the grating, a π jump in the phase of the index modulation allows lasing on a single wavelength. The phase mask chirp for inscription of the grating is 0.5 nm/cm and the grating length is 2 cm.

Appendix G

Distortions from electroabsorption and SOAs modulators

We discussed in chapter 1 the importance of reducing the complexity and costs of the WTPs in centralized ROF distribution links for wireless networks. To achieve this goal, the electrical-to-optical and optical-to-electrical conversion at the WTP must be as low cost and efficient as possible, especially for multiple antenna systems where the cost of the conversion is multiplied by the number of antenna elements, unless the ROF link is based on WDM architectures with multiple optical carriers sharing the same modulator. Indeed, the MZ modulator offers good performance, but it is a relatively expensive device. Most importantly, $LiNbO_3$ technology and precesses do not allow the integration of a MZ on the same substrate of other optical components as DFB lasers, filters, detectors and waveguides. The integrability of various optical devices on a so called photonic chip is considered an important development trend that should drive a decrease in optical devices production costs, as it happened for electronics when it moved from discrete to integrated components. [1]

In literature, EAMs are often proposed as external modulators for WTP applications [222, 223, 36]. A noteworthy publication is [224], where Yaakob studies the performance of EAMs with 802.11a signals. However, he does not evaluate the impact of modulator bias optimization. In order to clarify this point and verify if any bias optimization technique can be used with EAMs, we characterized the EVM and BER at the output of a EAM as a function of bias.

SOAs have been also proposed as modulators for WTPs [225, 226], because they offer also gain on the optical signal and because they can be integrated with other devices, like the detector [227]. Later in this section, we present a work published in

[1] Silicon photonics is a promising technology that should enable complex photonic chips. Several groups are developing silicon-based MZ modulators [219, 220, 221, 58, 59], silicon-based lasers, filters and detectors that could all be integrated together with the control electronics. However, such devices are not commercially available yet.

collaboration with Francesco Vacondio and Walid Mathlouthi exploring the linearity, EVM and BER performance of a semiconductor optical amplifier (SOA) used as a modulator for 2.5 GHz and 5 GHz OFDM signals. To our knowledge, this is the first characterization of high frequency OFDM transmission with a SOA modulator.

G.1 Distortions from electroabsorption modulator (EAM)

The EAM is a reverse-biased p-i-n diode built in such a way to partially absorb the optical signal in a range of wavelengths. An electrical field applied perpendicular to the p-i-n active layer can change the amount of absorption, i.e., modulate the optical loss for a given wavelength within the operation optical bandwidth. With respect to electro-optic modulators, the EAMs feature no bias drift, lesser polarization dependence and the potential of monolithic integration with other devices like DFB lasers. The main disadvantages of the EAMs are the insertion loss, which is typically higher than MZ modulators, and a low extinction ratio. Hence, they are limited to short range applications [157].

We measured the EVM at the output of a `CyOptics EAM1010` EAM. This device is designed for 10 Gbps optical links; it has low polarization sensitivity and a minimum insertion loss of about 7 dBm at 1550 nm. The experimental setup is shown in Fig. G.1: the EAM is fed with a 5 GHz RF signal and a variable bias voltage through a `Picosecond 5547` bias-tee. The optical carrier source is an `EXFO` DFB laser. After the modulator, the signal is attenuated to avoid detector saturation effects. The bias is set by a computer controlled voltage source.

For an input RF power of 5 dBm and optical power of about 0 dB, the detected average optical power, RF power and HD3 are shown in Fig. G.2: the detected RF power is maximum for a bias of about -0.5 V; the HD3 is not constant with bias but shows a clear valley for $V_{bias} \simeq -1$ V, where the output RF power penalty is relatively low (less than 3 dB below the maximum). This suggests that the EVM performance of the modulator should be optimum at $V_{bias} = -1$ V, which is confirmed by Fig. G.3. Note that for a RF modulation power of 5 dBm, the detected EVM is lower than the maximum fixed by the IEEE 802.11a protocol only over a very narrow range of bias value: the bias is not a free parameter that can be used to optimize the link gain.

For seek of completeness, in Fig. G.4 we report also the measured BER in the same conditions given for Fig. G.3, confirming that BER$< 10^{-6}$ can be achieved only in within a narrow range of bias values.

These results concord with the work of Watanabe [223], who measured the BER of an OFDM signal (not 802.11a compliant) at the output of an EAM as a function of its

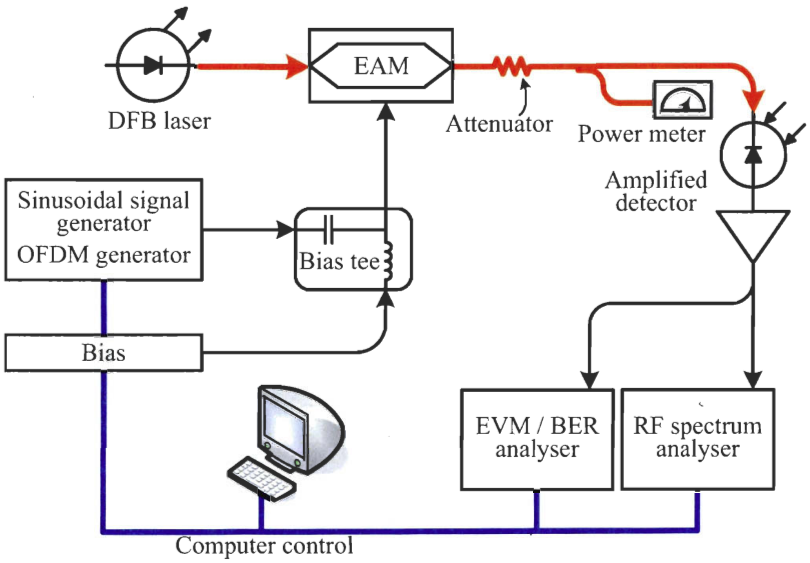

Figure G.1: Laser output power: 9.1 dBm; wavelength: 1550 nm. The EAM temperature is fixed at 18°Cby thermoelectric control (not shown). Laser: `EXFO`; EAM: `CyOptics EAM1010`; bias-tee: `Picosecond 5547`; bias generator: `HP 6634A`; signal generator: `Agilent E4438C`; signal analyzer: `Agilent E4440A`; detector: `Agilent 11982A`.

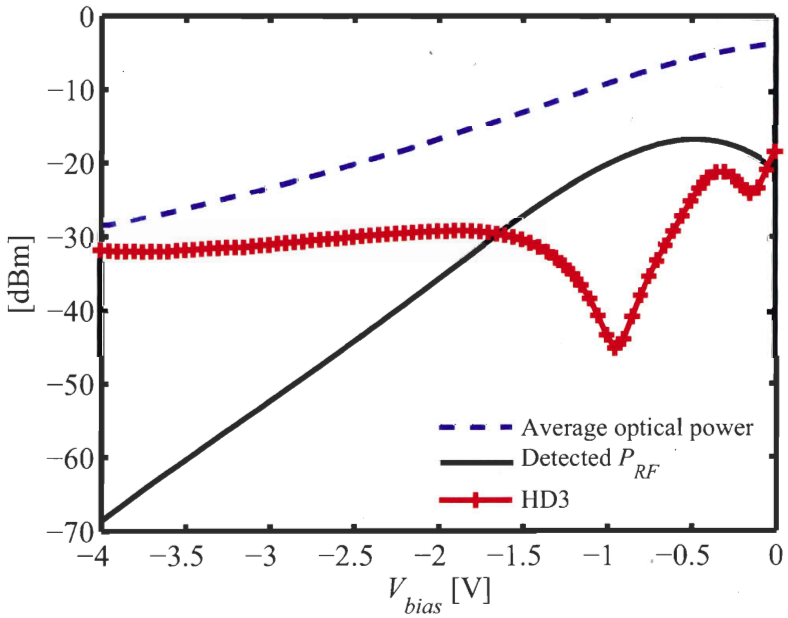

Figure G.2: Average optical power, detected RF power and harmonic distortion at the output of an EAM as a function of the bias voltage.

bias.

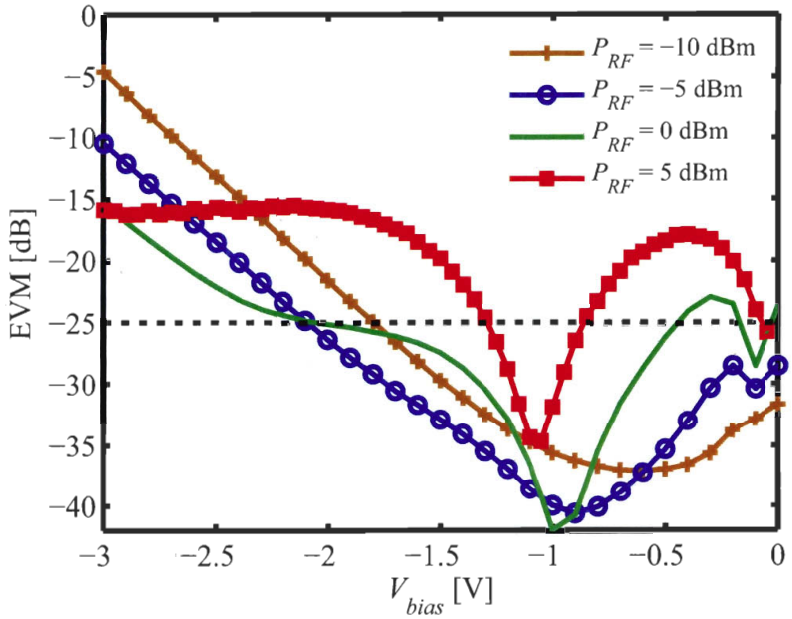

Figure G.3: EVM at the output of an EAM as a function of the modulation power P_{RF} and the bias. For $P_{RF} = -10\,\text{dBm}$ the EVM is essentially noise limited and it is minimum near $V_{bias} = 1\,\text{V}$, which provides maximum detected RF power. For higher P_{RF}, the minimum shifts towards -1 V. For $P_{RF} = 5\,\text{dBm}$, the EVM is distortion limited for all the values of bias in the measured range.

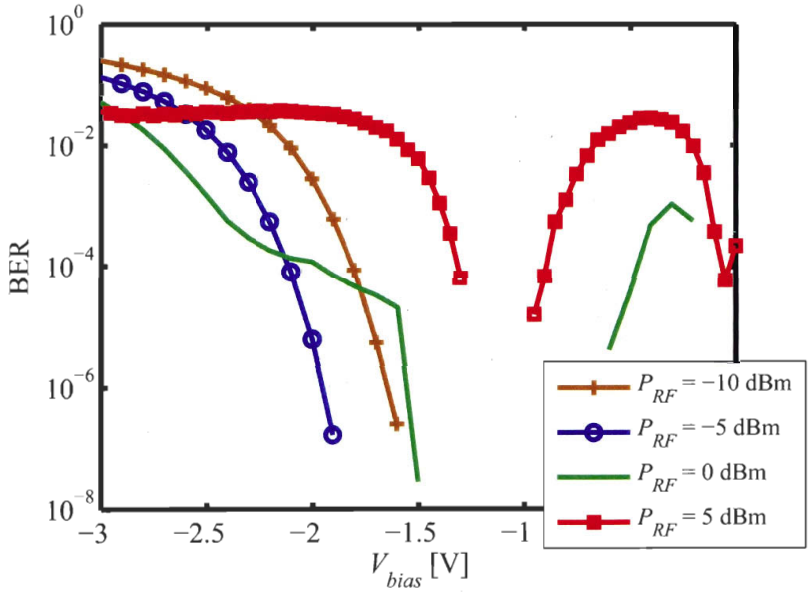

Figure G.4: BER at the output of an EAM as a function of modulation power P_{RF} and bias voltage.

G.2 Distortion from semiconductor optical amplifier (SOA) used as modulator

SOAs can be used as modulators by controlling the bias current. Direct current modulation of SOA have been proposed in literature by several authors [228, 226, 229, 230]. In [225], Metivier characterizes the harmonic distortion generated by a SOA modulator for frequency up to 5 GHz, and finds that HD3 decreases with frequency and average optical power at SOA input. In [231], Mork presents a theoretical analysis of the modulation response of a semiconductor laser amplifier, which is shown to be characterized by a resonance behavior similar to the well-known relaxation oscillation resonance found in semiconductor lasers.

In collaboration with Francesco Vacondio and Walid Mathlouthi, in [64] we reported original experimental results on using a SOA for electrical to optical conversion of 64-QAM 8022.11g/a OFDM signals at 54 Mbit/s on 2.5 GHz and 5 GHz RF carriers. This work was aimed to test the capabilities of direct modulation of the SOA current, by examining its linearity performance and modulation efficiency. This is believed to be the first characterization of high frequency OFDM transmission with a SOA modulator. Results show that it is possible to achieve a quality of service of 10^{-6} BER at both 2.5 GHz and 5 GHz using a SOA in deep saturation to decrease the ASE noise.

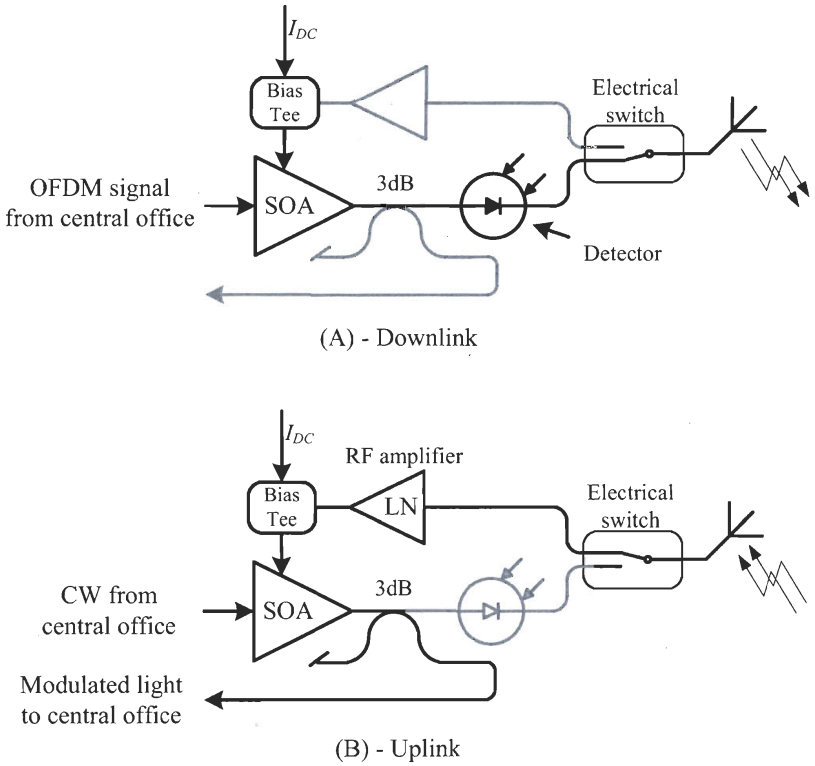

Figure G.5: Schematic diagram of a SOA-based WTP. (a) transmission from the CS to an antenna; (b) transmission from the antenna to the CS.

Direct modulation of a SOA would allow to build low cost WTPs where the same device has both amplification and modulation functions, respectively for signal propagation to the antenna (downlink) and from the antenna (uplink). Fig. G.5 presents a possible embodiment of such a WTP: in downlink mode, the modulated optical signal from the CS is amplified by the SOA before photodetection. In uplink mode, the RF signal from the antenna is amplified with a low noise amplifier, summed to a DC current (via a bias-tee), and injected into the SOA. In this case, the variations of SOA gain with injection current modulates a continuous wave (CW) optical signal from the CS.

The ideal characteristics of the SOA for the amplifier and modulator functions are in conflict: for amplification, a SOA with long carrier lifetime (i.e., long gain recovery time, defined as the time needed for the gain to rise from 10% to 90% of the saturation [232]) is preferable to reduce harmonic and intermodulation distortions [233, 234]. Instead, for modulation at high frequencies, a SOA capable of fast recovery of the gain is required [231]. In the work presented here, we focused on the study of the SOA performance as a modulator for IEEE 802.11a/g OFDM signals on 2.5 GHz and 5 GHz carriers, in order to investigate the feasibility of the proposed base station and to evaluate the constraints imposed by the tested SOA in modulation mode. We did not investigate the performance of the SOA as an amplifier. We used a bulk SOA (`OptoSpeed 1550MRI`) with a recovery time of about 350 ps: an average value for this type of SOAs [232]. The modulation bandwidth can be roughly estimated from the gain recovery time t_g as:

$$BW \simeq \frac{0.35}{t_g}, \tag{G.1}$$

which gives a theoretical modulation bandwidth of about 1 GHz.

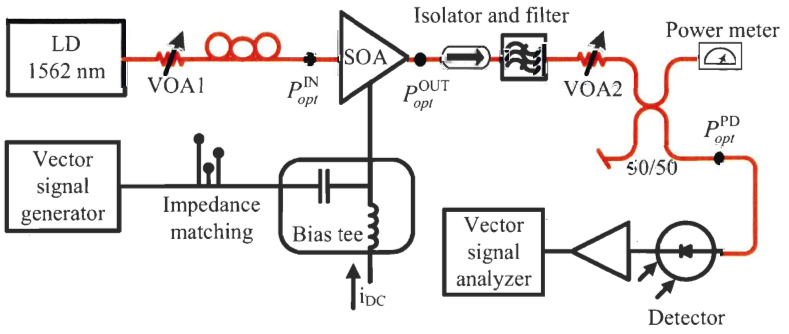

Figure G.6: Experimental setup for SOA modulation tests.

Fig. G.6 shows the experimental setup used for testing the SOA modulation: the output of a laser diode at 1562 nm, where the SOA amplification gain is maximum, is fed to the SOA through a variable attenuator and a polarization controller (this SOA is polarization sensitive). The bias current is supplied through a bias-tee in order to sum a DC term and an OFDM modulated signal, generated by a VSG (`Agilent E4440A`). The signal generator impedance is matched to the biasing circuit by a triple matching stub. Impedance matching is extremely helpful in our case because of the complex

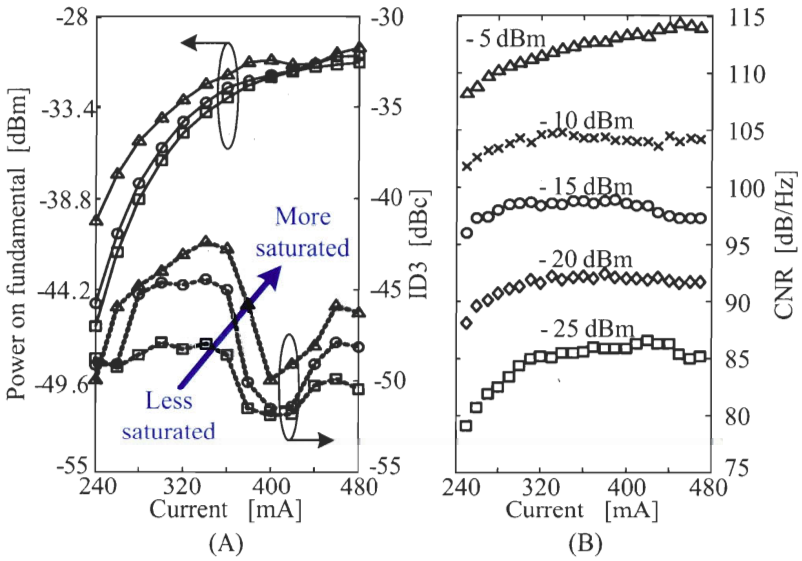

Figure G.7: A) Power of the fundamental and IMD3 and B) CNR versus bias current i_{DC} for different optical input powers to the SOA. $P_{opt}^{IN} = -5$ dBm (△), -10 dBm (x), -15 dBm (o), -20 dBm (◇) and -25 dBm (□).

impedance presented by the SOA, affected not only by the SOA chip itself, but also by the packaging and the biasing circuit.

To find an optimum operating point for the SOA we examined three criteria: the power of the fundamental component, the IMD3 and the CNR. Fig. G.7a shows the result of the inter-modulation distortion measurements. For these measurements the VSG produced two tones with 1 MHz spacing around 2.5 GHz, and we measured the ratio between the powers of the received tones versus the IMD3 products. The IMD3 contribution from the VSG was as low as -80 dBc. We varied the bias point and the level of saturation of the SOA for a fixed modulation power of +8 dBm per tone (+11 dBm total). We observed that the power of the fundamental component increases with the saturation level because of the greater power on the photodiode. At the same time, the IMD3 increases somewhat in the saturation regime. However, the measured distortion levels are well below -40 dB for all input powers and bias values, and have a very low impact on the signal EVM, as shown later on. It is important to note that low saturation gives reduced distortion even when the SOA is used as an amplifier [233, 234].

In Fig. G.7b, the VSG produced one tone at 2.5 GHz, and we measured the CNR as a function of the SOA bias point for various optical input powers. The CNR increases monotonically to some maximum value at moderate pump currents, and for high pump bias current the CNR stays fairly constant. In this test, at low bias current the CNR is mainly limited by system thermal noise because the received signal power is very low, as shown in Fig. G.7a. At currents higher than about 300 mA, the principal noise source is the SOA ASE, which decreases in deeper saturation. Hence, the CNR is improved by increasing the pump current and saturation level.

The measured nonlinearity is relatively low and constant with the input optical power and bias, and the ASE-induced reduction of the CNR appears to be a much stronger limitation on signal EVM. This is confirmed by Fig. G.8, where we shows the measured EVM as a function of SOA input optical power and modulation power. The bias current is fixed at 460 mA, which is near the maximum current bias accepted by the SOA, and the detected optical power is kept constant at -10 dBm. In these conditions, at low optical power the EVM is limited by ASE noise and decreases with saturation to a minimum level, where ASE noise contribution is minimum and system thermal noise and shot noise are dominant. In all tests, the detected EVM is noise limited so that EVM decreases linearly with the increase in modulation power.

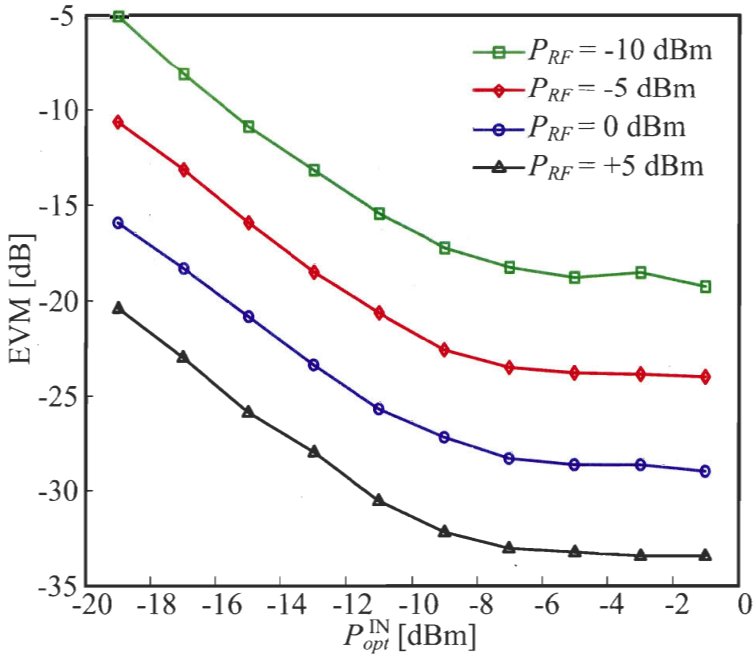

Figure G.8: EVM as a function of SOA input average optical power and modulation power. RF carrier: 2.5 GHz. The optical power on the photodetector is fixed at −10 dBm. The points under the dotted line correspond to BER< 10^{-6} with 802.11a-compliant FEC.

It appears that the optimum operating point for the SOA is at high bias current and high saturation. In fact, in all operating conditions the distortion is low enough to have a noise-limited EVM. Hence, increasing the received signal CNR improves the detected EVM. At strong bias current and saturation, SOA ASE is minimum, the detected signal is maximum, CNR is also maximum.

In figures G.9 and G.10 we show the detected BER, with and without convolutional coding as defined by the IEEE 802.11a protocol. Not surprisingly, the detected BER improves with input optical power to the SOA and modulation RF power. The 5 GHz carrier frequency is much higher than the theoretical modulation bandwidth of the SOA, and the device package was not designed for high frequency modulation. Hence, we observed a modulation power penalty of more than 13 dB between 2.5 GHz and 5 GHz modulations.

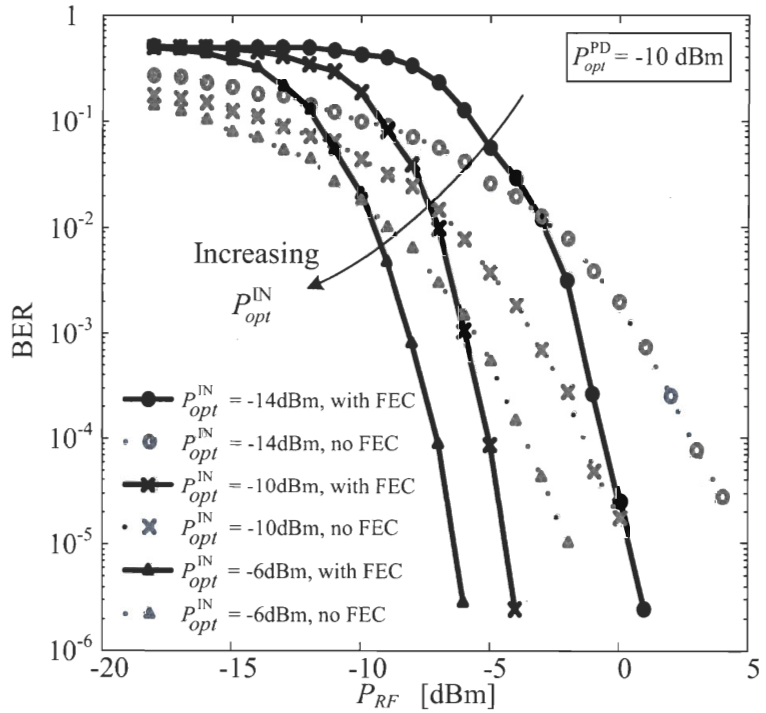

Figure G.9: Detected BER versus SOA RF modulation power and optical input power. The modulation signal is a 2.5 GHz OFDM modulated carrier. The optical power on the photodetector is fixed at -10 dBm.

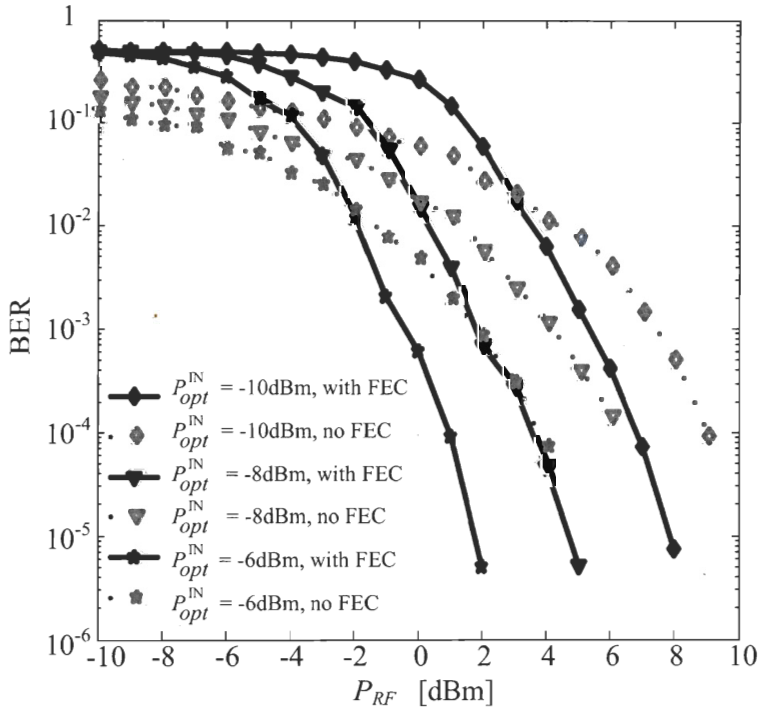

Figure G.10: Same as Fig. G.9, but with a 5 GHz carrier.

In conclusion, we demonstrated that electro-optical conversion of analog signals such as IEEE 802.11a/g OFDM signals on 2.5 GHz and 5 GHz carriers is possible by direct modulation of the injection current of a SOA. In all tests, the modulator output was noise limited, and IMD3 was well below -40 dBc. In order to improve the SOA modulation efficiency, the bias current must be as high as possible. Also, to reduce the modulator ASE contribution to noise, the SOA should be operated in saturation. We did not study the performance of the SOA as an amplifier.

Appendix H

Amplitude and delay response of the experimental gratings for the multichannel TS-BF

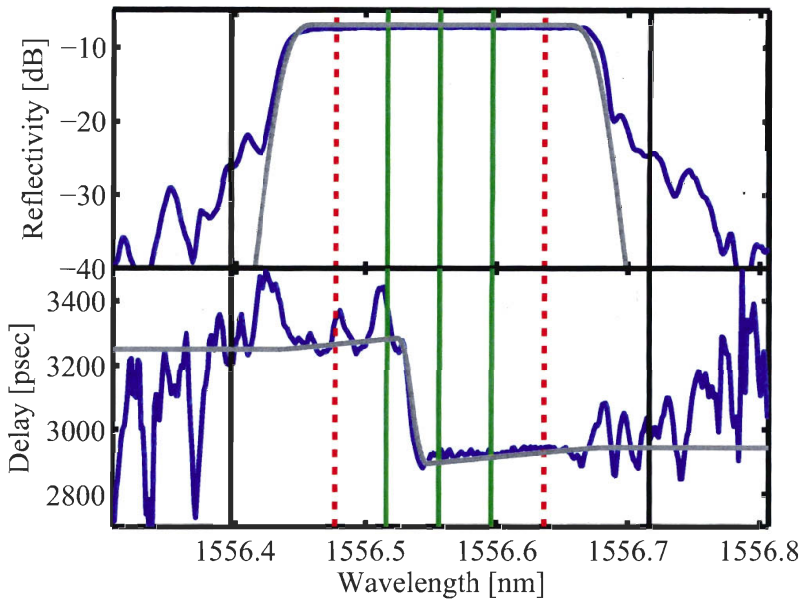

Figure H.1: Reflectivity and delay of the experimental FBG_L. In grey: design goal; in blue: actual grating. Green vertical lines represent the position of the optical carrier and modulation sidebands. Red dotted lines limit the region of maximum flat response. Black lines are the nearest position of the sidebands of the adjacent channels.

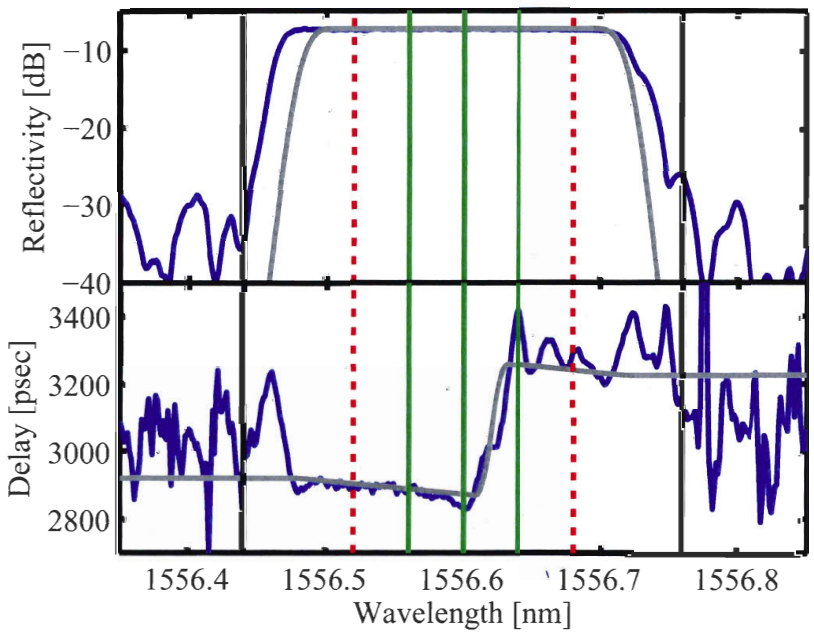

Figure H.2: Reflectivity and delay of the experimental FBG_U. Colors defined as Fig. H.1.

Bibliography

[1] IEEE, "IEEE Std 802.11a-1999 [ISO/IEC 8802-11:1999/Amd 1:2000(E)] (Supplement to IEEE Std 802.11, 1999 Edition) Part 11: Wireless LAN Medium Access Control (MAC) and Physical Layer (PHY) specifications: High-speed Physical Layer in the 5 GHz Band," Institute of Electrical and Electronics Engineers, Tech. Rep., 1999. Cited on pages x, 5, 10, 17, 18 and 30.

[2] IEEE 802.11 Committee, "Official IEEE 802.11 Working Group Project Timelines," June 2007. Available online: http://grouper.ieee.org/groups/802/11/Reports/802.11_Timelines.htm. Cited on page 1.

[3] G. Fleishman, "Metro Round-Up: Los Angeles Announces; Palo Alto Joins," February 2007. Available online: http://www.wifinetnews.com/archives/007409.html. Cited on page 2.

[4] V. Kopytoff and R. Kim, "Google offers S.F. Wi-Fi – for free," October 2005. Available online: http://sfgate.com/cgi-bin/article.cgi?file=/c/a/2005/10/01/MNGG9F16KG1.DTL. Cited on page 2.

[5] M. Unbehaun, "A Feasibility Study of Wireless Networks for 17 and 60 GHz and the Impact of Deployment Strategies on the System Performance," Ph.D. dissertation, Royal Institute of Technology, 2001. Cited on page 2.

[6] A. J. Paulraj, D. A. Gore, R. U. Nabar, and H. Bolcskei, "An overview of MIMO communications - a key to gigabit wireless," *Proceedings of the IEEE*, vol. 92, no. 2, p. 218, 2004. Cited on page 2.

[7] R. Rajavelsamy, V. Jeedigunta, B. Holur, M. Choudhary, and O. Song, "Performance evaluation of VoIP over 3G-WLAN interworking system," in *Wireless Communications and Networking Conference, 2005 IEEE*, vol. 4, 13-17 March 2005, pp. 2312–2317. Cited on page 2.

[8] E. Sadot, L. Yang, and P. Zerfos, "Architecture taxonomy for control and provisioning of wireless access points (CAPWAP)," IETF, Tech. Rep., June 2005. Available online: http://www.ietf.org/rfc/rfc4118.txt. Cited on page 3.

[9] "Comparing Centralized and Distributed Management." Available online: http://www.wireless-center.net/Business-Wireless/Comparing-Centralized-and-Distributed-Management.html. Cited on page 4.

[10] M. Birchler, P. Smyth, G. Martinez, and M. Baker, "Future of mobile and wireless communications," *BT Technology Journal*, vol. 21, no. 3, pp. 11 – 21, July 2003. Available online: http://dx.doi.org/10.1023/A:1025146712481. Cited on page 4.

[11] S. Roy, "Space-Time Processing Techniques with Application to Broadband Wireless Systems," Ph.D. dissertation, Carleton University, 2000. Cited on page 5.

[12] C. U. Saraydar, N. B. Mandayam, and D. J. Goodman, "Efficient power control via pricing in wireless data networks," *IEEE Transactions on Communications*, vol. 50, no. 2, pp. 291 – 303, 2002. Available online: http://dx.doi.org/10.1109/26.983324. Cited on page 5.

[13] S. A. Gandhi, R. Vijayan, D. J. Goodman, and J. Zander, "Centralized power control in cellular radio systems," *IEEE Transactions on Vehicular Technology*, vol. 42, no. 4, pp. 466 – 468, 1993. Available online: http://dx.doi.org/10.1109/25.260766. Cited on pages 6 and 7.

[14] D. Kim, K.-N. Chang, and S. Kim, "Efficient distributed power control for cellular mobile systems," *IEEE Transactions on Vehicular Technology*, vol. 46, no. 2, pp. 313 – 319, 1997. Available online: http://dx.doi.org/10.1109/25.580769. Cited on page 6.

[15] T. Bonald, S. Borst, and A. Proutiere, "Inter-cell coordination in wireless data networks," *European Transactions on Telecommunications*, vol. 17, no. 3, pp. 303 – 312, 2006. Available online: http://dx.doi.org/10.1002/ett.1118. Cited on page 6.

[16] H. Jiang, W. Zhuang, X. Shen, and Q. Bi, "Quality-of-service provisioning and efficient resource utilization in CDMA cellular communications," *IEEE Journal on Selected Areas in Communications*, vol. 24, no. 1, pp. 4 – 15, January 2006. Available online: http://dx.doi.org/10.1109/JSAC.2005.858897. Cited on page 6.

[17] V. K. N. Lau, "On the macroscopic optimization of multicell wireless systems with multiuser detection and multiple antennas - Uplink analysis," *IEEE Transactions on Wireless Communications*, vol. 4, no. 4, pp. 1388 – 1393, 2005. Available online: http://dx.doi.org/10.1109/TWC.2005.850257. Cited on page 6.

[18] H. B. Kim and A. Wolisz, "Load balancing for centralized wireless networks," in *IEEE 16th International Symposium on Personal, Indoor and Mobile Radio Communications, 2005. PIMRC 2005.*, IEEE, Ed., vol. 3. Berlin, Germany: IEEE, Sept. 2005, pp. 1875 – 1879. Cited on page 6.

[19] C. Mihailescu, X. Lagrange, P. Godlewski, and A. Acx, "Dynamic resource allocation in locally centralized cellular systems," in *48th IEEE Vehicular Technology Conference*, vol. 3, Ottawa, Can, 1998, pp. 1695 – 1699. Available online: http://dx.doi.org/10.1109/VETEC.1998.686045. Cited on page 6.

[20] C. Harvey, I. Symington, and D. Kirsten, "Cordless communications utilising radio over fibre techniques for the local loop," in *IEEE International Conference on Communications, 1991. ICC '91, Conference Record.*, IEEE, Ed., vol. 3. Denver, CO, USA: IEEE, June 1991, pp. 1171–5. Cited on page 6.

[21] A. Brandao, L. Lopes, and D. McLernon, "Base station macro-diversity combining merge cells in mobile systems," *Electronics Letters*, vol. 31, no. 1, pp. 12 – 13, 1995. Available online: http://dx.doi.org/10.1049/el:19950051. Cited on page 6.

[22] V. Y. Pan and Z. Q. Chen, "The complexity of the matrix eigenproblem," in *STOC '99: Proceedings of the thirty-first annual ACM symposium on Theory of computing.* New York, NY, USA: ACM Press, 1999, pp. 507–516. Cited on page 7.

[23] P. Leroux, S. Roy, and J.-Y. Chouinard, "An agent system to manage mobile connections in a distributed base station scheme," in *International Symposium on Personal, Indoor and Mobile Radio Communications, 2006 IEEE 17th*, IEEE, Ed. Helsinki, Finland: IEEE, Sept. 2006, pp. 1–6. Cited on page 7.

[24] F. Somers, "HYBRID: unifying centralised and distributed network management using intelligent agents," in *Network Operations and Management Symposium*, vol. 1, Kyoto, Jpn, 1996, pp. 34 – 43. Available online: http://dx.doi.org/10.1109/NOMS.1996.539390. Cited on page 7.

[25] D. M. Pozar, *Microwave Engineering, 2nd Edition.* John Wiley & Sons Inc., 1998. Cited on page 8.

[26] H. Al-Raweshidy and S. Komaki, *Radio over fiber technologies for mobile communications networks.* Boston ; London: Artech House, 2002. Cited on pages 8 and 9.

[27] K. Ajung, J. Young Hun, and K. Yungsoo, "60GHz wireless communication systems with radio-over-fiber links for indoor wireless LANs," *Consumer Electronics, IEEE Transactions on*, vol. 50, no. 2, p. 520, May 2004. Cited on page 8.

[28] T. Kuri, K. Kitayama, and K. Murashima, "Error-free DWDM transmission of 60-GHz-band fiber-radio signals with square-like response fiber Bragg gratings," in *International Topical Meeting on Microwave Photonics, 2001. MWP apos.* Long Beach, CA, USA: IEEE, January 2001, pp. 69–72. Cited on pages 8 and 17.

[29] P. Smulders, "60 GHz radio: prospects and future directions," in *Proc. IEEE 10th Symp. Commun. Veh. Technol*, 2003, pp. 1–8. Cited on pages 8 and 154.

[30] I. Djordjevic and B. Vasic, "Orthogonal frequency division multiplexing for high-speed optical transmission," *Optics Express*, vol. 14, no. 9, 2006. Cited on page 11.

[31] I. B. Djordjevic and B. Vasic, "100-Gb/s transmission using orthogonal frequency-division multiplexing," *IEEE Photonics Technology Letters*, vol. 18, no. 15, pp. 1576 – 1578, 2006. Available online: http://dx.doi.org/10.1109/LPT.2006.879590. Cited on page 11.

[32] A. J. Lowery, L. B. Du, and J. Armstrong, "Performance of optical OFDM in ultralong-haul WDM lightwave systems," *Journal of Lightwave Technology*, vol. 25, no. 1, pp. 131 – 138, 2007. Available online: http://dx.doi.org/10.1109/JLT.2006.888161. Cited on page 11.

[33] T. Berceli, M. Csornyei, B. Klein, and T. Banky, "Nonlinear effects in optical-wireless OFDM signal transmission," in *International Topical Meeting on Microwave Photonics, 2002.* Awaji, Japan: IEICE, Nov. 2002, pp. 225–8. Cited on page 11.

[34] J. Mitchell, "Performance of OFDM at 5.8 GHz using radio over fibre link," *Electronics Letters*, vol. 40, no. 21, pp. 1353 – 1354, 2004. Available online: http://dx.doi.org/10.1049/el:20046724. Cited on pages 11, 117, 122 and 149.

[35] T. Niiho, M. Nakaso, K. Masuda, H. Sasai, K. Utsumi, and M. Fuse, "Transmission performance of multichannel wireless LAN system based on radio-over-fiber techniques," *IEEE Transactions on Microwave Theory and Techniques*, vol. 54, pp. 980–989, Feb. 2006. Cited on page 11.

[36] P. K. Tang, L. C. Ong, A. Alphones, B. Luo, and M. Fujise, "PER and EVM measurements of a radio-over-fiber network for cellular and WLAN system applications," *Journal of Lightwave Technology*, vol. 22, no. 11, pp. 2370–2376, Nov. 2004. Cited on pages 11 and 209.

[37] J.-G. Wang and A. S. Mohan, "Modified Wiener beamforming for indoor multipath channels," in *Universal Personal Communications Record, 1997. Conference Record., 1997 IEEE 6th International Conference on*, vol. 2, San Diego, CA, Oct. 1997, pp. 823–827. Cited on page 12.

[38] R. Morelos-Zaragoza and M. Ghavami, "Combined Beamforming and Space-Time Block Coding for High-Speed Wireless Indoor Communications," in *4th International Symposium on Wireless Personal Multimedia Communications (WPMC'OI)*, Aalborg, Denmark, Sept. 9-12 2001, pp. 1427–1431. Cited on page 12.

[39] M. Katz and J. Ylitalo, "Extension of space-time coding to beamforming WCDMA base stations," in *Vehicular Technology Conference Proceedings, 2000. VTC 2000-Spring Tokyo. 2000 IEEE 51st*, vol. 2, Tokyo, Japan, 2000, pp. 1230–1234. Cited on page 12.

[40] S. S. Jeng, G. Xu, H. P. Lin, and W. J. Vogel, "Experimental study of antenna arrays in indoor wireless applications," in *Conference Record of The Twenty-Ninth Asilomar Conference on Signals, Systems and Computers*, Pacific Grove, CA, USA, 1996, pp. 766–70. Cited on pages 12 and 155.

[41] K. Hayashi and S. Hara, "A spatio-temporal equalization method for indoor wireless LANs with beamforming criterion selection," in *Vehicular Technology Conference, 2001. VTC 2001 Fall. IEEE VTS 54th*, vol. 1, 2001, pp. 506–510. Cited on page 12.

[42] Y. F. Chen and C. S. Wang, "Adaptive Antenna Arrays for Interference Cancellation in OFDM Communication Systems With Virtual Carriers," *IEEE Transactions on Vehicular Technology*, vol. 56, pp. 1837–1844, Jul. 2007. Cited on page 12.

[43] Y. C. Chung and R. L. Haupt, "Optimum amplitude and phase control for an adaptive linear array using a genetic algorithm," *IEEE Antennas and Propagation Society, AP-S International Symposium (Digest)*, vol. 2, pp. 1424–1427, 1999. Cited on pages 12 and 153.

[44] O. Gonzalez, S. Rodrguez, R. Perez-Jimenez, F. Delgado, and A. Ayala, "Multiuser adaptive orthogonal frequency-division multiplexing system for indoor wireless optical communications," *IET Optoelectronics*, vol. 1, pp. 68–76, Apr. 2007. Cited on page 12.

[45] A. T. Alastalo and M. Kahola, "Smart-antenna operation for indoor wireless local-area networks using OFDM," *IEEE Transactions on Wireless Communications*, vol. 2, no. 2, pp. 392–399, Mar. 2003. Cited on page 12.

[46] D. Gesbert, M. Shafi, D.-S. Shiu, P. J. Smith, and A. Naguib, "From theory to practice: An overview of MIMO space-time coded wireless systems," *IEEE Journal on Selected Areas in Communications*, vol. 21, no. 3, pp. 281 – 302, 2003. Available online: http://dx.doi.org/10.1109/JSAC.2003.809458. Cited on page 13.

[47] G. Foschini and M. Gans, "On Limits of Wireless Communications in a Fading Environment when Using Multiple Antennas," *Wireless Personal Communications*, vol. 6, no. 3, pp. 311–335, 1998. Cited on page 13.

[48] E. Telatar, "Capacity of Multi-Antenna Gaussian Channels," AT&T Bell Laboratories, Tech. Rep., June 1995. Cited on page 13.

[49] A. Feng, B. P. Ng, and Q. Yin, "Space-time coding/decoding with adaptive transmit beamforming in semi-correlated MIMO wireless communication systems," *2004. VTC2004-Fall. 2004 IEEE 60th Vehicular Technology Conference*, vol. 7, pp. 5036–5039, Sep. 2004. Cited on page 14.

[50] I. A. Kostko, M. E. M. Pasandi, M. M. Sisto, S. Larochelle, L. A. Rusch, and D. V. Plant, "A radio-over-fiber link for OFDM transmission without RF amplification," *2007. LEOS 2007. The 20th Annual Meeting of the IEEE Lasers and Electro-Optics Society*, pp. 339–340, Oct. 2007. Cited on pages 15, 19 and 106.

[51] M. Sauer, A. Kobyakov, L. Fields, F. Annunziata, J. Hurley, and J. George, "Experimental investigation of multimode fiber bandwidth requirements for 5.2 GHz WLAN signal transmission," in *Proceedings - OFCNFOEC 2006. 2006 Optical Fiber Communication Conference and National Fiber Optic Engineers Conference*, Anaheim, CA, USA, 2006, p. 3 pp. Cited on page 16.

[52] P. Hartmann, X. Qian, A. Wonfor, R. V. Penty, and I. H. White, "1-20 GHz directly modulated radio over MMF link," in *Microwave Photonics, 2005. MWP 2005. International Topical Meeting on*, vol. 2005, Seoul, South Korea, 2005, pp. 95–98. Cited on page 16.

[53] I. Gasulla and J. Capmany, "RF transfer function of analogue multimode fiber links using an electric field propagation model: application to broadband radio over fiber systems," in *Microwave Photonics, 2006. MWP '06. International Topical Meeting on*, Grenoble, France, 2006, pp. 301 – 304. Cited on page 16.

[54] L. Raddatz and I. White, "Overcoming the modal bandwidth limitation of multimode fiber by using passband modulation," *IEEE Photonics Technology Letters*, vol. 11, no. 2, pp. 266 – 268, 1999. Available online: http://dx.doi.org/10.1109/68.740725. Cited on page 16.

[55] I. Cox, C. H., L. M. Johnson, and G. E. Betts, "A theoretical and experimental comparison of directly and externally modulated fiber-optic links," in *Microwave Symposium Digest, 1989., IEEE MTT-S International*, Long Beach, CA, Jun. 1989, pp. 689–692. Cited on pages 16 and 41.

[56] I. Cox, C.H., G. Betts, and L. Johnson, "An analytic and experimental comparison of direct and external modulation in analog fiber-optic links," *IEEE Transactions on Microwave Theory and Techniques*, vol. 38, no. 5, pp. 501–9, 1990. Cited on pages 16, 62 and 75.

[57] L. Rosa, D. Passaro, S. Selleri, G. Tartarini, P. Faccin, and E. M. Fabbri, "Simulation and measurement of intermodulation induced by chirp-dispersion interaction in radio-over-fiber systems," in *Fourth IASTED International Conference on Antennas, Radar, and Wave Propagation*, Montreal, Que., Canada, 2007, pp. 46–51. Cited on page 16.

[58] L. Liao, D. Samara-Rubio, M. Morse, A. Liu, D. Hodge, D. Rubin, U. Kell, and T. Franck, "High speed silicon Mach-Zehnder modulator," *Optics Express*, vol. 13, no. 8, 2005. Cited on pages 16 and 209.

[59] D. Samara-Rubio, L. Liao, A. Liu, R. Jones, M. Paniccia, O. Cohen, and D. Rubin, "A gigahertz silicon-on-insulator Mach-Zehnder modulator," in *Optical Fiber*

Communication Conference, 2004. OFC 2004., vol. vol.2. Los Angeles, CA, USA: Opt. Soc. America, 2004, p. 3 pp. vol.2. Cited on pages 16 and 209.

[60] O. L. Coutinho, V. R. Almeida, and J. E. B. Oliveira, "Analysis of analog fiber optical links based on DSB+C and SSB+C modulation techniques," in *Microwave and Optoelectronics, 2005 SBMO/IEEE MTT-S International Conference on*, Jul. 2005, pp. 439–443. Cited on pages 17, 71 and 154.

[61] G. H. Smith, D. Novak, and C. Lim, "A millimeter-wave full-duplex fiber-radio star-tree architecture incorporating WDM and SCM," *Photonics Technology Letters, IEEE*, vol. 10, no. 11, p. 1652, Nov. 1998. Cited on page 17.

[62] M. Sauer, K. Kojucharow, H. Kaluzni, D. Sommer, W. Nowak, and A. Finger, "Radio-optical system design and transmission experiments for a mobile broadband communications system at 60 GHz," *Wireless Personal Communications*, vol. 14, no. 2, pp. 147–163, 2000. Cited on page 17.

[63] T. Kuri and K. Kitayama, "Novel channel-selection scheme of dense wavelength division multiplexed millimeter-wave-band radio-on-fiber signals with optical heterodyne detection," *IEICE Transactions on Electronics*, vol. E86-C, no. 7, pp. 1146–52, 2003. Cited on page 17.

[64] F. Vacondio, M. M. Sisto, W. Mathlouthi, L. A. Rusch, and S. LaRochelle, "Electrical-to-Optical Conversion of OFDM 802.11g/a Signals by Direct Current Modulation of Semiconductor Optical Amplifiers," in *Microwave Photonics, 2006. MWP apos;06. International Topical Meeting on*, Grenoble, France, 2006. Cited on pages 17, 185 and 213.

[65] K. J. Williams and R. D. Esman, "Design considerations for high-current photodetectors," *Journal of Lightwave Technology*, vol. 17, no. 8, pp. 1443–1454, Aug. 1999. Cited on pages 19 and 106.

[66] D. A. Tulchinsky, X. Li, N. Li, S. Demiguel, J. C. Campbell, and K. J. Williams, "High-saturation current wide-bandwidth photodetectors," *IEEE Journal of Selected Topics in Quantum Electronics*, vol. 10, no. 4, pp. 702–708, Jul./Aug. 2004. Cited on pages 19 and 106.

[67] L. Y. Lin, M. C. Wu, T. Itoh, T. A. Vang, R. E. Muller, D. L. Sivco, and A. Y. Cho, "High-power high-speed photodetectors-design, analysis, andexperimental demonstration," *IEEE Transactions on Microwave Theory and Techniques*, vol. 45, pp. 1320–1331, Aug. 1997. Cited on pages 19 and 106.

[68] K. J. Williams, L. T. Nichols, and R. D. Esman, "Photodetector nonlinearity limitations on a high-dynamic range 3 GHz fiber optic link," *Journal of Lightwave Technology*, vol. 16, no. 2, pp. 192–199, Feb. 1998. Cited on pages 19 and 106.

[69] V. J. Urick, M. S. Rogge, F. Bucholtz, and K. J. Williams, "Wideband (0.045-6.25 GHz) 40 km analogue fibre-optic link with ultra-high (¿40 dB) all-photonic gain,"

Electronics Letters, vol. 42, pp. 552–553, Apr. 2006. Cited on pages 19, 45, 73 and 106.

[70] B. Saltzberg, "Performance of an efficient parallel data transmission system," *IEEE Transactions on Communication Technology*, vol. COM-15, no. 6, pp. 805 – 811, 1967. Cited on page 23.

[71] A. Carlson, *Communication System*, 3rd ed. New York: McGraw-Hill, 1986. Cited on pages 24, 70 and 80.

[72] A. V. Oppenheim, R. W. Schafer, and J. R. Buck, *Discrete-time signal processing (2nd ed.)*. Upper Saddle River, NJ, USA: Prentice-Hall, Inc., 1999. Cited on page 25.

[73] S. Weinstein and P. Ebert, "Data Transmission by Frequency-Division Multiplexing Using the Discrete Fourier Transform," *Communications, IEEE Transactions on [legacy, pre - 1988]*, vol. 19, pp. 628–634, 1971. Cited on page 26.

[74] A. Peled and A. Ruiz, "Frequency domain data transmission using reduced computational complexity algorithms," *Acoustics, Speech, and Signal Processing, IEEE International Conference on ICASSP '80.*, vol. 5, pp. 964–967, Apr. 1980. Cited on page 26.

[75] X. Zhou and J. J. Caffery, "A new distribution bound and reduction scheme for OFDM PAPR," *2002. The 5th International Symposium on Wireless Personal Multimedia Communications*, vol. 1, pp. 158–162, Oct. 2002. Cited on page 28.

[76] Q. Shi, "OFDM in bandpass nonlinearity," *IEEE International Conference on Consumer Electronics, 5-7 June 1996*, vol. 42, no. 3, pp. 253–8, 1996. Cited on pages 28, 108 and 109.

[77] S. H. Han and J. H. Lee, "An overview of peak-to-average power ratio reduction techniques for multicarrier transmission," *IEEE Wireless Communications*, vol. 12, no. 2, pp. 56–65, Apr. 2005. Cited on page 28.

[78] K. M. Gharaibeh, K. G. Gard, and M. B. Steer, "Accurate estimation of digital communication system metrics - SNR, EVM and ρ in a nonlinear amplifier environment," in *ARFTG Microwave Measurements Conference, Fall 2004. 64th*, Dec. 2004, pp. 41–44. Cited on page 29.

[79] R. A. Shafik, S. Rahman, and A. R. Islam, "On the Extended Relationships Among EVM, BER and SNR as Performance Metrics," in *Electrical and Computer Engineering, 2006. ICECE '06. International Conference on*, Dhaka, Dec. 2006, pp. 408–411. Cited on page 29.

[80] J. G. Proakis, *Digital communications*, 4th ed. New York: McGraw-Hill, 1995. Cited on pages 29, 127 and 193.

[81] G. P. Agrawal, *Nonlinear fiber optics.* San Diego: Academic Press, 1995. Cited on pages 36 and 94.

[82] D. Sabido and L. Kazovsky, "Dynamic range of optically amplified RF optical links," *Microwave Theory and Techniques, IEEE Transactions on*, vol. 49, no. 10, pp. 1950–1955, 2001. Cited on pages 39 and 75.

[83] G. Betts, L. Johnson, and I. Cox, C.H., "Optimization of externally modulated analog optical links," *Proceedings of the SPIE - The International Society for Optical Engineering - Devices for Optical Processing, 23-24 July 1991*, vol. 1562, pp. 281–302, 1991. Cited on pages 39, 75, 82 and 100.

[84] C. H. Cox, *Analog Optical Links, Theory And Practice.* Cambridge, 2004. Cited on pages 40, 75 and 82.

[85] A. Daryoush, E. Ackerman, N. Samant, S. Wanuga, and D. Kasemset, "Interfaces for high speed fiber-optic links: analysis and experiment," *IEEE Transactions on Microwave Theory and Techniques - 1999 IEEE MTT-S International Microwave Symposium Digest, 13-19 June 1999 -1991 IEEE/MTT-S International Microwave Symposium - MTT '91, 10-14 June 1991*, vol. 39, no. 12, pp. 2031–44, 1991. Cited on pages 41, 62, 64, 65, 66, 67 and 75.

[86] G. E. Betts, L. M. Johnson, and C. H. I. Cox, "High-dynamic-range, low-noise analog optical links using external modulators. Analysis and demonstration." *Photonics Technology Letters, IEEE*, vol. 1345, pp. 2–10, Jul. 1990. Cited on page 41.

[87] W. Stephens and T. Joseph, "System characteristics of direct modulated and externally modulated RF fiber-optic links," *Journal of Lightwave Technology*, vol. 5, no. 3, pp. 380–387, Mar. 1987. Cited on page 41.

[88] M. M. Sisto, S. LaRochelle, and L. A. Rusch, "Gain Optimization by Modulator-Bias Control in Radio-Over-Fiber Links," *Lightwave Technology, Journal of*, vol. 24, no. 12, pp. 4974–4982, 2006. Cited on pages 43 and 185.

[89] B. Kolner and D. Dolfi, "Intermodulation distortion and compression in an integrated electrooptic modulator," *Applied Optics*, vol. 26, no. 17, pp. 3676–80, 1987. Cited on pages 43, 44, 47, 109, 110, 193, 194 and 195.

[90] E. Ackerman, S. Wanuga, D. Kasemset, A. S. Daryoush, and N. R. Samant, "Maximum dynamic range operation of a microwave external modulation fiber-optic link," *IEEE Transactions on Microwave Theory and Techniques*, vol. 41, no. 8, pp. 1299–1306, 1993. Cited on pages 43, 44, 65 and 75.

[91] B. Kolner and D. Bloom, "Electrooptic sampling in GaAs integrated circuits," *IEEE Journal of Quantum Electronics*, vol. QE-22, no. 1, pp. 79–93, 1986. Cited on page 44.

[92] C. Bulmer and W. Burns, "Linear interferometric modulators in Ti:LiNbO3," *Journal of Lightwave Technology*, vol. T-2, no. 4, pp. 512–21, 1984. Cited on page 44.

[93] E. I. Ackerman, G. E. Betts, W. K. Burns, J. C. Campbell, C. H. Cox, N. Duan, J. L. Prince, M. D. Regan, and H. V. Roussell, "Signal-to-noise performance of two analog photonic links using different noise reduction techniques," *2007. IEEE/MTT-S International Microwave Symposium*, pp. 51–54, Jun. 2007. Cited on pages 44 and 75.

[94] H. V. Roussell, M. D. Regan, J. L. Prince, C. H. Cox, J. X. Chen, W. K. Burns, G. E. Betts, E. I. Ackerman, and J. C. Campbell, "Gain, Noise Figure and Bandwidth-Limited Dynamic Range of a Low-Biased External Modulation Link," in *Microwave Photonics, 2007 IEEE International Topical Meeting on*, Oct. 2007, pp. 84–87. Cited on pages 44 and 75.

[95] M. Howerton, R. Moeller, G. Gopalakrishnan, and W. Burns, "Low-biased fiber-optic link for microwave downconversion," *IEEE Photonics Technology Letters*, vol. 8, no. 12, pp. 1692–4, 1996. Cited on page 44.

[96] M. Howerton, G. Gopalakrishnan, R. Moeller, and W. Burns, "Low-biasing the cascaded downconverting fiber-optic link," in *Optical Fiber Communications, 1996. OFC apos;96.* San Jose, CA, USA: Opt. Soc. America, 1996, pp. 211–13. Cited on page 44.

[97] M. Farwell, W. Chang, and D. Huber, "Increased linear dynamic range by low biasing the Mach-Zehnder modulator," *IEEE Photonics Technology Letters*, vol. 5, no. 7, pp. 779–82, 1993. Cited on page 44.

[98] L. T. Nichols, K. J. Williams, and R. D. Esman, "Optimizing the ultrawide-band photonic link," *IEEE Transactions on Microwave Theory and Techniques*, vol. 45, no. 8 pt 2, pp. 1384–1389, 1997. Cited on page 44.

[99] X. Zhang and A. Mitchell, "A simple black box model for erbium-doped fiber amplifiers," *IEEE Photonics Technology Letters*, vol. 12, no. 1, pp. 28–30, 2000. Cited on page 47.

[100] E. L. Wooten, K. M. Kissa, A. Yi-Yan, E. J. Murphy, D. A. Lafaw, P. F. Hallemeier, D. Maack, D. V. Attanasio, D. J. Fritz, G. J. McBrien, and D. E. Bossi, "A review of lithium niobate modulators for fiber-opticcommunications systems," *IEEE Journal of Selected Topics in Quantum Electronics*, vol. 6, no. 1, pp. 69–82, Jan./Feb. 2000. Cited on page 58.

[101] S. Gille, R. Radouani, J. P. Salvestrini, F. Abdi, L. Guilbert, and M. D. Fontana, "Optimization of integrated Mach-Zehnder interferometer modulator: electrical and optical studies," in *Lasers and Electro-Optics Europe, 2003. CLEO/Europe. 2003 Conference on*, Jun. 2003. Cited on page 58.

[102] H. Nagata, N. Papasavvas, and D. R. Maack, "Bias stability of OC48 x-cut lithium-niobate optical modulators: four years of biased aging test results," *IEEE Photonics Technology Letters*, vol. 15, no. 1, pp. 42–44, Jan. 2003. Cited on page 58.

[103] H. Nagata, K. Kiuchi, and T. Saito, "Studies of thermal drift as a source of output instabilities in Ti:$LiNbO_3$ optical modulators," *Journal of Applied Physics*, vol. 75, pp. 4762–4764, May 1994. Cited on pages 58 and 59.

[104] S. Yamada and M. Minakata, "DC drift phenomena in LiNbO3 optical waveguide devices," *Japanese Journal of Applied Physics*, vol. 20, no. 4, pp. 733–7, Apr. 1981. Cited on page 58.

[105] C. T. Mueller and J. G. Coffer, "Temperature-dependent bias drift in proton-exchanged lithium niobate Mach-Zehnder modulators," in *Lasers and Electro-Optics, 1999. CLEO '99. Summaries of Papers Presented at the Conference on*, Baltimore, MD, May 1999, pp. 291–292. Cited on page 58.

[106] A. R. Beaumont, B. E. Daymond-John, and R. C. Booth, "Effect of ambient water vapour on stability of lithium niobate electro-optic waveguide devices," *Electronics Letters*, vol. 22, pp. 262–263, Feb. 1986. Cited on page 58.

[107] C. H. Cox, "Gain and noise figure in analogue fibre-optic links," *IEE proceedings. Part J. Optoelectronics*, vol. 139, no. 4, pp. 238–42, 1992. Cited on page 62.

[108] I. Cox, C.H., E. Ackerman, and G. Betts, "Relationship between gain and noise figure of an optical analog link," in *Microwave Symposium Digest, 1996., IEEE MTT-S International*, vol. vol.3. San Francisco, CA, USA: IEEE, 1996, pp. 1551–4. Cited on pages 62, 75 and 79.

[109] S. J. Orfanidis, *Electromagnetic Waves and Antennas*. Published on the web, 2003. Available online: http://www.ece.rutgers.edu/~orfanidi/ewa/. Cited on pages 63, 64, 67, 153 and 161.

[110] Agilent, "Agilent AN 154 : S-Parameter Design," Agilent, Tech. Rep., 2000. Cited on page 63.

[111] B. J. Markey, D. K. Paul, R. Razdan, B. A. Pontano, and N. K. Dutta, "Impedance-matched optical link for C-band satellite applications," *IEEE Transactions on Antennas and Propagation*, vol. 43, no. 9, pp. 960–965, Sep. 1995. Cited on page 65.

[112] R. Fano, "Theoretical limitations on broadband matching of arbitrary impedances," *Franklin Institute – Journal*, vol. 249, no. 2, pp. 139–154, 1950. Cited on page 66.

[113] J. Fuster, J. Marti, J. Corral, V. Polo, and F. Ramos, "Generalized study of dispersion-induced power penalty mitigation techniques in millimeter-wave fiber-optic links," *Journal of Lightwave Technology*, vol. 18, no. 7, pp. 933–40, 2000. Cited on pages 69 and 126.

[114] L. Cheng, S. Aditya, and A. Nirmalathas, "An exact analytical model for dispersive transmission in microwave fiber-optic links using Mach-Zehnder external modulator," *IEEE Photonics Technology Letters*, vol. 17, no. 7, pp. 1525–1527, Jul. 2005. Cited on pages 69, 126, 129 and 131.

[115] H. Sotobayashi and K. Kitayama, "Cancellation of the signal fading for 60 GHz subcarrier multiplexedoptical DSB signal transmission in nondispersion shifted fiber usingmidway optical phase conjugation," *Journal of Lightwave Technology*, vol. 17, no. 12, pp. 2488–2497, Dec. 1999. Cited on page 71.

[116] C. Marra, A. Nirmalathas, D. Novak, C. Lim, L. Reekie, J. A. Besley, and N. J. Baker, "The impact of grating dispersion on transmission performance in a millimeter-wave fiber-radio system," *IEEE Photonics Technology Letters*, vol. 14, no. 9, pp. 1345–1347, Sep. 2002. Cited on pages 71 and 154.

[117] G. H. Smith, D. Novak, and Z. Ahmed, "Overcoming chromatic-dispersion effects in fiber-wireless systems incorporating external modulators," *IEEE Transactions on Microwave Theory and Techniques*, vol. 45, pp. 1410–1415, Aug. 1997. Cited on pages 71, 154 and 195.

[118] E. Ackerman, I. Cox, C., G. Betts, H. Roussell, K. Ray, and F. O'Donnell, "Input impedance conditions for minimizing the noise figure of an analog optical link," in *Microwave Theory and Techniques, IEEE Transactions on*, vol. vol.1. Denver, CO, USA: IEEE, 1997, pp. 237–40 BN – 0 7803 3814 6. Cited on pages 75 and 79.

[119] G. E. Betts, J. P. Donnelly, J. N. Walpole, S. H. Groves, F. J. O'Donnell, L. J. Missaggia, J. Bailey, and A. Nagoleone, "Semiconductor laser sources for externally modulated microwave analog links," *IEEE Transactions on Microwave Theory and Techniques*, vol. 45, pp. 1280–1287, Aug. 1997. Cited on page 75.

[120] L. G. Kazovsky, F. S. Yang, and C. L. Lu, "The performance and limitation of optically amplified analog links," in *Lasers and Electro-Optics Society Annual Meeting, 1997. LEOS '97 10th Annual Meeting. Conference Proceedings., IEEE*, vol. 1, San Francisco, CA, USA, Nov. 1997, pp. 356–357. Cited on page 78.

[121] H. Bulow, R. Fritschi, R. Heidemann, B. Junginger, H. G. Krimmel, and J. Otterbach, "Analog video distribution system with three cascaded 980 nm single-pumped EDFA's and 73 dB power budget," *IEEE Photonics Technology Letters*, vol. 4, no. 11, pp. 1287–1289, Nov. 1992. Cited on page 78.

[122] P. C. Becker, N. A. Olsson, and J. R. Simpson, *Erbium-doped fiber amplifiers: fundamentals and technology.* Academic Press, 1999. Cited on pages 80, 82 and 86.

[123] P. J. Winzer and A. Kalmar, "Sensitivity enhancement of optical receivers by impulsive coding," *Journal of Lightwave Technology*, vol. 17, no. 2, pp. 171–177, Feb. 1999. Cited on pages 82 and 83.

[124] K. S. Miller, "Complex Gaussian Processes," *SIAM Review*, vol. 11, no. 4, pp. 544–67, Oct. 1969. Cited on pages 83 and 201.

[125] W. McGee, "Complex Gaussian noise moments," *IEEE Transactions on Information Theory*, vol. 17, no. 2, pp. 149–157, Mar. 1971. Cited on pages 83 and 201.

[126] L. Mandel and E. Wolf, *Optical Coherence and Quantum Optics*. Cambridge University Press, September 1995. Cited on page 83.

[127] A. Papoulis, *Probability, Random Variables, and Stochastic Processes*, 3rd ed. Boston, MA: McGraw-Hill, 1991. Cited on pages 84, 88, 89 and 189.

[128] X. Fernando, "Improved Expression for Intensity Noise in Multimedia over Fiber Networks," in *Industrial and Information Systems, First International Conference on*, Aug. 2006, pp. 425–429. Cited on pages 85 and 97.

[129] P. Goldgeier and G. Eisenstein, "Broad-band microwave-optical fiber links transmitting over longdistances with optical amplification," *IEEE [see also IEEE Microwave and Wireless Components Letters] Microwave and Guided Wave Letters*, vol. 9, no. 1, pp. 40–42, Jan. 1999. Cited on page 87.

[130] A. L. Gaeta and R. W. Boyd, "Stochastic dynamics of stimulated Brillouin scattering in an optical fiber," *Physical Review A (Atomic, Molecular, and Optical Physics)*, vol. 44, no. 5, pp. 3205–9, Sep. 1991. Cited on page 87.

[131] E. Peral and A. Yariv, "Degradation of modulation and noise characteristics of semiconductor lasers after propagation in optical fiber due to a phase shift induced by stimulated Brillouin scattering," *IEEE Journal of Quantum Electronics*, vol. 35, no. 8, pp. 1185–95, 1999. Cited on page 87.

[132] M. Horowitz, A. Chraplyvy, R. Tkach, and J. Zyskind, "Broad-band transmitted intensity noise induced by Stokes and anti-Stokes Brillouin scattering in single-mode fibers," *Photonics Technology Letters, IEEE*, vol. 9, no. 1, pp. 124–126, 1997. Cited on page 87.

[133] X. Mao, G. Bodeep, R. Tkach, A. Chraplyvy, T. Darcie, and R. Derosier, "Brillouin scattering in externally modulated lightwave AM-VSB CATV transmission systems," *IEEE Photonics Technology Letters*, vol. 4, no. 3, pp. 287–9, 1992. Cited on pages 87 and 92.

[134] K. J. Williams and R. D. Esman, "Stimulated Brillouin scattering for improvement of microwave fibre-optic link efficiency," *Electronics Letters*, vol. 30, pp. 1965–1966, Nov. 1994. Cited on pages 87 and 88.

[135] J. Phillips and K. Kundert, "Noise in mixers, oscillators, samplers, and logic an introduction to cyclostationary noise," in *Custom Integrated Circuits Conference, 2000. CICC. Proceedings of the IEEE 2000*, Orlando, FL, May 2000, pp. 431–438. Cited on page 89.

[136] W. Gardner and L. Franks, "Characterization of cyclostationary random signal processes," *IEEE Transactions on Information Theory*, vol. 21, no. 1, pp. 4–14, Jan. 1975. Cited on pages 89 and 97.

[137] M. Jaworski and M. Marciniak, "Counteracting of stimulated Brillouin scattering in externally modulated lightwave AM-CATV systems," in *Laser and Fiber-Optical Networks Modeling, 2000. Proceedings of LFNM 2000. 2nd International Workshop on*, 2000, pp. 71–73. Cited on pages 90 and 96.

[138] M. M. Sisto, S. LaRochelle, and L. A. Rusch, "Carrier-to-noise ratio optimization by modulator bias control in radio-over-fiber links," *Photonics Technology Letters, IEEE*, vol. 18, no. 17, pp. 1840–1842, 2006. Cited on pages 90 and 185.

[139] L. Hu, A. Kaszubowska, and L. P. Barry, "Investigation of stimulated Brillouin scattering effects in radio-over-fiber distribution systems," *Optics Communications*, vol. 255, no. 4, pp. 253–60, Nov. 2005. Cited on page 96.

[140] M. Sauer, A. Kobyakov, and A. B. Ruffin, "Radio-Over-Fiber Transmission With Mitigated Stimulated Brillouin Scattering," *IEEE Photonics Technology Letters*, vol. 19, no. 19, pp. 1487–1489, Oct. 2007. Cited on page 96.

[141] G. Brochu, S. LaRochelle, and R. Slavik, "Modeling and experimental demonstration of ultracompact multiwavelength distributed Fabry-Perot fiber lasers," *Journal of Lightwave Technology*, vol. 23, no. 1, pp. 44–53, 2005. Cited on pages 98 and 178.

[142] R. Slavik, I. Castonguay, S. LaRochelle, and S. Doucet, "Short multiwavelength fiber laser made of a large-band distributed Fabry-Pe/spl acute/rot structure," *IEEE Photonics Technology Letters*, vol. 16, no. 4, pp. 1017–1019, Apr. 2004. Cited on pages 98 and 178.

[143] G. Brochu, "Lasers à fibre à contre-réaction répartie multifréquences : modélisation, fabrication, caractérisation," Ph.D. dissertation, Université Laval, to be published. Cited on page 98.

[144] J. Poette, S. Blin, G. Brochu, L. Bramerie, R. Slavik, J. C. Simon, S. LaRochelle, and P. Besnard, "Relative intensity noise of multiwavelength fibre laser," *Electronics Letters*, vol. 40, pp. 724–726, Jun. 2004. Cited on pages 99 and 105.

[145] G. A. Cranch, M. A. Englund, and C. K. Kirkendall, "Intensity noise characteristics of erbium-doped distributed-feedback fiber lasers," *IEEE Journal of Quantum Electronics*, vol. 39, no. 12, pp. 1579–1587, Dec. 2003. Cited on page 103.

[146] M. C. Jeruchim, P. Balaban, and K. S. Shanmugan, *Simulation of Communication Systems.* Springer US, 2002, ch. Modeling and Simulation of Nonlinear Systems, pp. 203–287. Cited on page 107.

[147] S. Wei, D. L. Goeckel, and P. E. Kelly, "A modern extreme value theory approach to calculating the distribution of the peak-to-average power ratio in OFDM systems," in *Communications, 2002. ICC 2002. IEEE International Conference on*, vol. 3, 2002, pp. 1686–1690. Cited on page 108.

[148] P. Banelli and S. Cacopardi, "Theoretical analysis and performance of OFDM signals in nonlinear AWGN channels," *IEEE Transactions on Communications*, vol. 48, no. 3, pp. 430–41, 2000. Cited on pages 108, 109 and 113.

[149] D. Dardari, V. Tralli, and A. Vaccari, "A theoretical characterization of nonlinear distortion effects in OFDM systems," *IEEE Transactions on Communications*, vol. 48, no. 10, pp. 1755–64, 2000. Cited on page 108.

[150] N. Horvath and I. Frigyes, "Effects of the nonlinearity of a Mach-Zehnder modulator on OFDM radio-over-fiber transmission," *IEEE Communications Letters*, vol. 9, no. 10, pp. 921–3, 2005. Cited on pages 108, 112 and 113.

[151] Z. Bo, Y. Lu, Z. Jinling, and Y. Biao, "Nonlinear Effect of OFDM in Radio-over-Fiber transmission," in *Microwave and Millimeter Wave Technology, 2007. ICMMT '07. International Conference on*, Apr. 2007, pp. 1–3. Cited on page 108.

[152] M. H. Taghavi, G. C. Papen, and P. H. Siegel, "On the Multiuser Capacity of WDM in a Nonlinear Optical Fiber: Coherent Communication," *IEEE Transactions on Information Theory*, vol. 52, no. 11, pp. 5008–5022, Nov. 2006. Cited on page 108.

[153] N. M. Blachman, "The output signals and noise from a nonlinearity with amplitude-dependent phase shift," *IEEE Transactions on Information Theory*, vol. IT-25, no. 1, pp. 77–9, 1979. Cited on pages 109 and 113.

[154] M. Rodrigues, J. Mitchell, and I. Darwazeh, "On the error probability performance of non-linearly distorted OFDM signals," in *Vehicular Technology Conference, 2003. VTC 2003-Spring. The 57th IEEE Semiannual*, vol. vol.2. Jeju, South Korea: IEEE, 2003, pp. 1278–82. Cited on page 109.

[155] H. Ku and J. S. Kenney, "Estimation of error vector magnitude using two-tone intermodulationdistortion measurements [power amplifier]," in *Microwave Symposium Digest, 2001 IEEE MTT-S International*, vol. 1, Phoenix, AZ, USA, 2001, pp. 17–20. Cited on page 109.

[156] A. Hilt, "Microwave harmonic generation in fiber-optical links," in *Microwaves, Radar and Wireless Communications. 2000. MIKON-2000. 13th International Conference on*, vol. vol.2. Wroclaw, Poland: Telecommun. Res. Inst, 2000, pp. 693–8. Cited on pages 110 and 195.

[157] T. Kurt, A. Yongacoglu, and J. Y. Chouinard, "Performance of external modulators for wireless local area networks under multi-path fading," in *Electrical and Computer Engineering, 2004. Canadian Conference on*, vol. 1, May 2004, pp. 277–280. Cited on pages 117 and 210.

[158] A. R. Islam, R. A. Shafik, and S. Ali, "Comparative Performance of Nonlinear Distortion Effects in an OFDM-RoF Link," in *TENCON 2006. 2006 IEEE Region 10 Conference*, Nov. 2006, pp. 1–4. Cited on page 117.

[159] G. Singh and A. Alphones, "Optical transmission performance of a Radio-over-Fiber system for wireless LAN," in *Information, Communications & Signal Processing, 2007 6th International Conference on*, Dec. 2007, pp. 1–5. Cited on page 117.

[160] K. Kikushima and H. Yoshinaga, "Distortion due to gain tilt of erbium-doped fiber amplifiers," *IEEE Photonics Technology Letters*, vol. 3, no. 10, pp. 945–947, 1991. Cited on page 117.

[161] S. L. Hansen, S. B. Andreasen, P. Thorsen, and K. Dybdal, "Experimental verification of new EDFA gain-tilt distortion theory," *IEEE Photonics Technology Letters*, vol. 5, no. 12, pp. 1433–1435, Dec. 1993. Cited on page 117.

[162] C. Y. Kuo and E. E. Bergmann, "Erbium-doped fiber amplifier second-order distortion in analog links and electronic compensation," *IEEE Photonics Technology Letters*, vol. 3, no. 9, pp. 823–831, Sep. 1991. Cited on page 117.

[163] E. Desurvire, "Analysis of transient gain saturation and recovery in erbium-doped fiber amplifiers," *IEEE Photonics Technology Letters*, vol. 1, no. 8, pp. 196–9, 1989. Cited on page 118.

[164] C. R. Giles, E. Desurvire, and J. R. Simpson, "Transient gain and cross-talk effects in erbium-doped fiber amplifiers," *Optics Letters*, vol. 14, pp. 880–882, Aug. 1989. Cited on page 118.

[165] M. M. Sisto, S. LaRochelle, L. A. Rusch, and P. Giaccari, "Erbium Amplifier Dynamics in Wireless Analog Optical Links With Modulator Bias Optimization," *IEEE Photonics Technology Letters*, vol. 19, no. 6, pp. 408–410, Mar. 2007. Cited on pages 118 and 185.

[166] D. H. Thomas and J. P. von der Weid, "Impairments of EDFA dynamic gain-fluctuations in packet-switched WDM optical transmissions," *Photonics Technology Letters, IEEE*, vol. 17, no. 5, pp. 1097–1099, 2005. Cited on page 120.

[167] E. Ackerman, C. Cox III, P. Inc, and M. Carlisle, "Effect of pilot tone-based modulator bias control on external modulation link performance," *Microwave Photonics, 2000. MWP 2000. International Topical Meeting on*, pp. 121–124, 2000. Cited on page 123.

[168] A. Bononi and L. A. Rusch, "Doped-fiber amplifier dynamics: a system perspective," *Journal of Lightwave Technology*, vol. 16, no. 5, pp. 945–956, May 1998. Cited on page 124.

[169] E. E. Bergmann, C. Y. Kuo, and S. Y. Huang, "Dispersion-induced composite second-order distortion at 1.5 µm," *IEEE Photonics Technology Letters*, vol. 3, no. 1, pp. 59–61, Jan. 1991. Cited on page 125.

[170] C. Kuo, "Fundamental second-order nonlinear distortions in analog AM CATV-transport systems based on single frequency semiconductor lasers," *Lightwave Technology, Journal of*, vol. 10, no. 2, pp. 235–243, 1992. Cited on page 125.

[171] C. Desem, "Composite second order distortion due to self-phase modulation inexternally modulated optical AM-SCM systems operating at 1550 nm," *Electronics Letters*, vol. 30, no. 24, pp. 2055–2056, Nov. 1994. Cited on page 125.

[172] E. Funk, A. Campillo, and D. Tulchinsky, "Nonlinear distortion and crosstalk in microwave fiber-radio links," *Microwave Symposium Digest, 2002 IEEE MTT-S International*, vol. 3, 2002. Cited on page 125.

[173] M. Phillips, T. Darcie, D. Marcuse, G. Bodeep, and N. Frigo, "Nonlinear distortion generated by dispersive transmission of chirped intensity-modulated signals," *IEEE Photonics Technology Letters*, vol. 3, no. 5, pp. 481–3, 1991. Cited on page 125.

[174] J. L. Corral, J. Marti, and J. M. Fuster, "General expressions for IM/DD dispersive analog optical links with external modulation or optical up-conversion in a Mach-Zehnder electrooptical modulator," *IEEE Transactions on Microwave Theory and Techniques*, vol. 49, pp. 1968–1976, Oct. 2001. Cited on pages 126, 129 and 194.

[175] C. Tae-Sik and K. Kiseon, "Effect of third-order intermodulation on radio-over-fiber systems by a dual-electrode Mach-Zehnder modulator with ODSB and OSSB signals," *Lightwave Technology, Journal of*, vol. 24, no. 5, pp. 2052–2058, 2006. Cited on pages 126, 129 and 134.

[176] G. K. Gopalakrishnan, T. J. Brophy, and C. Breverman, "Experimental study of fibre induced distortions in externally modulated 1550 nm analogue CATV links," *Electronics Letters*, vol. 32, no. 14, pp. 1309–1310, Jul. 1996. Cited on page 126.

[177] F. Ramos, J. Marti, V. Polo, and J. Fuster, "On the use of fiber-induced self-phase modulation to reducechromatic dispersion effects in microwave/millimeter-wave opticalsystems," *Photonics Technology Letters, IEEE*, vol. 10, no. 10, pp. 1473–1475, 1998. Cited on page 126.

[178] F. Ramos and J. Marti, "Compensation for fiber-induced composite second-order distortion in externally modulated lightwave AM-SCM systems using optical-phase conjugation," *Journal of Lightwave Technology*, vol. 16, no. 8, pp. 1387–1392, 1998. Cited on page 126.

[179] F. Ramos, J. Marti, and V. Polo, "Compensation of chromatic dispersion effects inmicrowave/millimeter-wave optical systems using four-wave-mixing inducedin dispersion-shifted fibers," *Photonics Technology Letters, IEEE*, vol. 11, no. 9, pp. 1171–1173, 1999. Cited on page 126.

[180] F. W. Willems, W. Muys, J. C. van der Plaats, and R. Nuyts, "Experimental verification of self-phase-modulation induced nonlinear distortion in externally modulated AM-VSB lightwave systems," *Electronics Letters*, vol. 32, no. 14, pp. 1310–1311, Jul. 1996. Cited on page 126.

[181] M. Sisto, F. Vacondio, S. LaRochelle, and L. Rusch, "Low Distortion Transmission of 802.11 a/n Signals in Amplified Radio Over Fibre Links with Modulator Bias Optimization," in *Antennas, Radar, and Wave Propagation ARP 2007* . Montreal, QC, Canada: IASTED, June 2007. Cited on pages 126, 135 and 185.

[182] R. J. Mailloux, *Phased Array Antenna Handbook*, 2nd ed. Artech House, 2005. Cited on page 153.

[183] M. M. Sisto, M. E. Mousa Pasandi, S. Doucet, S. LaRochelle, and L. A. Rusch, "Optical Phase And Amplitude Control For Beamforming With Multiwavelength Gires-tournois Bragg Grating Cavities," in *Fourth Iasted International Conference On Antennas, Radar, And Wave Propagation (ARP 2007)*, Montreal, Canada, May 30 June 1 2007. Cited on pages 153, 162 and 185.

[184] R. Khanna and R. Saxena, "Output SNR improvement in array processing architectures of WCDMA systems by low side lobe beamforming," *Wireless Personal Communications*, vol. 40, no. 2, pp. 205–214, Jan. 2007. Cited on page 153.

[185] Y. Lu and B.-K. Yeo, "Adaptive wide null steering for digital beamforming array with thecomplex coded genetic algorithm," in *Phased Array Systems and Technology, 2000. Proceedings. 2000 IEEE International Conference on*, Dana Point, CA, USA, 2000, pp. 557–560. Cited on page 153.

[186] B. Ortega, J. Cruz, J. Capmany, M. Andres, and D. Pastor, "Variable delay line for phased-array antenna based on a chirped fiber grating," *IEEE Transactions on Microwave Theory and Techniques*, vol. 48, no. 8, pp. 1352–60, 2000. Cited on page 154.

[187] D. T. K. Tong and M. C. Wu, "Programmable dispersion matrix using Bragg fibre grating for optically controlled phased array antennas," *Electronics Letters*, vol. 32, no. 17, pp. 1532–3, 1996. Cited on page 154.

[188] L. Yunqi, Y. Jianliang, and J. Yao, "Continuous true-time-delay beamforming for phased array antenna using a tunable chirped fiber grating delay line," *IEEE Photonics Technology Letters*, vol. 14, no. 8, pp. 1172–4, 2002. Cited on pages 154 and 155.

[189] D. B. Hunter, M. E. Parker, and J. L. Dexter, "Demonstration of a continuously variable true-time delay beamformer using a multichannel chirped fiber grating," *IEEE Transactions on Microwave Theory and Techniques*, vol. 54, no. 2, pp. 861–7, 2006. Cited on page 154.

[190] B. Ortega, J. L. Cruz, J. Capmany, M. V. Andres, and D. Pastor, "Analysis of a microwave time delay line based on a perturbed uniform fiber Bragg grating operating at constant wavelength," *Journal of Lightwave Technology*, vol. 18, no. 3, pp. 430–6, 2000. Cited on pages 154 and 155.

[191] J. L. Corral, J. Marti, S. Regidor, J. M. Foster, R. Laming, and M. J. Cole, "Continuously variable true time-delay optical feeder for phased-array antenna employing chirped fiber grating," *IEEE Transactions on Microwave Theory and Techniques*, vol. 45, no. 8, pp. 1531–6, 1997. Cited on pages 154 and 155.

[192] J. Stulemeuer, F. E. van Vliet, K. W. Benoist, D. H. Maat, and M. K. Smit, "Photonic integrated beamformer for phased-array antennas," in *Optical Communication, 1998. 24th European Conference on*, 1998, pp. 131–134. Cited on page 154.

[193] K.-I. Kitayama, "Architectural considerations of fiber-radio millimeter-wave wireless access systems," *Fiber and Integrated Optics*, vol. 19, no. 2, pp. 167–186, 2000. Cited on page 154.

[194] R. Prasad and B. C. Van Lieshout, "Cochannel interference probability for micro- and picocellular systems at 60 GHz," *Electronics Letters*, vol. 29, pp. 1909–1910, Oct. 1993. Cited on page 154.

[195] B. Kuhlow, G. Przyrembel, H. Ehlers, G. Grosskopf, R. Eggemann, D. Rohde, and S. Zinal, "Optical beam forming of MM-wave array antennas in a 60 GHz radio over fiber system," in *Optical Fiber Communications Conference, 2003. OFC 2003*, Mar. 2003, pp. 732–734. Cited on page 154.

[196] G. Grosskopf, R. Eggemann, D. Rohde, and M. S. Choi, "155 Mbit/s data transmission at 60 GHz using a 14 patch array antenna with variable optical delay lines," in *Microwave Symposium Digest, 2001 IEEE MTT-S International*, vol. 3, Phoenix, AZ, May 2001, pp. 1821–1824. Cited on page 154.

[197] F. Zeng and J. Yao, "Dispersion effects of fiber Bragg gratings on true-time-delay beamforming networks," in *Electrical and Computer Engineering, 2003. IEEE CCECE 2003. Canadian Conference on*, vol. vol.1. Montreal, Que., Canada: IEEE, 2003, pp. 299–302. Cited on page 154.

[198] A. Loayssa, D. Benito, and M. J. Garde, "Single-sideband suppressed-carrier modulation using a single-electrode electrooptic modulator," *IEEE Photonics Technology Letters*, vol. 13, no. 8, pp. 869–71, Aug. 2001. Cited on page 154.

[199] R. Montgomery and R. DeSalvo, "A novel technique for double sideband suppressed carrier modulationof optical fields," *IEEE Photonics Technology Letters*, vol. 7, no. 4, pp. 434–436, Apr. 1995. Cited on page 154.

[200] L. Zhuang, C. G. H. Roeloffzen, R. G. Heideman, A. Borreman, A. Meijerink, and W. van Etten, "Single-chip optical beam forming network in LPCVD waveguide technology based on optical ring resonators," in *Microwave Photonics, 2006. MWP '06. International Topical Meeting on*, Grenoble, Oct. 2006, pp. 1–4. Cited on page 154.

[201] O. Raz, R. Rotman, and M. Tur, "Wavelength-controlled photonic true time delay for wide-band applications," *Photonics Technology Letters, IEEE*, vol. 17, no. 5, pp. 1076–1078, 2005. Cited on page 155.

[202] S.-S. Lee, Y.-H. Oh, and S.-Y. Shin, "Photonic microwave true-time delay based on a tapered fiber Bragg grating with resistive coating," *IEEE Photonics Technology Letters*, vol. 16, no. 10, pp. 2335–2337, 2004. Cited on page 155.

[203] C. K. Madsen and J. Zhao, *Optical Filter Design and Analysis: A Signal Processing Approach*. New York: John Wiley & Sons, Inc., 1999. Cited on page 163.

[204] B. Ortega, D. Pastor, J. Mora, J. Capmany, and M. V. Andres, "Advanced optical processing of microwave signals," *EURASIP Journal on Applied Signal Processing*, vol. 1, no. 10, pp. 1462–84, Jul. 2005. Cited on pages 168 and 169.

[205] Y. Yan and J. Yao, "A tunable photonic microwave filter with a complex coefficient using an optical RF phase shifter," *IEEE Photonics Technology Letters*, vol. 19, no. 19, pp. 1472–1474, Oct. 2007. Cited on page 168.

[206] S. Doucet, S. LaRochelle, and M. Morin, "Multi-channel tunable chromatic dispersion compensator and profiler," in *Optical Communication, 2005. ECOC 2005. 31st European Conference on*, vol. vol.3. Glasgow, UK: IEE, 2005, pp. 421–2. Cited on page 169.

[207] J. Skaar, L. Wang, and T. Erdogan, "On the synthesis of fiber Bragg gratings by layer peeling," *IEEE Journal of Quantum Electronics*, vol. 37, no. 2, pp. 165–173, Feb. 2001. Cited on page 172.

[208] R. Weigel, M. Schmidt, D. Pimingsdorfer, and L. Maurer, "On the Role of SAW Devices in Current and Future Radio Systems," in *Proceedings of the Second International Symposium an Acoustic Wave Devices for Future Mobile Communication Systems*, 2004. Cited on page 179.

[209] G. Fischerauer, T. Ebner, P. Kruck, K. Morozumi, R. Thomas, and M. Pitschi, "SAW filter solutions to the needs of 3G cellular phones," in *Microwave Symposium Digest, 2001 IEEE MTT-S International*, vol. 1, Phoenix, AZ, USA, 2001, pp. 351–354. Cited on page 179.

[210] R. Slavik, S. Doucet, and S. LaRochelle, "High-performance all-fiber Fabry-Perot filters with superimposed chirped Bragg gratings," *Journal of Lightwave Technology*, vol. 21, no. 4, pp. 1059–1065, Apr. 2003. Cited on page 181.

[211] A. Papoulis, "Random modulation: a review," *IEEE Transactions on Acoustics, Speech and Signal Processing*, vol. ASSP-31, no. 1, pt.1, pp. 96–105, 1983. Cited on page 190.

[212] M. H. Hayes, *Statistical Digital Signal Processing and Modeling.* Wiley, 1996. Cited on page 191.

[213] K. Panta and J. Armstrong, "Spectral analysis of OFDM signals and its improvement by polynomial cancellation coding," *IEEE Transactions on Consumer Electronics*, vol. 49, no. 4, pp. 939–943, Nov. 2003. Cited on page 191.

[214] S. Walklin and J. Conradi, "Effect of Mach-Zehnder modulator DC extinction ratio on residual chirp-induced dispersion in 10-Gb/s binary and AM-PSK duobinary lightwave systems," *IEEE Photonics Technology Letters*, vol. 9, no. 10, pp. 1400–1402, Oct. 1997. Cited on page 192.

[215] S. L. Zhang, P. M. Lane, and J. J. O'Reilly, "Assessment of the nonlinearity tolerance of different modulationschemes for millimeter-wave fiber-radio systems using MZ modulators," *IEEE Transactions on Microwave Theory and Techniques*, vol. 45, pp. 1403–1409, Aug. 1997. Cited on page 195.

[216] D. A. Frickey, "Conversions between S, Z, Y, H, ABCD, and T parameters which arevalid for complex source and load impedances," *IEEE Transactions on Microwave Theory and Techniques*, vol. 42, no. 2, pp. 205–211, Feb. 1994. Cited on page 198.

[217] P. Grivet, *Physique des lignes de haute frquence et d'ultra-haute frquence - Tome II.* Paris: Masson., 1974. Cited on page 199.

[218] I. Reed, "On a moment theorem for complex Gaussian processes," *IEEE Transactions on Information Theory*, vol. 8, no. 3, pp. 194–195, Apr. 1962. Cited on page 201.

[219] L. Gu, W. Jiang, X. Chen, and R. T. Chen, "Silicon Photonic Crystal Waveguide Modulators," in *Group IV Photonics, 2006. 3rd IEEE International Conference on*, Ottawa, Ont., 2006, pp. 43–45. Cited on page 209.

[220] G. V. Treyz, "Silicon Mach-Zehnder waveguide interferometers operating at 1.3 µm," *Electronics Letters*, vol. 27, pp. 118–120, Jan. 1991. Cited on page 209.

[221] Q. Xu, B. Schmidt, S. Pradhan, and M. Lipson, "Micrometre-scale silicon electro-optic modulator," *Nature*, vol. 435, no. 7040, pp. 325–327, May 2005. Cited on page 209.

[222] K. Samardzic, "Pico cell radio base unit for a centralized wireless access architecture," in *Telecommunications in Modern Satellite, Cable and Broadcasting Service, 2003. TELSIKS 2003. 6th International Conference on*, vol. 1, Oct. 2003, pp. 101–103. Cited on page 209.

[223] R. Watanabe, Y. Horiuchi, H. Tanaka, and M. Suzuki, "Optical modulation characteristics of 5.8 GHz OFDM signal with electro-absorption modulator," in *Proceedings of International Topical Meeting on Microwave Photonics (MWP2002)*, Awaji, Japan, 2002, pp. 221–4. Cited on pages 209 and 210.

[224] S. Yaakob, M. A. Ismail, R. Mohamad, M. R. Yahya, A. F. A. Mat, M. R. Mokhtar, and H. A. A. Rashid, "Adopting Electroabsorption Modulator for the WLAN 802.11a Radio over Fibre System," in *Semiconductor Electronics, 2006. ICSE '06. IEEE International Conference on*, Kuala Lumpur, Malaysia, Oct./Dec. 2006, pp. 871–875. Cited on page 209.

[225] G. Metivier and M. A. Ali, "Simulation of multi-channel AM-VSB CATV optical link employing semiconductor optical amplifier as an external modulator," *IEEE Photonics Technology Letters*, vol. 8, no. 1, pp. 122–124, Jan. 1996. Cited on pages 209 and 213.

[226] E. Udvary, T. Berceli, T. Marozsak, and A. Hilt, "Semiconductor optical amplifiers in analog optical links," *Transparent Optical Networks, 2003. Proceedings of 2003 5th International Conference on*, vol. 2, no. -, p. 206 vol.2, 2003. Cited on pages 209 and 213.

[227] A. Tauke-Pedretti, M. Dummer, J. S. Barton, M. N. Sysak, J. W. Raring, and L. A. Coldren, "High saturation power and high gain integrated photoreceivers," *IEEE Photonics Technology Letters*, vol. 17, no. 10, pp. 2167–2169, Oct. 2005. Cited on page 209.

[228] L. H. Spiekman, "Semiconductor optical amplifiers for reconfigurable optical networks (Invited)," *Journal of Optical Networking*, vol. 6, no. 11, pp. 1247–1256, Nov. 2007. Cited on page 213.

[229] F. Koyama, T. Yamatoya, and K. Iga, "Highly gain-saturated GaInAsP/InP SOA modulator for incoherentspectrum-sliced light source," in *Indium Phosphide and Related Materials, 2000. Conference Proceedings. 2000 International Conference on*, Williamsburg, VA, USA, 2000, pp. 439–442. Cited on page 213.

[230] G. Giuliani, P. Cinguino, and V. Seano, "Multifunctional characteristics of 1.5-m two-section amplifier-modulator-detector SOA," *IEEE Photonics Technology Letters*, vol. 8, no. 3, pp. 367–369, 1996. Cited on page 213.

[231] J. Mork, A. Mecozzi, and G. Eisenstein, "The modulation response of a semiconductor laser amplifier," in *Selected Topics in Quantum Electronics, IEEE Journal of*, vol. 5, no. 3, Nara, May/Jun. 1999, pp. 851–860. Cited on pages 213 and 214.

[232] F. Girardin, G. Guekos, and A. Houbavlis, "Gain recovery of bulk semiconductor optical amplifiers," *IEEE Photonics Technology Letters*, vol. 10, no. 6, pp. 784–786, Jun. 1998. Cited on page 214.

[233] A. A. M. Saleh, "Modeling of nonlinearity in semiconductor optical amplifiers," in *Global Telecommunications Conference, 1989, and Exhibition. 'Communications Technology for the 1990s and Beyond'. GLOBECOM '89., IEEE*, Dallas, TX, Nov. 1989, pp. 665–670. Cited on pages 214 and 215.

[234] J. Herrera, F. Ramos, and J. Marti, "Nonlinear distortion generated by semiconductor optical amplifier boosters in analog optical systems," *Optics Letters*, vol. 28, no. 13, pp. 1102–4, Jul. 2003. Cited on pages 214 and 215.